High-fidelity Hydrostructural Optimization of Composite Hydrodynamic Lifting Surfaces

by

Yingqian Liao

A dissertation submitted in partial fulfillment
of the requirements for the degree of
Doctor of Philosophy
(Naval Architecture and Marine Engineering and Scientific Computing)
in the University of Michigan
2021

Doctoral Committee:

Professor Yin Lu Young, Co-Chair
Professor Joaquim R. R. A. Martins, Co-Chair
Professor Carlos E. S. Cesnik
Professor Pingsha Dong
Associate Professor Kevin J. Maki

Yingqian Liao

yqliao@umich.edu

ORCID iD: 0000-0001-6904-8844

To my grandfather, who first taught me science, music, art, and appreciation for nature.

Acknowledgments

I feel writing acknowledgments is not easier than the rest of my dissertation as I found it difficult to enumerate all the people that have helped me during graduate school and to find words to express my thanks.

First, I want to thank my advisors, Professor Yin Lu (Julie) Young and Professor Joaquim R. R. A. Martins. I feel fortunate to work with them on this project. The work in this dissertation would not be possible without their guidance and support. Professor Young always finds time to discuss my questions, debug issues, provide constructive feedback, review my papers, and help me to improve. Likewise, Professor Martins always gives me advice on how to investigate problems, present research works, and optimize work and life. Thank you both for being patient with me and being supportive. Your knowledge and advice do not only help me do better research but also help my self-development in various aspects.

I thank Professor Kevin Maki, Professor Carlos Cesnik, and Professor Pingsha Dong for sharing their knowledge and expertise in and outside class. Thank you for serving on my committee. I appreciate your valuable feedback on my doctoral work.

The work in this dissertation is supported by US Office of Naval Research, Contracts N00014–16–1–2972 and N00014–18–1–2333 managed by Ms. Kelly Cooper, and N00014–19–1–2017 managed by Dr. Ki-Han Kim. Thank you, Ms. Cooper and Dr. Kim, for the funding support.

I would like to thank people in the MDO Lab and colleagues at the Naval Architecture and Marine Engineering Department. Everyone has helped me in different aspects and made my graduate school a wonderful time. I would like to thank Nitin Garg for assisting me to start my Ph.D. research. Tim Brooks helped me to get started and get familiar with TACS. I thank Charles (Sandy) Mader for patiently helping me understand the framework and assisting me to identify problems. There were many times that Anil Yildirim helped me tackle convergence issues and his work provides a foundation for the work presented in this dissertation. I appreciate Sicheng He's guidance on coupled adjoint development and debugging. I would like to thank Yayun Shi and Ping He for improving my CFD meshing skills, and Nicolas Bons for sharing his knowledge and experience with MACH. Thank you, Neil Wu, Marco Mangano, and Galen Ng, for helping me review and improve this dissertation. To John Jasa, Shamsheer Chauhan, Eirikur Jonsson, Sabet Seraj, Alastair

Gray, Joshua Anibal, Xiaosong Du, Deniz Akcabay, Rachel Gouveia, Jacob Woeste, Manavendra Desai, Sharath Yerneni, Zetao Jin, Xianjun Pei, Yuning Zhang, Ping Wang, and Yuxi Zhang, thank you for many technical, professional, and philosophical discussions that fulfill my Ph.D. journey.

I also want to thank other people I met at the University of Michigan: the students and researchers (Shue Wang, Luciana Rosselli-Murai, Matthew Boban, Catherine Snyder, Kenneth Ho, Andrea Poli, James Gose) who helped me and gave me advice while I was doing shockwaves experiments; two great ELI lecturers who helped me improve on academic writing, Trisha Dowling and Christine Feak; Lisa Kisabeth and Nathalie Fiveland who are always helpful with my administrative problems.

I thank my two roommates Ying Wang and Hao Yuan for their accompany and making the living place like home. I would also like to thank my friends who are physically on the other side of the ocean but always virtually stand by me.

Lastly but certainly not least, I want to deeply thank my family for their understanding, trust, and love. I would not be here without your sacrifice and support.

TABLE OF CONTENTS

Chapter

LIST OF FIGURES

FIGURE

LIST OF TABLES

TABLE

LIST OF APPENDICES

APPENDIX

LIST OF ACRONYMS

CFD computational fluid dynamics

BEM boundary element method

FEM finite element method

MDO multidisciplinary design optimization

RANS Reynolds-averaged Navier–Stokes

NAB nickel aluminum bronze

FFD free-form deformation

FSI fluid-structure interaction

LES large eddy simulation

CFRP carbon fiber reinforced polymers

GFRP glass fiber reinforced polymers

MACH MDO for aircraft configurations with high-fidelity

TACS Toolkit for the Analysis of Composite Structures

LIST OF SYMBOLS

A_ref	Reference area [m^2] $A_\text{ref} = bc_\text{mean}$
$\bar{A}_\text{cav}$	Non-dimensionalized weighted cavitation inception area
C_{l_2D}, C_l	Sectional 2-D lift coefficient
C_{dv_2D}, C_{dv}	Sectional friction drag coefficient
C_{d_2D}, C_d	Sectional total drag coefficient
C_f	Skin friction coefficient
P_atm	Atmospheric pressure [kPa]
P_vapor	Saturated vapor pressure [kPa]
b	Semi-span [m]
g	Gravitational constant [m/s^2]
c	Chord [m]
h	Water depth [m]
k	Transition sharpness parameter
γ	Transition shift parameter
c_root	Root chord [m]
c_mean	Mean chord [m]
C_L	Lift coefficient, $C_L = \frac{L}{0.5\rho_\text{water}U_\infty^2 A_\text{ref}}$
C_D	Drag coefficient, $C_D = \frac{D}{0.5\rho_\text{water}U_\infty^2 A_\text{ref}}$
C_p	Pressure coefficient, $C_p = \frac{P_\text{local}-P_\text{ref}}{0.5\rho_\text{water}U_\infty^2}$
E_i	Young's modulus [GPa]
KS_f	Aggregated material failure indicator
G_{ij}	Shear modulus [GPa]
S_{ij}	Shear strength [MPa]
Y_T	Longitudinal tensile strength [MPa]
Y_C	Longitudinal compressive strength [MPa]
X_T, Z_T	Transverse tensile strength [MPa]
X_C, Z_C	Transverse compressive strength [MPa]
f	Material failure indicator
ν_{ij}	Poisson's ratios
ω	Bending displacement [m]
wt	Weight
Re_rc	Root chord based Reynolds number, $Re = \frac{\rho_\text{water}U_\infty c_\text{root}}{\mu}$
σ_v	Von Mises stress [MPa]
σ_{ij}	Stress [MPa]

σ	Cavitation number
ρ_{CFRP}	CFRP density [kg/m^3]
ρ_{water}	Water density [kg/m^3]
ρ_{KS}	Aggregation parameter in KS function
ρ_{power}	Aggregation parameter in induced power method
θ_f	Fiber orientation angle [°]
θ_{tip}	Tip twist [°]
λ	Sweep variable angle [°]. Positive values indicate backward sweep, while negative values indicate forward sweep.
U_∞	Inflow velocity [m/s]
U_{cav}	Cavitation inception speed [m/s]

ABSTRACT

To improve efficiency, functionality, and reliability of hydrodynamic lifting surfaces, such as propeller blades, control surfaces, and hydrofoils, composite materials are increasingly used because of their high strength-to-weight ratio, corrosion resistance, and desired fatigue properties. Despite these superior properties, their design remains challenging for maritime applications due to the need to operate over a broad range of flow conditions, and associated complex physics, including separation, cavitation, high loading, and complex material failure mechanisms. Additionally, considering both the coupling between fluid forces and structural responses, and the interplay effects between the many geometry and material design variables, the optimal design is not intuitive.

Multidisciplinary design optimization (MDO) is a powerful tool that can tackle these design challenges by considering various design requirements simultaneously and effectively evaluating the tradeoffs. With advances in computing, it is possible to use coupled high-fidelity hydrostructural simulations to better capture the flow physics and predict the structural failure onset. However, using high-fidelity simulations with MDO is still limited due to the high computational cost, especially when considering a large number of design variables needed for composite hydrodynamic lifting surfaces with complex geometries and material configurations. The objective of this dissertation is to use an efficient high-fidelity MDO framework to explore the design of composite hydrodynamic lifting surfaces and examine relevant design and research questions that are important but still unresolved so far. To address the issue of high computational cost, this dissertation uses a gradient-based optimization approach and leverages the adjoint method to compute the gradient efficiently. The contributions of this dissertation are the development of methods that optimize composite hydrodynamic lifting surface designs. Optimizations are performed to yield novel findings on the tradeoffs and coupling effects between design conditions and design variables.

First, a more effective cavitation constraint, a solid composite element for the structural solver, and the corresponding failure initiation criteria are implemented in the framework. Second, this dissertation pioneers the use of a displacement constraint as a surrogate for dynamic loading consideration to yield a safer and more reliable design. With these developments, this dissertation presents an optimized composite hydrofoil with significantly delayed cavitation inception. A series of optimization studies are conducted to investigate how planform variables, material configurations, and failure initiation model uncertainties affect composite lifting surface designs.

This dissertation also advances the methodology to consider a more complex detailed geometry problem – optimization of a structure with junction shape, which commonly exists and is critical to the overall performance. Specifically, this is demonstrated and investigated with hydrodynamic optimization of a hydrofoil-strut system. These optimization studies show the framework can adjust the junction shape to avoid junction cavitation and flow separation, all while improving efficiency.

The framework and presented optimization studies in this dissertation demonstrate the usefulness of the developed methods for hydrodynamic lifting surface designs. The discussions also provide valuable insights for designers and future research.

CHAPTER 1

Introduction

Climate change and environmental issues create greater incentives for decarbonization. For the marine sector, this puts pressure on decarbonizing shipping and transitioning to renewable energy. In 2018, International Maritime Organization adopted a greenhouse gas strategy that describes a vision of reducing shipping CO_2 emissions by at least 40% by 2030 compared to 2008[1]. This requirement compels the marine sector to develop novel technologies to improve efficiency and reduce fuel burn. This dissertation focuses on the design of hydrodynamic lifting surfaces because of their widespread use in surface and subsurface vehicles, energy saving systems, and energy harvesting systems. Their applications include hydrofoils, marine propellers, energy saving devices, tidal turbines, rudders, and other control surfaces.

Recent advances in material science and manufacturing technologies have provided promising solutions to increasing the efficiency of hydrodynamic lifting surfaces. However, without careful designs, composite materials can experience performance degradation, such as material failure, excessive deformation, noise, vibrations, and even instability issues. The objective of this dissertation is to use an efficient high-fidelity MDO framework to explore the design of composite hydrodynamic lifting surfaces and examine relevant unresolved design questions on performance and reliability enhancement. This chapter reviews some relevant concepts and explains how the proposed work contributes to the design of composite hydrodynamic lifting surfaces.

---

[1] `https://www.imo.org/en/MediaCentre/HotTopics/Pages/Reducing-greenhouse-gas-emissions-from-ships.aspx`

In the rest of this chapter, I first introduce why there is interest in using composite materials for hydrodynamic lifting surfaces. Next, I discuss the main design challenges for composite hydrodynamic lifting surfaces. This will be followed by the benefits of using multidisciplinary design optimization (MDO), the need for a large number of design variables and high-fidelity tools, and the importance of considering interference effects between components in designs. Lastly, I list the main contributions and explain the organization of this dissertation.

1.1 Composite hydrodynamic lifting surfaces

Conventionally, most hydrodynamic lifting surfaces have been made of metallic alloys. One advantage of using metallic materials is that it simplifies the design process because of the rigid/stiff response. Another reason for using metallic alloys is that a great deal of experience and data on their use and properties already exists, streamlining the production process. For hydrodynamic lifting surfaces, one metallic alloy commonly used is nickel aluminum bronze (NAB) [8–10]. NAB is favored because of its advantages of high-stiffness, anti-biofouling, good corrosion resistance in salt water, and high resistance to cavitation erosion.

Despite these advantages, the cost of using NAB to manufacture complex geometries is high. This high cost will eventually limit the use of NAB because advanced hydrodynamic lifting surfaces are increasingly leveraging complex geometries to increase efficiencies. In the meantime, metallic hydrodynamic lifting surfaces are reaching their performance limits. One major limitation is that a wide range of operating conditions is often required for marine structures, but these metallic hydrodynamic lifting surfaces can experience a significant performance decay at off-design conditions. This limitation results from the rigid geometries that are optimized at given design conditions but tend to be suboptimal under another load case. Another limitation is their low damping, which can cause severe vibrations and increase noise. Yet another challenge is that metals have electromagnetic signatures and are susceptible to corrosion in sea environments [9].

To address these issues, the marine sector has been developing alternatives to metallic materials.

One increasingly popular alternative is composite materials. Composite materials are often made of a polymer matrix reinforced with strong fibers. The matrix is used to bond the fibers to form a specific geometry and transmit the loading [11]. Common reinforcement materials are CFRP and glass fiber reinforced polymers (GFRP). Composite materials are preferred because of their higher strength-to-weight ratio, long fatigue life, non-existent electromagnetic signatures, corrosion resistance, and higher damping for reducing vibrations and mitigating noise [12, 13], and self-adaptability through strategic tailoring of material bend-twist coupling behaviors. The high strength-to-weight ratio enables a much lighter structure while keeping an acceptable load capacity when compared to metallic alloys [11]. Being lighter also eases offshore installations and maintenance. Although it is hard to quantify the failure performance, GFRP and CFRP generally have high strengths under fatigue loading and are more durable [11, 14]. Composite materials hardly corrode, except for galvanic corrosion, which occurs when carbon fibers are contacted with aluminum. A further benefit of using composite materials is that, it eases the sensing, control, and health monitoring of marine structures by allowing embedding optical fiber sensors inside the composites. These benefits have been demonstrated by several marine applications [15, 16]. Using embedded sensors eliminates modifications to the structure surface, which can change the hydrodynamic performance and even lead to significant performance degradation.

After the Second World War, composites were increasingly used for ship constructions, but mainly non-critical parts [9]. Among these early applications, lifting surface examples include fins and rudders. It was not until the 1960s that a Soviet fishing vessel first adopted a composite propeller [9]. Later on, most of the publicly known composite propeller applications were for recreational crafts. There are several recent uses on larger ships, including the Triton Trimaran by QinetiQ, a Netherland Navy mine hunter, the 499G/T Chemical Tanker “TAIKO-MARO”, and the vessel in the FabHeli project [17, 18]. On the renewable energy side, during the last two decades, many tidal turbine projects have used composites for blade constructions. These include SeaGen by Marine Current Turbines (now SIMEC Atlantis Energy), AR1500 and AR2000 by SIMEC Atlantis Energy, and SR2000 and O2 turbines by Orbital Marine Power Ltd. A wider use can be observed in modern sailing boat designs. Overall, although composites are increasingly used for the main loading (lifting) devices in water, the applications so far are still limited to recreational vessels.

On the other hand, composite materials have already been widely used in aerospace and wind energy applications. CFRP have become one of the main materials in aircraft since their introduction in the 1970s [19, 20]. Aeroelastic tailoring via composite material layup has shown to be capable of increasing the critical divergence and flutter speed [21]. A more recent work by Brooks et al. [22] showed a reduction in fuel burn and wing weight when using numerical optimization to design high-aspect-ratio wings with composites. Hayat and Ha [23] showed that adding ply-thickness unbalance to ply-angle and ply-material unbalances in wind turbine design reduced the fatigue load and reduced the pitch-actuator duty. Many concepts in aeroelastic tailoring are beneficial for hydrodynamic lifting surface designs in similar manners [24]. However, compared to in-air designs, hydrodynamic lifting surfaces face additional design challenges due to the harsh marine environment and higher loadings caused by the high fluid density of water.

1.2 Design challenges of hydrodynamic lifting surfaces

Compared to their in-air counterparts, the additional challenges originate from flow characteristics that are unique in water. For example, corrosive water environments damage structures resulting in high maintenance costs. Other unique characteristics include free surface effects, separation, cavitation, ventilation, and high fluid density, areas on which this dissertation focuses. In the following subsections, I will first review the fundamentals of these flow physics and how they impact the performance of hydrodynamic lifting surfaces, as well as a derived design challenge of evaluating the tradeoffs between the associated design considerations.

1.2.1 Free surface effects, separation, cavitation, and ventilation

Generally, a free surface refers to the interface between two homogeneous fluids. In the context of this dissertation, the free surface is the air-water interface in oceans, seas, rivers, and lakes. The free surface has both unsteady and steady influence on the hydrodynamic lifting surface forces and motions. These effects pose challenges on vehicle maneuvering, positioning controls, and stabilities. One important free-surface effect is wave motions. Water waves cause perturbations in marine environments, and they are unique to hydrodynamics. Wave motions change the inflow directions and velocities for hydrodynamic lifting surfaces and hence lead to changes in the effective angle of attack, load fluctuations, wave-induced motions, and vibrations [25]. In addition to the unsteady and oscillatory wave effects, the presence of the free surface also affects the steady lift and drag of hydrodynamic lifting surfaces [2]. These forces can change with the submergence depth and the operating speed.

Another phenomenon of concern is flow separation. Separation occurs when the boundary layer encounters a strong adverse pressure gradient and detaches from the surface. Flow separation can increase drag substantially and lead to efficiency loss. Additionally, the induced vortex shedding can cause vibrations and noise, which impair the system performance. Although separation is not unique to hydrodynamics, its relationships with other flow physics, such as cavitation and ventilation, can potentially make the outcome worse.

Cavitation and ventilation are special forms of multiphase separated flow. When operating near the free surface, cavitation and ventilation are likely to happen due to low hydrostatic pressures and vicinity to an air source. Susceptibility increases with operating speeds because higher speeds are associated with lower local pressure on the lifting surface, which will act to draw the free surface down. This interaction with the free surface and waves can generate vortices, which can become paths for air ingress. When cavitation or ventilation is well developed, the induced air bubbles can expand to larger scale cavities, which affect the surrounding flow and the forces on structures [26]. Specifically, they can cause loss of mean lift or thrust, load fluctuations, noise, and vibrations for hydrodynamic lifting surfaces [27, 28]. While both are harmful to the operations of the structures that are not designed to cavitate or ventilate, their physics are fundamentally different.

To introduce cavitation, we can borrow the concept of boiling, which is similar to cavitation but is more widely known. Cavitation is similar to boiling in that it involves a phase change, from liquid to vapor. However, the phase change to vapor follows different thermodynamics paths. Cavitation occurs when the local absolute pressure drops to or becomes slightly lower than the saturated vapor pressure, while boiling begins at sufficiently high temperature [29, 30]. Different types of cavitation include bubble cavitation, attached cavitation, cloud cavitation, vortex cavitation, and shear cavitation [30, 31]. Depending on the position of cavity collapse on the lifting surface, the induced cavities can be characterized as partial cavities or super cavities [26]. The cavity is called a tip vortex cavity once vapor develops somewhere in the low pressure and high vorticity tip vortex core. Once cavitation develops, not only does the large-scale cavity shedding damage the structures, but the formation and collapse of cavitation bubbles can lead to local shock impact on the structures, which can cause surface erosion and material failure [32, 33]. Hence, avoiding cavitation is crucial to hydrodynamic lifting surfaces when possible, especially composite ones because composites are less resistant to cavitation pitting damage.

Ventilation is fundamentally different from cavitation because it does not involve a phase change. Instead, ventilation is the entrainment of non-condensable gas into the region surrounding the structures, which requires a gas resource to develop the cavity. For a surface-piercing hydrofoil, the flow is fully wetted when there is no significant gas entrainment. In terms of ventilated flow, there are two main flow regimes: fully ventilated and partially ventilated [1], as shown in Figures 1.1 and 1.2, respectively. Fully ventilated flow develops when the air is entrained and a cavity develops across the entire submerged span on the suction side. The flow is partially ventilated when the cavity does not cover the entire submerged span (Figure 1.2a and Figure 1.2b).

Cavitation and ventilation are tied to flow separation. Flow separation increases disturbance, which introduces a higher level of microscopic voids and weakness in the liquid, stimulating cav-

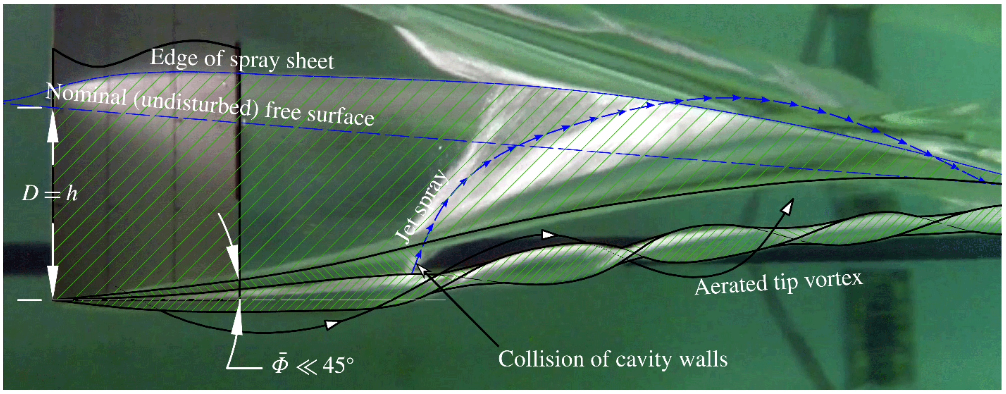

Figure 1.1: Fully ventilated surface-piercing hydrofoil [1]

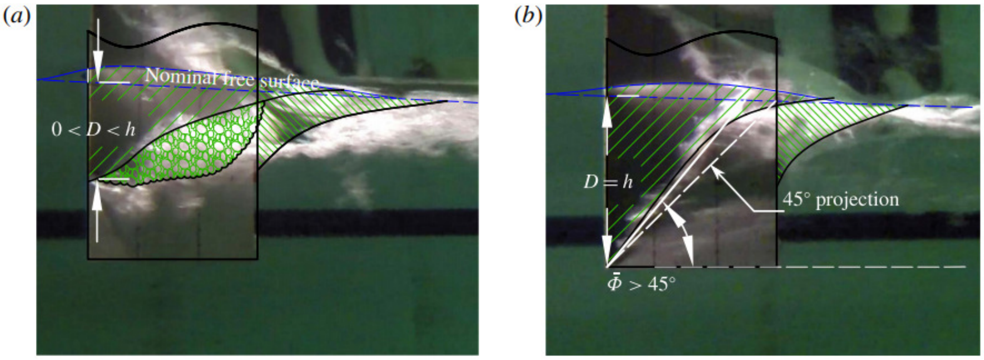

Figure 1.2: Partial ventilation of a surface-piercing hydrofoil [1]

itation [26, 29, 30]. Separated regions can also trap these voids so that microbubbles grow and expand. Experimental studies have shown that ventilation correlates to boundary layer separation [34, 35]. To prevent deterioration in the system performance, shape optimization, sensing, and control techniques have been used to avoid separation, cavitation, and ventilation.

1.2.2 High loading in marine environments and fluid-structure interaction response

Another unique characteristic that presents challenges to hydrodynamic lifting surface designs is the high loading in water environments. Hydrodynamic loadings are proportional to water density, which is three orders of magnitude higher than air. This higher density results in higher loading compared to aerospace and wind energy applications. For instance, one pronounced consequence is the added mass effect. Added mass is a weighted integration of the mass of fluid particles whose acceleration is affected by body movements [36]. This increased fluid inertial force lowers the natural frequencies compared to in-air operating conditions and can change the modal response of the structures. The modal response governs the vibration characteristics of the structure. Hence, the fluid forces can have a strong influence on the dynamic response, and a higher nonlinearity is introduced as the fluid forces depend on the direction and speed of movements. The strong coupling between fluid forces and structural response raises the need for consideration of fluid-structure interaction (FSI) during design.

As the solid-to-fluid density ratio lowers from a value between 7–8 for NAB to below 1.5 for composites, fluid inertial and damping effects become much more critical than metallic designs [8, 37]. Due to the strong fluid inertial effect, composite hydrodynamic lifting surfaces have lower resonance frequencies in water than their metallic counterparts, which make them more susceptible to resonance [8, 38]. Composite hydrodynamic lifting surfaces have a greater likelihood of resonance, dynamic load amplifications, vibrations, noise, and hydroelastic instabilities [8, 26, 39–42]. The comparison of unsteady responses between rigid and flexible composite propellers by Motley et al. [43] shows that higher modes could be excited for adaptive propellers due to the lower natural frequencies caused by the reduced rigidity. Akcabay and Young [41, 42] also showed that new divergence and flutter modes appear in lightweight composite lifting surfaces at high speeds in water because the fluid damping and disturbance force terms are proportional to speed and speed square respectively, which affects the system natural frequencies, damping, dynamic response, and stability.

In addition, the order of the modes, the natural frequencies, and damping coefficients of hydrodynamic lifting surfaces can change with submergence, cavitation, and ventilation [44–47]. Furthermore, as the structural responses vary between different composite layup designs, the corresponding added mass effects are not the same, which further complicates the analysis and design of composite lifting surfaces. The natural frequencies of composite plates are much lower in water than in air, and the in-water to in-air frequency ratios for different modes change with fiber orientation [48]. This change in natural frequencies in water can lead to frequency coalescence and associated dynamic loading amplifications [49].

Due to the higher hydrodynamic loading, hydrodynamic lifting surfaces tend to have solid interior structures rather than the hollow or core-type structures (with or without spars) that are commonly used in aerospace and wind energy applications. This solid interior structure limits the freedom to modify the center of gravity, the elastic axis position, and the structural stiffness. As a result, the shape design of hydrodynamic lifting surfaces has a direct impact on the structural response [50].

1.2.3 Tradeoffs between design considerations

The complex governing flow physics and high loading introduce a variety of design considerations, which add complexities to the design of hydrodynamic lifting surfaces. While some of these design considerations drive design variables to change similarly, some require conflicting changes. For instance, despite the reduction in frictional and form drag, a thin structure is susceptible to structural failure due to low structural stiffness and strength. Another example is the conflict between avoiding cavitation and delaying trailing edge separation. While both cavitation and ventilation are special forms of separated flow, avoiding cavitation and delaying trailing edge separation lead to different preferences on the cross-sectional shape of the hydrodynamic lifting surfaces. Since cavitation is associated with low pressure, when hydrodynamic lifting surfaces exhibit high suctions peaks, leading edge cavitation is likely to occur. To avoid these high suction peaks, it is preferred to distribute loading downstream (closer to the trailing edge), which results in high local camber near the trailing edge, as shown in Figure 1.3. While this higher camber near the trailing edge benefits cavitation performance, it increases the likelihood of separation occurrence because this high camber creates a high adverse pressure gradient that stimulates the boundary layer detachment.

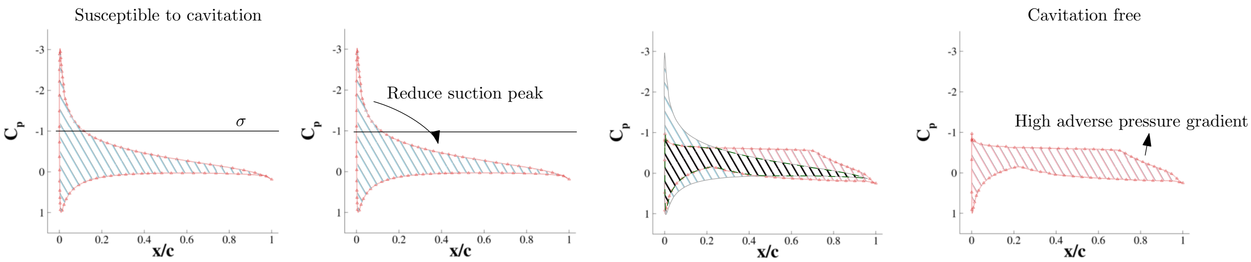

Figure 1.3: Demonstration of the contradicting effects on camber distribution between avoiding leading edge cavitation and delaying trailing edge separation. With the same loading (the area inside the C_p curve), reducing the low-pressure suction peak can lead to a high adverse pressure gradient at the trailing edge.

1.3 Multidisciplinary design optimization

Advances in computing and mathematics have promoted the use of numerical methods in engineering designs. Numerical simulations provide faster performance evaluation and easier access to design space explorations. Conducting experimental testing for a full-scale product is rarely possible due to the high cost and unknown risks. Even a model scale test can be costly and have long test periods, so it is not possible for early-stage designs. Additionally, testing a scaled model might not be able to capture all physics because it is often impossible to achieve complete similarity [37, 51, 52].

Despite the increasingly powerful numerical tools, the task of finding an optimal design remains challenging due to non-intuitive relationships between various design considerations and couplings between disciplines. To be able to design hydrodynamic lifting surfaces with improved performance and conformity to stringent regulations, the tradeoffs between disciplines and design considerations need to be evaluated. MDO emerges as a solution to this problem by being able to handle the coupling between components and explore the potential of each design variable simultaneously [53], which is suitable for designing composite lifting surfaces. MDO minimizes human intervention, and this removes potential empirical bias and accelerates the design process. In the aerospace field, the attempt to use MDO in engineering designs started in the 1960s [54]. Since then, aerospace applications of MDO expand [55, 56]. In the meanwhile, MDO has received increasing interest in marine applications [57–59].

1.3.1 Optimization of composite hydrodynamic lifting surfaces

During the last two decades, researchers and designers started to investigate the design of composite hydrodynamic lifting surfaces using MDO. Lin and Lee [60] optimized the stacking sequence of composite propellers with a genetic algorithm. Plucinski et al. [61] used genetic algorithms to optimize a multi-layer composite propeller by minimizing the difference between the optimal operating angles and the deformed pitched angles over several flow conditions. Liu and Young [62] developed a two-level design methodology to optimize the performance of composite propellers using a 3-D coupled boundary element method (BEM)- finite element method (FEM) solver. Motley and Young [43] advanced the design into a probability-based method. They demonstrated the importance of considering the performance in the full operational space, and although the efficiency discrepancy is small between a rigid and an adaptive composite propeller, the composite propeller can yield improved cavitating performance significantly at both steady and unsteady conditions. Strategic layers of the composites can enable self-adaptability of flexible lifting surfaces to delay cavitation and ventilation [24, 43, 62]. The blade tip experiences high loading with the highest rotation velocity, which is needed to accommodate high advance speed. The decreased effective angle of attack induced by the material anisotropy reduces the tip loading at high speeds, and thus reduces the strength of the tip vortex and delays flow separation, which further delays tip vortex cavitation and ventilation.

1.3.2 The need for high-fidelity tools

Most of these previous works used low fidelity methods, such as potential flow methods (e.g. BEM or vortex lattice methods) and beam/plate structural models because of their low computational cost.

Inviscid methods are fast while retaining sufficient accuracy for cases where potential flow assumptions are valid. They are suitable for preliminary designs, as the range of design variables might be broad and massive iterations are needed. However, these inviscid methods fail to predict the viscous hydroelastic performance at off-design conditions that might involve separation, stall, and vortex occurrence, which can be critical for composite hydrodynamic lifting surfaces because of their flexibility, lower resonance frequencies, and unpredictable sea environments.

On the structural side, low fidelity models, such as beam models, can predict the basic structural response. However, composite structures have complex failure mechanisms that require a more accurate prediction of the structural states. Hence, high-fidelity models, such as shell or solid elements are needed to determine stress distributions and predict material failure, and eventually design structures with structural integrity. Hence, to accurately capture the FSI effect and predict fatigue performance, it is preferred to use high-fidelity models such as coupled computational fluid dynamics (CFD) and structural FEM simulations. The works in this dissertation are based on a framework that couples a Reynolds-averaged Navier–Stokes (RANS) solver and a 3-D structural FEM solver. RANS is the most prevalent CFD method used for FSI analysis of flexible hydrodynamic lifting surfaces, and it can evaluate the performance well at general design conditions, though tools using higher fidelity, such as large eddy simulation (LES) or direct numerical simulations are preferred for extreme off-design conditions such as crashback. Works have been done on using the RANS method to optimize marine lifting surfaces, such as hydrofoils [63] and marine current turbines [64]. The advantages of using coupled RANS and FEM solvers for hydrodynamic lifting surface designs have been demonstrated in several recent works [65, 66].

1.3.3 The need for detailed structural modeling and reliable material failure predictions

Depending on the combinations and layups, composite materials feature different mechanical characteristics. The failure modes and mechanisms of CFRP and GFRP are complicated due to the mixture of different materials and strong dependence on the plies' properties and manufacturing methods. Common failure modes include fiber failures, matrix cracking, and delamination. Although designing an equivalent unidirectional composite is sufficient and effective to achieve the optimal deformation and hydrodynamic performance for hydrodynamic lifting surfaces [38, 43, 66], real engineering applications are typically featured with multidirectional plies to sustain various loadings, especially in different directions. In addition, detailed modeling of the actual multidirectional plies can be important to better predict material failure, particularly for delamination.

However, even with detailed modeling of the composite plies, which can be computationally expensive because of the large number of layers present in typical full-scale composite structures, it is still challenging to accurately and reliably estimate material failure for composite structures due to the complex failure mechanisms. In the second world-wide failure exercise [67, 68], they summarized the results of twelve theories on the prediction of failure behavior of fiber-reinforced polymer composites under various triaxial loadings. The better theories could only predict no more than 40% of all test cases with a variation less than 10% compared to the experimental data [67]. Despite numerous existing failure models for composite laminates, there is high variability between each model's prediction. In the third world-wide failure exercise, a comparison between twelve failure criteria for predicting the matrix cracking damage progression in continuous fiber-reinforced polymer composites under multi-axial loadings shows that, for all the thirteen test cases, the ratio between the highest predicted value and the lowest value varied from 1.14 to approximately 20 [69]. Reasons for this large variation include material nonlinearity, lack of failure parameter data, different assumptions and simplifications in each model, and calibration of models [67, 69]. Hence, it is important to consider possible failure model uncertainties in the design and optimization of composite structures.

1.3.4 The need for a large number of design variables

The harsh environment and the demanding flow conditions drive the shapes of hydrodynamic lifting surfaces to be complex. It also has been shown that shape optimization can help to address relevant problems and mitigate damages [65, 70–75]. Marine propellers typically feature low aspect ratios and highly skewed blades to reduce the bending moment and to reduce the unsteady pressure fluctuation between propulsors and ship hulls. Figure 1.4 shows two propellers with highly complex shapes.

Figure 1.4: Propellers with highly skewed and curved blades [2]

In addition to aspect ratios and skew, for marine propellers and turbines, other geometric variables include the number of blades, blade pitch, rake, blade cross-sectional shape, overall outlines, and area. The pitch, skew, rake, and cross-section can vary along the radius. Skew and rake describe how far the blade section moves away from the reference line. Skew describes the tangential offset and rake describes the axial offset.

For the section geometry, the NACA (National Advisory Committee for Aeronautics) sections are often used due to a large amount of data and well-developed design procedures. Various other sections have also been developed to delay cavitation [70–72]. Radial pitch and geometry act to redistribute the spanwise lift to achieve desirable loading for both fluid and structure perspectives.

Advanced manufacturing technologies have promoted the use of unconventional geometries to achieve further performance improvement. We can observe this adoption in the field of competitive sailing. In the 36th America's Cup, hydrofoil-supported monohulls were used in the competition. By lifting the main hull out of the water, the vessel's resistance significantly decreases, allowing it to achieve higher speeds. The designs of the main foils and rudder varied substantially between teams. Figures 1.5 and 1.6 [3] show the designs of the main foils and rudders of the four competing teams.


(a) New Zealand team main foils

(b) Luna Rossa team foils

(c) INEOS team foils

(d) American Magic team foils

Figure 1.5: The main foil designs from the 36th America's Cup (Photo credit: Gilles Martin-Raget)

From the above examples of propeller rudders, and sailing boat foils and rudders, we observe junctions in every design. Junctions are associated with most hydrodynamic lifting surfaces be-

---

[2] https://twitter.com/EngageStrategy1/status/1355144711481282560

[3] https://www.martin-raget.com/

(a) New Zealand team rudder

(b) Luna Rossa team rudder

(c) INEOS team rudder

(d) American Magic team rudder

Figure 1.6: The rudder designs from the 36th America's Cup (Photo credit: Gilles Martin-Raget)

cause they are typically intersected with other components, such as hubs, hulls, or vertical struts. The junction shape plays an important role in vortex occurrence and interference drag. One typical junction flow problem in aerodynamics is the wing-body junction flow. Secondary flow such as horseshoe vortices and corner separation can cause performance degradation for aircraft [76]. These vortices are also common in hydrodynamics, as shown in Figure 1.7. Junction geometries also have significant impacts on structural integrity. Hence, junction shape design is critical to the performance of hydrodynamic lifting surfaces. Performing shape optimization on the junction shape can allow remarkable improvements.

The complex geometries of hydrodynamic lifting surfaces raise a need for a large number of design variables and a robust geometry parameterization tool, which are still challenges given the state-of-art design methods and geometric parameterization capabilities. For composite hydrodynamic lifting surfaces, in addition to geometric design variables, we need to consider material variables, layer thickness, and fiber orientations when fiber-reinforced polymers are used, which adds complexity to designs. As a result, it is desirable to use many design variables when designing composite hydrodynamic lifting surfaces, but this demand brings additional challenges to the computational cost, limiting most previous optimizations of composite hydrodynamic lifting surfaces to a small number of variables.

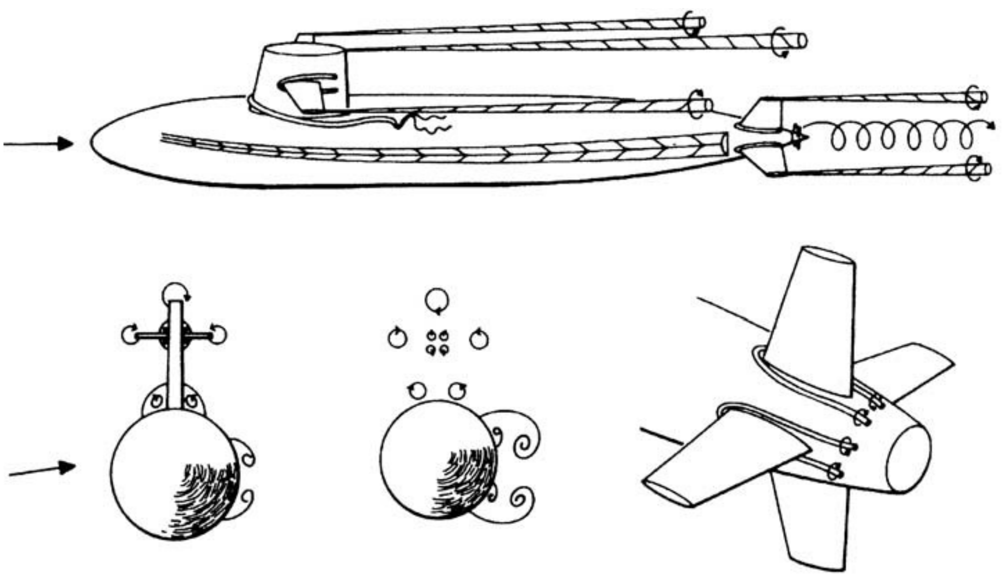

Figure 1.7: Examples of vortex configurations in hydrodynamics [2, 3]

1.3.5 Gradient-based optimization

The need for using higher-fidelity tools to predict FSI and for considering a large number of design variables in the designs motivates more efficient approaches. It has been shown that gradient-based optimization algorithms can ease this computational burden by reducing the number of evaluations [77, 78]. An efficient gradient computation approach, such as the adjoint method, offers additional improvements because the cost of computing the gradient becomes independent of the number of design variables [79–81]. In aerospace applications, the merit of high-fidelity adjoint-based optimization with a large number of variables in aerodynamic shape design has been demonstrated by Lyu et al. [82–84]. Improved performance provided to coupled aerostructural design has been shown by Kenway and Martins [85], Burdette et al. [86, 87], Brooks et al. [22, 88], and Bons et al. [89, 90]. The same methodology has been extended for hydrodynamic lifting surface designs by Garg et al. [65, 73]. They performed hydrodynamic optimization with 210 shape design variables that yielded increased lift-to-drag ratio and higher cavitation inception speed compared to a baseline NACA 0009 hydrofoil with a tapered planform. Their later work on designing flexible metallic hydrofoils with hydrostructural optimization presented an optimized hydrofoil that was thicker than the baseline but still yielded an average increase in efficiency (lift-to-drag ratio) of 29% for lift coefficients ranging from -0.15 to 0.75 compared to the baseline hydrofoil [65]. This significant improvement in the optimized hydrofoil performance compared to the baseline was confirmed via experimental measurements (29%), which compared well with numerical predictions (31%) [65, 91].

1.4 Objectives

To address the issues and the challenges associated with hydrodynamic lifting surface designs, this dissertation focuses on using MDO to design hydrodynamic lifting surfaces. The objective is to develop an efficient, high-fidelity tool for coupled hydrostructural optimization of adaptive composite hydrodynamic lifting surfaces with a large number of geometric and material design variables, to advance the geometric parametrization to include junctions, and to consider the free surface effects. This dissertation aims to answer the following major research questions:

1. How do the combined effect of material anisotropy and sweep affect the hydrostructural performance of hydrodynamic lifting surfaces?
2. How do sectional geometry and 3-D effects change the cavitation performance of hydrodynamic lifting surfaces?
3. What is the role of planform variables in designing hydrodynamic lifting surfaces?
4. How do different material configurations affect the designs?
5. How do uncertainties in material failure models affect the optimization and analysis?
6. How much benefit can optimizing the junction shape provide?

To delay separation and cavitation, reduce tip vortex, avoid material failure of composites, high-fidelity tools and a large number of design variables are needed. A gradient-based optimization with an adjoint method is used to tackle the computation cost challenge that comes with high-fidelity simulations and a large number of design variables. The work uses the MDO for aircraft configurations with high-fidelity (MACH) framework developed by the MDO Lab at the University of Michigan.

I first extend the framework's capability to predict the structural response and material failure onset of composite hydrodynamic lifting surfaces and implement the corresponding derivatives to enable efficient gradient-based optimization. Then I improve the cavitation constraint to provide more desired cavitation behavior and better optimization convergence. Using these developments in the framework, I present hydrostructural optimizations of a general 3-D composite hydrodynamic lifting surface. I perform a series of optimization studies to discuss several design and research questions: 1) how sectional geometry and 3-D effects affect cavitation performance; 2) the influence of inclusions of planform variables on cavitation-free hydrodynamic lifting surface designs; 3) the influence of different material configurations and composite material failure initiation model uncertainties on optimized designs. I extend the framework's capability to enable hydrodynamic optimization of a T-shaped hydrofoil-strut system as the first step towards high-fidelity design optimizations of a more complex system with considerations of junction geometry. I perform optimization studies to assess the tradeoffs between delaying cavitation and trailing edge separation and determine the pros and cons of designing the detailed junction geometry. Lastly, I implement an equivalent negative image method in the CFD solver and discuss how the free surface affects the steady forces on lifting surfaces at high Froude number conditions.

1.5 Thesis outline

I have provided a high-level overview of the current state and challenges for hydrodynamic lifting surfaces designs and objectives of this dissertation. I will give more specific introductions and literature reviews for each topic later in each section. This dissertation is organized as follows. In Chapter 2, I introduce the framework that is used in this dissertation. Chapters 3, 4, 5, and 6 focus on the composite hydrofoil design problem. In Chapter 3, I first explore the fundamentals of composite hydrofoils by conducting parametric studies, in which I investigate the combined effect of composite material anisotropy and sweep on a linearly-tapered canonical NACA 0009 hydrofoil. Working from this understanding of the interplay effect between planform variables and material anisotropy, I present multipoint hydrostructural optimizations of a full-scale canonical composite hydrofoil in Chapter 4. Chapter 5 investigates how different material configurations affect the designs of composite lifting surfaces. Chapter 6 examines how uncertainties of composite failure models affect the designs of composite lifting surfaces. To address the problem of a design with an intersection, I present hydrodynamic optimization studies on a T-shaped hydrofoil-strut system in Chapter 7. In Chapter 8, the formulation of the infinite Froude number boundary condition is shown. Preliminary analyses and validation are given. Lastly, Chapter 9 summarizes the conclusions, major contributions and proposes future work.

CHAPTER 2

Optimization Framework

We use the MACH framework for analyses and optimizations in this dissertation. MACH enables the optimization of lifting surfaces with respect to both external shape and structural sizing while accounting for flexibility. MACH is computationally efficient as it efficiently computes coupled derivatives required by the gradient-based optimizer using a coupled-adjoint method [92].

Figure 2.3 shows the overall optimization architecture of a hydrostructural optimization problem. Pre-processing steps shown in Figure 2.3 include geometry and mesh generations. We use ANSYS ICEM-CFD to generate surface meshes. The surface meshes are extruded to volume meshes using the pyHyp module [93], which solves hyperbolic equations to determine the volume layer positions. The generated meshes are provided to the framework. A geometry parameterization module and a mesh deformation module are used together to update the meshes for the next-step computation.

2.1 Geometric parameterization

For the geometric parametrization, we use a free-form deformation (FFD) approach that is integrated into the pyGeo module[1] [94]. In this approach, CFD surface mesh nodes and structural mesh nodes are embedded in a defined control volume defined by a set of control points, as shown

---

[1] https://github.com/mdolab/pygeo

in Figure 2.1. The parametric coordinates of the mesh points are mapped to the FFD control points using B-splines. The movements of control points move the mesh nodes through the parametric mapping. This approach allows us to define both local shape variables and global variables, such as twist and sweep, which are defined by the simultaneous displacement of groups of control points. The global variables often reply on defining a reference axis. The geometric variables will be described in detail for each problem respectively in later chapters. For the composite hydrofoil problem, the description can be found in Section 4.2.2; for the T-shaped hydrofoil-strut system, the description is given in Section 7.2.3. The geometric parametrization also allows nested FFD volumes. A two-level FFD approach will be demonstrated later in Section 4.2.2.

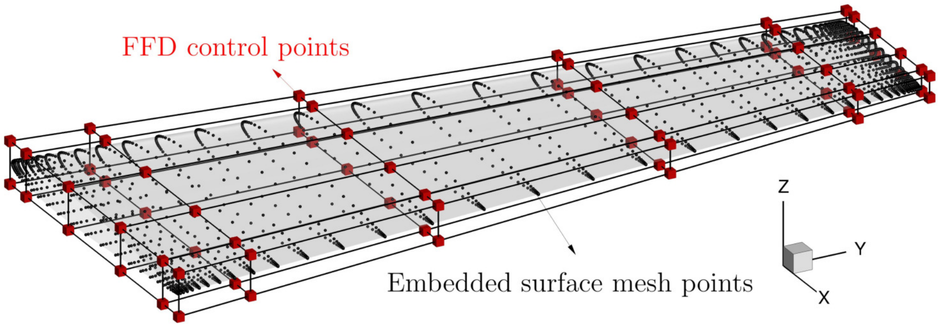

Figure 2.1: The geometric parametrization uses FFD control points to deform the embedded surface mesh points.

The geometry parametrization tool allows the users to specify geometric constraints to limit the design space, preventing infeasible results. Some geometric constraints that are used throughout this dissertation are thickness constraints and leading edge and trailing edge constraints, as depicted in Figure 2.2. At specified locations, thickness constraints are evaluated as the distances between the projected points on the upper and lower surfaces. The leading edge constraint is a linear constraint that restricts the upper and bottom FFD control points at the leading edge to move in only opposite directions with the same distance. The trailing edge constraint applies the same restriction at the trailing edge. These two constraints together avoid shear twists, which can couple with the defined twist variables and cause optimization difficulties.

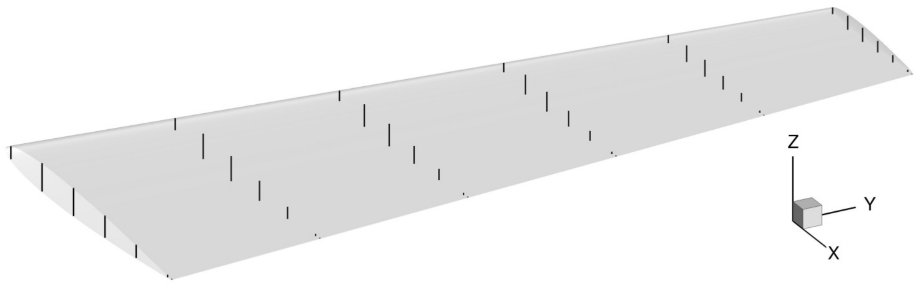

(a) Thickness constraints

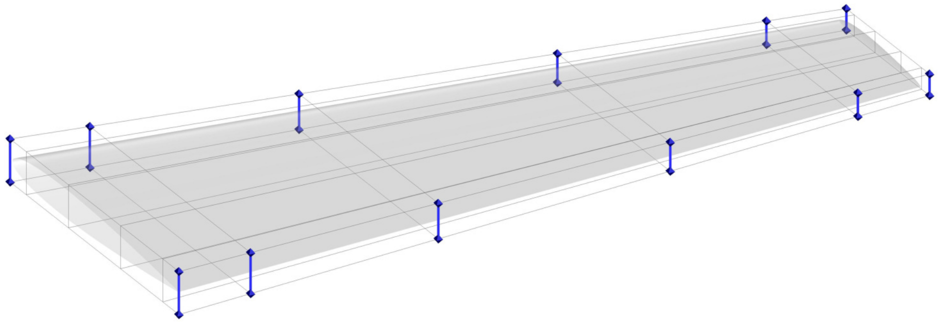

(b) Leading edge and trailing edge constraints

Figure 2.2: Geometric constraints in MACH

2.2 Multi-component surface mesh deformation

As stated above, the surface mesh gets updated according to the change of the FFD control points. However, for a problem like the hydrofoil-strut system in Chapter 7, when multiple components are involved with complex intersection features, we need an additional tool to properly manipulate the geometry and preserve the mesh quality near the intersection. Here, we use a recently developed component-based surface mesh deformation algorithm [95, 96]. We use the pyGeo module together with the pySurf module to achieve the complete function. We use separate FFD volumes to parametrize the design of each component. To track the geometric changes at the component intersection, we use triangulated surface meshes. These triangulated meshes are used to perform geometry operations, including computing piecewise linear intersection curves and feature curves. Since these triangulated meshes are not used in CFD solutions, they can be much finer than the actual CFD mesh to accurately represent the surface geometry. Once recomputing and remeshing the intersection and feature curves are complete, we use an inverse-distance weighted deformation approach to deform the CFD surface nodes near the intersection between components. This algorithm has been analytically differentiated to be suitable for use in gradient-based optimization. For more details on the surface mesh deformation algorithm, readers can refer to works by Secco et al. [95] and Yildirim et al. [96].

2.3 Volume mesh deformation

We use a mesh warping process to update the CFD volume mesh at each iteration instead of remeshing. Compared to remeshing, mesh warping is more efficient and provides a more consistent representation of the geometry throughout the optimization. For the CFD volume mesh warping process, the surface mesh deformation is propagated into volume mesh using an inverse-distance mesh warping algorithm[2] [93, 97]. The corresponding mesh deformation derivatives are computed

---

[2] `https://github.com/mdolab/idwarp`

using automatic differentiation. This mesh deformation process and the derivative computation are fully parallelized and only take about 0.1% of the CFD runtime [93]. The initial or the update CFD meshes are then provided to the CFD solver for predicting the hydrodynamic response.

2.4 CFD solver

The CFD solver used for the flow simulation is ADflow[3], which is a second-order finite volume solver [98]. ADflow can solve compressible flow with Euler, laminar Navier-Stokes, and RANS equations with multi-block meshes or overset meshes. For the results shown in this dissertation, since most cases are fully turbulent conditions, we solve the RANS equations with the Spalart-Allmaras turbulence model unless otherwise specified. For the T-shaped hydrofoil-strut system problem shown in Chapter 7, to better handle the relative movement between individual meshes and to have a better quality mesh for each component, we use the overset mesh approach in the CFD simulations [99]. In this approach, cells can be blanked, interpolated, or actual compute cells. The role of each volume cell is determined by an implicit hole cutting process [100].

We start solving the flow using a Runge-Kutta method and switch to an approximate Newton-Krylov method [101] when the residual drops certain tolerance relative to the initial free flow residual. The approximate Newton-Krylov solver can solve the flow with improved speed and robustness. After converging to a lower relative tolerance, the final convergence is achieved using a Newton-Krylov method to accelerate the process further. Kenway et al. [102] have implemented an adjoint method in ADflow to enable efficient gradient computation.

As mentioned previously, cavitation can lead to significant efficiency deterioration, material surface erosion, and cavity-induced vibrations. Although the CFD solver cannot simulate actual cavities, it can impose a cavitation constraint using a metric based on local pressure because cavitation inception is associated with low local pressure. Details about the cavitation constraint are

---

[3] `https://github.com/mdolab/adflow`

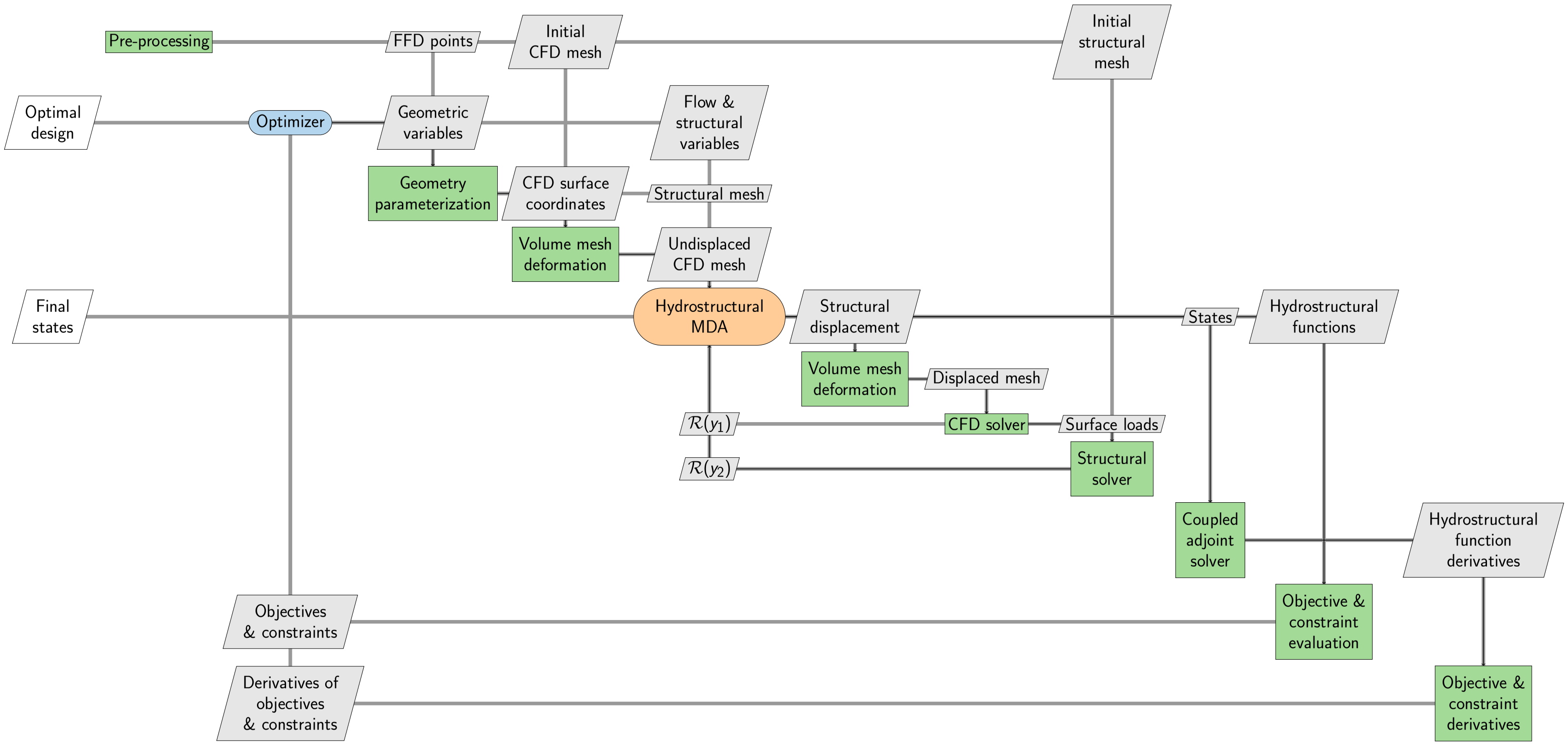

Figure 2.3: XSDM diagram of hydrostructural optimization with MACH [4]

given in Section 4.2.3. Similarly, the CFD solver can impose separation constraints based on the local flow direction. The details about the separation constraint are given in Section 7.2.

2.5 Structural solver

We use a FEM solver called Toolkit for the Analysis of Composite Structures (TACS) to solve for the structural response [103]. TACS is a parallel, general 3-D FEM solver for structural analysis that can also compute gradients using an adjoint method. It was initially developed to solve thin-shell problems typical in aircraft structures [103]. A solid interior structure is required for hydrodynamic lifting surfaces due to the higher fluid loading. Therefore, we use solid elements in the structural model, more specifically, an 8-node brick element (CHEXA8). Garg et al. [65] extended TACS to handle solid elements, which are required for accurate simulations of hydrodynamic lifting surfaces. To enable optimization of composite hydrodynamic lifting surfaces, we have added and verified an orthotropic solid element implementation [104]. In this dissertation, we only consider linear elastic structural analyses.

TACS can impose physical structural constraints, such as material failure constraint, displacement constraint, and buckling constraints. The material failure is evaluated at the centroid of each element in the structural model. Specifically, to compute the material failure for each element in the structural model, elemental centroid stresses are averaged from Gauss integration points and multiplied by a safety factor if one is considered. We use averaged stresses here because we want to avoid considering nonphysical stress singularities induced by imperfect elements in optimizations.

This dissertation does not consider progressive damage of the material or dynamic response, so the material failure is defined as the material failure initiation and assessed based on static strengths. For optimizations of composite lifting surface in this dissertation, two sets of failure initiation criteria are implemented in TACS to evaluate material failure. The first criteria (MHY) is a combination of maximum stress criterion for fiber breaking, Hashin-type criterion [5] for matrix cracking, and Ye-delamination criterion [105] for delamination. The details of this failure criteria can be found in Section 4.2.4. The second criteria (MCO) is a combination of maximum stress criterion for fiber breaking, Cuntze criterion [106] for matrix tensile cracking, and Ochoa-Engblom criterion [6] for delamination. As a result, each element has several failure values that correspond to different failure modes. We assume that once the failure initiation criteria values reach the critical value, the current element experiences material failure. Rather than considering the value for each failure mode, we use the Kreisselmeier–Steinhauser (KS) function to aggregate these different failure mode values to yield a conservative maximum approximation, which serves as the material failure value for the current element [107, 108], The purpose of using aggregation is to reduce the computational cost for adjoint calculation. For metallic cases, the material failure initiation criterion is non-dimensional von Mises stress (normalized by material yield strength). Once we compute the material failure for each element, we again use the KS function to aggregate the failure values of all elements to yield a final approximation of the maximum, which will be used as the constraint in the optimization.

2.6 Hydrostructural solver

The CFD and the structural solvers described above are coupled to predict the static hydroelastic response, including hydrodynamic loads, solid stresses, and deformations for given flow conditions. The hydrodynamic loads (pressure and shear stress distributions) computed by ADflow are transferred to the structural solver using the method of virtual work [92, 109]. The displacements from the structural solution are extrapolated to CFD surface mesh through rigid links [92, 109], and propagate to the volume mesh using the same mesh warping algorithm described in Section 2.3.

The coupled governing equations for the fluid and structure can be written as follows

$$R = \begin{bmatrix} R_F(\zeta, u) \\ R_S(u, \zeta) \end{bmatrix} = 0 \tag{2.1}$$

where R_F, ζ, represent the fluid residual and fluid states; R_S, u represent the structural residual and structural states. The coupled hydrostructural response is solved by a block Gauss–Seidel method. During each Gauss–Seidel iteration, we only partially converge the flow. Overly tight flow convergence results in unnecessary costs when the deformed shape is not close to the final state. When fluid governing equations are partially converged, the load will be evaluated and transferred to the structure. After computing the structural response, the displacements are used to deform the CFD mesh to find a new CFD solution. The calculations iterate until the pre-set coupled tolerance is achieved. The procedure is discussed in detail by Kenway et al. [92]. An efficient coupled adjoint solver is used to compute the gradients of functions of interest from the hydrostructural response. The function values and gradients are then provided to the optimizer, which will determine the design variables for the next step.

2.6.1 Gradient computation

MACH uses an adjoint method to efficiently compute the coupled derivatives with respect to a large number of variables required by gradient-based optimizers. Kenway et al. [92] derived the adjoint equations of the coupled aerostructural system based on the approach outlined by Martins et al. [110]. We briefly review the coupled adjoint method. For a given function of interest, I, the total derivative with respect to design variables x is

$$\frac{\mathrm{d}I}{\mathrm{d}x} = \frac{\partial I}{\partial x} + \begin{bmatrix} \frac{\partial I}{\partial \zeta} & \frac{\partial I}{\partial u} \end{bmatrix} \begin{bmatrix} \frac{\mathrm{d}\zeta}{\mathrm{d}x} \\ \frac{\mathrm{d}u}{\mathrm{d}x} \end{bmatrix}, \tag{2.2}$$

where ζ represents fluid states and u represents structural states. One approach to compute the total derivatives is to solve directly for $\frac{\mathrm{d}\zeta}{\mathrm{d}x}$ and $\frac{\mathrm{d}u}{\mathrm{d}x}$. However, these total derivatives are more computationally expensive than partial derivatives, as they require the solutions of the residual equation and the cost of solving the linearized residual equations is proportional to the number of design variables. For an optimization problem with a large number of variables, e.g., hydrostructural optimization, the adjoint method is preferred.

Considering the governing equations for the FSI problem in Eqn (2.1), Since the residual equation must be satisfied under any values of the design variables x, the derivatives of residuals with respect to design variables must be equal to a matrix of zeros, which are shown as follows

$$\frac{\mathrm{d}R}{\mathrm{d}x} = \begin{bmatrix} \frac{\mathrm{d}R_F}{\mathrm{d}x} \\ \frac{\mathrm{d}R_S}{\mathrm{d}x} \end{bmatrix} = \begin{bmatrix} \frac{\partial R_F}{\partial x} \\ \frac{\partial R_S}{\partial x} \end{bmatrix} + \begin{bmatrix} \frac{\partial R_F}{\partial \zeta} & \frac{\partial R_F}{\partial u} \\ \frac{\partial R_S}{\partial \zeta} & \frac{\partial R_S}{\partial u} \end{bmatrix} \begin{bmatrix} \frac{\mathrm{d}\zeta}{\mathrm{d}x} \\ \frac{\mathrm{d}u}{\mathrm{d}x} \end{bmatrix} = 0. \tag{2.3}$$

Solving for the total derivatives, $\begin{bmatrix} \frac{\mathrm{d}\zeta}{\mathrm{d}x} & \frac{\mathrm{d}u}{\mathrm{d}x} \end{bmatrix}^T$, we have

$$\begin{bmatrix} \frac{\mathrm{d}\zeta}{\mathrm{d}x} \\ \frac{\mathrm{d}u}{\mathrm{d}x} \end{bmatrix} = - \begin{bmatrix} \frac{\partial R_F}{\partial \zeta} & \frac{\partial R_F}{\partial u} \\ \frac{\partial R_S}{\partial \zeta} & \frac{\partial R_S}{\partial u} \end{bmatrix}^{-1} \begin{bmatrix} \frac{\partial R_F}{\partial x} \\ \frac{\partial R_S}{\partial x} \end{bmatrix}. \tag{2.4}$$

Substituting the solutions Eqn (2.4) into Eqn (2.2), yields,

$$\frac{\mathrm{d}I}{\mathrm{d}x} = \frac{\partial I}{\partial x} - \underbrace{\begin{bmatrix} \frac{\partial I}{\partial \zeta} & \frac{\partial I}{\partial u} \end{bmatrix} \begin{bmatrix} \frac{\partial R_F}{\partial \zeta} & \frac{\partial R_F}{\partial u} \\ \frac{\partial R_S}{\partial \zeta} & \frac{\partial R_S}{\partial u} \end{bmatrix}^{-1}}_{\Psi^T} \begin{bmatrix} \frac{\partial R_F}{\partial x} \\ \frac{\partial R_S}{\partial x} \end{bmatrix}, \tag{2.5}$$

where $\Psi = \left[\psi_F^T \;\; \psi_S^T\right]^T$ is the adjoint vector. The ψ_F and ψ_S are obtained by solving

$$\begin{bmatrix} \frac{\partial R_F}{\partial \zeta} & \frac{\partial R_F}{\partial u} \\ \frac{\partial R_S}{\partial \zeta} & \frac{\partial R_S}{\partial u} \end{bmatrix}^T \begin{bmatrix} \psi_F \\ \psi_S \end{bmatrix} = \begin{bmatrix} \frac{\partial I}{\partial \zeta} & \frac{\partial I}{\partial u} \end{bmatrix}^T , \tag{2.6}$$

which is the coupled adjoint equation. Rearrange Eqn (2.5), yields

$$\frac{\mathrm{d}I}{\mathrm{d}x} = \frac{\partial I}{\partial x} - \psi_F^T \left(\frac{\partial R_F}{\partial x}\right) - \psi_S^T \left(\frac{\partial R_S}{\partial x}\right). \tag{2.7}$$

Compared to Eqn (2.2), the adjoint method only requires partial derivatives, which are much cheaper to compute. The details of the computation of the required partial derivatives can be found in Kenway et al. [92].

2.7 Optimizer

We use SNOPT as our optimizer through the pyOptsparse interface[4] [111–113]. SNOPT is a sequential quadratic programming optimizer that solves large-scale problems with sparse nonlinear constraints. The loop continues until the feasibility and optimality conditions are satisfied. The feasibility describes the violation level of the nonlinear constraints and the optimality is the maximum complementarity gap. Both values are small when getting close to the optimal solution.

---

[4] `https://github.com/mdolab/pyoptsparse`

CHAPTER 3

Sweep and anisotropy effects on the viscous hydroelastic response of composite hydrofoils

3.1 Introduction

Hydrodynamic lifting surfaces are usually swept to improve the performance or to achieve specific functions, such as delaying cavitation and stall, reducing unsteady load fluctuations and associated pressure pulses on the hull, and avoiding entanglement with underwater debris by sweeping back to allow debris to easily slide off.

Sweep changes the hydrodynamic performance of lifting surfaces by changing the effective inflow velocity and the spanwise loading distribution through upwash and downwash [114]. Hodges and Pierce [115] illustrated the sweep effect on the aeroelastic characteristics of a wing. Sweep changes the effective streamwise angle of attack in the local foil section when the lifting surface bends due to lift, coupling the spanwise bending and torsion deformations. This sweep-induced geometric bend-twist coupling complicates the static hydroelastic response, as well as the vibration and noise characteristics of hydrodynamic lifting surfaces.

In marine propulsors, sweep is usually referred to as *skew*. Many marine propulsors are designed with highly skewed blades to delay the cavitation and alleviate the unsteady load fluctuations on the propeller blades, shaft, and hull surfaces caused by the spatially varying inflow due to hull-propulsor-rudder interactions and by shaft inclination. Experimental hydrofoil results by Ihara et al. [116] show that partial cavitation-induced oscillations were attenuated with increased sweep angle. Cumming et al. [117] also found that increasing skew led to decreased unsteady thrust and torque fluctuations, and delayed cavitation inception for marine propellers. Sweep can also cause a secondary flow and change the spanwise cavity shape and shedding frequency spectrum [116, 118].

The anisotropy effects that this dissertation focuses on are the material anisotropy effects of composites. Composite materials have a high strength-to-weight ratio, improved damping, better fatigue performance, and lower maintenance cost relative to metallic alloys [8, 9]. In addition, the material-induced bend-twist coupling can be introduced by tailoring the composite layups. Well-designed composite hydrodynamic lifting surfaces can increase the efficiency, and delay cavitation, separation, and stall [24, 38, 62].

Recent research efforts have improved the understanding of the individual effects of sweep and material anisotropy on the performance of hydrodynamic lifting surfaces, but not much work has been focused on the interplay between these two factors. Recently, Akcabay and Young [42] showed that sweep largely influenced the hydroelastic response of composite lifting surfaces. They demonstrated that divergence and flutter could be delayed or avoided by carefully designing the sweep and material anisotropy. More thorough investigations on this interplay have been done in aircraft wings [119–123]. The propensity of forward-swept wings to static divergence can be prevented by tailoring the composite layup [119]. Weisshaar et al. [122, 123] demonstrated that the bend-twist coupling induced by material anisotropy can counteract the undesirable characteristics of forward-swept wings, and discussed the influence of elastic tailoring on the spanwise center of pressure and lateral control effectiveness.

Before using MACH to design composite hydrodynamic lifting surfaces considering materials selection and ply layup, as well as geometric parameters including shape and planform variables, we first need to understand the interaction between sweep and material anisotropy in viscous flow, so that we can gain insights for our design optimization studies. To achieve this objective, the main task of this chapter is to investigate how the following hydrofoil characteristics are affected by sweep and material anisotropy: 1) in-vacuo free vibration characteristics; 2) trends of hydrodynamic coefficients, deformation, separation, stall, and static divergence behavior; 3) cavitation inception; 4) vortex structure; 5) susceptibility to material failure.

3.2 Problem setup

In this section, we will describe the problem setup, including the hydrofoil model, investigated flow conditions, and verification study.

3.2.1 Hydrofoil model

We generate simple hydrofoil models with a linear taper and a modified NACA 0009 cross-section for our studies. The hydrofoils have the same geometry as previous experimental studies [8, 124], but varying linear sweep is added. In this chapter, we will compare hydrofoils made with two different materials, stainless steel and CFRP. We use stainless steel cases with different sweep angles to investigate the sweep effects. These stainless steel cases also serve as references for investigating the effects of material anisotropy. For composite hydrofoil cases, the material is simplified as unidirectional CFRP to study the interplay between fiber angle and sweep. This model has been extensively studied experimentally and numerically in recent research [10, 66, 125]. The hydrofoils have a root chord of 0.12 m and a semi-span of 0.3 m. The sweep (λ) is defined as the angle between the mid-chord axis and the global y-axis. The fiber angle (θ_f) is defined as the angle between the fiber longitudinal direction and the mid-chord axis, as shown in Figure 3.1. The sweep angle is positive when swept backward. The fiber angle is positive when swept forward. Note that the these definitions of λ and θ_f vary slightly for Chapters 4 and 5. These differences will be explained and demonstrated later in Chapter 4. The flow velocity is aligned with the x direction and positive, as shown by the arrows in Figure 3.1.

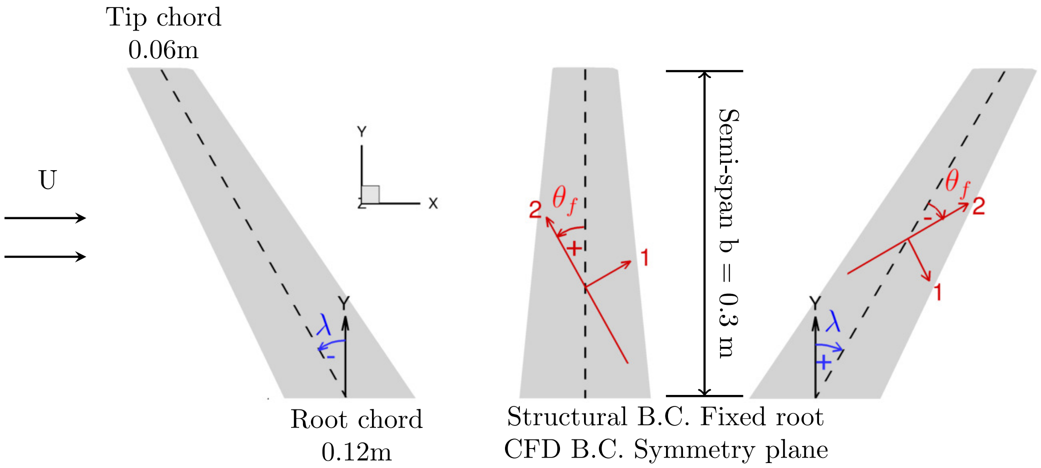

Figure 3.1: Definition of sweep (λ) and fiber angle (θ_f). The sweep angle is defined positive when swept backward. The fiber angle is defined positive when swept forward. Dashed lines represent the mid-chord axis. The material coordinates are shown in red.

Consistent mesh sizes are used for hydrofoils with different sweeps. A mesh convergence study is shown later in Section 3.2.3.1. Previous efforts have validated the CFD solver against experimental results [65, 91] and the composite solid element in the FEM solver has been verified against the commercial FEM software ABAQUS [104]. Examples of the CFD and FEM meshes of the unswept hydrofoils used in the hydrostructural simulation are shown in Figure 3.2. The CFD mesh has 10,222,080 cells and a maximum $y^+ = 0.4$, while the FEM mesh has 121,200 8-node brick elements.

The material anisotropy is modeled with orthotropic solid elements using the properties of unidirectional CFRP. The material properties are listed in Table 3.1. For stainless steel hydrofoils, we use stainless steel 316 properties, which are listed in Table 3.2.

3.2.2 Hydrofoil features, flow conditions, and post-processing

We conducted a series of modal analyses and hydrostructural simulations for nine hydrofoils featuring different sweep angles (+30°, 0°, and −30°,) and different materials (stainless steel, CFRP +30°, CFRP −30°) to compare the performance. The sweep angles and fiber angles chosen

Table 3.1: CFRP material properties, where the 1, 2, and 3 directions represent the Cartesian coordinates defined with respect to the fiber axis, as shown in Figure 3.1.

Symbol	Description	Value	Units
ρ_{CFRP}	Solid density	1590	kg/m^3
E_1,E_3	Young's modulus	13.40	GPa
E_2	Young's modulus	117.80	GPa
G_{12}, G_{23}	Shear modulus	3.90	GPa
ν_{21}, ν_{23}	Poisson's ratio	0.25	–
ν_{13}	Poisson's ratio	0.45	–
X_T, Z_T	Transverse tensile strength	81	MPa
X_C, Z_C	Transverse compressive strength	250	MPa
S_{12}, S_{23}	Shear strength	136	MPa
S_{13}	Shear strength	50	MPa

Table 3.2: Stainless steel 316 material properties

Symbol	Description	Value	Units
ρ_{steel}	Solid density	7870	kg/m^3
E	Young's modulus	200	GPa
ν	Poisson's ratio	0.27	–
σ_{yield}	Yield strength	290	MPa

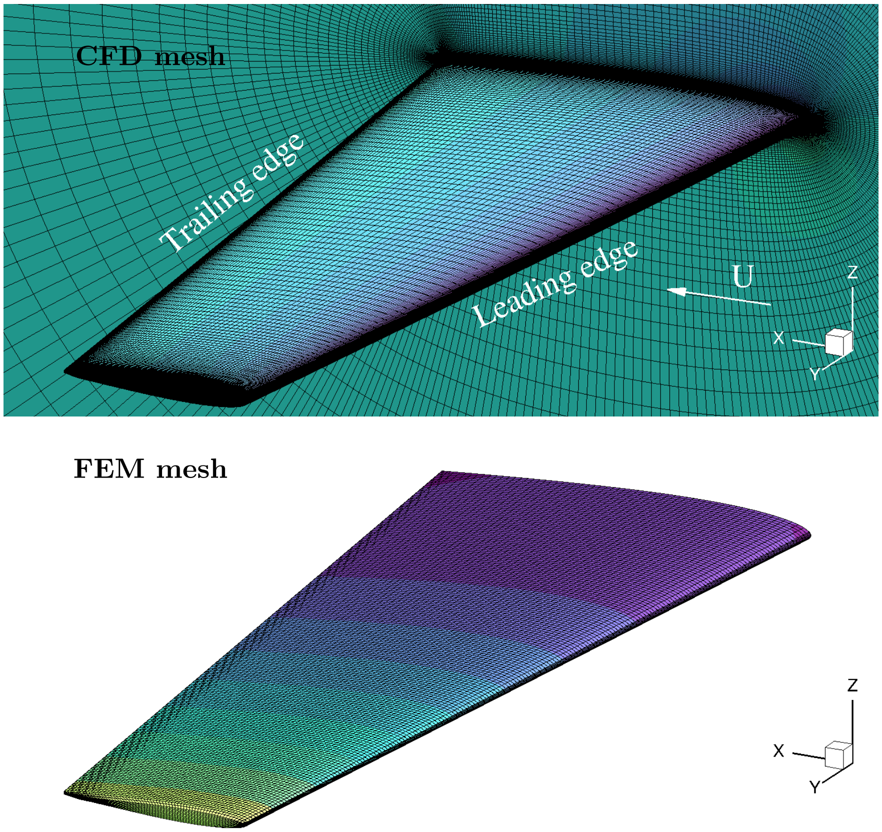

Figure 3.2: CFD and FEM meshes for the stainless steel unswept hydrofoil

here might not be practical or optimal; they are chosen to provide greatly simplified examples to show the fundamental differences in performance. To avoid confusion in the terms that refer to hydrofoils, we use “forward” to indicate the hydrofoil with the negative sweep ($\lambda = -30°$), “unswept” for $\lambda = 0°$, and “backward” for $\lambda = +30°$, together with material configurations stainless steel, CFRP $+30°$ ($\theta_f = +30°$), and CFRP $-30°$ ($\theta_f = -30°$). In reality, lifting surfaces are required to sustain a given design load, so all the hydroelastic responses shown in the results section are compared at the same lift coefficient $C_L = 0.65$ except where noted. A fixed Reynolds number of 10^6 (mean-chord based) is used in all hydrostructural simulations. We compare the vortex structures of different hydrofoils using λ_2 vortex criterion, which is one of the commonly used definitions used for vortex identification[126]. The λ_2 criterion is computed using a Tecplot add-on and the tensor eigensystem tool in Tecplot. Some observations are limited to the hydrofoil model used in this study, but the explanations and the underlying physics should be generally applicable for most hydrodynamic lifting surfaces.

3.2.3 Verification

3.2.3.1 CFD mesh convergence

To compare the performance of different hydrofoils, it is important to use CFD meshes that converge to a small tolerance and to the same level for different geometries. We compared the predicted C_L and C_D values from hydrodynamic-only simulations at angle of attack $\alpha = 4^\circ$ for five meshes with different sizes, ranging from 403,200 to 25,804,800 cells for three hydrofoils with different sweeps, as shown in Table 3.3. The C_D value for the mesh with about 10 million cells (L2) differs from the finest mesh (L1) by less than 10^{-4} and the largest C_L difference is only 0.4%, so we use the L2 CFD mesh for all our hydrostructural simulations.

3.2.3.2 FEM mesh convergence

We used modal analysis to assess the convergence of the structural meshes. We compared the first two in-vacuo natural frequencies of three different mesh sizes for three CFRP -30° hydrofoils with different sweep values. The natural frequency comparison is shown in Table 3.4. For the first in-vacuo natural frequencies, the largest discrepancy between L2 and L3 meshes is only 0.6% (backward case), and this discrepancy decreases to 0.3% between L2 and L1 meshes. For the second in-vacuo natural frequencies, the largest discrepancy between L2 and L1 meshes is only 0.4% (backward case). As a result, we select the L2 FEM mesh with 121,200 elements for all our hydrostructural simulations.

Table 3.3: Based on the CFD convergence study (hydrodynamic only, $\alpha = 4°$), we chose the L2 mesh for our hydrostructural simulations.

Mesh	Level	Mesh size	y^{+}_{max}	C_L	C_D
Unswept	L1	25,804,800	0.26	0.32769	$\underline{0.018}64$
	L2	10,222,080	0.35	0.32841	$\underline{0.018}76$
	L3	3,225,600	0.53	0.32970	0.02021
	L4	1,277,760	0.74	0.33057	0.02194
	L5	403,200	1.10	0.33163	0.02609
Forward	L1	25,804,800	0.27	0.29270	$\underline{0.0166}6$
	L2	10,222,080	0.37	0.29400	$\underline{0.0166}8$
	L3	3,225,600	0.56	0.29577	0.01786
	L4	1,277,760	0.78	0.29717	0.01934
	L5	403,200	1.10	0.29928	0.02272
Backward	L1	25,804,800	0.24	0.30377	$\underline{0.01742}$
	L2	10,222,080	0.40	0.30377	$\underline{0.01742}$
	L3	3,225,600	0.53	0.30475	0.01869
	L4	1,277,760	0.72	0.30497	0.02027
	L5	403,200	1.30	0.30386	0.02397

Table 3.4: First two in-vacuo natural frequencies of CFRP $-30°$ hydrofoils. Based on the FEM convergence study, we chose the L2 FEM mesh for our hydrostructural simulations.

Mesh	Level	Mesh size	Mode 1 (Hz)	Mode 2 (Hz)
Unswept	L1	210,816	84.998	355.516
	L2	121,200	85.139	356.221
	L3	62,208	85.391	357.461
Forward	L1	210,816	67.104	284.743
	L2	121,200	67.284	285.702
	L3	62,208	67.607	287.408
Backward	L1	210,816	57.619	244.079
	L2	121,200	57.813	245.045
	L3	62,208	58.162	246.781

3.3 Results

We first examine the influence of sweep and material anisotropy on the natural frequencies and mode shapes obtained from the modal analysis. We then compare the steady-state hydroelastic response of stainless steel, CFRP $+30^\circ$, and CFRP -30° hydrofoils for three sweep configurations at the same lift condition ($C_L = 0.65$) to investigate how sweep and material anisotropy affect the loading, flow streamlines and pressure distributions, deformation patterns, as well as the resultant forces and efficiency. Since cavitation is related to low pressure coefficient (C_p) that drops to saturated vapor pressure on the lifting surface, sectional C_p curves are shown to compare the susceptibility to cavitation. We also discuss the vortex structure based on iso-surfaces of the λ_2 criterion, since strong vortices can cause severe noise or vibration issues. Finally, we show the matrix compressive/tensile cracking index contours to assess the influence of sweep and material anisotropy on susceptibility to structural failure.

3.3.1 Modal analysis

The modal analysis computes in-vacuo natural frequencies and mode shapes, which are related to structural mass and stiffness, and can be used to predict the structural response. Additionally, we want to understand the influence of sweep and material anisotropy on the natural frequencies and mode shapes to avoid dynamic load amplification and vibrations in a real design. This is especially important for hydrodynamic lifting surfaces, where the vibration characteristics can be further complicated by hydrodynamic added mass effects, as well as speed- and frequency-dependent hydrodynamic damping and de-stiffening effects [40, 41, 44, 45, 127–129].

The first and second modes of all the stainless steel hydrofoils presented here are bending-dominated because the structural spanwise dimension (structural span) is larger than the chordwise dimension, and the hydrofoils are cantilevered at the root. Based on the first modes of stainless steel hydrofoils, these three hydrofoils primarily undergo bending when observed along the structural

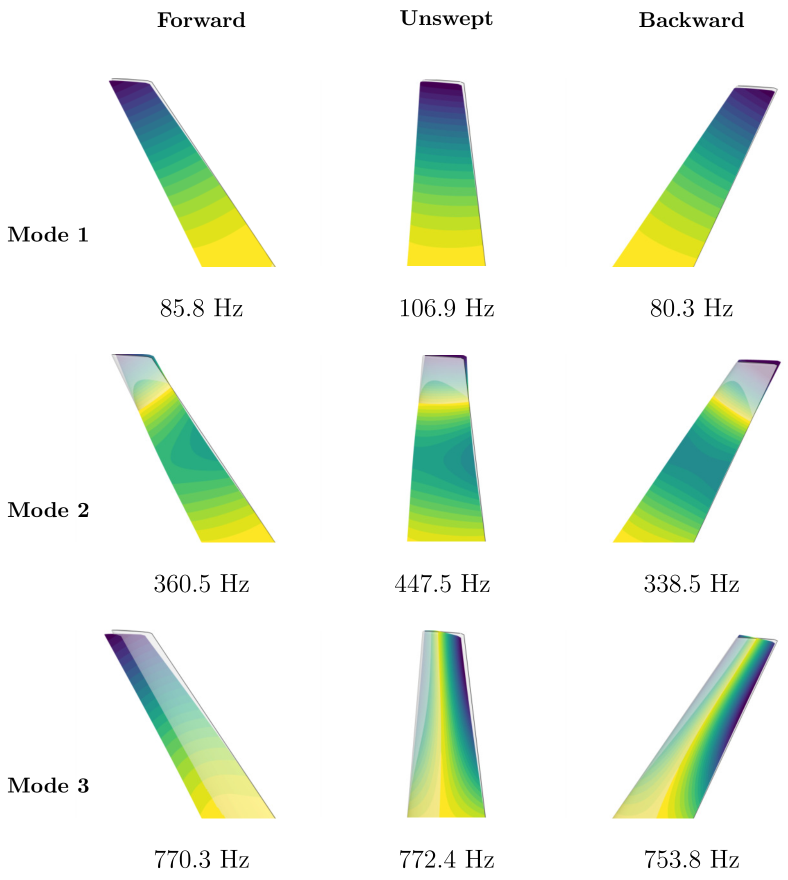

Figure 3.3: First three in-vacuo modes and natural frequencies of stainless steel hydrofoils with different sweep angles. Sweep decreases the natural frequencies because of the extended structural span. The light gray shape indicates the undeformed geometry, while the color contours of displacement magnitude are shown on the deformed geometry.

span.

As shown in Figure 3.3, sweep reduces the natural frequencies due to the extended structural span. This reduction is more significant for the bending-dominated modes than for the twisting-dominated modes. The bending rigidity of the forward stainless steel hydrofoil is decreased to the extent that its third mode is an in-plane bending mode, while the third modes for the unswept and backward hydrofoils are twisting-dominated. This difference in the third mode between forward hydrofoils and backward hydrofoils is caused by the asymmetry about the mid-chord of the NACA 0009 cross-section, which is thicker towards the leading edge.

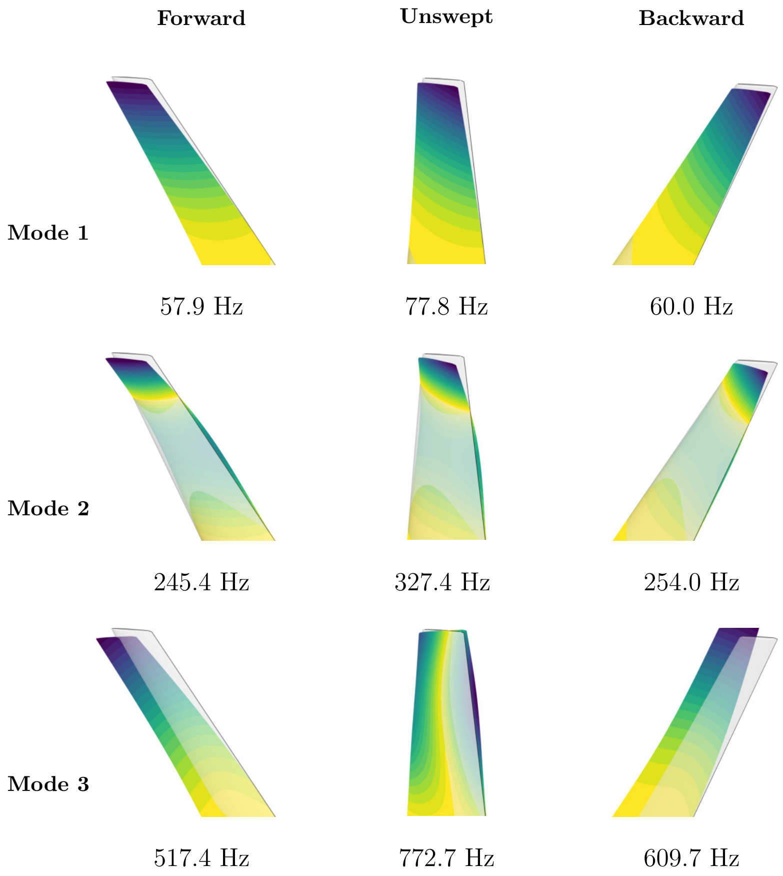

Figure 3.4: First three in-vacuo modes and natural frequencies of CFRP +30° hydrofoils with different sweep angles. The off-axis fiber layup decreases the natural frequencies. The light gray shape indicates the undeformed geometry, while the color contours of displacement magnitude are shown on the deformed geometry.

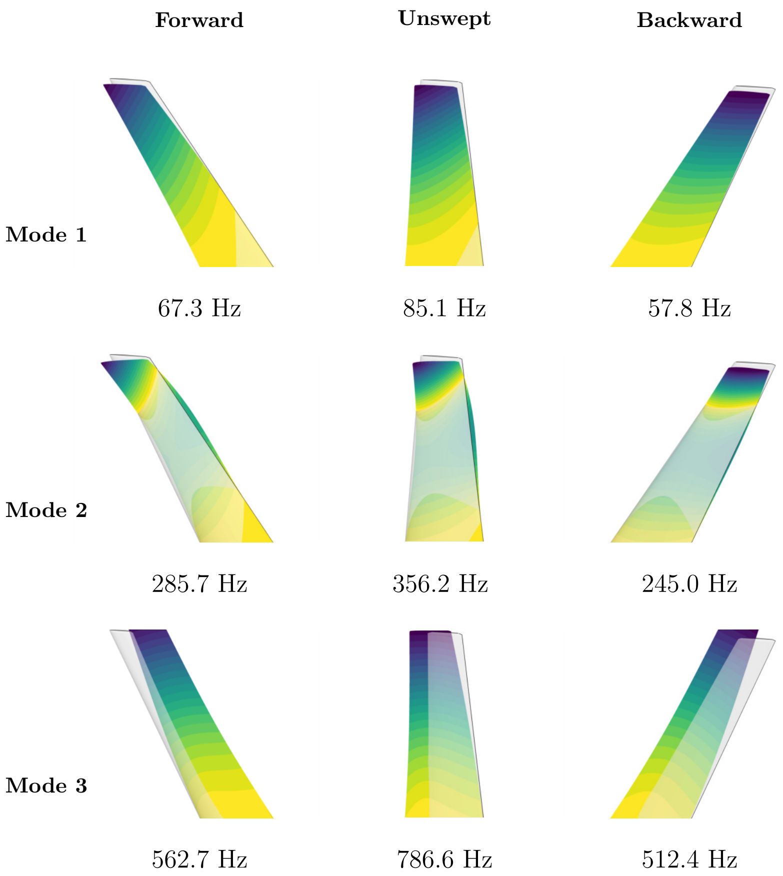

Figure 3.5: First three in-vacuo modes and natural frequencies of CFRP -30° hydrofoils with different sweep angles. The off-axis fiber layup decreases the natural frequencies. The light gray shape indicates the undeformed geometry, while the color contours of displacement magnitude are shown on the deformed geometry.

The bending mode natural frequencies are further reduced in water due to the added mass effect, particularly for lightweight composite structures that have a lower solid-to-fluid density ratio. The bending mode frequencies are expected to decrease more than the twisting mode frequencies underwater because the added mass effect is dependent on the direction of the movement, and bending motions move a higher volume of the surrounding fluid. Therefore, sweep changes the susceptibility to mode switching, since the gap between a bending mode frequency and an adjacent twisting mode frequency varies with sweep [49, 130].

Comparing Figures 3.3–3.5, we see that off-axis fiber layup further decreases the bending rigidity compared to stainless steel hydrofoils, which reduces the natural frequencies of the bending-dominated modes. For backward hydrofoils, CFRP -30° and CFRP $+30^\circ$ change the third mode from twisting-dominated to bending-dominated compared to the stainless steel hydrofoil because of the lower bending stiffness. Similarly, for unswept hydrofoils, the CFRP -30° hydrofoil has a bending-dominated third mode while the stainless steel hydrofoil has a twisting-dominated third mode. Different from the CFRP -30° hydrofoil, the unswept CFRP $+30^\circ$ hydrofoil has a twisting-dominated third mode due to the cross-section asymmetry. The corresponding in-water natural frequencies and modes can be significantly different from stainless steel hydrofoils due to the direction-dependency of the added mass. Additionally, the damping coefficient in water, which is related to the modes, also impacts the vibration behavior of hydrodynamic lifting surfaces [40, 41, 44, 45, 127–129].

3.3.2 Steady-state hydroelastic response

The modal analysis has shown the effect of sweep and material anisotropy on the structural stiffness, which can affect the hydroelastic response. To understand the influence of sweep and material isotropy on the hydroelastic response, we compare the hydrostructural simulation results of different hydrofoils at the same loading condition ($C_L = 0.65$), as shown in Figure 3.6. The comparison includes the hydrodynamic efficiency (lift-to-drag ratio), tip twist angle θ_{tip}, pressure contours, streamlines, spanwise sectional lift coefficient C_l, and normalized lift distributions. Note that C_l and $C_{l_{\text{2D}}}$ are used interchangeably in this dissertation, both representing 2-D sectional lift coefficient. The spanwise C_l distribution is the sectional lift coefficient along the span, while normalized lift distribution is the lift per unit length normalized by the total lift along the span.

We first compare results of hydrostructural simulations of the stainless steel hydrofoils, and then results of the composite hydrofoils with different fiber orientation and sweep angles to demonstrate the interaction between sweep and material anisotropy. All hydrofoils shown here bend up (towards the suction side) for all cases when the lift is positive.

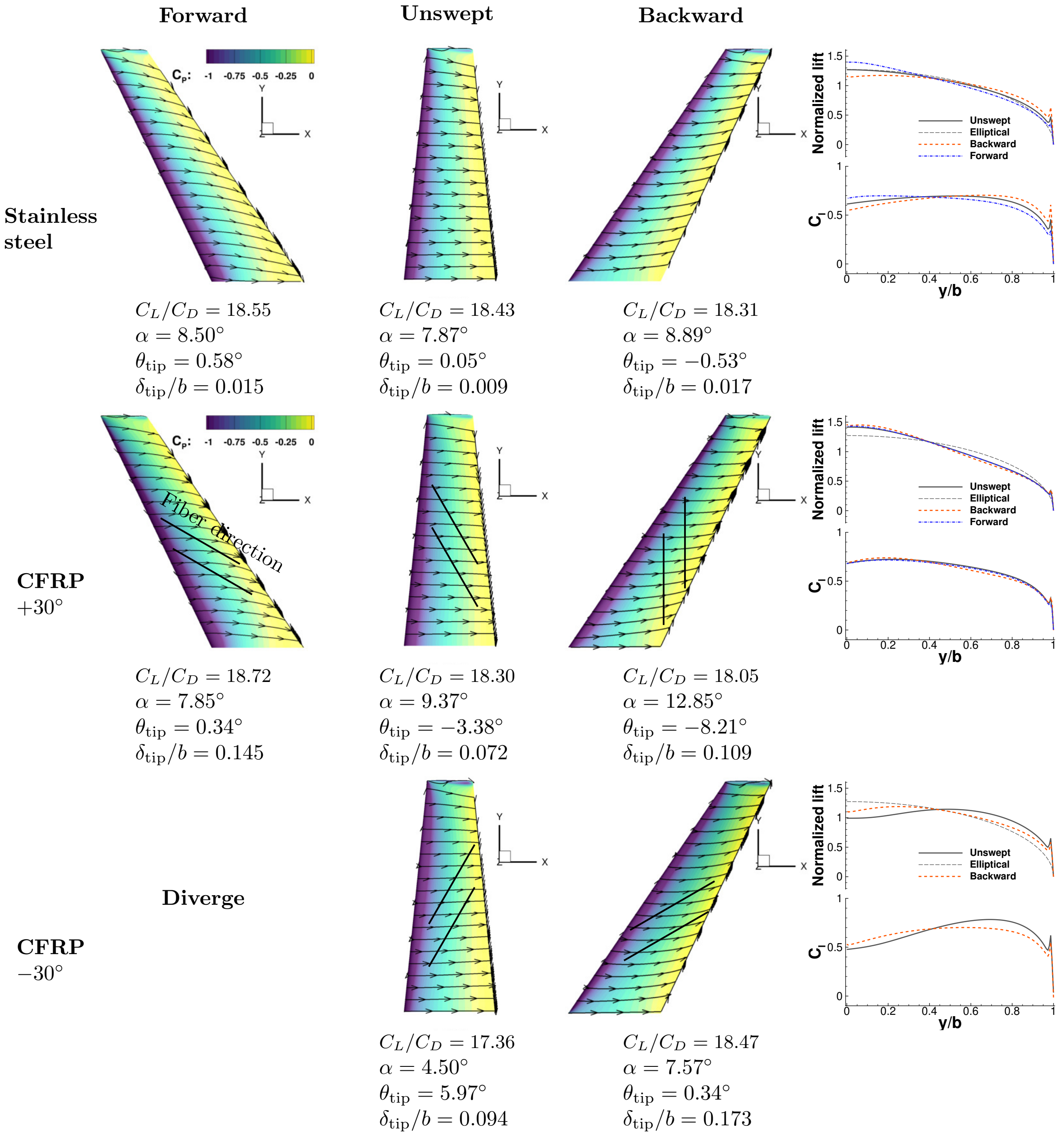

Figure 3.6: Hydroelastic response of different hydrofoils at $C_L = 0.65$, showing pressure contours and streamlines on the suction side. The right column shows the spanwise C_l and normalized lift distribution. The black solid lines represent the fiber direction. The forward CFRP $-30°$ hydrofoil diverges due to the excessive nose-up bend-twist coupling.

3.3.2.1 Influence of Sweep

The effects of sweep can be discussed based on the hydroelastic responses of the stainless steel hydrofoils, which are shown in the first row in Figure 3.6. According to the angle of attack (α) values listed under each hydrofoil in Figure 3.6, the required α to achieve $C_L = 0.65$ is higher for both swept hydrofoils than for the unswept hydrofoil because the effective inflow velocity and the effective incidence are reduced for swept hydrofoils.

Sweep changes the spanwise lift distribution through the vorticity-induced downwash and upwash effects. Forward sweep causes more downwash outboard and more upwash inboard, while backward sweep causes more downwash inboard and more upwash outboard [131, Sec. 9.3.4.3] [114, Sec. 8]. The C_l distribution in the first row of Figure 3.6 shows that backward sweep decreases the C_l at the root and increases the C_l near the tip, while the forward hydrofoil exhibits the opposite trend, which suggests that the backward hydrofoil has a stronger tip vortex.

This C_l redistribution caused by the sweep is also evident from the C_p contours. For the forward stainless steel hydrofoil, the negative portion (suction peak, which could lead to cavitation) on the C_p contours is smaller at the tip compared to other spanwise stations, while the suction peak is lower at the root for the backward stainless steel hydrofoil. Hence, backward sweep may increase the tendency of the hydrofoil to cavitate in the tip region, including tip vortex cavitation. Moreover, the backward hydrofoil is susceptible to the tip stall, while the forward hydrofoil is prone to the root stall. From the normalized lift distributions, the backward stainless steel hydrofoil has a higher bending moment because of the higher outboard loading.

From Figure 3.6, we see that the unswept stainless steel hydrofoil exhibits a lift distribution closer to the elliptical than the other two swept hydrofoils. This suggests a lower lift-induced drag compared to the two swept hydrofoils, since an elliptical lift distribution leads to the lowest theoretical lift-induced drag for planar wakes.

However, from the stainless steel results shown in Figure 3.6, the total drag coefficient (C_D) of the forward sweep hydrofoil decreases by 0.67% compared to the unswept hydrofoil, while sweeping the hydrofoil backward increases the drag by 0.62%. These changes in C_D are reflected in the efficiencies (C_L/C_D), since $C_L = 0.65$ for all the cases. These small drag differences are a result of both lift-induced drag and form drag. In spite of the low lift-induced drag, the form drag of the unswept hydrofoil is higher than the swept hydrofoils because of the more significant flow separation at the blunt trailing edge, so the total drag is close to that of the swept foils.

The unswept stainless steel hydrofoil has a pair of vortices that shed from the top and bottom edges of the thick trailing edge (see Figure 3.7), which indicates a strong reverse pressure gradient that could result in a von Karman vortex street with a distinct vortex shedding frequency that could result in noise and vibration issues.

On the other hand, swept foils exhibit reduced strength and coherence of the vortices shed behind the thick foil trailing edge, as evident by the less distorted streamlines. The spanwise component of flow for the swept hydrofoils (as shown by the streamlines in Figure 3.6) attenuates the reverse pressure gradient on the trailing edge, keeping the flow attached. Therefore, the unswept hydrofoil has the highest form drag, while the forward hydrofoil has the lowest.

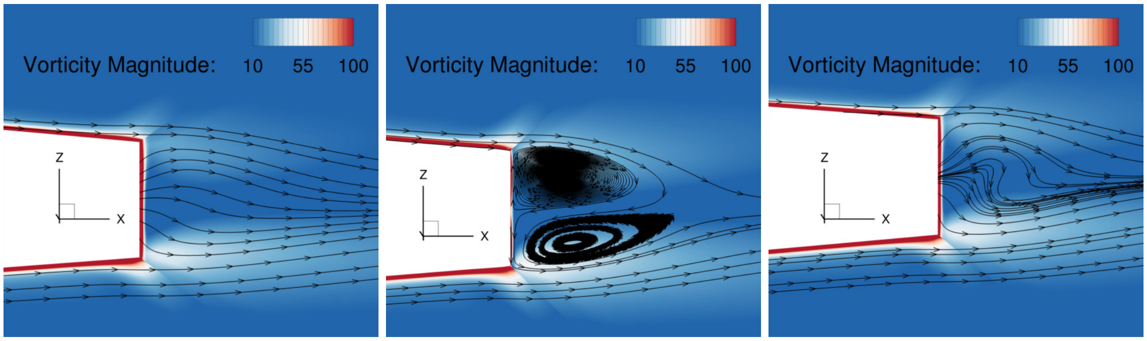

(a) Forward (b) Unswept (c) Backward

Figure 3.7: Streamlines downstream of trailing edge at the mid semi-span for forward, unswept, and backward stainless steel hydrofoils. Swept hydrofoils induce a spanwise flow, as observed in the streamlines shown in Figure 3.6, which mitigates the separation and coherent vortex structures behind the blunt foil trailing edge.

To exclude the lift-induced drag and the influence of structural displacement, we performed pure hydrodynamic simulations without structural coupling at $C_L = 0$ to compute the zero-lift

C_D. The swept forward hydrofoil has the lowest zero-lift drag coefficient ($C_D = 0.01201$), while the backward hydrofoil value is a little higher ($C_D = 0.01244$), and the unswept hydrofoil has the highest value ($C_D = 0.01315$). In addition to form drag reduction, the trailing edge vortex suppression and incoherent structure suggest the possibility of using sweep to reduce vortex-induced vibration and noise for hydrodynamic lifting surfaces, such as propellers and turbines.

In addition to changing the spanwise lift distributions, sweep also changes the deformations, as indicated by the tip deflection normalized by the semi-span (δ_{tip}/b) and tip twist angles (θ_{tip}) shown beneath the C_p contour plot for each hydrofoil in Figure 3.6. As illustrated by the stainless steel hydrofoils results without material-induced bend-twist coupling, sweep modified the deformations, although all these deformations are small because of the high structural stiffness.

From the modal analysis, we can see that sweep reduces the bending stiffness, so the δ_{tip}/b of the swept hydrofoils (either forward or backward swept) are higher than that of the unswept hydrofoil. For the unswept stainless steel hydrofoil, the θ_{tip} is positive (i.e. nose-up) because of the hydrodynamic pitching moment caused by the center of pressure being upstream of the elastic axis, as shown in Figure 3.12. In addition to the hydrodynamic pitching moment, sweep causes a geometric bend-twist coupling. As explained by Hodges and Pierce [115, 4.2.6], when observed from the direction perpendicular to the inflow, the streamwise bending gradient results in an equivalent change in the twist measured from the global y-axis, the direction perpendicular to the inflow, as shown in Figure 3.8.

The geometric bend-twist coupling is nose-up for the forward stainless steel hydrofoil, which adds to the twist caused by hydrodynamic pitching moment, as evidenced by the higher θ_{tip} value compared to the unswept case. On the other hand, the geometric bend-twist coupling is nose-down for the backward swept case, which countered the nose-up twist caused by hydrodynamic pitching moment and resulted in a net negative θ_{tip}. The nose-down twist near the tip also countered part of the higher loading near the tip caused by the induced upwash. Since the stainless steel hydrofoils are relatively stiff in terms of twist, the effect of the geometric bend-twist coupling on the spanwise loading distribution is less significant than the vorticity-induced downwash and upwash effects. Hence, if the loading is properly tailored, we can improve the performance of swept hydrofoils.

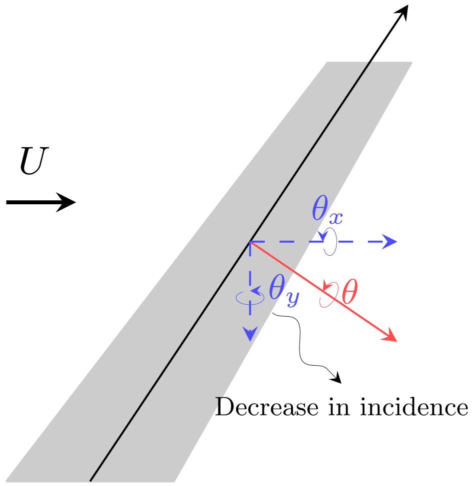

Figure 3.8: Sweep induced geometric bend-twist coupling. θ is the twist around the corresponding axis.

3.3.2.2 Coupled Influence of Sweep and Material Anisotropy

Material anisotropy can couple with sweep to change the hydrofoil deformation and thus the performance. With a positive angle of attack, positive fiber orientation (fibers swept forward) induces a bending-up and nose-down bend-twist coupling, while negative fiber orientation (fibers swept backward) causes a bending-up and nose-up bend-twist coupling.

The hydrodynamic pitching moment caused by the center of pressure being upstream of the elastic axis leads to a nose-up twist for all investigated hydrofoils here. As shown in Figure 3.6, for the unswept CFRP $+30°$ hydrofoil, the nose-down material bend-twist coupling overcomes the nose-up twist caused by the hydrodynamic pitching moment, leading to net negative θ_{tip}, which decreases the effective incidence angle, and hence requires a higher α to achieve $C_L = 0.65$ compared to the unswept stainless steel hydrofoil. The unswept CFRP $-30°$ hydrofoil exhibits the opposite trend, since both the twist caused by the hydrodynamic pitching moment and material bend-twist couplings are nose-up, and hence the required α to achieve $C_L = 0.65$ is lower than the unswept stainless steel hydrofoil. Therefore, given the same geometric configuration (the same sweep angle), the CFRP $+30°$ hydrofoils have the lowest θ_{tip} value compared to the stainless steel and CFRP $-30°$ hydrofoils.

Since both forward sweep and negative fiber orientation contribute to the nose-up twist when the hydrofoil bends up, the simulations for the forward CFRP $-30°$ hydrofoil diverged due to the excessive nose-up bend-twist coupling, and hence a rapid increase in the tip twist. A too bending-up and nose-up bend-twist coupling leads to early stall and flow-induced vibrations. Another extreme case is the backward CFRP $+30°$ hydrofoil, for which the twist is the most negative ($\theta_{\text{tip}} = -8.21°$), and the required α to achieve the target lift is the highest among all the cases investigated ($12.85°$).

3.3.3 Hydrodynamic coefficients, deformation, separation, and stall

In the previous discussion, separation does not occur at $C_L = 0.65$ for all hydrofoils except for the diverged forward CFRP $-30°$ hydrofoil. To further discuss the difference in trends, separation, and stall, we perform additional hydrostructural simulations with $\alpha = 0°$, $6°$, and $12°$, as well as at $C_L = 0.2$, 0.3, and 0.4. Figure 3.9 shows C_L, C_D, pitch moment coefficient C_M, non-dimensional tip bending δ_{tip}/b, and θ_{tip}. The C_M is calculated about the mid-chord point at the root. Separation onset is identified from the reduction in the slope of the C_L and C_M curves.

For all cases investigated, the C_L increases with α, but with different slopes, as shown in Figure 3.9. Swept hydrofoils have lower $\frac{\partial C_L}{\partial \alpha}$ slopes, as shown in the top left plot in the stainless steel results. These smaller $\frac{\partial C_L}{\partial \alpha}$ slopes are due to the decreased effective inflow velocity compared with the unswept hydrofoil.

Although the unswept stainless steel hydrofoil has a higher $\frac{\partial C_L}{\partial \alpha}$ slope, the swept stainless steel hydrofoils experience earlier separation, as suggested by the decreased $\frac{\partial C_L}{\partial \alpha}$ slopes when the angle

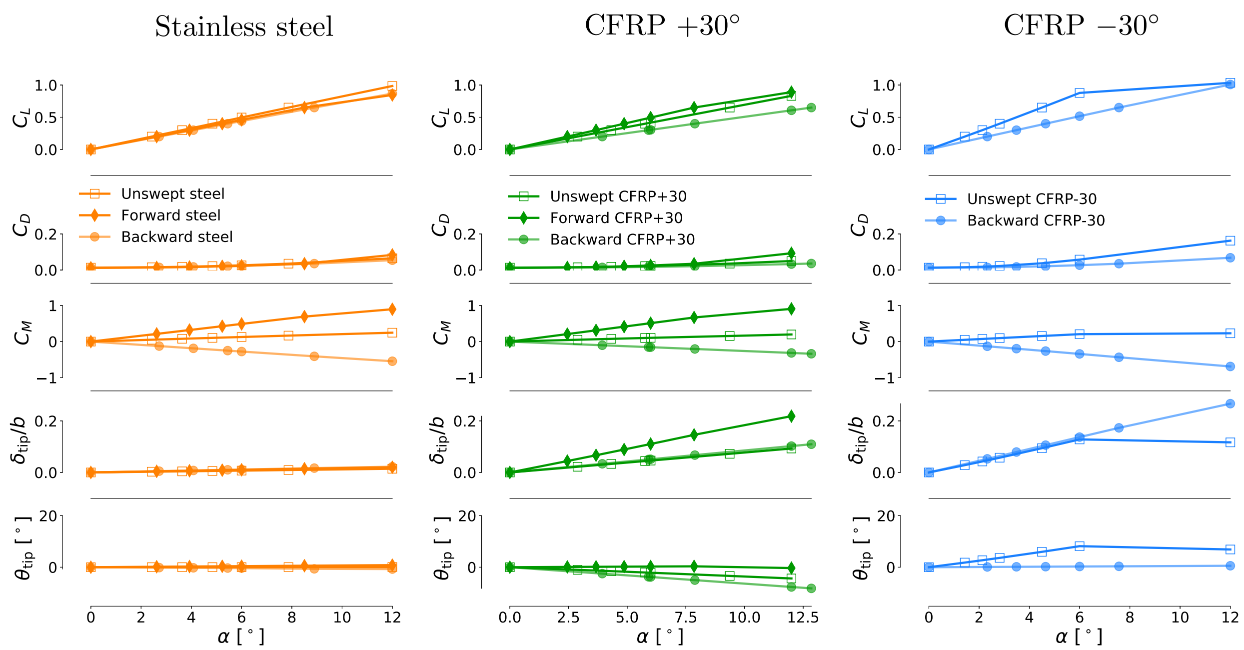

Stainless steel

CFRP +30°

CFRP −30°

Figure 3.9: Force coefficients and deformations for CFRP hydrofoils with different fiber orientations and the stainless steel hydrofoils. Different combinations of sweep angle and material show different trends and separation behaviors with repect to α.

of attack increases up to 12°. This earlier separation occurs because of local high loading caused by introducing a non-zero sweep angle. In the previous subsection, we showed that the sweep redistributes the spanwise loading through vorticity-induced upwash and downwash, and hence makes the lift distribution uneven and the hydrofoil becomes more susceptible to flow separation. Among the CFRP +30° hydrofoils, the forward one experiences the earliest separation because the upwash near the root and the nose-down θ_{tip} induced by material anisotropy both act to move the lift inboard, and this additional inboard load induces an earlier separation on the suction side.

As the hydrofoil becomes more flexible, the effect of geometric bend-twist coupling caused by sweep affects the hydroelastic performance more strongly. Among the hydrofoils shown in Figure 3.9, the C_L of the unswept CFRP −30° hydrofoil increases with the highest rate because the material-induced bend-twist coupling acts to induce a nose-up twist and there is no counteracting effect from the geometric bend-twist coupling. This high $\frac{\partial C_L}{\partial \alpha}$ slope also suggests an early separation and stall. The C_M of the forward and backward hydrofoils have opposite signs because the center of lift is shifted away from the middle of the root chord in different directions, which is a similar effect to that of geometric bend-twist coupling.

Using CFRP with off-axial fiber orientations decreases the bending stiffness, so CFRP $+30^\circ$ and CFRP -30° hydrofoils have higher δ_{tip} values compared to the stainless steel hydrofoils. The θ_{tip} shows a combined effect from the geometric bend-twist coupling, material bend-twist coupling, and hydrodynamic pitching moment. The θ_{tip} curves of CFRP $+30^\circ$ concentrate in the negative regime, while the curves of CFRP -30° stay in the positive regime. Given the sweep angles, fiber angles, and material properties we selected, the geometric bend-twist coupling has a similar significance to the material bend-twist coupling, so the θ_{tip} curves of the forward CFRP $+30^\circ$ hydrofoil and the backward CFRP -30° hydrofoil remain close to zero, as shown in Figure 3.9.

3.3.4 Efficiency (lift-to-drag ratio)

To evaluate the hydrodynamic efficiency, we compare C_L/C_D over a range of lift coefficients for the hydrofoils in Figure 3.10. The simulations conditions are the same as in Section 3.3.3. As mentioned previously, the spanwise flow induced by sweep reduces the form drag, which plays a significant role in the total drag of hydrofoils with a thick trailing edge. As a result, for the stainless steel C_L/C_D curves, swept hydrofoils have higher C_L/C_D at low C_L conditions. When C_L increases to values high enough that the lift-induced drag becomes dominant, the C_L/C_D of the unswept hydrofoil approaches those of swept hydrofoils, and even outperforms the backward hydrofoil at $C_L = 0.65$, as shown from the stainless steel results in Figure 3.6.

Poor combinations of fiber orientation and sweep lead to early separation and stall, which cause efficiency loss. Although forward hydrofoils have the highest C_L/C_D during low to intermediate C_L range, the efficiencies of the forward stainless steel and forward CFRP $+30^\circ$ hydrofoils drop rapidly for $C_L > 0.65$ because of the early root separation caused by the high loading near the root. The nose-up geometric bend-twist coupling caused by forward sweep and the nose-down material

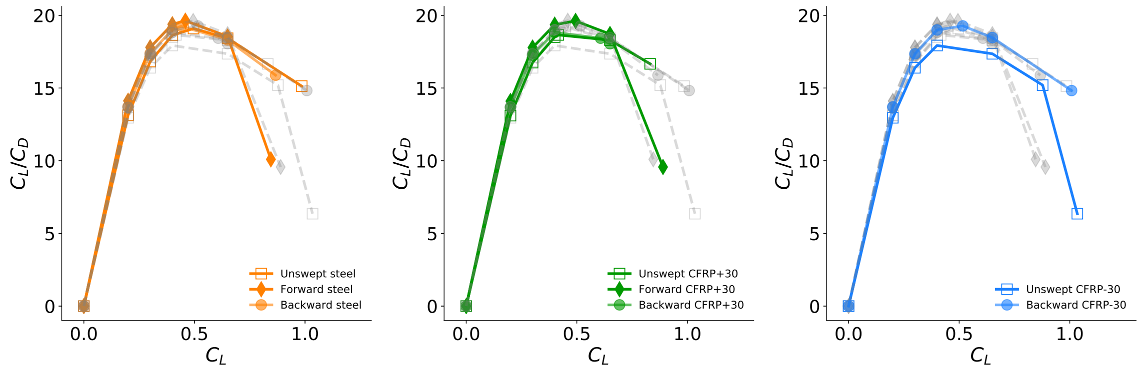

(a) Stainless steel (b) CFRP $+30°$ (c) CFRP $-30°$

Figure 3.10: C_L/C_D versus C_L for all hydrofoils. Each subplot shows data of all cases. The color-highlighted solid lines correspond to the material in the title, while data of the other two material configurations are shown as gray dashed lines for comparison. Flow separation is responsible for the sudden drop in efficiency.

induced bend-twist coupling caused by CFRP $+30°$ have a comparable and opposite effect, so the net twist is small (Figure 3.9), leading to a C_L/C_D curve and a separation behavior similar to the forward stainless steel hydrofoil. For CFRP $-30°$, the efficiency of the unswept hydrofoil drops at a lower C_L due to separation.

3.3.5 Static divergence

Static divergence is a static instability behavior when the hydrodynamic disturbing moment is equal to or exceeds the structural elastic restoring moment. Although material failure usually happens before static divergence, it is critical to understand the static divergence behavior to avoid excessive deformation. The forward CFRP $-30°$ hydrofoil has an excessive nose-up bend-twist coupling, causing flow separation, and the hydrofoil is unable to generate enough restoring moment to overcome the hydrodynamic disturbing moment. Therefore, the solution diverged and a static solution cannot be obtained even at a small initial angle of attack. We assess the static divergence behaviors of the rest cases by plotting θ_{tip} versus C_L in Figure 3.11. If the θ_{tip} increases with C_L, static divergence is theoretically possible for the hydrofoil when the increasing rate or the

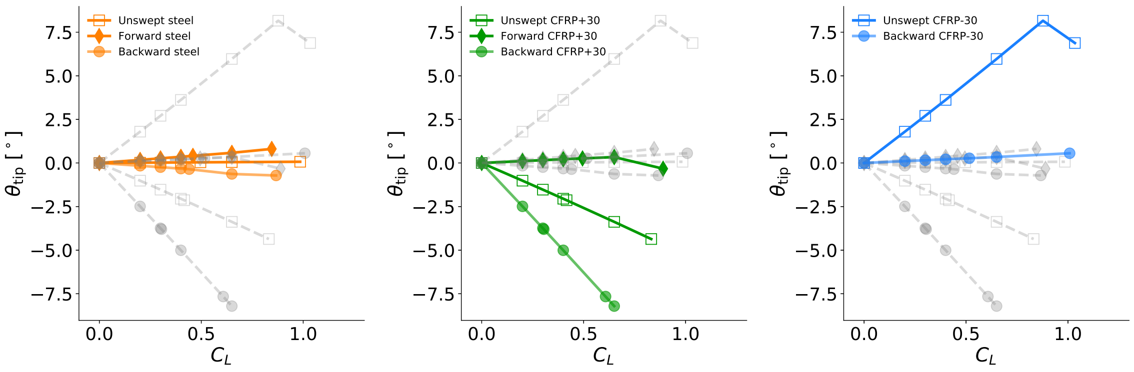

(a) Stainless steel (b) CFRP $+30°$ (c) CFRP $-30°$

Figure 3.11: Tip hydroelastic twist versus lift coefficient for all hydrofoils. Nose-up bend-twist coupling increases the likelihood of static divergence. The geometric bend-twist coupling and material bend-twist coupling can counteract each other. Each subplot shows the data for all cases. The color-highlighted solid lines correspond to the material in the title, while data of the other two material configurations are shown as gray dashed lines for comparison. Note that the sudden trend change of θ_{tip} at high C_L is due to flow separation, reducing the twisting moment because the center of pressure shifts to near the mid-chord.

dynamic pressure is sufficiently high. The unswept CFRP $-30°$ is expected to have the lowest static divergence speed, since θ_{tip} increases the fastest with higher C_L, which acts to further increase the load and hence deformation. Although the backward CFRP $+30°$ hydrofoil is not susceptible to static divergence because of the nose-down twist, the twist amplitude is still so large that it can compromise the structural integrity. Therefore, designs that have θ_{tip} decreasing mildly with C_L are preferred, such as the backward stainless steel hydrofoil.

Finally, note that the sudden trend change of θ_{tip} at high C_L is due to flow separation, reducing the twisting moment because the center of pressure shifting to near the mid-chord.

3.3.6 Cavitation inception

We have shown how the sweep changes the hydrodynamic performance, and how the sweep and material anisotropy interact to affect the hydroelastic response of hydrofoils. In this section, we study how the sweep and material anisotropy affect the susceptibility to cavitation because cavitation inception significantly impacts efficiency and structural safety. The hydrostructural solver used in this work is not capable of directly modeling cavitation, but a preliminary understanding of susceptibility to cavitation can be gained from the pressure distribution, since a low local pressure tends to encourage cavitation inception.

Since we are interested in identifying regions of low local pressure, we examine ten spanwise sections along the span and select the section with the lowest C_p for each hydrofoil, together with two sections at $y/b = 0.2$ and $y/b = 0.8$ as fixed references (see Figure 3.12). The minimum pressure coefficient $C_{p_{\min}}$ values are summarized in Table 3.5.

From the sectional C_p distributions of the stainless steel hydrofoils shown in Figure 3.12, we see that sweep makes cavitation more likely because it increases the maximum C_l, as shown on the rightmost plots in Figure 3.6, and therefore leads to a lower $C_{p_{\min}}$. However, when the material anisotropy contributes to the hydroelastic response, the spanwise loading is redistributed because of the change in angle of attack by the material bend-twist coupling, and the cavitation inception behavior is different from that of the stainless steel hydrofoils.

Combining the C_l plots in Figure 3.6 and the spanwise positions where $C_{p_{\min}}$ occurs, we can see that the location most susceptible to cavitation is around where the maximum C_l develops. For the forward hydrofoils, the nose-down tip twist induced by CFRP $+30°$ balances the nose-up geometric bend-twist coupling and hydrodynamic pitching moment, which results in an evenly distributed loading. This reduces the suction peak, which helps the forward CFRP $+30°$ to avoid or delay cavitation compared to the forward stainless steel hydrofoil. For the unswept hydrofoil, the CFRP $+30°$ does not contribute to preventing cavitation because the C_l distribution is already even and thus there is no locally high C_l for the stainless steel hydrofoil. The nose-down tip twist and the shift of the loading towards the root makes the backward CFRP $+30°$ hydrofoil more susceptible to cavitation compared to the backward stainless steel hydrofoil. The CFRP $-30°$ helps the backward hydrofoil mitigate cavitation because the nose-down geometric bend-twist coupling is balanced by the nose-up material bend-twist coupling and hydrodynamic pitching moment.

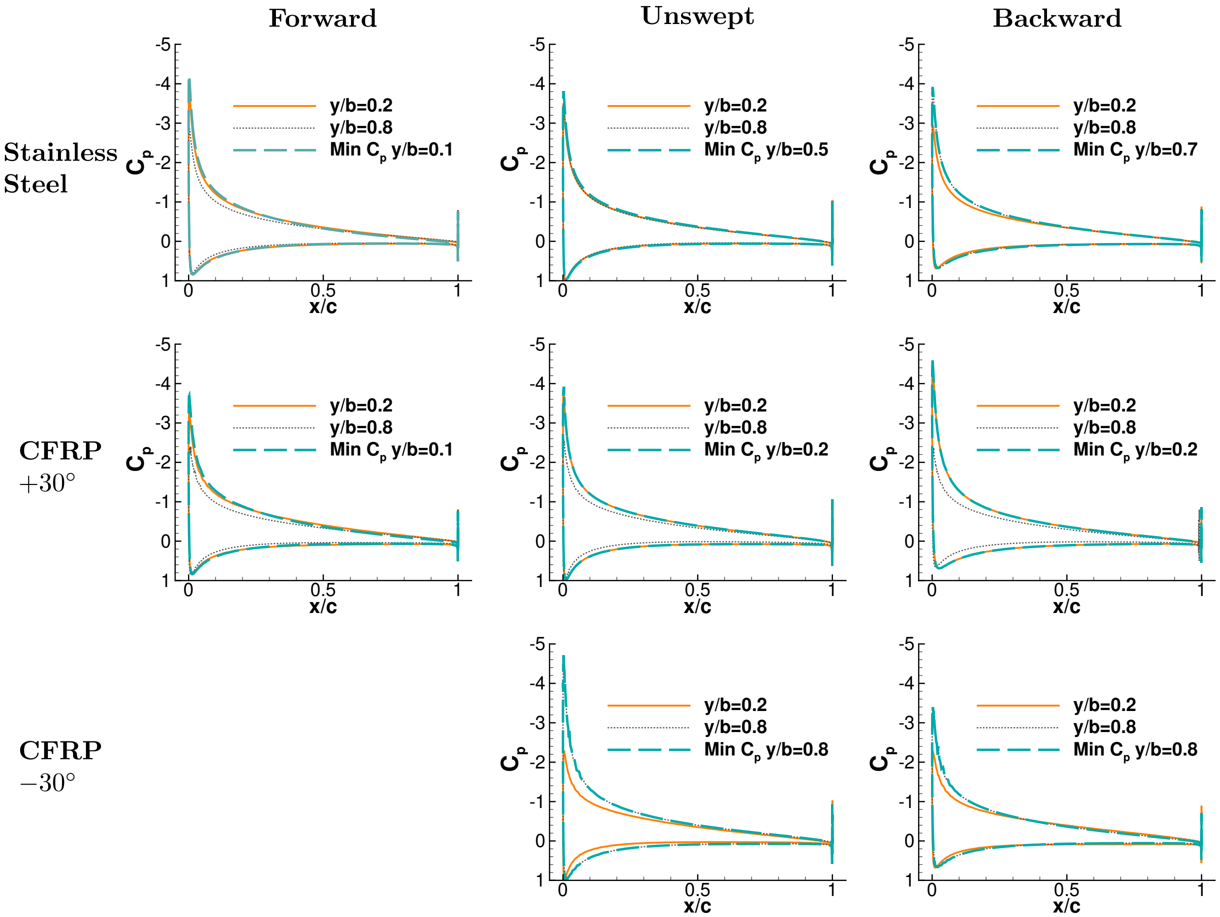

Figure 3.12: Sectional C_p for all hydrofoils at $C_L = 0.65$. The sections with the lowest C_p are shown together with the sections at $y/b = 0.2$ and $y/b = 0.8$. The unswept CFRP $-30°$ hydrofoil is the most susceptible to cavitation.

Besides the local pressure, the susceptibility to cavitation is also dependent on the ambient pressure. That being said, the minimum operating water depth for cavitation-free operation can be affected by the material and planform geometry. The cavitation number σ is conventionally used for characterizing the cavitation potential and represents the difference between the absolute ambient hydrostatic pressure ($P_\infty = P_{\text{atm}} + \rho_{\text{water}} g h$) and the vapor pressure (P_{vapor}):

$$\sigma = \frac{P_\infty - P_{\text{vapor}}}{0.5 \rho_{\text{water}} U_\infty^2}. \tag{3.1}$$

When the minimum local absolute pressure $P_{\text{min}} = P_\infty + 0.5 C_{p_{\text{min}}} \rho_{\text{water}} U_\infty^2$ is lower than P_{vapor}, cavitation inception occurs, which is equivalent to

$$\sigma \leq -C_{p_{\text{min}}}. \tag{3.2}$$

We assume $P_{\text{vapor}} = 2$ kPa, $P_{\text{atm}} = 101.3$ kPa, $\rho_{\text{water}} = 1000$ kg/m^3, $g = 9.8$ m/s^2, a mean-chord of 0.09 m, and a forward speed of 9.6 m/s. If the hydrofoil is operated at 7 m water depth, the cavitation number is 3.64. From Table 3.5, the backward CFRP $-30°$ hydrofoil is the only one that can operate without cavitation at this water depth. To operate the forward CFRP $-30°$ hydrofoil cavitation-free, the required depth is 18 m, which is substantially deeper than for the backward CFRP $-30°$ hydrofoil. However, the NACA 0009 section used here is prone to cavitation, so these computed values are used simply for comparison purposes.

Table 3.5: Minimum pressure coefficient $C_{p_{\text{min}}}$ among selected sections for different hydrofoils.

	Forward	Unswept	Backward
Stainless steel	-4.21	-3.82	-3.92
CFRP $+30°$	-3.71	-3.92	-4.59
CFRP $-30°$	N/A	-4.71	-3.39

3.3.7 Vorticity contours (λ_2-criterion)

Vortex structure can affect the vibration, noise, cavitation, and ventilation of hydrodynamic lifting surfaces. Extremely low pressure can occur in the core of a strong tip vortex, which suggests the potential for tip vortex cavitation. Additionally, pressure fluctuations in the tip vortex can cause vibration and surface erosion issues on the structures downstream. In this section, we show the λ_2-criterion iso-surfaces for the hydrofoils at $C_L = 0.65$ to study how sweep, material anisotropy, and their interaction change the vortex structure.

The λ_2 criterion determines the existence of a local pressure minimum due to vortical motion [126, 132]. This criterion is given by

$$\lambda_2(S^2 + \Omega^2) < 0, \tag{3.3}$$

where S is the symmetric part of the velocity gradient tensor ∇u, and Ω is the asymmetric part of ∇u.

All hydrofoils feature a prominent tip vortex, as shown in Figure 3.13. The different combinations of sweep and material anisotropy not only change the strength of the vortex structure, but also the extent and direction of the vortex. The CFD mesh is probably not sufficiently fine downstream of the foil trailing edge to resolve the tip vortex, but it is sufficient to illustrate the relative differences between the foils with varying sweep and fiber angles. The forward hydrofoils have a larger tip vortex diameter, while the tip vortices of the unswept and backward hydrofoils have smaller diameters. However, the iso-surfaces only show a constant λ_2, so it is hard to distinguish the difference in the strength.

To show the difference in vortex strength, we plot slices of the backward hydrofoils with 2D contours of λ_2. The λ_2 contours on y-z plane at the slice 0.05 m downstream from the tip trailing edge of all backward hydrofoils are shown at the bottom of Figure 3.13. From the rear view shown in the 2D plots of the backward hydrofoils, we see that the tip vortex of stainless steel, CFRP $+30^{\circ}$, and CFRP -30° propagate downstream in slightly different directions. Comparing the 2D contours, the backward stainless steel and CFRP -30° hydrofoil have tip vortices with similar strengths due to the balance of backward sweep induced nose-down bend-twist coupling and CFRP -30° induced nose-up bend-twist coupling, and both vortices are stronger than the CFRP $+30^{\circ}$ case, as indicated by the lower λ_2 contour values inside the vortex cores. Overall, the CFRP $+30^{\circ}$ hydrofoils have weaker tip vortices because of reduced tip loadings.

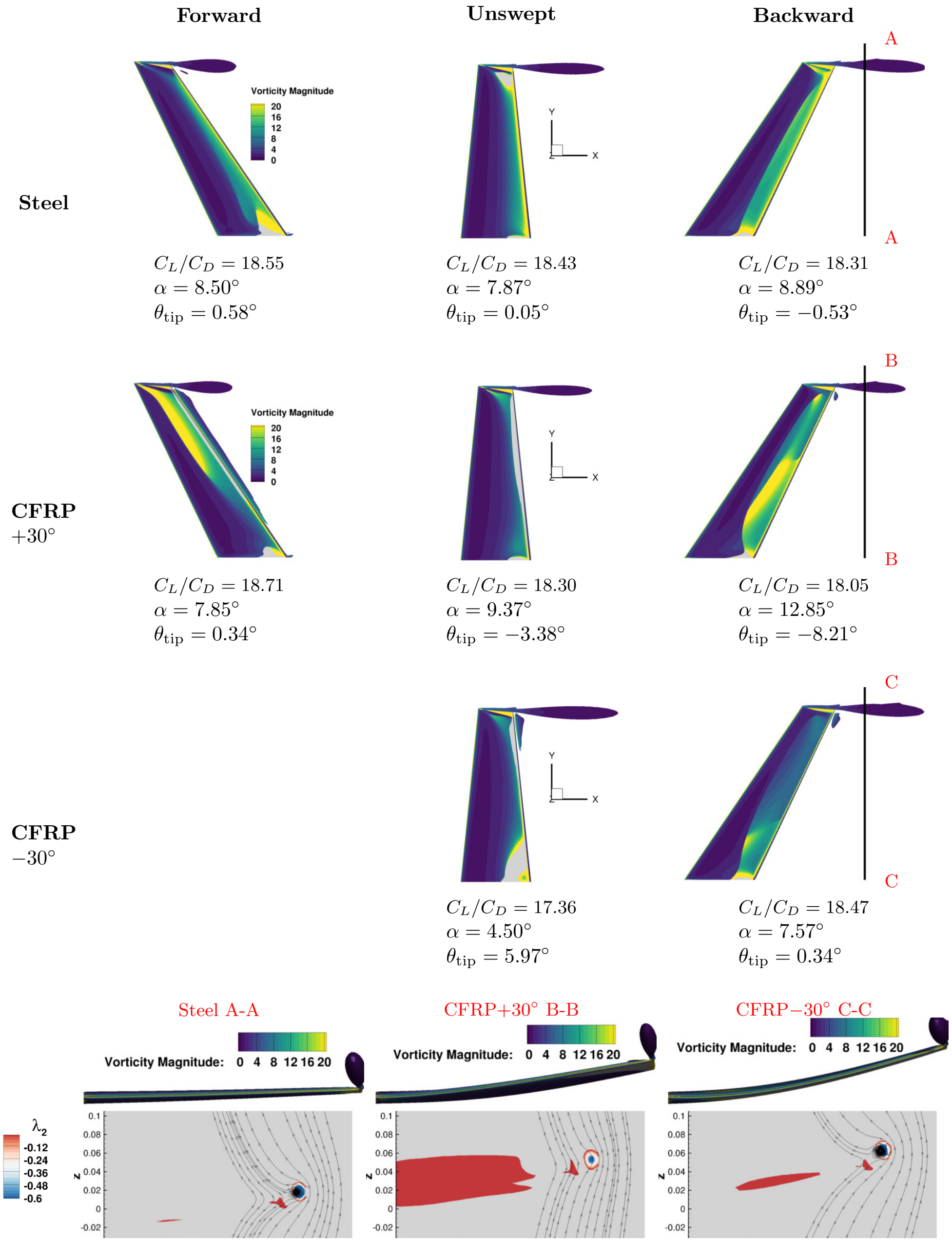

Figure 3.13: Iso-surfaces of λ_2-criterion at λ_2=-0.01, for different hydrofoils at $C_L = 0.65$. The contours on the iso-surfaces represent the vorticity magnitude. Bottom: λ_2 contours in the y-z plane at slice 0.05 m downstream from the tip trailing edge of three backward hydrofoils. Backward stainless steel and CFRP $-30°$ hydrofoils have stronger tip vortices compared to the CFRP $+30°$ hydrofoil.

3.3.8 Material failure inception

In addition to the steady-state hydroelastic response, it is important to consider the structural integrity of the designs. First, we show how the sweep affects the structural failure by comparing the non-dimensional von Mises stress results for the stainless hydrofoils with different sweep angles. Second, we compare the matrix compressive/tensile cracking index contours of CFRP hydrofoils with different θ_f and λ to investigate the coupled influence of sweep and material anisotropy on material failures. Since the matrix cracking failure is more likely to happen in tension, it is more important to check the tension side, which is the pressure side of the hydrofoil. Therefore, we show the hydrofoil undersides to show the side in tension. The stainless steel hydrofoils are also shown with the pressure side to be consistent.

3.3.8.1 Influence of Sweep

As discussed in Section 3.3.1, sweep reduces the bending stiffness, which leads to higher bending deformations for the swept hydrofoils compared to the unswept hydrofoil when subject to the same lift, as shown in Figure 3.14. The unswept hydrofoil has the highest non-dimensional von Mises stress at the maximum thickness location at the root, since the bending moment is the largest at the root for a cantilevered structure and the maximum bending stress occurs at the point that is the farthest from the midplane. For the forward hydrofoil, the combination of positive θ_{tip} and δ_{tip} results in a higher total bending deformation near the leading edge compared to the downstream portion. As a result, the stress concentration deviates towards the leading edge for the forward hydrofoil; the opposite trend is observed for the backward hydrofoil.

3.3.8.2 Coupled Influence of Sweep and Material Anisotropy on Matrix Failure Inception

Composite structures have complicated failure mechanisms. The matrix inside a composite is weak and can contribute to the initiation of material failure. Here, we use the matrix compres-

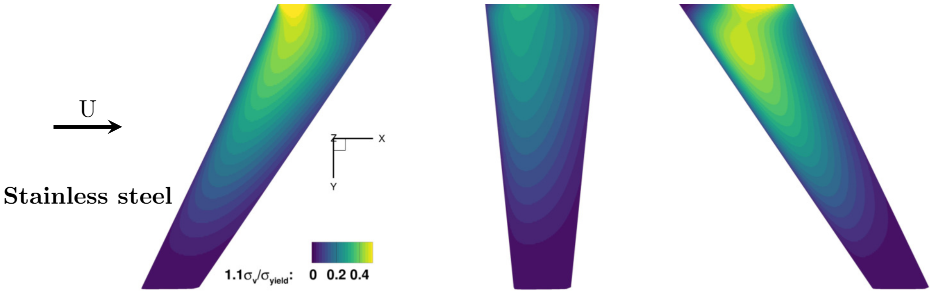

$\theta_{\mathrm{tip}} = 0.58°$
$\delta_{\mathrm{tip}}/b = 0.015$

$\theta_{\mathrm{tip}} = -0.05°$
$\delta_{\mathrm{tip}}/b = 0.009$

$\theta_{\mathrm{tip}} = -0.53°$
$\delta_{\mathrm{tip}}/b = 0.017$

Figure 3.14: Non-dimensional von Mises stress distributions on the pressure side of stainless steel hydrofoils at $C_L = 0.65$. The combined deformation from bending and twisting determines the structural failure susceptibility and failure locations.

sive/tensile cracking criterion to evaluate the material failure susceptibility and identify the failure location. The criterion is defined as,

$$I_M = \left(\frac{\sigma_{11}}{X_T}\right)^2 + \left(\frac{\sigma_{12}}{S_{12}}\right)^2 + \left(\frac{\sigma_{13}}{S_{13}}\right)^2, \text{when } \sigma_{11} > 0 \tag{3.4}$$

$$I_M = \left(\frac{\sigma_{11}}{X_C}\right)^2 + \left(\frac{\sigma_{12}}{S_{12}}\right)^2 + \left(\frac{\sigma_{13}}{S_{13}}\right)^2, \text{when } \sigma_{11} < 0 \tag{3.5}$$

The matrix compressive/tensile cracking failure index contours are shown in Figure 3.15. Both sweep and fiber orientation change failure inception and the failure location. The location of failure depends on the deformation and the fiber direction. As shown in Equations (3.4) and (3.5), since the material properties used correspond to unidirectional CFRP, the matrix cracking failure is strongly dependent on the normal stress in the direction transverse to the fiber. As a result, the effect of the fiber orientation on the material failure is not only shown by the resultant deformation but also by the stress transformation from the global coordinate to the local coordinate.

As shown in Figure 3.15, all regions susceptible to material failure are perpendicular to the fiber directions, in which large deformation developed due to a lower stiffness, and failure is more likely to happen due to a lower strength compared to along the fiber direction. The backward CFRP $+30°$

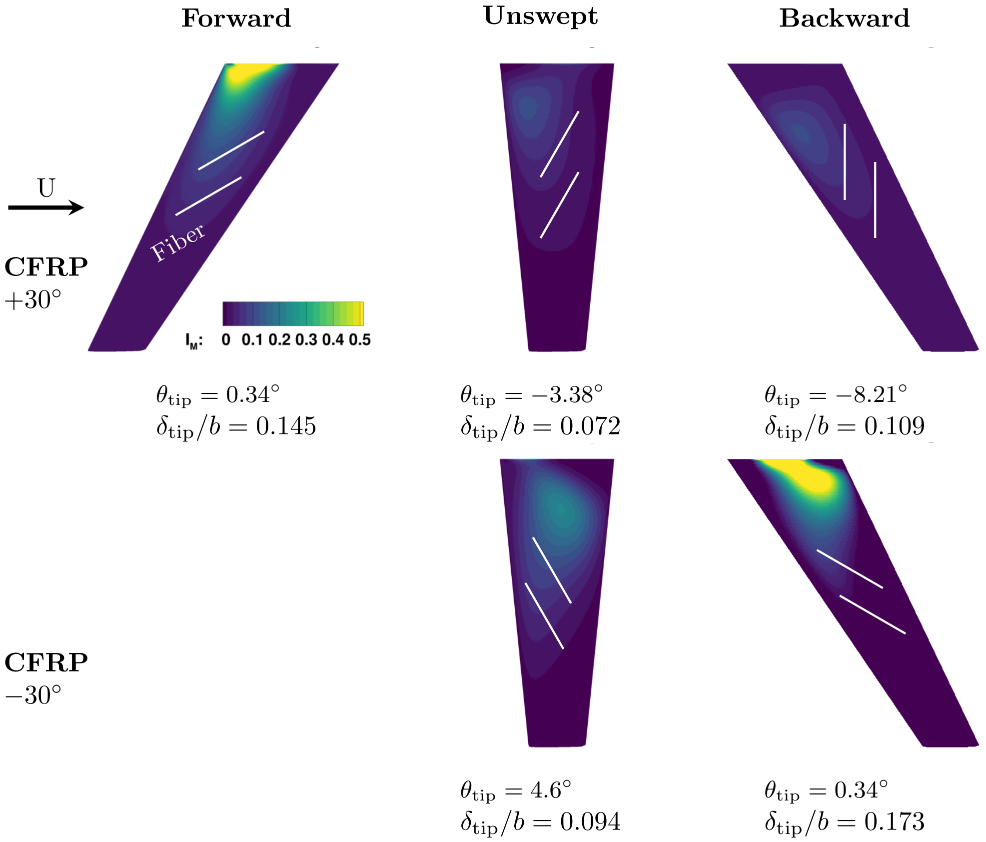

Figure 3.15: Matrix compressive/tensile cracking index contour of composite hydrofoils at $C_L = 0.65$. The results are from steady-state hydrostructural simulation. White lines represent the fiber directions. Contours are shown for the pressure side, which is the side in tension. The combined deformation from bending and twisting determines the structural failure susceptibility and failure locations. Since unidirectional CFRP is used in simulations and matrix compressive/tensile cracking is considered, the material failure is governed by the relative direction between the fiber orientation and the normal bending stress due to the poor strength in the direction transverse to fibers.

and the unswept CFRP $+30°$ are less susceptible to matrix cracking, as shown in Figure 3.15. For the backward case, this is because most of the bending stresses can be taken by the fiber, so only a small portion is in the direction transverse to fibers after the transformation, while the latter unswept case is due to a low structural deformation. On the other hand, the forward CFRP $+30°$ and backward CFRP $-30°$ hydrofoils have larger deformations and higher normal stresses in the transverse direction because the fiber direction is less aligned with the bending stress direction, so these two hydrofoils are most susceptible to matrix compressive/tensile cracking. Although cases with fibers aligned with sweep angle are not investigated in this chapter, it is likely that aligning fibers with geometric sweep can avoid excessive deformation and material failure more effectively because this alignment enhances the bending rigidity and distributes more loading along the fiber longitudinal direction.

3.4 Conclusions

In this chapter, we investigate the influence of sweep and material anisotropy on hydrofoils using a set of parametric studies comparing the natural frequencies, mode shapes, hydroelastic response (lift, drag, and moment coefficients, as well as deformation patterns), separation, stall, hydrodynamic efficiency, susceptibility to cavitation, vortex structure, and material failure.

Investigated cases include hydrofoils with three sweep angles and three different material configurations (one stainless steel and two unidirectional CFRP with two different fiber orientations). All hydrofoils undergo bending towards the suction side due to lift. For unswept and isotropic hydrofoils, the hydrodynamic pitching moment leads to a nose-up twist because the center of pressure is upstream of the elastic axis. Sweep decreases the bending rigidity due to the extended structural span, and moves the spanwise axis away from the rotation axis, which results in geometric bend-twist coupling. Forward sweep leads to a nose-up geometric bend-twist coupling, while backward sweep leads to a nose-down geometric bend-twist coupling.

With the introduction of material anisotropy, these changes in bending rigidity and bend-twist coupling behavior become more complicated. Forward leaning fiber orientation ($\theta_f > 0^\circ$) leads to bending-up and nose-down twist, while backward leaning fiber orientation ($\theta_f < 0^\circ$) leads to bending-up and nose-up twist. Changes in structural stiffness lead to different dynamic characteristics, and changes in the mode shape affect the system resonance frequencies and damping response. The reduction in bending stiffness due to the extended structural span or off-axis fiber layup challenges structural safety, since dynamic amplification or other instabilities might occur.

Sweep changes the spanwise lift distribution due to vorticity-induced upwash and downwash, which can increase or decrease the lift-induced drag based on the actual lift profile. Both forward and backward sweep reduce the form drag compared to the unswept hydrofoils due to the spanwise flow that acts to reduce the strength and coherent structure of the vortices shed from the suction and pressure sides of the thick foil trailing edge. Hence, among all cases investigated in this chapter, swept hydrofoils exhibit a higher lift-to-drag ratio at low or intermediate C_L range. Sweeping the hydrofoil forward gives higher form drag reduction because the unswept baseline has an initial forward swept trailing edge. This sweep-induced reduction in trailing edge vortex strength also suggests that we can purposely design sweep angle to mitigate separation, flow-induced vibration, and noise.

In addition to the hydrodynamic effects caused by the induced downwash and upwash of a swept hydrofoil, the geometric and material bend-twist coupling contribute to the loading distribution and hence the change in hydroelastic response. A proper design can improve the performance, while an unfavorable combination can cause divergence, efficiency losses, early separation and stall, cavitation, flow-induced vibrations and noise, and material failures. Due to an excessive bending-up and nose-up bend-twist coupling, the forward CFRP -30° hydrofoil physically diverges. On the other hand, the backward CFRP $+30^\circ$ hydrofoil has the maximum bending-up and nose-down bend-twist coupling and hence has the most negative tip twist, thus requiring the highest α to achieve $C_L = 0.65$.

A strong tip vortex can increase lift-induced drag, the susceptibility to tip vortex cavitation, and the susceptibility to severe flow-induced vibration and noise. Hence we compared the tip vortex structures of the hydrofoils at $C_L = 0.65$. From this, the CFRP $+30°$ hydrofoils have weaker tip vortices due to lower tip loadings. As a result of this lower tip loading and the form drag reduction due to the swept trailing edge, the forward CFRP$+30°$ has the highest lift-to-drag ratio among the investigated cases at $C_L = 0.65$. In addition, the combined effects of the sweep-induced downwash and upwash, the geometric bend-twist coupling, and the material bend-twist coupling result in a relatively flat spanwise C_l distribution for this forward CFRP$+30°$ hydrofoil at $C_L = 0.65$, achieving the highest cavitation inception speed.

The geometric bend-twist effect of sweep can vary the deformation and stress concentration location, depending on the sweep direction. As shown by the modal analysis, the bending rigidity of a swept hydrofoil is lower than an unswept hydrofoil. Hydrostructural simulations of stainless steel hydrofoils with different sweeps show that the forward and backward swept hydrofoils are subject to higher tip deformations and higher stresses at the root relative to the unswept one.

Due to the anisotropic behavior of composite materials, the material failure has a fiber-direction dependency. If the hydrofoil is loaded in a way such that a significant portion of the stresses are transverse to the reinforced direction, material failure is likely to occur. Strategic material design is required not only to consider the optimal hydroelastic response but also on adequate structural safety to avoid material failure. Although cases with fibers aligned with sweep angle were not investigated in this chapter, it is likely that aligning the fibers with the sweep angle can more effectively reduce deformations and avoid material failures of composite lifting surfaces.

The sweep angles and fiber angles investigated in this chapter are not optimized. We chose these combinations of parameters to illustrate the geometric and material bend-twist coupling effects. In a real design, if a specific sweep configuration is required to achieve certain functions, material anisotropy can help to redistribute the loading to reduce the drag and improve efficiency. The selection of sweep, material, and fiber layup should be decided together with other design variables based on high-fidelity hydrostructural optimization to ensure maximum hydrodynamic performance while avoiding cavitation, flow-induced vibration, and noise, as well as ensuring structural stability and safety. It is challenging to consider all the coupled effects and tradeoffs when a large number of variables are involved with a conventional design method because the interactions might not be intuitive, which highlights the necessity of numerical design optimization. Using low-fidelity tools can greatly reduce the benefits of numerical optimization, as it is important to consider viscous effects and the susceptibility to material and instability failure. Therefore, there is a strong motivation to conduct high-fidelity design optimization based on the hydrostructural models with a large number of geometric and material design variables, which is the problem that we will address in the next chapter.

CHAPTER 4

High-fidelity hydrostructural optimization of unidirectional CFRP hydrofoils

Now that the previous chapter advanced the understanding of the material anisotropy effect on the hydroelastic responses together with sweep, we will perform hydrostructural optimization to design composite hydrodynamic lifting surfaces with a focus on delaying cavitation. We will first investigate the problem with a unidirectional CFRP model with one equivalent layer.

4.1 Introduction

Although evolving manufacturing technologies are gradually removing the bottleneck imposed by the nonstandard manufacturing process of composites, designing composite hydrodynamic lifting surfaces still has challenges. One major challenge is cavitation. Compared to metals, composite materials are even more susceptible to the negative effects of cavitation for three main reasons. First, composites rely on surface coatings to protect against cavitation pitting damage. The formation and collapse of cavitation bubbles generate local shocks and micro jet impingements on the structure's surface [29, 133], which can cause erosion damage [32]. Available coatings for composites show less resistance against cavitation erosion than nickel aluminum bronze, which is commonly used for hydrodynamic lifting surfaces [8]. Repeated cavitation-induced shockwaves can accumulate heat, which eventually harms the coating and polymer composites. The second reason is due to the characteristics of composite materials. To achieve cost-effectiveness and to take full advantage of material tailoring, composite hydrodynamic lifting surfaces can consist of multi-layers with diverse properties. When cavitation-induced shock waves propagate through the structures, the acoustic impedance mismatch between layers causes wave reflections and shear stresses that can lead to delamination between layers. The third reason has to do with vibrations and hydroelastic instabilities. Recent experimental studies have shown that cavitation affected the resonant frequencies and damping characteristics of flexible hydrofoils; in turn, the hydrofoil vibrations affected the cavity shedding dynamics [26, 134–136].

To address these issues, in this chapter, we will focus on designing a cavitation-free composite hydrodynamic lifting surface. In the late 1970s and early 1980s, Shen and Eppler used a surface vorticity panel method coupled with a boundary layer solver to yield hydrofoil sections that effectively delay cavitation [70, 71]. To prevent boundary-layer separation near the trailing edge, they specified the region of pressure recovery and closure contribution to avoid excessively steep pressure recovery [70]. Some earlier designs, such as NACA 16-series and NACA 66 (MOD) series, can operate cavitation-free with a negative minimum pressure coefficient $-C_{p_{\text{min}}}$ down to 0.25. However, good cavitation performance is maintained only within a small range of angles of attack (0–2°). At a higher sectional lift coefficient $C_{l_{\text{2D}}}$, the cavitation performance degrades substantially. The designs presented by Shen and Eppler [70] have a wider cavitation-free operating range compared to those earlier designs. One of their designs, the E1127 section, is a profile designed to have a maximum cavitation-free operation $C_{l_{\text{2D}}}$ range at a $-C_{p_{\text{min}}}$ of 0.6 [70]. The design condition used for the E1127 section was Re of 10^7 and $C_{l_{\text{2D}}}$ of 0.3. Later in 1994, Scherer and Stairs [72] presented a more streamlined design methodology with a 2-D full second-order panel method to generate propeller blade sections that delay cavitation. These series of sections are often referred to as OS sections. Compared to the conformal mapping approach used by Shen and Eppler [70, 71], Scherer and Stairs used analytic parametric equations with continuous second-order derivatives to create foil sections to ensure smoothness and manufacturability [72]. Some OS sections have the lowest $-C_{p_{\min}}$ of about 0.25, which is similar to specific NACA 16-series sections and NACA 66 (MOD) series sections but with a wider optimal range. Compared to profiles designed by Shen and Eppler [70], the optimal operation ranges of these OS sections are still limited ($C_{l_{2D}}$ of 0.05 to 0.35).

While these designs were successful in delaying cavitation inception for hydrodynamic lifting surfaces, they are limited in that they considered only 2-D hydrodynamic effects. This is an important limitation because the optimal performance in a 2-D case might degrade when strong 3-D effects exist [133], especially for hydrodynamic lifting surfaces. Compared to aerodynamic designs, hydrodynamic lifting surfaces typically have strong 3-D effects because of complex geometries and low aspect ratios due to the need to delay cavitation, reduce unsteady interactions with adjacent components, and sustain the high loading in sea environments. To optimize 3-D cavitating marine propellers, Mishima and Kinnas developed a method called CAVOPT-3D that uses a 3-D potential flow-based vortex lattice method [137, 138]. Building on this work, Griffin and Kinnas improved CAVOPT-3D to allow quadratic skew distribution and implemented a minimum pressure constraint in CAVOPT-3D to prevent bubble and mid-chord cavitation [139]. While these early designs succeeded at improving cavitation performance for 3-D cases, they did not consider the coupled FSI response. Unlike for rigid metallic counterparts, predicting this coupled hydrostructural response is crucial for designing composite hydrodynamic lifting surfaces because they are more flexible, which allows their (deformed) shapes to vary with loading conditions. This load-dependent shape variation can be so significant that deformed shapes are required to predict the correct hydrodynamic performance.

Recently, researchers have used a BEM coupled with an FEM to analyze the performance of adaptive composite marine propellers [24, 38, 62, 140]. Motley and Young [43] used a probability-based optimization methodology to improve the performance of composite marine propellers. They found that the strategic layering of the composites can enable the self-adaptability of flexible lifting surfaces to significantly reduce the cavitation volume compared to the metallic counterpart.

However, to better predict cavitation onset, we need to consider viscous effects, especially at low and intermediate Reynolds number range [133]. Laminar separation, turbulence transition, fluctuating pressure in the boundary layer, and vortex occurrence have impacts on cavitation inception and cavitation development [30, 31, 141, 142]. An experimental study by Ram et al. [143] showed that microbubbles could travel upstream inside the low-speed boundary layer region under adverse pressure gradient to become nuclei to trigger new attached cavitation events.

Using a higher fidelity method, such as RANS based CFD, LES, or direct numerical simulation (DNS), allows better prediction of separation, stall, and cavitation onset. Li and Van Terwisga [144] qualitatively investigated RANS's capability to predict the unsteady cavitating performance and the implication on cavitation-induced erosion. Li et al. [145] showed that using RANS with a modified SST k-ω model produced reasonably comparable results with the experiment. Ji et al. [146] presented an LES simulation with a homogeneous cavitation model for predicting unsteady cavitating flow. Their simulated results showed a good comparison with the experiment.

Among all these methods with higher fidelities, RANS is used widely for hydrodynamic lifting surface designs because it provides a good balance between computation cost and accuracy. Recently, Garg et al. conducted hydrostructural optimization to design metallic hydrofoils [65, 73] with the consideration of susceptibility to cavitation. The optimized hydrofoil presented by Garg et al. was thicker than the baseline but still yielded an average increase in efficiency (lift-to-drag ratio) of 29$\%$ for lift coefficients ranging from -0.15 to 0.75 compared to the baseline hydrofoil [91].

Volpi et al. [66] presented an architecture called multi-criterion adaptive sampling multidisciplinary optimization with a gradient-free method to conduct an optimization of a composite hydrofoil. They used a Karhunen-Loève expansion to reduce the design space dimensionality. Their architecture was shown to converge and sample faster than the multidisciplinary feasible architecture. However, training a surrogate model for the optimization can require unnecessary computational cost, and they only conducted a single-point optimization.

These recent hydrofoil designs only focused on metallic hydrofoils, or they did not consider planform variables or did not conduct a multi-point optimization. Planform variables can have an enormous impact on hydrodynamic performance and structural response. As discussed in Chapter 3, sweep modifies the loading distribution, the flow behavior, cavitation inception speed, and susceptibility to structural failure. In addition to modifying the cavitation inception speed, as well as the location of cavitation inception, sweep also introduces 3-D variations in the cavity shedding, which changes the frequency response of the foil in cavitating conditions.

Overall, previous works on designing cavitation-free hydrofoils rarely simultaneously considered 3-D effects, the use of composite, viscous effects, FSI, planform variables, and a large number of total variables. Hence, this chapter aims to design cavitation-free, efficient, and structurally sound 3-D composite hydrofoil with respect to a large number of design variables, including shape, planform, and fiber orientation using high fidelity tools. We use a hydrofoil model because it is a canonical representation of more complex hydrodynamic lifting surfaces. We describe our optimization problem in Section 4.2, including our baseline model and problem statement. The baseline hydrofoil in this chapter is made of an equivalent single layer unidirectional CFRP. We show our optimization results in Section 4.3. In addition to the comparison with the baseline composite hydrofoil, we also compare the optimized result with the Eppler Section 1127, which has been widely known as a gold standard section that is designed to delay cavitation [70]. We show a comparison of optimizations with and without sweep and chord variables in Section 4.3.6 to assess the effects of those variables on cavitation-free composite hydrofoil designs.

4.2 Optimization problem setup

We define the optimization problem as minimizing the weighted drag coefficient of a hydrofoil at three different lift conditions. Design variables include geometric variables and one structural variable, fiber orientation. The MACH framework can handle more structural variables, but only the effective fiber orientation of an equivalent unidirectional carbon fiber reinforced polymer is used here for simplicity. Meanwhile, we consider constraints on cavitation inception, material failure, and maximum bending (z-direction) displacement. There are other constraints that we use to make the optimization problem well-posed.

4.2.1 Model

Different from the scaled model used in Chapter 3, we use a full-scale linearly tapered hydrofoil with a NACA 0009 cross-section as the baseline geometry. The hydrofoil model has a blunt trailing thickness equal to 0.2% of the local chord length. This trailing edge might be too thin for composite hydrofoil manufacturing in reality. We use this thin trailing edge here to minimize the possible drag overestimation associated with the trailing edge vortex effect, which was discussed in Chapter 3. We assume a water depth of 1 m. The model has a semi-span b of 0.9 m, a root chord c_{root} of 0.36 m, and a tip chord c_{tip} of 0.18 m, as shown in Figure 4.1a. We apply the symmetry plane boundary condition at the foil root in the CFD simulations.

On the structural side, the hydrofoil is cantilevered at the root, as shown in Figure 4.1b. We use linear eight-node brick (solid) elements to model the structure because hydrodynamic lifting surfaces typically have a lower aspect ratio. Additionally, the loading in water is higher, so the structure is typically not in hollow form. As explained by Young [147] and Herath et al. [125], using solid elements potentially provides more accurate load and displacement transfer and thus better predicts the coupled hydrostructural response. We create the structural model shape such that it closely matches the CFD surface to ensure accurate load and displacement transfer.

Figure 4.1 shows the full-scale hydrofoil dimensions and different levels of CFD and structural meshes. Table 4.1 lists the dimensions of each mesh level. The three different levels of CFD meshes and FEM meshes are used for the mesh convergence study, which will be shown in Section 4.3. The reported y^+_{max} values correspond to the condition used in the mesh convergence study, which has the same Re_{rc} as our nominal design condition and a similar C_L to the nominal condition. We use six elements across the thickness for the L3 structural mesh and ten elements for the

L1 structural mesh, as listed in Table 4.1. The finest and coarsest meshes are used for verifying the optimization benefits on different mesh sizes.

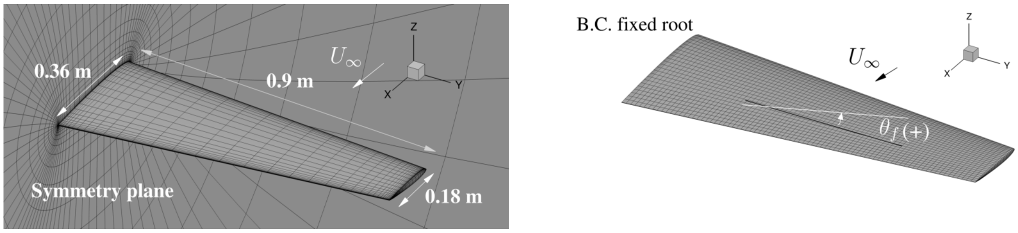

(a) L3 CFD mesh, 166,560 cells.

(b) L3 structural mesh, 11,664 elements.

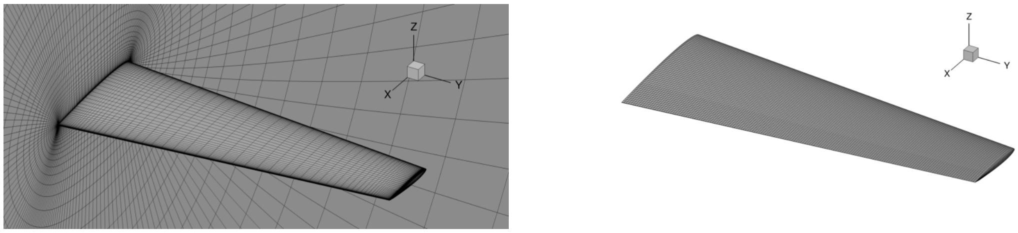

(c) L2 CFD mesh, 1,332,480 cells.

(d) L2 structural mesh, 62,208 elements.

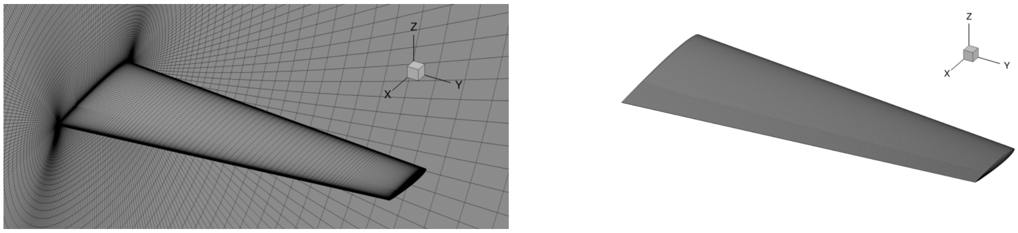

(e) L1 CFD mesh, 10,659,840 cells.

(f) L1 structural mesh, 174,960 elements.

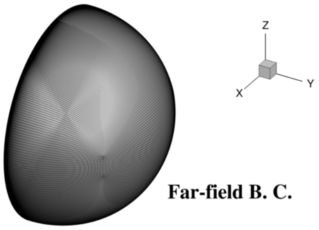

(g) L1 CFD mesh far-field boundary condition

Figure 4.1: CFD surface mesh and structural mesh

CFRP are commonly used in hydrodynamic lifting surfaces. To simplify the problem and obtain a straightforward understanding of the influence of material anisotropy on the hydrofoil performance, we only model the hydrofoil with a single layer of unidirectional CFRP in this chap-

Table 4.1: CFD and FEM mesh details

Mesh	Level	Mesh size	y^+_{max}			
CFD	L1	10,659,840	0.8			
	L2	1,332,480	1.3			
	L3	166,560	2.4			
Mesh	Level	Mesh size	Chordwise	Spanwise	Thickness	Tip span
FEM	L1	174,960	72	240	10	3
	L2	62,208	48	160	8	2
	L3	11,664	24	80	6	1

ter. The fiber orientation θ_f is defined relative to the y-axis as shown in Figure 4.1b. Note that this definition is different from Chapter 3 which defines θ_f as relative to the foil mid-chord line. The reason for changing the reference for defining θ_f is that the geometric variables allow a curved mid-chord line. Giving the θ_f value relative to the global axis is more clear and straightforward. θ_f is positive when the fiber is oriented towards the leading edge near the tip (fibers sweep forward) and negative when oriented towards the trailing edge. We list the material properties in Table 4.2. Note that the material coordinates differ from the journal publication for consistency throughout this dissertation. The material coordinates follow the same convention as in Chapter 3. While we can model multi-layer in the framework, using an equivalent single layer provides allows us to investigate the influence of material anisotropy and understand the physics better. In addition, using an equivalent single layer can provide sufficient accuracy for steady loads and deformation so the approach used in this chapter does not lose generality [43, 148]. In this chapter, the baseline is a composite hydrofoil that has an equivalent single layer with $\theta_f = 0°$. A case with more layers of unidirectional CFRP will be shown in the next chapter, which will demonstrate the sufficiency of using one equivalent single layer to achieve desirable hydrodynamic performance.

Table 4.2: CFRP material properties, where the subscript 2 represents the fiber longitudinal direction.

Symbol	Description	Value	Units
ρ_{CFRP}	Solid density	1590	kg/m^3
E_1,E_3	Young's modulus	13.40	GPa
E_2	Young's modulus	117.80	GPa
G_{12}, G_{13}	Shear modulus	3.90	GPa
ν_{21}, ν_{23}	Poisson's ratio	0.25	–
ν_{13}	Poisson's ratio	0.45	–
Y_T	Longitudinal tensile strength	1970	MPa
Y_C	Longitudinal compressive strength	1200	MPa
X_T, Z_T	Transverse tensile strength	50	MPa
X_C, Z_C	Transverse compressive strength	250	MPa
S_{21}, S_{23}	Shear strength	43	MPa
S_{13}	Shear strength	25	MPa

4.2.2 Geometric variables and constraints

For geometric variables, we consider twist, chord, sweep, and local shape variables. The chosen geometry design space is sufficient for a typical hydrofoil design. Twist, chord, and sweep are global variables that can be controlled by moving a group of control points relative to the corresponding reference axis. Local shape variables control the individual movement of FFD control points along the z direction and are responsible for creating camber.

To mimic a realistic, smooth chord variation, we use a two-level FFD approach. One FFD volume is typically adequate for a foil-only design. However, we want fewer control sections for chord variables compared to twist variables to avoid a wavy chord distribution. Using a two-level FFD approach allows chord variables to be defined on a separate volume with fewer control sections. This larger volume with fewer control sections is called the parent FFD, as shown in Figure 4.2. The smaller one is called the child FFD. Control points of child FFD are embedded in the parent FFD and are modified by the parent FFD change in a similar way to the surface mesh deformation procedure described in Chapter 2. The four sections near the root of the parent FFD will not be modified during the optimization to fix the root chord. These four sections are assigned near the root to ensure the root chord of the child FFD is not changed because the parent FFD points are far away from the child FFD control points. Twist, sweep, and local shape variables are defined on the child FFD, as shown in Figure 4.2. The child FFD has 72 control points in total. The control points are distributed following the cosine spacing in both the streamwise and spanwise directions. The parent FFD has 96 control points in total, while only 32 are active.

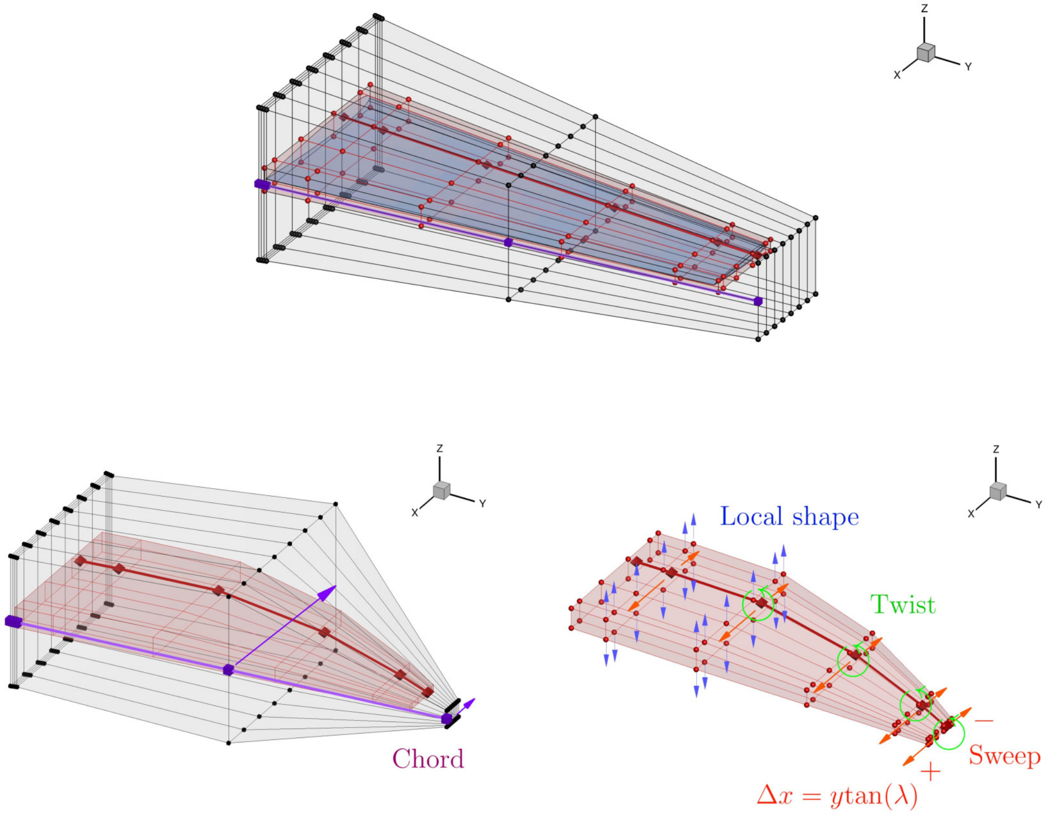

Figure 4.2: Demonstration of the undeformed and deformed FFDs. The gray volume is the parent FFD, and the red volume is the child FFD. The parent FFD controls chord variables, and the child FFD controls the sweep, twist, and local shape variables. Chords are changed with respect to the parent FFD reference axis located at the trailing edge. Twist variables are defined with respect to the child FFD reference axis located at the quarter-chord. The blue shade represents the baseline CFD surface. The chord variable at the midspan is specified as 1.5 times the original value and the one at the tip is specified as 0.25 of the original value. A sweep angle λ of 10° is used.

The reference axis of chord variables differs from that of twist and sweep variables. Chord variables are defined relative to the trailing edge (as shown by the purple line in Figure 4.2), and thus the trailing edge remains straight. This chord reference axis location is defined based on the chord optimizations using Euler equations presented by Bons et al. [149], who showed that defining the reference axis at the trailing edge allowed the optimization to double the drag reduction compared to using a quarter-chord reference axis. Chord scaling variables are allowed to increase up to 1.5 times the original chord length of the FFD volume (c_0) and decrease to a quarter of c_0. Since the chord variables correspond to the change of the FFD volume, the actual chord length of the hydrofoil does not strictly follow the chord variable values.The change in chord variables could result in an equivalent sweep angle, which will be shown in the later demonstration. Twist variables are defined with respect to the quarter chord (as shown by the thick red line in Figure 4.2), so the sections are rotated about the quarter chord. The sweep angle variable λ results in a shear sweep in the streamwise direction x. The shear distance Δx at each section is determined by,

$$\Delta x = y\tan(\lambda) \tag{4.1}$$

Following typical foil definitions, the sweep angle is positive when the foil tip moves downstream (swept backward) of the foil root, opposite the material fiber angle definition.

We apply arbitrary chord variables and λ to deform the FFD volumes to demonstrate the geometric changes. The deformed FFD volumes are shown in Figure 4.2. We increased the midspan chord to 1.5 times the original midspan chord and reduced the tip chord variable to a quarter of the original tip chord. We use a λ of $10°$ in the demonstration. The variables on the parent FFD are always applied first. The bottom left in Figure 4.2 illustrates the deformed FFDs after applying chord variables. We can see that applying the chord variables results in a forward sweep for the inboard part and a backward sweep for the hydrofoil's outboard. Built on the chord change, the bottom right in Figure 4.2 illustrates the deformed child FFD after applying the sweep variable.

We also apply a monotonic constraint on chord variables (i.e., the chord length decreases monotonically towards the tip) to get a reasonable chord distribution. Leading edge and trailing edge constraints are used to avoid shear twist. A projected area constraint is used to ensure that the optimization does not increase the planform area to reduce sectional 2-D lift coefficients $C_{l_{\text{2D}}}$ to delay cavitation.

4.2.3 Cavitation constraint

As mentioned previously, cavitation can lead to significant efficiency deterioration, material surface erosion, and cavity-induced vibrations. The cavitation constraint used here is modified from the one presented by Garg et al. [73], which is similar to the buffet constraint that Kenway and Martins [150] used for aircraft design. Cavitation occurs when the local pressure is lower than the saturated vapor pressure, which is given as

$$-C_p \geq \sigma, \tag{4.2}$$

where σ is the cavitation number defined as

$$\sigma = \frac{(P_{\text{atm}} + \rho_{\text{water}} g h) - P_{\text{vapor}}}{\frac{1}{2}\rho_{\text{water}} U_\infty^2}, \tag{4.3}$$

and P_{atm} is the atmospheric pressure at the sea level, ρ_{water} is the water density, h is the water depth, g is the gravitational constant, U_∞ is the inflow speed, and P_{vapor} is the saturated vapor pressure. Hence, the susceptibility to cavitation depends on the pressure on the hydrofoil and the inflow speed U_∞ and water depth h. We use $P_{\text{atm}} = 101.3$ kPa, $\rho_{\text{water}} = 1025$ kg, $g = 9.81$ m/s^2, and $P_{\text{vapor}} = 2.34$ kPa.

The cavitation sensor X can be defined as

$$X = \begin{cases} 1 & \text{if } -C_p \geq \sigma \\ 0 & \text{if } -C_p < \sigma \end{cases}. \tag{4.4}$$

This is a local quantity that can be computed for each CFD surface cell. To blend the discontinuity, a smoothed Heaviside function was used in previous works [65, 91, 151],

$$\bar{X} = \frac{1}{1 + e^{2k(C_p+\sigma)}}, \tag{4.5}$$

We will call the cavitation constraint defined in Eqn (4.5) the *original* cavitation constraint. Although this original cavitation constraint is not used in this chapter, it will be used in the single-point optimizations in Chapter 7.

To penalize more on the cells with high $-C_p$ values, we modified the smoothed Heaviside function to take into account the amount that $-C_p$ exceeds σ. To avoid negative function values, we use $(-C_p - \sigma)^2$ as the penalty weight. As a result, the function we used here is

$$\bar{X} = \frac{(-C_p - \sigma)^2}{1 + e^{2k(C_p+\sigma+\gamma)}}, \tag{4.6}$$

where k is a free parameter and determines the transition sharpness; γ is a free parameter that determines the transition shift. We use a k of 15 and γ of 0.2. We will call the cavitation constraint defined in Eqn (4.6) *improved* cavitation constraint. This improved cavitation constraints are used for all multipoint optimization throughout this dissertation. We use improved for multipoint optimization cases because it more effectively reduces suction peaks and have been shown to converge better for multipoint optimizations. A comparison of these two types of cavitation sensors is shown in Figure 4.3.

The cavitation constraint is formulated as the integral of $\bar{X}$ over the hydrofoil surface except

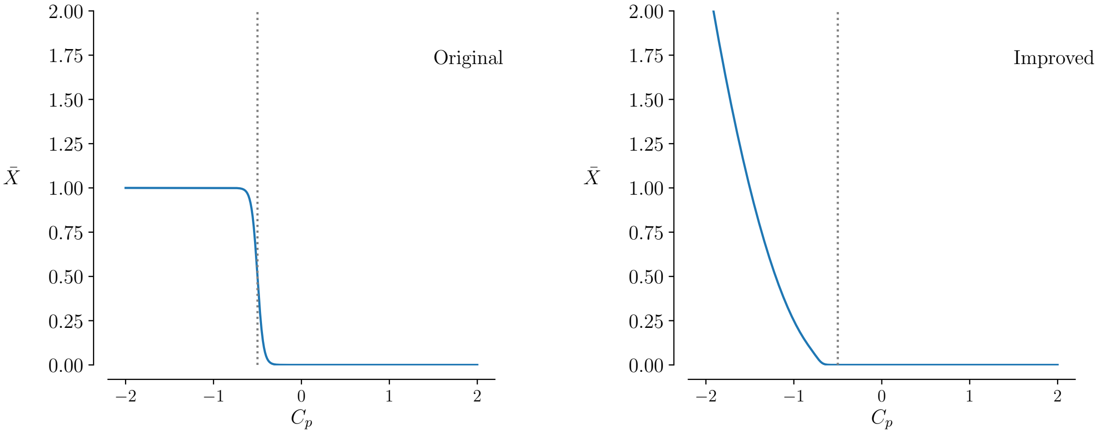

Figure 4.3: Original and improved cavitation sensors. Both use a sharpness parameter k of 15. The offset parameter γ used in improved is 0.2. A cavitation number σ of 0.5 is assumed in this demonstration.

for the trailing edge surface due to numerical oscillations (as shown in Figure 4.6), which suggests the total weighted surface area that is susceptible to cavitation.

$$\bar{A}_{\text{cav}} = \frac{1}{2A_{\text{ref}}} \iint_A \bar{X} dA, \tag{4.7}$$

where $A_{\text{ref}} = 0.243 \text{ m}^2$ is the reference area, which is the product of the mean chord and semi-span b, and $\bar{A}_{\text{cav}}$ is the non-dimensional weighted cavitation-inceptive area. The cavitation sensor does not go to zero, and thus we cannot enforce $\bar{A}_{\text{cav}} \leq 0$. Instead, we require

$$\bar{A}_{\text{cav}} \leq 2 \times 10^{-5}. \tag{4.8}$$

We scale both sides of this weighted cavitation-inceptive area constraint again by this limit value 2×10^{-5} to formulate the actual constraint value used in the optimization,

$$\frac{\bar{A}_{\text{cav}}}{2 \times 10^{-5}} \leq 1. \tag{4.9}$$

This reformulation is to provide a constraint value around the order of one to make the optimization well-posed.

4.2.4 Material failure constraint

We formulated the material failure constraints following the work by Papanikos et al. [152]. We consider three types of failure modes and use a different criterion for each failure type. We use maximum strain criterion for fiber breaking, Hashin-type criterion [5] for matrix cracking, and Ye-delamination criterion [105] for delamination. This set of failure criteria will be referred as *MHY* criteria.

The fiber breaking indicator constraints are,

$$\begin{aligned} I_1 &= \frac{\sigma_{22}}{Y_T} \leq 1, \\ I_2 &= -\frac{\sigma_{22}}{Y_C} \leq 1. \end{aligned} \tag{4.10}$$

The matrix tensile or compressive cracking indicator constraints are,

$$\begin{aligned} I_3 &= \left(\frac{\sigma_{11}}{X_T}\right)^2 + \left(\frac{\sigma_{12}}{S_{12}}\right)^2 + \left(\frac{\sigma_{13}}{S_{13}}\right)^2 \leq 1, \\ I_4 &= \left(\frac{\sigma_{11}}{X_C}\right)^2 + \left(\frac{\sigma_{12}}{S_{12}}\right)^2 + \left(\frac{\sigma_{13}}{S_{13}}\right)^2 \leq 1. \end{aligned} \tag{4.11}$$

The delamination in tension or compression indicator constraints are,

$$\begin{aligned} I_5 &= \left(\frac{\sigma_{33}}{Z_T}\right)^2 + \left(\frac{\sigma_{23}}{S_{23}}\right)^2 + \left(\frac{\sigma_{13}}{S_{13}}\right)^2 \leq 1, \\ I_6 &= \left(\frac{\sigma_{33}}{Z_C}\right)^2 + \left(\frac{\sigma_{23}}{S_{23}}\right)^2 + \left(\frac{\sigma_{13}}{S_{13}}\right)^2 \leq 1. \end{aligned} \tag{4.12}$$

The σ_{ij} are the element centroid stresses in different directions in the material coordinates. For an equivalent single CFRP layer, the delamination criterion here is equivalent to an out-of-plane matrix cracking criterion. From the above formulas, we have six failure indicator constraints for each element. We constrain the maximum of the six values,

$$\max\{I_1, I_2, I_3, I_4, I_5, I_6\} \leq 1. \tag{4.13}$$

To avoid the discontinuous nature of the maximum function, we use the Kreisselmeier–Steinhauser (KS) function to aggregate these six values to approximate the maximum [107, 108],

$$f = \mathrm{max}_i(I_i) + \frac{1}{\rho_{\mathrm{KS}}}\mathrm{ln}\left(\sum_{i=1}^{6} e^{\rho_{\mathrm{KS}}(I_i - \mathrm{max}_i(I_i))}\right), \tag{4.14}$$

where ρ_{KS} is the aggregation parameter. Consequently, each element has one aggregated failure constraint $f \leq 1$. To avoid having a large number of failure constraints, we use the KS function again to aggregate f over all the solid elements,

$$\mathrm{KS}_f = \mathrm{max}_j(f_j) + \frac{1}{\rho_{\mathrm{KS}}}\mathrm{ln}\left(\sum_{j=1}^{n} e^{\rho_{\mathrm{KS}}(f_j - \mathrm{max}_j(f_j))}\right), \tag{4.15}$$

where j is the element number in the structural mesh and n is the total number of solid elements. We consider a ρ_{KS} of 100 in the optimization. We use a safety factor of three here as a conservative consideration of the fatigue strength, variability in the material strengths, and uncertainties in material failure prediction and loading conditions. This safety factor value is chosen based on the recommendations from the first world-wide failure exercise [153]. The original elemental centroid stresses are multiplied by the safety factor to evaluate the failure indicator values of that element. The KS_f and f values shown later are the final values that take the safety factor into consideration. For efficiency, we only consider the region of the hydrofoil between the root and $y/b = 0.09$ when evaluating the material failure constraint, since stress concentration typically happens near the root.

4.2.5 Displacement constraint

While the material failure constraints provide considerations of structural integrity, the hydrofoil can still be susceptible to flow-induced vibrations, noise, and accelerated fatigue issues because we only analyze the steady-state performance. To address these issues, we enforce a displacement constraint as a surrogate for dynamic response constraints to avoid excessive displacements and vibrations. This is because a large deformation usually implies severe flow-induced vibrations, which can lead to significant dynamic load amplification. We use a discrete induced power aggregation method to aggregate the bending (z-direction as shown in Figure 4.1) displacement ω. This aggregation is chosen instead of the KS function because the KS function provides an overly conservative aggregated displacement value without an extremely high ρ_{KS}, and hence the optimizer might not be able to satisfy the displacement constraint. We also want to avoid using an extremely high ρ_{KS} because of the difficulties of estimating the second derivatives due to a large curvature [154]. The discrete induced power aggregation is written as,

$$\omega_{\text{DIP}} = \frac{\sum_j |\omega_j|^{\rho_{\text{power}}+1}}{\sum_j |\omega_j|^{\rho_{\text{power}}}}, \tag{4.16}$$

where ρ_{power} is the aggregation parameter. We consider a ρ_{power} of 100 in the optimization. Kennedy and Hicken [108] presented more details on this induced power aggregation method. To efficiently compute the aggregation, we only consider a small tip region between 90% span and the tip because this region undergoes the largest bending deflection for a cantilevered structure.

4.2.6 Design conditions

Table 4.3 lists the operating conditions that we use in the multipoint optimization, including inflow velocities U_∞, root-chord based Reynolds number Re_{rc}, lift coefficients C_L, cavitation numbers σ, as well as the operation probability weights. Foil size is shown in Figure 4.1. We choose

$C_L = 0.3$ at $U_\infty = 20$ m/s as the nominal condition with 60% probability of operation, while the highest lift condition is assumed to be at $C_L = 0.6$ at $U_\infty = 17$ m/s with 10% probability, and the maximum cruising speed is 24 m/s with $C_L = 0.2$ with 30% probability. The cavitation number σ is determined based on an assumed operation depth of 1 m. The lowest design Re_{rc} is 6×10^6, and hence we assume fully turbulent flow over the hydrofoil. Table 4.4 summarizes the optimization problem setup. The material failure and displacement constraints are enforced only at the $C_L = 0.6$ condition with the highest loading for computational efficiency.

Table 4.3: Design conditions with a submergence depth of 1 m. The foil geometry is shown in Figure 4.1.

Condition	U_∞	Re_{rc} (10^6)	C_L	σ	Weight
1	24 m/s	8.4	0.2	0.35	30 %
2	20 m/s	7.0	0.3	0.5	60 %
3	17 m/s	6.0	0.6	0.7	10 %

Table 4.4: Optimization problem setup

Category	Function/Variables	Description	Lower	Upper	Units
Objective	$\sum \text{wt}_i \times C_{Di}$	Weighted drag coefficient	-	-	-
Design variables	α	Angle of attack	-5	10	[°]
	s	Shape (FFD control points)	-0.3	0.3	m
		Twist	-5	5	[°]
	λ	Sweep	-30	30	[°]
	c	Chords	$0.25c_0$	$1.5c_0$	[m]
	θ_f	Fiber orientation	-40	40	[°]
		total number of design variables			**83**
Constraints	$C_L - C_L^*$	Lift coefficient	0.0	0.0	
		Fixed leading edge and trailing edge			
		Monotonic chord constraint			
	$\bar{A}_{\text{cav}}$	Non-dimensional weighted cavitation inception area	-	2×10^{-5}	
	t_{2D}	Thickness constraint	$0.5t_0$	-	m
	t_{1D}	Trailing edge thickness constraint	t_0	-	m
	c_{root}	Root chord constraint	c_{root_0}	c_{root_0}	m
	S	Projected area constraint	S_0	S_0	m^2
	KS$_f$	Structural failure constraint (at $C_L = 0.6$)	-	1	-
	w_{DIP}	Bending displacement constraint (at $C_L = 0.6$)	-	$0.05b$	[m]
		total number of constraints			**63**

4.3 Results

Figure 4.4 shows the CFD mesh convergence study using the three levels of CFD meshes shown in Figure 4.1. Bons and Martins [89] used a multi-level approach to accelerate aerostructural optimizations. Their single-point optimization results showed that the majority of the benefits came from the coarsest level optimization. The advantage of switching to finer meshes was resolving the shock wave more accurately. In our case, coarse meshes can predict the cavitation inception and other hydrodynamic performance reasonably well, as shown later in Section 4.3.2. Even though the assumption is that the improvements relative to the baseline design yielded from the coarsest level optimization are still valid on finer meshes, we acknowledge that finer meshes give more accurate performance prediction. Finer meshes better resolve the leading edge suction peak and tip vortex (and hence cavitation susceptibility) and provide a more accurate drag prediction.

Table 4.5 shows a convergence study of structural meshes using modal analysis. The L3 mesh natural frequencies only differ by 0.3% (mode one), 0.2% (mode two), and 0.6% (mode three) from the L1 mesh. The L3 structural mesh gives a reasonable prediction of the structural response. Thus, the coarsest (L3) CFD and structural meshes are used in the optimization study. However, to evaluate the optimized design benefits more accurately, we conduct the final analyses using the finest CFD and structural meshes (L1) with the optimized design variables.

Table 4.5: Structural mesh convergence using modal analysis of the baseline hydrofoil in vacuum

Mesh level	Mode 1 [Hz]	Mode 2 [Hz]	Mode 3 [Hz]
L1	58.81	155.79	236.44
L2	58.84	155.86	236.67
L3	59.00	156.15	237.81

We first compare the hydrodynamic performance of the baseline and the optimized result using the L3 level meshes. The comparison focuses on pressure coefficient C_p distribution, force coefficients, and deformations. To demonstrate that the optimization improvements are also valid

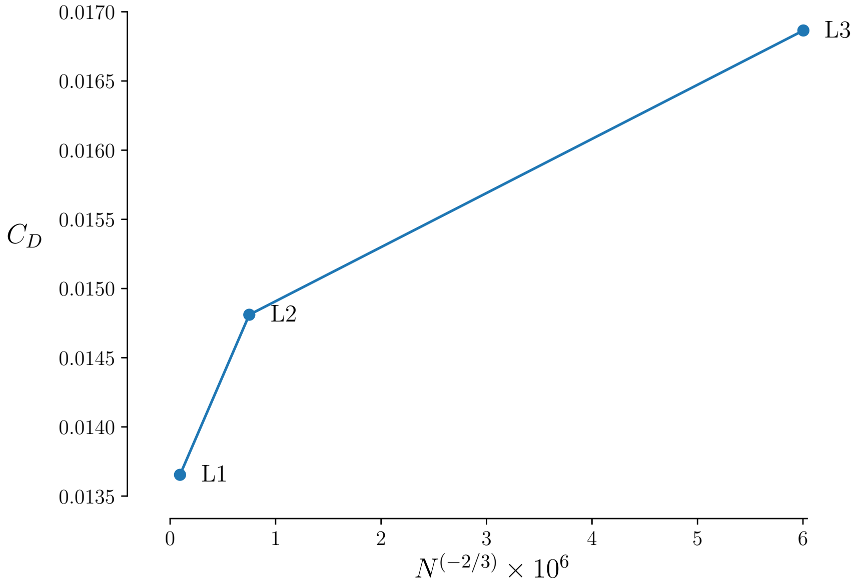

Figure 4.4: CFD mesh convergence study on the baseline hydrofoil. C_D is drag coefficient. N is the number of cells in the CFD mesh. The simulations are performed with an inflow velocity of 20 m/s and an angle of attack of $4°$.

when evaluating with finer meshes, we compare the performance between the optimized result with L3 meshes and the analysis on L1 meshes with optimized design variables. Later on, we use L1 meshes for further comparisons and discussions. To understand the tradeoffs between loading conditions, we compare the spanwise lift and drag coefficient distributions at all design conditions. In Section 4.3.4, in addition to the comparison with the baseline hydrofoil, we also compare the cavitation performance of our optimized result with a hydrofoil that uses the E1127 shape (designed by Shen and Eppler [70]) as the cross section. The reason for selecting the E1127 section for comparisons instead of other previously optimized sections, such as NACA 16-series, NACA 66 (MOD) series, or OS sections, is because the E1127 section is optimized at similar C_L ($C_{l_{2D}}$) conditions and has a wide optimal $C_{l_{2D}}$ range. Along with the hydrodynamic performance, structural performance is also a fundamental concern for hydrofoil designs. To compare the structural performance between the baseline and the optimized design, we show the static deformation and modal analysis results for these two cases in Section 4.3.5. To assess the effect of sweep and chord variables, we perform another optimization without sweep and chord variables in Section 4.3.6.

4.3.1 Comparison of the optimized hydrofoil and the baseline hydrofoil

Figure 4.5 shows the convergence histories of the objective function along with the snapshots of the baseline and optimized undeformed geometries at selected iterations, which include two intermediate steps and the final step. From this shape evolution, we observe that the cross-sectional shapes and planform are modified during the early stage of the optimization. After that, the most significant change is the sweep angle. The final optimized hydrofoil has a backward sweep λ of $22°$, and a backward swept fiber angle θ_f of $-23°$ [1] (defined relative to the y-axis and positive leaning forward). The θ_f is almost aligned with the λ so that the fiber longitudinal direction takes a majority of the load with higher strength. This alignment also ensures the maximum bending stiffness and highest bending resonance frequency. The results suggest there is benefit to use material anisotropy to balance the bend-twist coupling and to modify the directional strength to reduce the susceptibility to excessive deformation and material failure when sweep presents. The optimized configuration shows that the tip chord variable reaches its lower limit, a quarter of the initial parent FFD tip chord. The tip chord length of the optimized hydrofoil is 0.094 m, which is 52.2% of the initial tip chord length of 0.18 m. The inboard chord variable increases accordingly to satisfy the projected area constraint. Cross-sectional shape features added camber and modified thickness distribution as shown in Figures 4.5 and 4.6. The camber and twist distributions are non-uniform along the span. The thickness is increased except for the region near the tip.

Figure 4.5 also shows the convergence histories of the cavitation constraints, displacement constraint at $C_L = 0.6$, material failure constraint at $C_L = 0.6$, sweep angle λ, and the fiber angle θ_f. The cavitation constraint at $C_L = 0.3$ converges to 2% of the bound value. The cavitation constraints at $C_L = 0.2$ ($\sigma = 0.35$) and $C_L = 0.6$ ($\sigma = 0.7$) are at the bound of one because the cavitation requirements are more demanding at these two conditions. At $C_L = 0.2$, it is due

---

[1] Note that this value is slightly different from the journal version due to a different rounding approach.

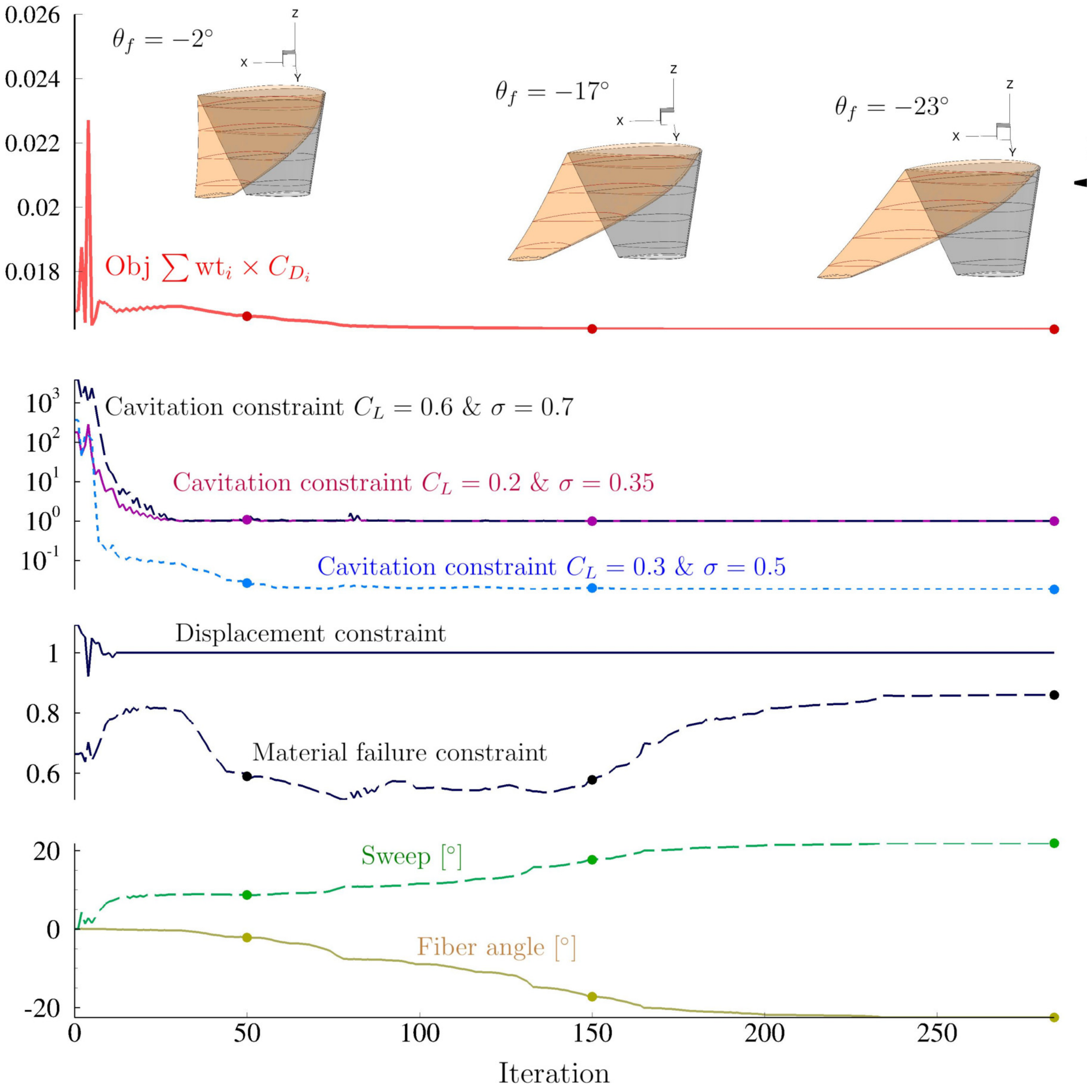

Figure 4.5: Optimization convergence history with undeformed shapes comparison between baseline (gray shaded) and the optimized (orange shaded) designs at two intermediate steps and the final step (correspond to the symbols marked on the histories). The total CPU time for the hydrostructural optimization over the three C_L conditions is 1.7 days (108 cores, 3.0 GHz Intel Xeon Gold 6154).

to the low cavitation number; while at $C_L = 0.6$, it is because of the high C_L requirement. The displacement constraint stays around the bound, while the material failure constraint stays below the bound. The displacement constraint places a more conservative requirement on the structural stiffness than the material failure constraint. However, an equivalent unidirectional CFRP might result in underestimating the material failure indicator than a multi-layer composite hydrofoil in reality because most mechanistic material failure models were not developed for thick unidirectional CFRP with combined bending and torsional load.

The left side of Figure 4.6 shows pressure coefficient C_p contours and the non-dimensional bending (z-direction) displacement, ω/b, contours on the pressure side for all design conditions. The right side of Figure 4.6 shows cross-sectional shapes and C_p profiles at three slices along the spanwise direction: A ($y/b = 0.2$), B ($y/b = 0.5$), and C ($y/b = 0.8$). The cross-sectional shapes are shown in non-dimensional coordinates for easy comparisons. The leading edge coordinates differ between the baseline and the undeformed optimized result because of the chord and sweep variables.

In Figure 4.6, the dark purple region on the C_p contours implies that the pressure is at or lower than the vapor pressure, suggesting cavitation inception. As shown in these C_p contours, the optimized hydrofoil delays cavitation compared to the baseline. Note that the actual cavity tends to be larger because of the modification to the boundary layer once a cavity develops. The sectional C_p profiles on the right provide a more straightforward and detailed comparison. The baseline leading edge has high suction peaks at all design conditions, while this high suction peak is not observed for the optimized hydrofoil. As shown by the sectional shapes, the optimized hydrofoil introduces camber and modifies the thickness distributions to reduce the suction peaks and achieve a near-flat C_p distribution on the suction side. Shen and Eppler [70] used a flat velocity distribution to conduct inverse designs, which also resulted in designs with flat C_p distributions. Comparisons with a 3-D E1127 foil will be shown later in Figures 4.12 and 4.14–4.18. The C_p crossing near the leading edge at a low C_L is unavoidable to maintain near-flat suction side pressure

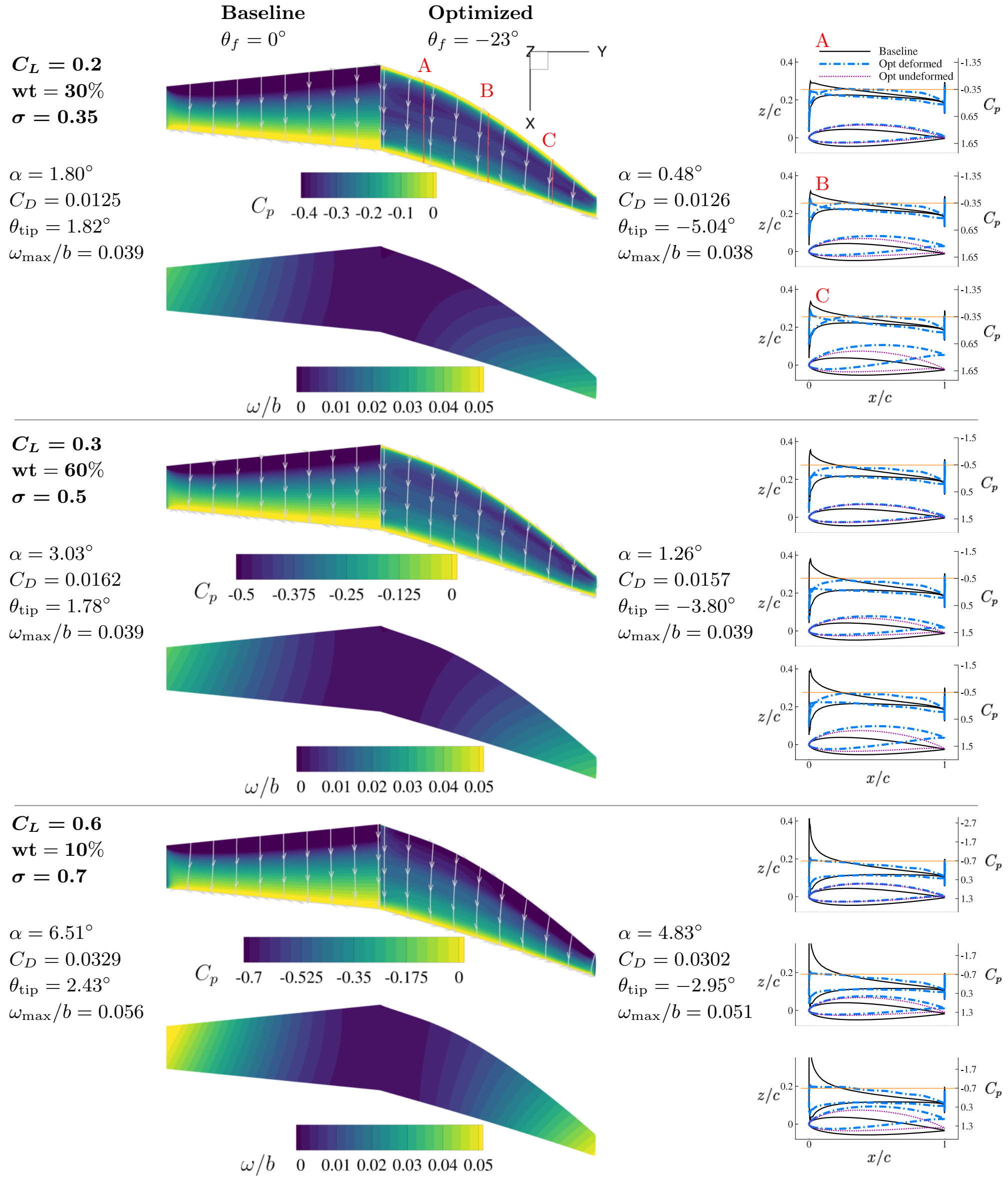

Figure 4.6: Pressure coefficient C_p contours on the suction side and non-dimensional bending displacement (ω/b) contours are shown on the left; sectional C_p and non-dimensional cross-sectional shapes at three different slices are shown on the right. For the optimized hydrofoil, both undeformed and deformed shapes are shown in the sectional plots on the right. The orange horizontal lines in the sectional plots on the right indicate the critical boundary of cavitation occurrence. The optimized hydrofoil yields lower C_D and avoids cavitation at the nominal operating condition $C_L = 0.3$ with a weight (wt) of 60%. The maximum bending displacement at the tip and cavitation susceptibility are also substantially reduced for the optimized hydrofoil compared to the baseline.

distribution at high C_L. Similar behaviors were observed by the optimized foils shown by Shen and Eppler [70]. The pressure recovery region near the trailing edge has a higher adverse pressure gradient compared to the baseline, which increases the likelihood of flow separation. However, no flow separation occurs on both foils, as indicated by the flow streamlines in Figure 4.6.

The pressure distribution and structural stiffness determine the deformation, which alters the flow and affects structural integrity. As shown by θ_{tip} values, ω/b contours, and sectional plots at *C* in Figure 4.6, the optimized hydrofoil has a nose-down tip twist ($\theta_{\text{tip}} < 0°$) at each design condition compared to the nose-up tip twist ($\theta_{\text{tip}} > 0°$) for the baseline. The nose-up tip twist of the baseline composite hydrofoil ($\theta_f = 0°$) is mainly caused by the center of pressure being upstream of the elastic axis. The near-flat C_p distributions move the centers of pressure downstream for the optimized hydrofoil compared to the baseline. This shift reduces the nose-up pitching moment and nose-up θ_{tip}. In addition, the backward sweep induces a nose-down bend-twist coupling. Comparing the θ_{tip} of the optimized hydrofoil between design conditions, we notice that the tip twist magnitude $|\theta_{\text{tip}}|$ decreases with the total dimensional lift ($L = C_L \times (0.5\rho_{\text{water}} U_\infty^2 A_{\text{ref}})$). This reduction in $|\theta_{\text{tip}}|$ is caused by the change in the center of pressure. As discussed previously, the optimized hydrofoil has a C_p crossing at $C_L = 0.2$. At upstream of this C_p crossing, the pressure side is subject to a pressure lower than the suction side, resulting in a downward force. When C_L increases, the C_p curve crossing moves towards the leading edge and finally disappears at $C_L = 0.6$. In other words, this downward force that occurs before the C_p crossing decreases with higher C_L, which moves the center of lift upstream when C_L increases. As a result, the nose-down pitching moment decreases with higher C_L and leads to the reduction in $|\theta_{\text{tip}}|$.

From Figure 4.6, the total weighted drag coefficient decreases from 0.0168 to 0.0162. Although the optimized hydrofoil shows more drag reduction at the $C_L = 0.6$ condition, most of the weighted drag reduction comes from the nominal condition at $C_L = 0.3$ because of a higher weight. Despite the small weighted drag reduction, the most significant improvement is on the cavitation inception speeds. A detailed discussion will be given in the next Section (4.3.2).

4.3.2 Comparison of the coarse and finer meshes

To get a more accurate performance evaluation, we apply the optimized design variables to the finer L1 level CFD and FEM meshes. In the following discussions, the L1 baseline refers to the baseline analysis using L1 meshes, and the L1 optimized refers to the analysis using L1 meshes with the optimized design variables. Figure 4.7 shows a comparison of C_p distributions and structural failure inception indicator f contours between L3 optimized and L1 optimized results. The L1 optimized result shows almost identical C_p and f distributions to the coarser L3 optimized result, but with a more accurate (lower) C_D and (higher) f_{max}. The L1 optimized result has higher f_{max} values because using a finer mesh gives a more accurate stress prediction that tends to be higher in areas with stress concentration. This highly local concentration leads to a maximum material failure indicator value slightly larger than one, but the violation is minor We use L1 mesh results for later discussions unless otherwise specified.

Figure 4.8 shows a comparison between the L1 baseline and the L1 optimized results. The weighted drag coefficient decreases from 0.0137 (baseline) to 0.0136 (optimized) when using L1 meshes. The drag change at each design condition follows the same trend as the L3 results. As shown in Figure 4.8, the C_D at $C_L = 0.2$ increases slightly compared to the baseline while decreasing at other C_L conditions. The overall weighted reduction C_D of the optimized compared to the baseline at L1 meshes is 1.2% compared to 2.3% for the L3 level meshes. The quantified drag reduction might not be meaningful considering the prediction accuracy and manufacturing uncertainties. The study presented by Garg et al. [91] shows a mean error of 5% for drag coefficients, 2.9% for lift coefficients, and 3% for moment coefficients between numerical prediction and experimental measurements. The stringent cavitation requirement might limit the drag reduction. In previous works by Garg et al. [65, 91], they showed designs with more significant drag reductions while using a much more relaxed cavitation constraint (the lowest cavitation number was set to 1.6 in Garg et al. [65, 91] compared to 0.35 here). However, the improvement on the cavitation performance will contribute to efficiency significantly at the design conditions, even though the

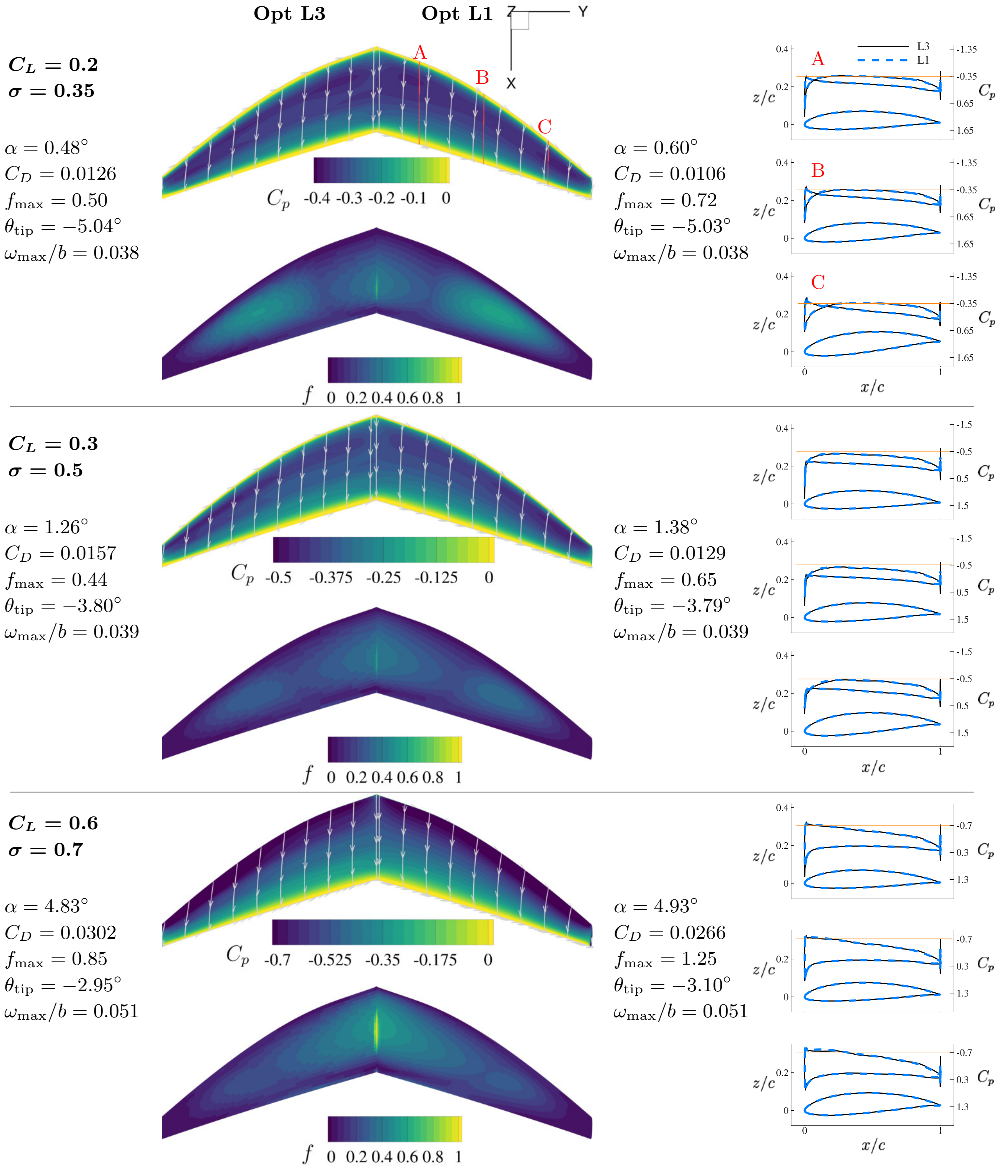

Figure 4.7: Pressure coefficient C_p, failure indicator f contour, and overall performance comparison between L1 (fine) and L3 (coarse) CFD and FEM meshes. The mesh details are given in Table 4.1. Similarity between the pressure coefficient and failure indicator distributions suggests numerical convergence and asserts the validity of using a coarser mesh for optimization to minimize the computational cost.

contribution to drag reduction is not directly demonstrated here because of the modeling limitation. The primary focus of this chapter is to maximize the cavitation inception speed. As shown in Figure 4.8, the cavitation inception speed increases relative to the baseline hydrofoil at the three design conditions are 24%, 82%, and 94%. The weighted improvement on cavitation inception speed is 65.8%. These are very significant improvements. Note that once a leading edge cavitation bubble incepts, the bubble expands quickly, leading to lower lift and lift fluctuations, and hence form a barrier for further increases in speed. Hence, the cavitation inception speed is often taken as the maximum speed for a lifting device that is not intentionally designed to operate in cavitating states.

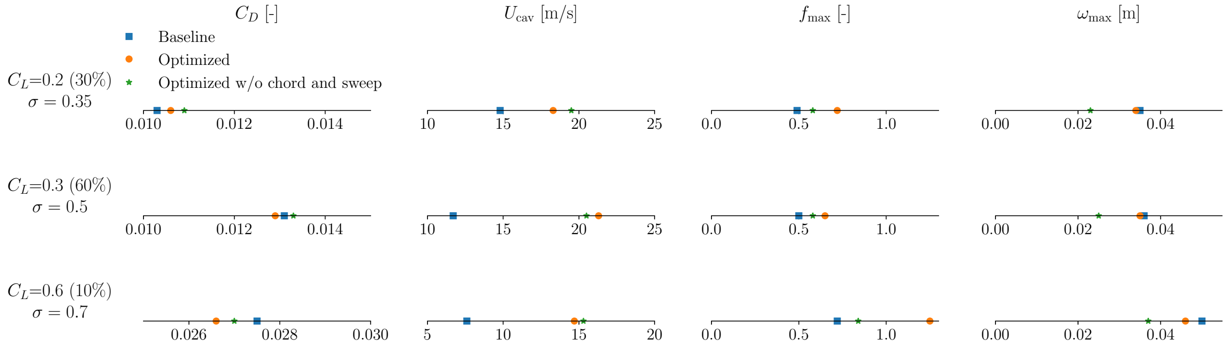

Figure 4.8: Summary of results evaluated with L1 mesh. The results include the baseline case, the optimized result with planform variables, and the analysis of optimized result without planform variables. U_{cav} is cavitation inception speed. f_{max} is the material failure indicator value. $\omega_{\max}$ is the largest bending displacement (bending). Orange dots are for the optimized hydrofoil. Blue squares are for the baseline hydrofoil. Green stars are for the optimized hydrofoil without chord and sweep variables. This optimization result will be discussed in Section 4.3.6. The optimized hydrofoil has a much higher cavitation inception speed, lower weighted drag, and $\omega_{\max}$ compared to the baseline hydrofoil.

4.3.3 Tradeoffs between different conditions

To better understand the tradeoffs between loading conditions, we show spanwise normalized lift distributions, sectional 2-D lift coefficient $C_{l_{2\text{D}}}$ distributions, sectional friction drag coefficient $C_{dv_{2\text{D}}}$ distributions, and sectional total (friction and pressure) drag coefficient $C_{d_{2\text{D}}}$ distributions in

Figure 4.9. The baseline result is shown on the left side, and the optimized result is shown on the right.

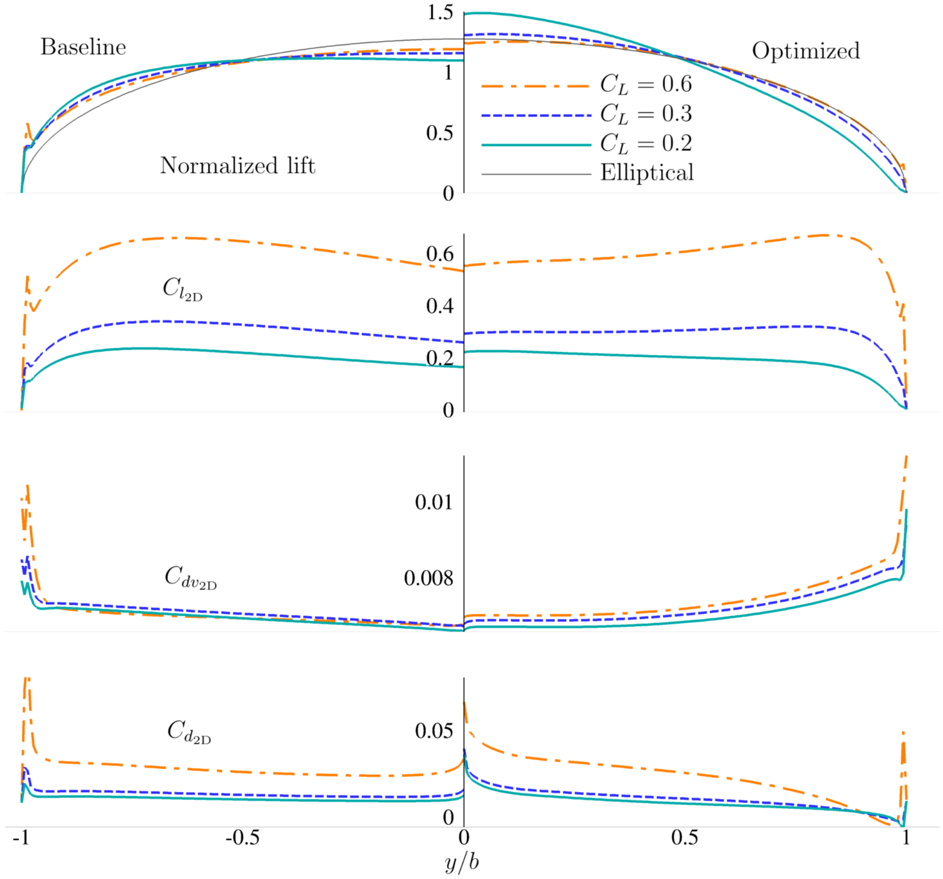

Figure 4.9: Spanwise normalized lift distributions, 2-D sectional lift coefficient ($C_{l_{2D}}$) distributions, sectional friction drag coefficient ($C_{dv_{2D}}$) distributions, and sectional total drag coefficient ($C_{d_{2D}}$) distributions. Compared to the baseline, the optimized hydrofoil shifts the loading towards the root to reduce the lift-induced drag at high C_L conditions caused by the large tip vortex, and to reduce the bending moment and thus limit deformation.

The normalized lift is the lift per unit span normalized by the total lift. Without non-planar wake effects, an elliptical normalized lift distribution indicates the least lift-induced drag for a given span and total lift. For the optimized result, the $C_L = 0.6$ condition has a normalized lift condition closest to the elliptical, whereas the $C_L = 0.2$ shows the largest deviation from the elliptical. This deviation from the elliptical distribution at $C_L = 0.2$ is even larger than the baseline, which explains the higher drag of the optimized hydrofoil at this condition. At a low lift condition, lift-induced drag constitutes a small part of the total drag, so the optimization does not drive the normalized lift distribution to be elliptical. The lift-induced drag reduction at a low lift condition contributes little to the overall efficiency when multiple conditions are considered. The effort required to achieve this reduction can degrade the performance at other conditions and might not pay off when considering the overall response. At a higher lift condition, it is more worthwhile to have an elliptical normalized lift distribution. These observations suggest that single-point optimization can cause biased results and highlight the need to do multipoint optimizations to yield a better overall performance [65, 89].

Compared to the baseline, the optimized hydrofoil increases the lift at the root and has a lower lift at the tip for all conditions, indicating a lower tip loading and hence a weaker tip vortex. This low tip loading results from the nose-down tip twist and the shortened chord length near the tip. A weaker tip vortex is essential to avoid or delay tip vortex cavitation and associated noise issues. From the pressure iso-surfaces in Figure 4.18 that we show later, it is evident that the baseline hydrofoil has a larger tip vortex cavity than the optimized hydrofoil at $C_L = 0.6$.

Figure 4.9 shows that the $C_{l_{\mathrm{2D}}}$ of the optimized result is increased near the root compared to the baseline due to the added camber. With the same root chord, the optimization adds a camber to increase the $C_{l_{\mathrm{2D}}}$ and thus the lift, which helps to achieve a loading distribution closer to the elliptical. The $C_{l_{\mathrm{2D}}}$ distribution of the optimized hydrofoil also shows larger spanwise variations than the baseline due to a larger sweep angle. Chapter 3 showed a similar observation. The backward sweep leads to a downwash effect on the inboard portion, which reduces the inboard $C_{l_{\mathrm{2D}}}$. Nevertheless, this contribution is not significant enough to offset the increase induced by the added camber. On the contrary: the inboard part causes an upwash effect on the tip and increases the $C_{l_{\mathrm{2D}}}$ locally. Although the added camber and backward sweep both increase the tip loading, this addition does not counteract the reduction in lift caused by the nose-down θ_{tip} and the shortened tip chord length. Hence, the optimized hydrofoil has a lower normalized lift at the tip than the baseline case.

From sectional friction drag coefficient $C_{dv_{\mathrm{2D}}}$ distributions, the optimized hydrofoil has higher $C_{dv_{\mathrm{2D}}}$ over the entire span because of the increased thickness and modified pressure distribution. Nevertheless, the pressure drag (lift-induced drag and form drag components) of the optimized hydrofoil is lower, and thus the total drag is lower than the baseline. Figure 4.10 shows the skin friction drag coefficient (C_f) contours of the baseline and optimized hydrofoils. The optimized hydrofoil shows higher C_f over the region where the local pressure is lower than the baseline hydrofoil. According to Bernoulli's equation, a lower local pressure indicates a higher velocity on the outer edge of the boundary layer. This higher local velocity causes a higher velocity gradient near the wall, and thus higher shear stress. Another reason for the increased $C_{dv_{\mathrm{2D}}}$ is the higher thickness-to-chord ratio. Nevertheless, the friction component is small, so the increase does not significantly affect the overall efficiency.

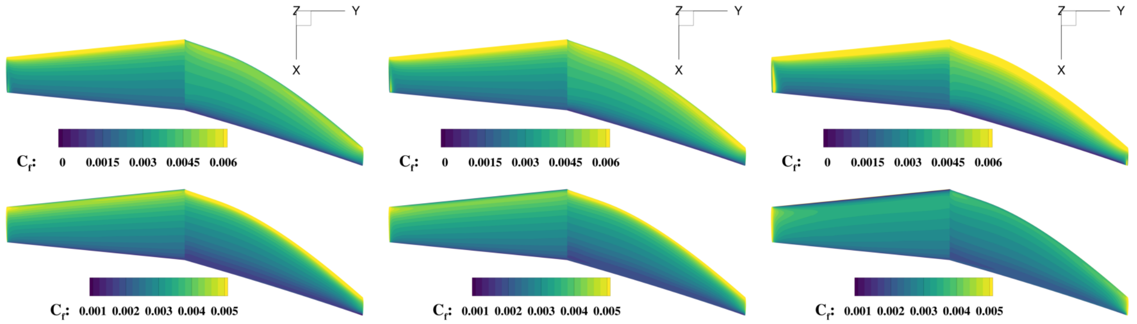

(a) $C_L = 0.2$

(b) $C_L = 0.3$

(c) $C_L = 0.6$

Figure 4.10: C_f contour comparison between the baseline (left) and the optimized (right) hydrofoil using L1 meshes. The suction side is shown on the top; the pressure side is shown on the bottom. While the baseline has lower frictional drag, the optimized hydrofoil has lower total weighted drag.

4.3.4 Comparison of the optimized hydrofoil and an E1127 hydrofoil

In Section 4.3.1, we showed that the optimization removed the suction peaks and delayed cavitation compared to the baseline. To further discuss the optimized hydrofoil cavitation improvement, we compare the sectional geometries and cavitation performance of our optimized hydrofoil with the baseline hydrofoil and the E1127 design. Since the E1127 section is a 2-D design and our optimized hydrofoil is designed with 3-D simulations, we complete the comparison in both 2-D and 3-D ways to ensure a fair comparison.

In terms of 2-D comparison, we first compare 2-D sectional geometries between the optimized hydrofoil sections, the baseline hydrofoil section (NACA 0009), and the E1127 section, as shown in Figure 4.11a. For the optimized hydrofoil, cross-sectional shapes at sections $y/b = 0.2$ (inboard), $y/b = 0.5$ (midspan), and $y/b = 0.8$ (outboard) are similar. The outboard section has a slightly higher thickness-to-chord ratio than the other two sections. The other two sections share an almost identical thickness-to-chord ratio. The shapes of the midspan section and the inboard section are similar, with a slight difference near the trailing edge. The local camber at the trailing edge increases when moving from inboard to outboard, as shown in Figure 4.11c, which explains the higher $C_{l_{\text{2D}}}$ at $y/b = 0.8$ compared to $y/b = 0.2$ at $C_L = 0.3$ and $C_L = 0.6$ conditions as shown in Figure 4.9, even though the hydrofoil undergoes a nose-down tip twist. When viewing from the non-dimensional coordinates shown in Figure 4.11a, the E1127 section is thicker than the optimized sections approximately between $x/c = 0.2$ and $x/c = 0.6$. As shown by the enlarged leading edge geometries in Figure 4.11b, the E1127 lower surface near the leading edge is more convex than the optimized sections. In contrast, the upper surface is less convex than the optimized sections, suggesting that the optimized sections have higher cavitation inception speeds at a high lift coefficient range (high angle of attack range).

The 2-D cavitation performance in Figure 4.12 shows how cavitation performance varies for these geometries. The figure includes a cavitation bucket comparison and a detailed C_p profile comparison. Cavitation bucket describes the cavitation performance of a hydrofoil profile by

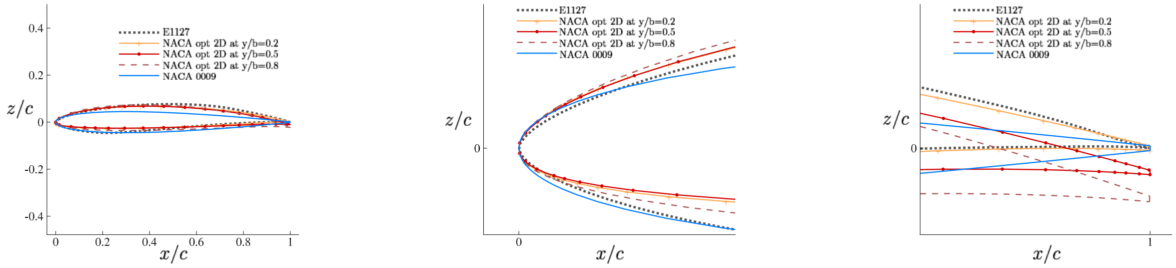

(a) Whole section comparison.

(b) Comparison enlarged at the leading edge

(c) Comparison enlarged at the trailing edge

Figure 4.11: Sectional shape comparison. Comparison of sectional shapes of the optimized hydrofoil at three different slices with NACA 0009 and E1127. Shapes are shown in non-dimensional coordinates.

plotting lift coefficient versus cavitation inception speed U_{cav} (top x-axis) or negative minimum pressure coefficient $-C_{p_{\min}}$ (bottom x-axis), as shown in Figure 4.12a. It forms a bucket shape when rotating the plot 90° counter-clockwise. The foil is cavitation-free when operating within the bucket, while cavitation develops when operating outside of the bucket. A deeper cavitation bucket indicates higher cavitation inception speeds at the operating conditions covered by the bucket bottom. In comparison, a wider cavitation bucket indicates the hydrofoil has a wider range of cavitation-free conditions. In the middle of the cavitation bucket where it has the greatest depth, the hydrofoil is most susceptible to the mid-chord cavitation because the high suction pressure is likely to occur aft of the foil leading edge. Leading edge suction side cavitation and pressure side cavitation develop when operating outside of the bucket on the top and bottom curves, respectively.

To construct the 2-D cavitation buckets for the baseline hydrofoil sections and the optimized hydrofoil sections, we first extract the sectional C_p and $C_{l_{2\text{D}}}$ at the three sections corresponding to those in Figure 4.11a from 3-D simulations. We ran these simulations with $Re_{\text{rc}} = 7 \times 10^6$. The $C_{p_{\min}}$ values are then read from these sectional C_p curves. We exclude the trailing edge when extracting the $C_{p_{\min}}$ value. From the sectional plots in Figure 4.7, we see a strong C_p oscillation at the trailing edge. This numerical oscillation could be caused by the blunt trailing edge and

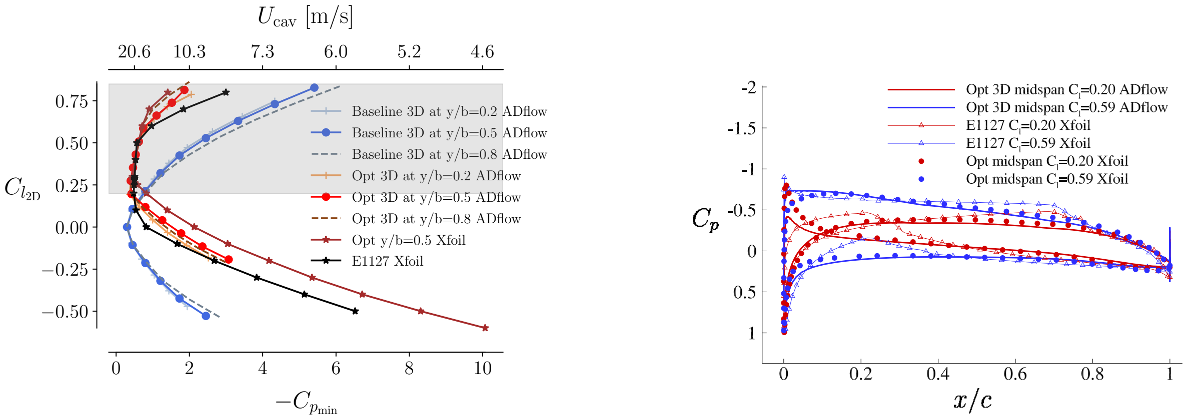

(a) 2-D cavitation buckets of the baseline sections, the optimized hydrofoil sections and the E1127 section. The optimized sections outperform (higher cavitation inception speed, U_{cav}) the baseline sections and the E1127 section at $C_{l_{2\text{D}}} > 0.2$.

(b) C_p profiles comparison between the optimized hydrofoil midspan section ($y/b = 0.5$) and E1127 section. The optimized hydrofoil midspan result include the extracted data from 3-D ADflow simulations and the 2-D simulation using Xfoil.

Figure 4.12: 2-D cavitation performance comparison. The local chord based Re ranges from 6.6×10^6 to 3.5×10^6 for the curves shown.

inadequate mesh at the trailing edge. When using the L1 mesh, the oscillation is substantially reduced compared to the L3 mesh results. However, this exclusion should not affect the values because the lowest C_p occurs relatively upstream rather than at the trailing edge, as shown by the L1 mesh results in Figure 4.7. We also show analyses with Xfoil (a widely used 2-D boundary element method coupled with a boundary layer solver [155]) for the optimized hydrofoil midspan section to compare the 2-D response because the E1127 section was optimal under 2-D flow assumptions. For simplicity, in later discussions, we will use the word “extracted” for these 2-D results that are extracted from 3-D simulations. These extracted results and the additional 2-D Xfoil result for the optimized hydrofoil midspan section are then compared to the E1127 section results obtained using Xfoil. For Xfoil simulations, we use 160 panels for the E1127 section and use 200 panels for the optimized hydrofoil midspan section. We ran these Xfoil simulations with $Re = 6.3 \times 10^6$.

The comparison between the extracted 2-D cavitation buckets of baseline hydrofoil sections, optimized hydrofoil sections, and the E1127 cavitation bucket from Xfoil is shown in Figure 4.12a. The NACA 0009 baseline sections have symmetric cavitation buckets about $C_{l_{\text{2D}}} = 0$ due to the shape symmetry about the chord line. When $C_{l_{\text{2D}}} > 0.1$, the optimized hydrofoil sections and the E1127 section show wider and deeper cavitation buckets than the extracted NACA 0009 baseline results, as both the optimized sections and the E1127 section are designed asymmetrically to achieve better performance at positive lift conditions. When $C_{l_{\text{2D}}} \geq 0.2$ (the gray range highlighted in Figure 4.12a), the optimized sections outperform E1127; when $C_{l_{\text{2D}}} < 0.2$, E1127 shows a better cavitation performance. This observation is consistent with the difference we observe in the leading edge nose geometries. The cause is that the operating conditions we use in our optimization focus on $C_L \geq 0.2$ conditions. At equivalent 2-D conditions $C_{l_{\text{2D}}} = 0.2$, $C_{l_{\text{2D}}} = 0.3$, and $C_{l_{\text{2D}}} = 0.6$, cavitation buckets of the optimized sections show greater depths than the E1127 section. From Figure 4.12b, the extracted $C_{p_{\text{min}}}$ of the optimized hydrofoil midspan is -0.42, which is higher than that of the E1127 section with $C_{p_{\text{min}}} = -0.48$ at $C_{l_{\text{2D}}} = 0.2$. At $C_{l_{\text{2D}}} = 0.59$, $C_{p_{\text{min}}}$ of the extracted optimized midspan result and the E1127 Xfoil result are -0.74 and -0.97 respectively.

Even though the extracted results are 2-D, they still include 3-D effects. To compare the optimized hydrofoil sections and the E1127 section more fairly and understand the difference between 2-D data extracted from 3-D results and 2-D simulation results, we run additional simulations for the optimized hydrofoil midspan section ($y/b = 0.5$) using Xfoil. The result is shown by the brown line with star symbols in Figure 4.12a. Similarly, the optimized hydrofoil midspan section outperforms the E1127 section at $C_{l_{\text{2D}}} > 0.25$ except for $C_{l_{\text{2D}}} \approx 0.5$. For the optimized hydrofoil midspan section, the extracted cavitation buckets and the 2-D Xfoil cavitation bucket share similar shapes and widths, with an offset in the $C_{l_{\text{2D}}}$ range. This shift is likely to be caused by the downwash. Downwash causes a reduction in the effective angle of attack for the local foil section. Hence, to compensate for the incidence loss and yield the same $C_{l_{\text{2D}}}$, sections in a 3-D simulation require higher inflow angles than in a 2-D simulation. This inflow angle variation leads to the change in the suction peak and thus results in a different $C_{p_{\text{min}}}$ value. Figure 4.12b shows the extracted C_p

curves and the 2-D Xfoil C_p for the optimized hydrofoil midspan section. At $C_{l_{\text{2D}}} = 0.2$, the extracted result has a much lower suction peak than the Xfoil result. Since this suction peak occurs on the pressure side, the incidence increase required for compensating the downwash effect reduces the suction peak. At $C_{l_{\text{2D}}} = 0.59$, the inflow angle is high enough that the required incidence increase introduces a slight decrease in C_p on the suction side for the 3-D hydrofoil section, while the Xfoil result does not show a suction peak. We know that a foil with an elliptical normalized lift distribution has a constant downwash along the span. From the normalized lift distribution shown in Figure 4.9, the normalized lift distributions of the baseline hydrofoil do not deviate much from the elliptical one. Hence, the downwash stays more or less constant along the span. This nearly constant downwash effect along the span explains the almost overlapped cavitation buckets of different spanwise sections for the baseline hydrofoil, as shown in Figure 4.12a.

In terms of the 3-D comparison, we model a 3-D E1127 hydrofoil with the same procedure as the baseline hydrofoil. The 3-D E1127 hydrofoil has zero-twist throughout the span and has the same planform as the baseline, while the cross-section is changed from the NACA 0009 section to the E1127 section. The E1127 hydrofoil simulations are performed with hydrodynamic analysis using a CFD mesh with 10,444,800 cells, similar to the L1 mesh size for the baseline hydrofoil and the optimized hydrofoil. The E1127 section has high local curvatures, which causes difficulties in meshing and numerical simulations. The 3-D E1127 hydrofoil result has waviness in C_p distributions. We apply a smoothing procedure to surface C_p for the E1127 hydrofoil using Tecplot as a post-processing step to remove extreme oscillations. For the Tecplot smoothing procedure, we use five passes with a coefficient of 0.5. The boundary option is fixed. Figure 4.13 compares the original C_p contour with the smoothed C_p contour for the E1127 hydrofoil at $C_L = 0.6$. The C_p contour is smoother and the $C_{p_{\text{min}}}$ after smoothing increases by 0.03. For later discussions, we apply this smoothing procedure to all the E1127 results.

Figure 4.14 compares the 3-D cavitation buckets of the L1 baseline, the L1 optimized, and the E1127 hydrofoils. We also excluded the trailing edge when extracting $C_{p_{\text{min}}}$. In addition, we

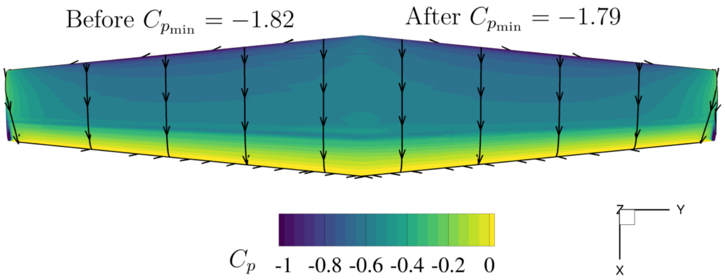

Figure 4.13: Original C_p contour on suction side and smoothed C_p contour on suction side for the E1127 hydrofoil at $C_L = 0.6$ and $Re_{\text{rc}} = 6 \times 10^6$

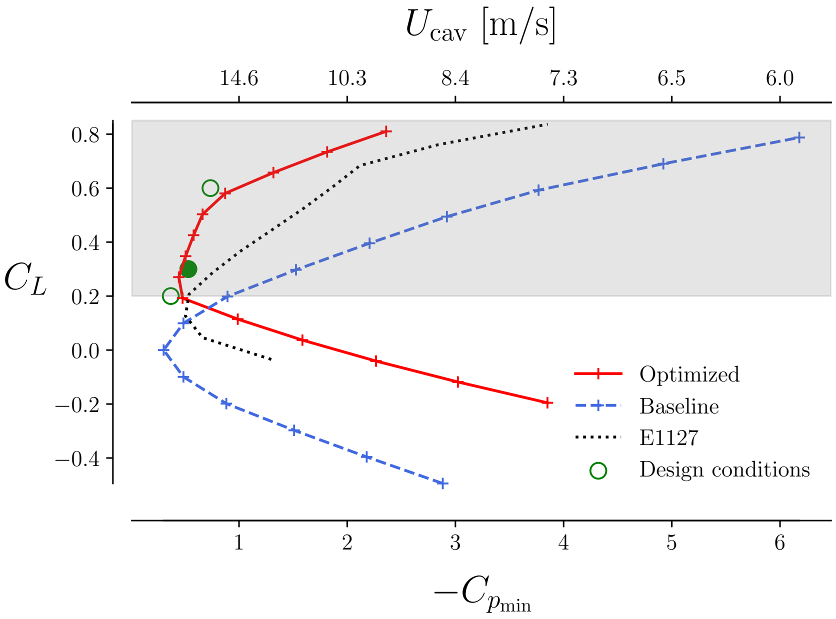

Figure 4.14: 3-D cavitation buckets of the baseline hydrofoil, the optimized hydrofoil, and the E1127 hydrofoil, plotted in the form of the 3-D lift coefficient C_L versus $-C_{p_{\min}}$ and cavitation inception speed U_{cav}. The optimized hydrofoil outperforms (higher cavitation inception speed, U_{cav}) the baseline and the E1127 hydrofoils at $C_L > 0.2$. The design C_L range is highlighted by gray color. The green-filled circle indicates the nominal operating condition ($C_L = 0.3$), while the green open circles marked the other two design conditions with lower weights ($C_L = 0.2$ and $C_L = 0.6$).

excluded the tip surface to avoid extreme values caused by imperfect grids on the highly curved tip surface.

Like the 2-D cavitation buckets, the 3-D cavitation bucket shows that the optimized hydrofoil has higher cavitation inception speeds than the baseline, and the optimized hydrofoil outperforms the E1127 hydrofoil when $C_L \geq 0.2$ (as shown in the gray range highlighted in Figure 4.14). The green-filled circle in Figure 4.14 indicates the nominal operating condition ($C_L = 0.3$), while the green open circles marked the other two design conditions with lower weights ($C_L = 0.2$ and $C_L = 0.6$). The lowest and highest loading conditions are slightly outside of the optimized hydrofoil cavitation bucket because they are at the bounds of the design range and the cavitation constraint tolerances are not tight enough at these two loading conditions. The determination of a suitable tolerance is not trivial and relies on trials and errors. The tolerance cannot be excessively tight because the value of the cavitation sensor is never zero, even for the cavitation-free area. However, the two conditions outside the cavitation buckets have lower probabilities of operation, so the impact on overall performance is not significant. Additionally, it is also possible to conduct optimization with a wider range of operating conditions to address this issue. Moreover, it is possible that if we use tighter tolerances for the cavitation constraint and the optimization feasibility, we can achieve cavitation-free at all design conditions. This wider range of design conditions can lead to a wider cavitation bucket that even outperforms the E1127 design when $C_L < 0.2$, but there could be a tradeoff on the weighted drag and hence efficiency.

To show the cavitation performance in a more realistic sense, we show the dimensional loading-speed envelopes in Figure 4.15. These envelopes are computed using the same set of data in Figure 4.14. At the same allowable speed, the optimized hydrofoil can carry a significantly higher load than the baseline and the E1127 hydrofoils because it has higher $C_{p_{\text{min}}}$ values (and hence higher cavitation inception speeds) at a higher C_L range.

Note that we focus on a positive lift design range in this dissertation, and hence the optimized result has a non-symmetrical section and a cavitation bucket that is skewed towards positive load-

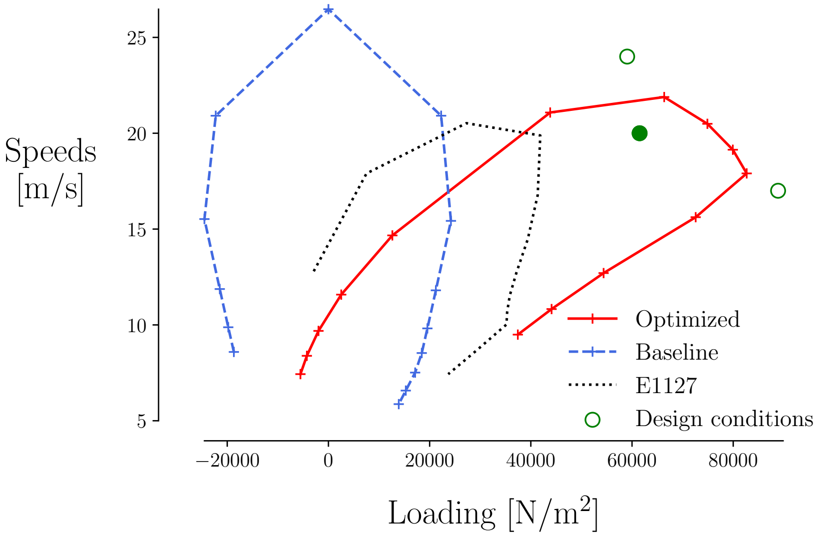

Figure 4.15: Loading-speed envelopes of the baseline, the optimized, and the E1127 hydrofoils. The optimized hydrofoil has the highest maximum loading. The nominal operating condition shown in the green-filled circle is inside the cavitation bucket of the optimized hydrofoil, while the two other operating conditions points shown in green open circles are outside of the bucket because of more relaxed cavitation constraint values.

ing. However, a design that can operate with high cavitation inception speeds around zero lift might be preferred at certain circumstances, such as for rudders and other control surfaces, whose sections and cavitation buckets are typically symmetrical. Eppler and Shen [71] also made a comment in 1979 that, it is difficult to find one hydrofoil section that can be applied in all applications. Since each section has its pros and cons, the choice should be made based on the actual operating conditions.

By comparing Figures 4.12a and 4.14, the cavitation bucket of the E1127 hydrofoil is narrower compared to the 2-D cavitation buckets due to the 3-D effects. This degradation is mainly caused by the tip vortex. Even though we did not explicitly consider the tip vortex C_p when constructing the cavitation buckets in Figure 4.14, the tip vortex will induce a low-pressure region on the foil surface near the tip due to the accelerated flow. This low-pressure region on the surface affects the surface $C_{p_{\min}}$ value, as shown in Figure 4.16. In our optimization, the susceptibility to tip vortex cavitation can be indirectly taken into account in the cavitation constraint through this low-pressure region on the foil surface induced by the tip vortex. In addition, the objective to minimize the drag should drive the solution to minimize the tip vortex strength, which will lower the susceptibility to tip vortex cavitation as a side effect. To show the influence of the tip vortex on the surface pressure, we present the C_p contours near the tip for the baseline, the optimized, and the E1127 hydrofoils in Figure 4.16 with $C_L = 0.6$ and $Re_{\text{rc}} = 6 \times 10^6$. The baseline case has $C_{p_{\min}} = -3.7$; the optimized case has $C_{p_{\min}} = -0.97$; the E1127 hydrofoil has $C_{p_{\min}} = -1.79$. For the baseline hydrofoil, $C_{p_{\min}}$ occurs at the leading edge. The optimized hydrofoil and the E1127 hydrofoil have concentrated low-pressure regions near the tip, and their $C_{p_{\min}}$ occurred on the suction surface near the tip. As a result, at $C_L = 0.6$, leading edge cavitation occurs first for the baseline hydrofoil while tip vortex cavitation occurs first for both the optimized hydrofoil and the E1127 hydrofoil.

To compare susceptibility to suction side cavitation and tip vortex cavitation, we show pressure iso-surfaces of the saturated vapor pressure (i.e., $P = P_{\text{vapor}}$) and the vorticity magnitude contours at selective streamwise positions at 35.2%, 64.8%, and 94.4% of the chord from the tip leading

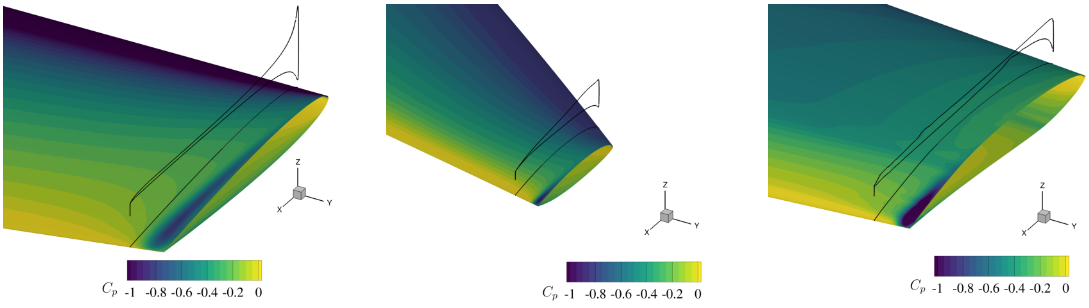

(a) Baseline (b) Optimized (c) E1127

Figure 4.16: C_p contour near the foil tip along with sectional C_p distribution at $y/b = 97.8\%$ for $C_L = 0.6$ and $Re_{\text{rc}} = 6 \times 10^6$. The baseline shows the lowest C_p at the foil leading edge (most susceptible to suction side cavitation), while the E1127 hydrofoil shows the lowest C_p near the tip (most susceptible to tip vortex cavitation).

edge in Figures 4.17 ($C_L = 0.3$) and 4.18 ($C_L = 0.6$). The actual cavity size is likely to be bigger because cavitation inception will modify the boundary layer, increasing the maximum cavity size. The actual cavity also tends to undergo periodic growth, collapse, and shedding cycles [134, 135].

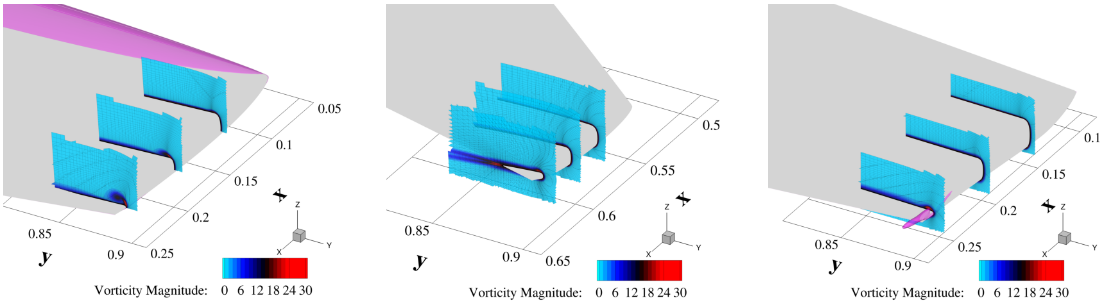

(a) Baseline (b) Optimized (c) E1127

Figure 4.17: Pressure iso-surfaces (pink) of the saturated vapor pressure (i.e., $P = P_{\text{vapor}}$) and the vorticity magnitude contours at the relative streamwise position at 35.2%, 64.8%, and 94.4% from the tip leading edge. Results are shown for $C_L = 0.3$ and $Re_{\text{rc}} = 7 \times 10^6$. The E1127 hydrofoil shows the strongest tip vortex. The optimized hydrofoil is cavitation-free while leading edge cavitation occurs for the baseline hydrofoil, and tip vortex cavitation occurs for the E1127 hydrofoil.

From the pressure iso-surfaces, we observe that the optimized hydrofoil is cavitation-free at $C_L = 0.3$ and $Re_{\text{rc}} = 7 \times 10^6$ while leading edge cavitation occurs for the baseline hydrofoil and

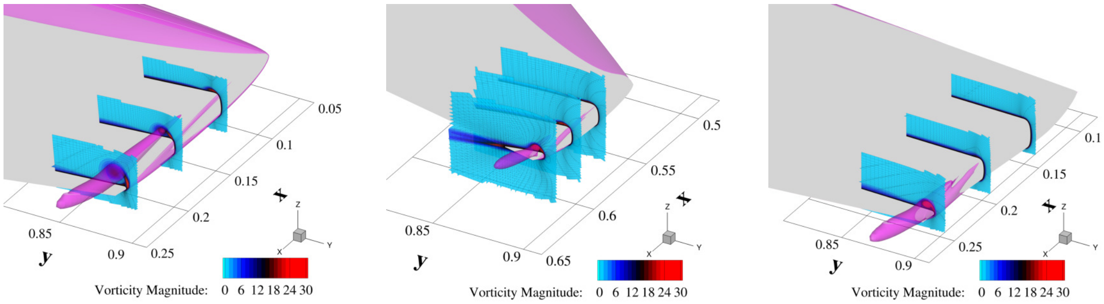

(a) Baseline (b) Optimized (c) E1127

Figure 4.18: Pressure iso-surfaces (pink) of the saturated vapor pressure (i.e., $P = P_{\text{vapor}}$) and the vorticity magnitude contours for relative streamwise positions at 35.2%, 64.8%, and 94.4% from the tip leading edge. Results are shown for $C_L = 0.6$ and $Re_{\text{rc}} = 6 \times 10^6$. All three hydrofoil are subjected to cavitation. The baseline experiences the most significant leading edge cavitation, while the E1127 experiences the largest tip vortex cavitation. Some leading edge cavitation is visible on the suction side for the optimized hydrofoil because of slightly more relaxed cavitation constraint at this operating condition.

tip vortex cavitation occurs for the E1127 hydrofoil. Figure 4.18 shows that, at $C_L = 0.6$ and $Re_{\text{rc}} = 6 \times 10^6$, all three hydrofoils are susceptible to both leading edge and tip vortex cavitation. As demonstrated by the leading edge cavity sizes in Figure 4.18a, the baseline experiences the most significant leading edge cavitation while the E1127 hydrofoil has the smallest leading edge cavity. As explained earlier, the optimized hydrofoil experiences leading edge cavitation because the $C_{p_{\text{min}}}$ was not strictly below $\sigma = 0.7$ near the leading edge, as shown in Figure 4.7, which might be caused by the cavitation constraint tolerance and scaling. Nevertheless, the highest suction peak was much greater for the baseline than the optimized hydrofoil, as shown in Figures 4.6 and 4.17, suggesting that the actual size of the leading edge cavity of the leading edge cavity will be much greater for the optimized hydrofoil. For the tip vortex cavitation, the baseline and the E1127 hydrofoils have larger tip vortex cavities than the optimized hydrofoil. At $C_L = 0.6$ and $Re_{\text{rc}} = 6 \times 10^6$, the E1127 hydrofoil experiences the most significant tip vortex cavitation because it has the lowest pressure at the tip vortex core ($P \approx -214.7$ kPa) compared to the baseline ($P \approx -75.4$ kPa) and the optimized ($P \approx -74.6$ kPa) hydrofoils. The reason for the greatest tip vortex cavitation of the E1127 hydrofoil could be the spanwise C_p variation, as shown in Figures 4.13 and 4.16c, and the tip geometry, where both are sub-optimal.

Even though the baseline hydrofoil has a larger tip vortex cavity than the optimized hydrofoil, Figure 4.16 shows that the surface C_p near the tip is lower for the baseline hydrofoil. To investigate this contrast, we compare the vorticity magnitude contours in Figure 4.18. As shown by the streamwise evolution of the vorticity magnitude contour, although the tip vortex of the baseline hydrofoil originates earlier (more upstream) than the optimized hydrofoil and the E1127 hydrofoil, it has a lower strength, which leads to a lower flow acceleration and thus less C_p reduction on the foil surface. This lower tip vortex strength can be caused by a smaller pressure difference between the upper and lower surface near the tip at the trailing edge. As shown by the C_p curve at the selected slice ($y/b = 97.8\%$) in Figure 4.16, downstream near the tip trailing edge, the baseline hydrofoil experiences a smaller pressure difference compared to the optimized hydrofoil and the E1127 hydrofoil. This smaller pressure difference provides less momentum for the tip vortex growth. Since the baseline hydrofoil has a greater pressure difference upstream (near the foil leading edge), the tip vortex of the baseline hydrofoil develops more upstream.

Another possible reason for the lower tip vortex strength for the baseline is a greater diffusion. This diffusion could be either physical or numerical. On the one hand, the boundary layer growth across the tip surface that causes the tip vortex roll-up occurs closer to the lower surface (pressure side) for the baseline hydrofoil than the optimized hydrofoil, which makes the tip vortex propagate further in the bending (z) direction and hence become more diffusive physically. On the other hand, larger cells can contribute to a higher numerical diffusion. The CFD cell size increases with the distance from the foil surface. As shown by the meshes on the selective streamwise slices in Figures 4.17 and 4.18, the region where the baseline tip vortex core is located has larger cells than the region where the optimized hydrofoil tip vortex core is located. These larger cells artificially weaken the tip vortex. The optimized hydrofoil has the highest vorticity magnitude (45 s^{-1}) in the core, which is slightly higher than the E1127 hydrofoil (41 s^{-1}). Again, this high vorticity magnitude could result from a smaller grid size due to the shortened tip chord length and that the tip vortex is closer to the foil surface.

Apart from the cavitation performance, we are also interested in the drag of the optimized and the E1127 hydrofoils. We plot C_D versus C_L in Figure 4.19 for the baseline, the optimized, and the E1127 hydrofoils. The optimized hydrofoil shows a lower drag than the baseline hydrofoil when $C_L > 0.25$, and shows a lower drag than the E1127 hydrofoil during $C_L \geq 0$.

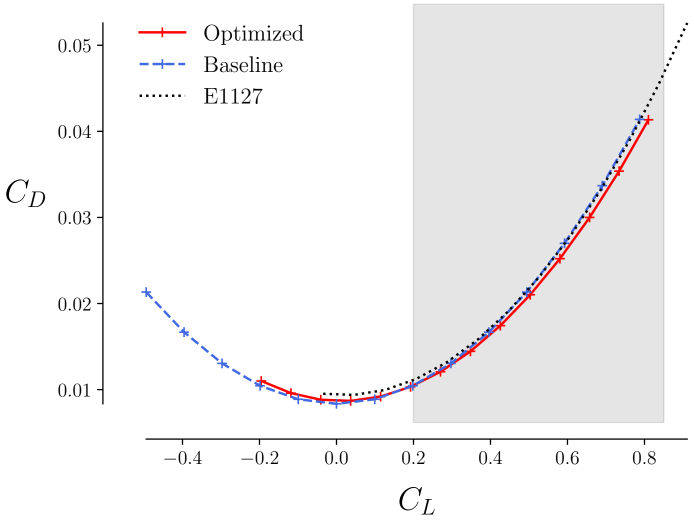

Figure 4.19: Lift-drag polars of the baseline, optimized and E1127 hydrofoils. The optimized hydrofoil outperforms (lower C_D) the E1127 hydrofoil. The design range is highlighted by gray colored region.

4.3.5 Structural performance of the optimized hydrofoil

Structural safety is as important as hydrodynamic performance. The design must be structurally safe. Figure 4.20 shows the failure indicator f contours and non-dimensional bending (z) displacement ω/b contours at the $C_L = 0.6$ condition for the baseline and optimized hydrofoils obtained using the L1 meshes. The optimization keeps the λ and θ_f values aligned, as shown by the convergence histories in Figure 4.5. In this way, more loading is taken along the fiber. Thus, the structure becomes less susceptible to material failure because the bending rigidity is increased, and the strength is much higher along the fiber direction. The optimized hydrofoil has a higher f_{max} value than the baseline mainly due to higher normal stresses in the x direction caused by the large sweep angle. Although the optimized hydrofoil exhibits a f_{max} value higher than one when evaluated with the fine L1 meshes, the violation is relatively minor. Given that we consider failure initiation criteria for all modes and a safety factor of three in the optimization, the failure indicator value is conservative. The simplified structural model and the local mesh quality also impact the stress concentration and the material failure evaluation.

For the bending displacement, the maximum bending displacement ω_{max} of the optimized is lower compared to the baseline. The ω_{max}/b of the optimized hydrofoil is slightly higher than the critical value of 0.05 because the induced power aggregation method tends to underestimate the maximum value. Hence, when the aggregated value ω_{DIP}/b satisfies the constraint, the local ω_{max}/b slightly exceeds the set tolerance. For a swept composite hydrofoil, the hydrofoil may have a large deformation without causing structural failure by optimizing the fiber orientation. Hence, the material constraint was not active in our optimization, and the final design has an adequate margin for material failure. Figure 4.8 includes the f_{max} and ω_{max} values at the two lower loading conditions. At these two conditions, the optimized hydrofoil also has lower f_{max} and lower ω_{max} compared to the baseline.

The increased rigidity can also be demonstrated by the increased natural in-vacuum frequencies shown in Figure 4.21. Besides, the optimized hydrofoil modes show a slightly stronger mixture of bending and twisting modes. This stronger mixed bend-twist coupling results from the modified geometry centroid, the backward sweep, and the CFRP material anisotropy.

4.3.6 The effect of sweep and chord variables in optimizations

Although we have discussed in detail how the optimization improved the design, it might not be straightforward to see the effect of each variable. It is not possible to accurately quantify the

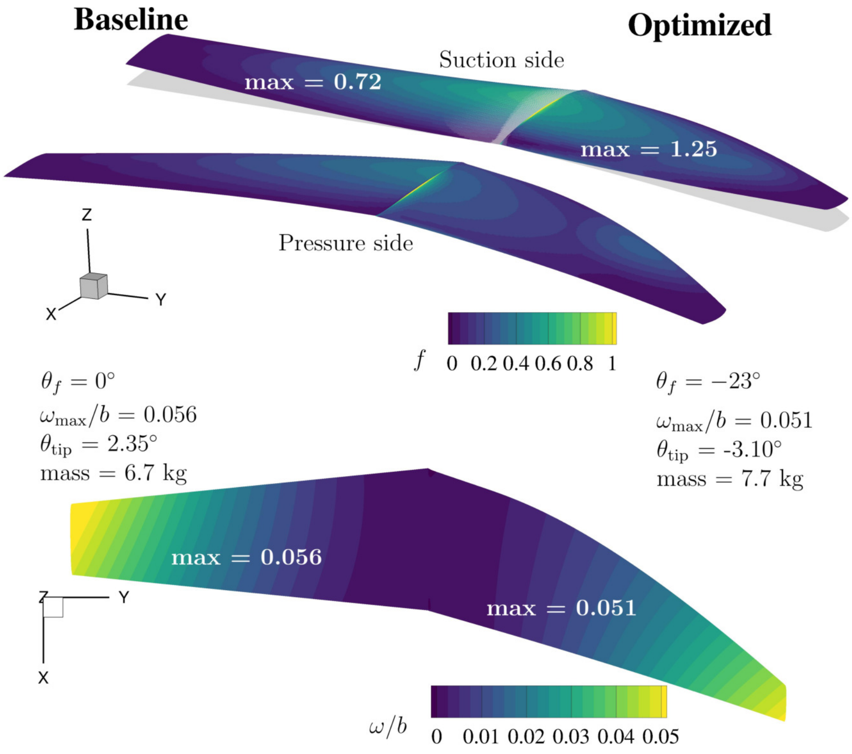

Figure 4.20: Failure indicator f and non-dimensional bending displacement ω/b contours at $C_L = 0.6$. The baseline is shown on the left and the optimized result is shown on the right. The results shown here are obtained using L1 meshes.

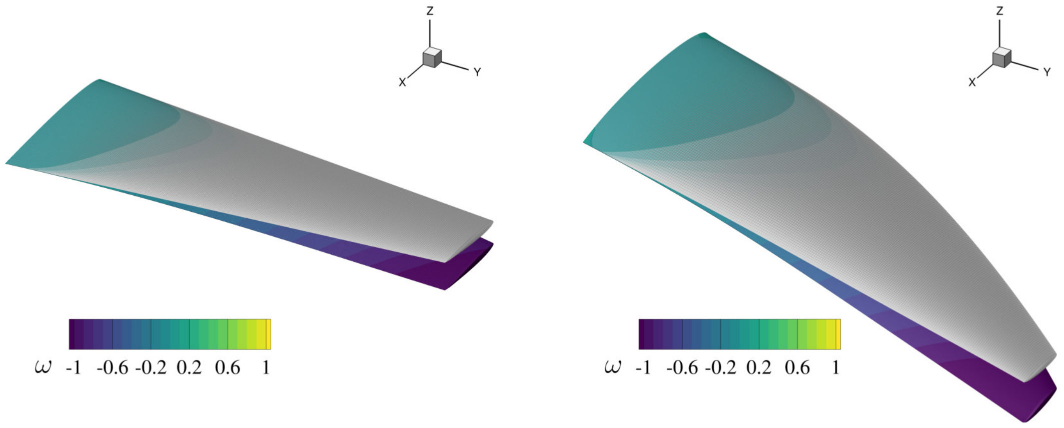

(a) Baseline mode 1: 59 Hz

(b) Optimized mode 1: 66 Hz

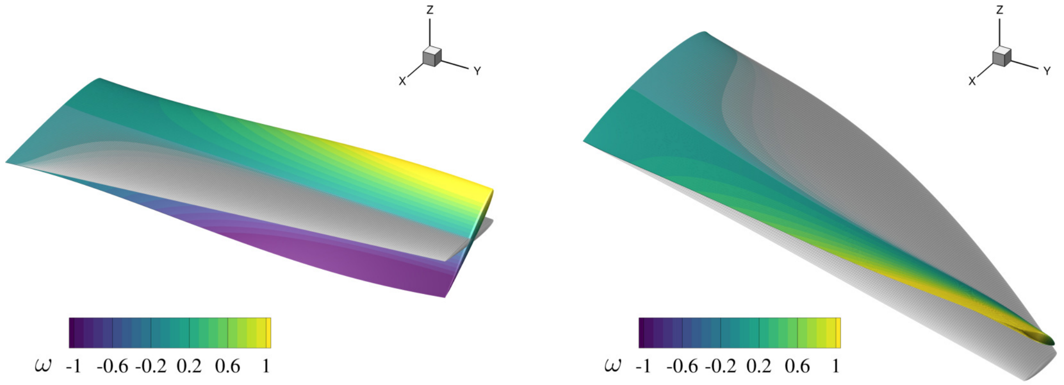

(c) Baseline mode 2: 156 Hz

(d) Optimized mode 2: 176 Hz

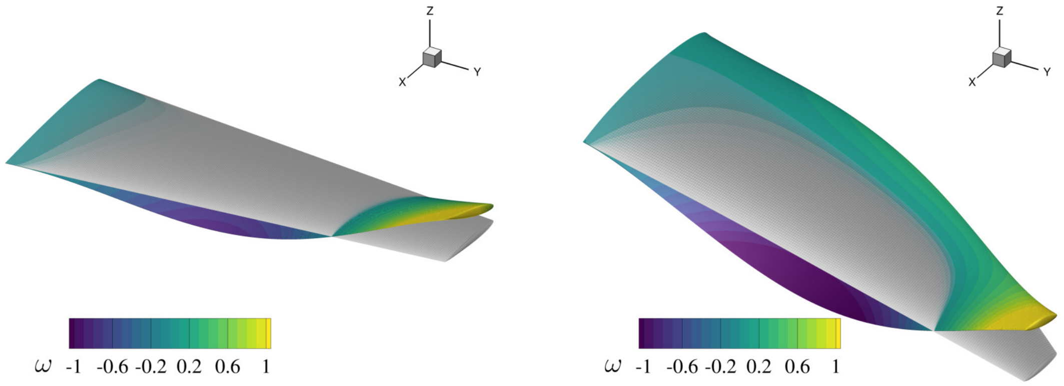

(e) Baseline mode 3: 236 Hz

(f) Optimized mode 3: 253 Hz

Figure 4.21: First three modes of the baseline and optimized hydrofoils in vacuum. The gray shape represents the undeformed shape. The contours show the bending (z direction) component of the eigenvectors. The baseline θ_f is $0°$ and the optimized θ_f is $-23°$. Results are obtained using L1 meshes.

contribution of each variable without considering the interaction. The optimizer automatically explores and finds the optimal design. Nevertheless, we can still investigate a qualitative trend and the first-order effect.

In this section, we study the effect of planform variables, especially sweep and chord, because they have not been thoroughly explored in previous work, and they impact the hydroelastic response significantly. In addition, the effect of planform variables is relatively straightforward to discuss. To assess the effect of planform variables, we performed an additional optimization with the same problem formulation except that no sweep and chord variables are considered. The result shown in this section is different from the journal version, where the comparison is made with an analysis result.

The comparison of the functions of interest is shown in Figure 4.8. This summary shows that the drag slightly increases at all design conditions compared to the optimized result, resulting in a 3% increase in the total weighted drag due to less optimal lift distributions caused by the sub-optimal planform. As shown in Figure 4.22, the optimized result has normalized lift distributions closer to the elliptical at all conditions. The sweep and chord variables contribute to the spanwise lift distribution. These variables are coupled with the other variables to find a balance between different design conditions and to achieve better overall performance.

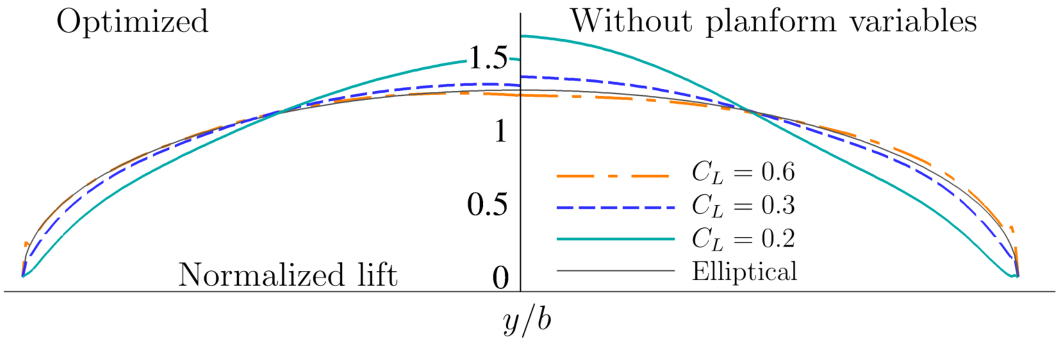

Figure 4.22: Normalized spanwise distributions of the optimized hydrofoils with and without chord and sweep variables. Without chord and sweep variables, the lift distributions deviate from the elliptical distribution compared to the optimized result.

For the optimization result without chord and sweep variables, the cavitation inception speeds are approximately the same as the optimized result with planform variables. From Figure 4.23a, the optimization without chord and sweep variables create thicker sections at outboard of the hydrofoil. This increased thickness is mainly a result of delaying cavitation when sweep and chord variables are not considered. We have discussed in previous sections that two important effects of sweep are the bend-twist coupling effect and the downwash effect. Both of these effects have influences on the local angle of attacks at different spanwise positions. Through proper design and tailoring, the optimal sweep angle provides the optimal effective angle of attack for local sections, together with the spanwise twist distribution. While the spanwise twist distribution can also contribute to creating the optimal effective angle of attack, this contribution is the same across all design conditions because spanwise twist distribution does not change from condition to condition unless active morphing is considered. On the contrary, the sweep effects on the local effective angle of attack are load-dependent, or condition-dependent. This load-dependency allows the optimizer to leverage the variation in effective angle of attack to delay cavitation at higher loading conditions or higher speeds. Hence, sweep is beneficial when considering multipoint conditions during designs. Without this load-dependent adjustment of the effective angle of attack, the optimization with no sweep and chord variable creates a rounder leading edge and a thicker section to ensure that the cross-section does not lead to excessively low local pressure across the design conditions. We observed from the optimization history that during late stage of the optimization, introducing backward sweep leads to slight drag reduction. This slight drag reduction is achieved by tailoring the combined load-dependant effects of sweep and other variables so that the thickness can be reduced while still maintaining the cavitation performance. Previous optimization done by Garg et al. [65] did not consider sweep and chord variables, and their optimized hydrofoil showed increased thickness compared to the baseline. The relationship between sweep and multipoint designs can also be indicated from the study by Volpi et al. [66]. Since they conducted only single-point optimizations, negligible sweep angle was observed. In addition to the rounder leading edge and thicker sections, comparing the undeformed shapes between these two optimizations, the one without sweep and chord variables has a more obvious pre-twist distribution than the other case as an effort to provide optimal local effective angle of attack. Despite the benefits of sweep that we demonstrated here using numerical simulations, it might be challenging to achieve the exact same performance in reality. The reason is that this realization requires the correct effective angle of attack to be achieved by the pre-twist, the structural deformation, and the 3-D hydrodynamic effects, which is challenging considering uncertainties in simulations and current manufacturing techniques. Uncertainty quantification can help evaluate the design practicality. The chord variables mainly contribute to drag reduction and improve structural integrity by achieving optimal lift distribution and bending moments.

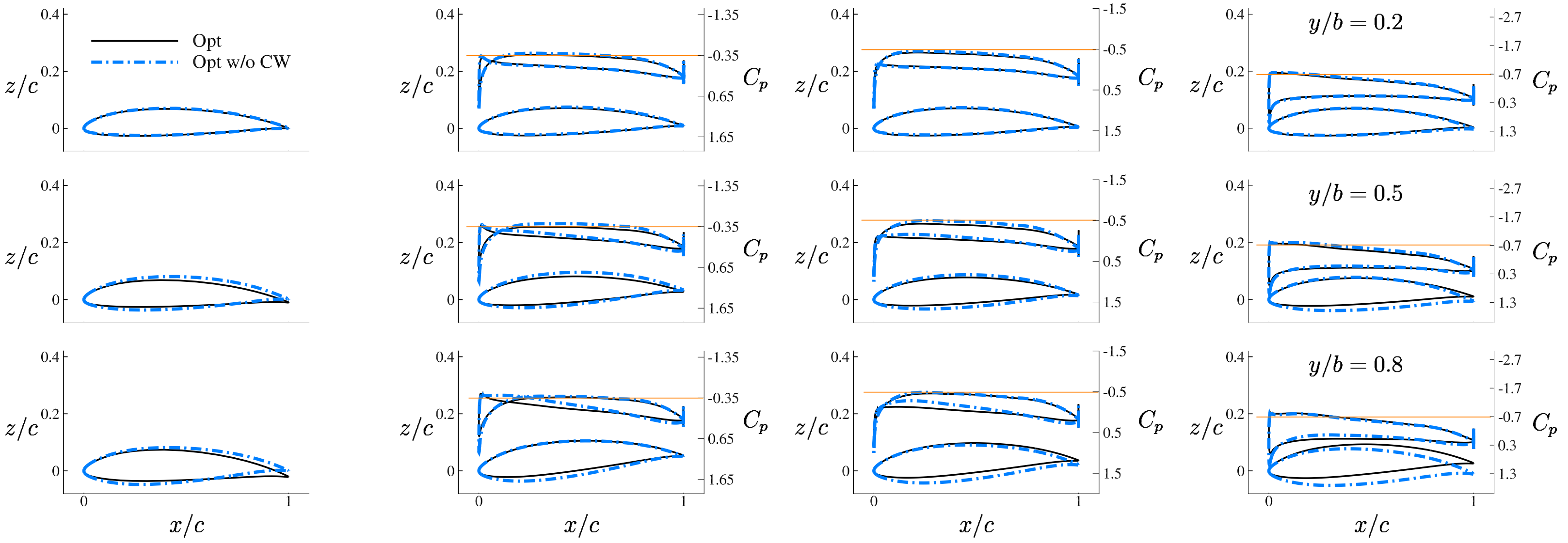

(a) Undeformed shapes (b) $C_L = 0.2$ (c) $C_L = 0.3$ (d) $C_L = 0.6$

Figure 4.23: Sectional deformed shapes and C_p profiles comparison between the optimized (black solid lines) hydrofoil and the optimization without chord and sweep variables (blue dashed-dotted lines) using L1 meshes. Sweep can change the loading distribution and improve cavitation performance through bend-twist coupling and upwash or downwash effects.

For the structural performance, without chord and sweep, the optimized hydrofoil undergoes lower bending deformation because of its higher thickness. It is less susceptible to structural failure than the optimized result, which again illustrates the effect of sweep on the structural response.

This comparison demonstrates the potential benefits of including chord and sweep variables in the optimization to delay cavitation and reduce drag. It also highlights the need to consider coupled hydrostructural response to evaluate the performance more accurately and ensure structural safety.

4.4 Conclusions

In this chapter, we conducted multipoint high-fidelity hydrostructural optimizations to design a full-scale cavitation-free composite hydrofoils with improved efficiency while ensuring structural integrity. We first discussed a case with a full set of design variables, and compared this first case with an optimization without sweep and chord variables.

We used the coarsest fluid and structural meshes in the optimization for efficiency and verified the performance improvement by evaluating the optimized design with the finest fluid and structural meshes. The optimization introduced camber, modified the thickness distribution, and added backward sweep and nonlinear tapered planform. The optimized result showed a 1.2% decrease in the weighted drag compared to the baseline when evaluated over C_L between 0.2 and 0.6 with the finest mesh for both foils. The optimized hydrofoil showed a nose-down tip twist, whereas the baseline underwent a nose-up tip twist. The optimized hydrofoil has a nonlinear variation in chord length from the root to the tip. The tip chord of the optimized foil was shortened to the lowest limit to reduce the tip loading. The reduced tip loading resulted in load alleviation at the highest loading condition and normalized lift distributions closer to the elliptical, which reduced the lift-induced drag and lowered the susceptibility to tip vortex cavitation. We discussed the tradeoffs between achieving a lower C_D at each condition and improving the overall efficiency. Multipoint optimization is necessary to balance the tradeoffs between the performance at different conditions and achieving different objectives.

The cavitation inception speed increased by 82% at the nominal operating condition of $C_L = 0.3$ compared to the baseline. 3-D effects, such as downwash and tip vortex, significantly altered the cavitation performance. The 3-D E1127 hydrofoil (with the same planform and zero-twist as the baseline) that we investigated suffered from tip vortex cavitation at $C_L = 0.3$. This is possibly due to the spanwise pressure variation caused by the combination of the cross-section and suboptimal planform, as well as the tip geometry. The 2-D cavitation performance of the optimized hydrofoil sections and the E1127 section was comparable, while the 3-D cavitation performance of the E1127 hydrofoil was significantly degraded due to tip vortex cavitation.

On the structural side, the optimized hydrofoil was stiffer than the baseline. The nose-down twist deformation and shorter tip chord length of the optimized hydrofoil reduced bending moments, deformations, and stress concentrations, ensuring structural integrity. The optimization kept the fiber orientation and sweep aligned to distribute more loading along the fiber to avoid material failure and maximize bending stiffness. The results also suggest that with optimal fiber orientation, a geometrically swept hydrofoil can undergo large deformations without causing structural failure. This large deformation can however lead to severe vibrations, noise, and accelerated fatigue issues. Since vibration analyses were not considered in the optimization and these analyses are costly, we used a displacement constraint to limit the maximum deformation as a surrogate for such dynamic analyses.

The comparison between optimization studies with and without chord and sweep variables shows that sweep benefits delaying cavitation across a range of operating conditions by adjusting the local effective angle of attack to be optimal. The chord distribution mainly contributes to the loading distribution to reduce drag and to adjust bending moments.

CHAPTER 5

High-fidelity hydrostructural optimization of hydrofoils with different material configurations

In the previous chapter, we used a high-fidelity hydrostructural optimization tool to design cavitation-free lifting surfaces with an equivalent single-layer unidirectional CFRP. We discussed how sectional geometry and 3-D effects impact designs, and what the influences of sweep and chord variables are. Another research question of interest is how different material properties affect optimization, especially quantifying how much benefit using composite materials provides relative to metallic materials for cavitation-free hydrodynamic lifting surface designs. To further assess the benefits of using composites and understand how the use of composite affects the performance, we conduct two additional hydrostructural optimizations in this chapter. The first optimization is an aluminum case. The second optimization is a multidirectional CFRP hydrofoil with two fiber orientations. In reality, composite laminates are often manufactured with multidirectional plies to sustain loading in different directions and to deter crack propagation. We will call the second case the multi-layer CFRP later in this section. The motivation of the second case is to investigate if varying the fiber orientation along the thickness provides more benefits.

5.1 Introduction

This chapter is organized as follows. We first introduce the material properties used for the aluminum case and how we model the multi-layer CFRP hydrofoil in Section 5.2.1.

In the result section 5.3, we first compare the hydrodynamic performance of the optimized hydrofoils, including the pressure coefficient C_p contours, streamlines, the cross-sectional shapes, sectional C_p curves, and the spanwise lift distributions. The hydrodynamic performance comparison is then followed by the structural performance comparison. We make the comparison on the coarsest mesh L3 because we focus on the relative performance between these optimization cases.

5.2 Optimization problem setup

Two additional optimization cases are shown in this chapter, one aluminum case and one multi-layer CFRP case. We will compare these two cases with the single-layer CFRP hydrofoil from the previous chapter. The optimization problem is the same as the problem shown by Table 4.4 in Chapter 4.

5.2.1 Model

5.2.1.1 Aluminum hydrofoil

For the aluminum case, we use the same geometry and L3 meshes as shown in Figures 4.1a and 4.1b in Chapter 4. The material properties used for the aluminum case is aluminum 6061, as shown in Table 5.1. Metallic materials do not exhibit failure modes as complex as composite materials. Instead of the mixed failure criteria used for composite structures that were described in the previous chapter, we use von Mises stress normalized by the yield strength as the failure indicator.

$$f = \frac{\sigma_v}{\sigma_{\text{yield}}} \tag{5.1}$$

Same as the composite case, we use the KS function to aggregate the failure indicator values over the constraint domain and a safety factor of three is used. Therefore, the f values shown later in this chapter all consider this safety factor. We use the yield strength here to make a fair comparison with the CFRP cases because ultimate strengths are used for CFRP optimizations. However, since failure initiation criteria are used for composites and a safety factor of three is considered, the material failure prediction is still conservative. We consider the CFRP to be brittle so there is no yield point. One setup in the aluminum case that differs from other optimizations is that the aluminum hydrofoil optimization considers the entire domain for material failure constraint, instead of being limited to the region between the root and $y/b = 0.09$, where stress concentration typically occurs, as explained in Chapter 4 Section 4.2.4. This is because we observe that the material failure can occur beyond $y/b = 0.09$ for the aluminum hydrofoil due to the change in chord and sweep distribution. Figure 5.1 shows an aluminum hydrofoil optimization result with the material failure constraint imposed only from the root to $y/b = 0.09$. As shown in Figure 5.1, the material failure occurs around $y/b = 0.3$. This material failure is dominated by the normal stress in y direction and the shear stress in the xy plane, as shown by the stress distributions in Figure A.1.

Table 5.1: Aluminum 6061 material properties

Symbol	Description	Value	Units
ρ_{al}	Solid density	2700	kg/m^3
E	Young's modulus	69	GPa
ν	Poisson's ratio	0.33	–
σ_{yield}	Yield strength	276	MPa

5.2.1.2 Multi-layer CFRP hydrofoil

For the multi-layer CFRP case, we create a new structural mesh with separate components so that we can specify different design variables to different components. The mesh is shown in Figure 5.2. The final mesh has 21,120 linear eight-node brick elements (CHEXA8). There are

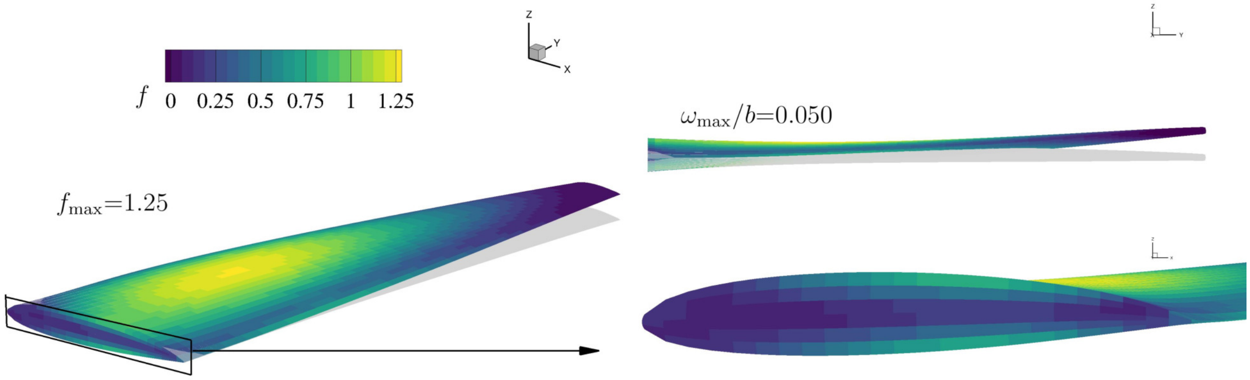

Figure 5.1: Without enforcing the material failure constraint over the whole structural domain, the optimized aluminum hydrofoil experiences material failure. The material failure onset occurs around $y/b = 0.3$.

eight elements along the thickness direction. We evenly split the elements along the thickness direction into four parts, with each part having two elements in the thickness direction. Since composite plate structures typically have symmetric layups in reality, we combine the top and bottom layers into one group and combine the inner two layers into another group. Each layer has the same material properties as the single-layer CFRP optimization described in the previous chapter. We assign one design variable (fiber orientation θ_f) to one group, so we have a total of two fiber orientations as structural design variables for the multi-layer CFRP case, as shown in Figure 5.2. The fiber orientation follows the same definition in Chapter 4. This multi-layer case uses the MHY criteria described in Chapter 4.

5.3 Results

In this section, we first compare the modes of the optimized hydrofoil to assess the differences in structural characteristics. Next, we compare the hydrodynamic performance of the optimization cases. This will be followed by the comparison of material failure. As shown in Figure 5.4, all three optimization cases feature a backward sweep, and the tip chord variables reduce to the lower limit. It is evident that the aluminum case has a smaller sweep angle ($\lambda = 11°$) than the other

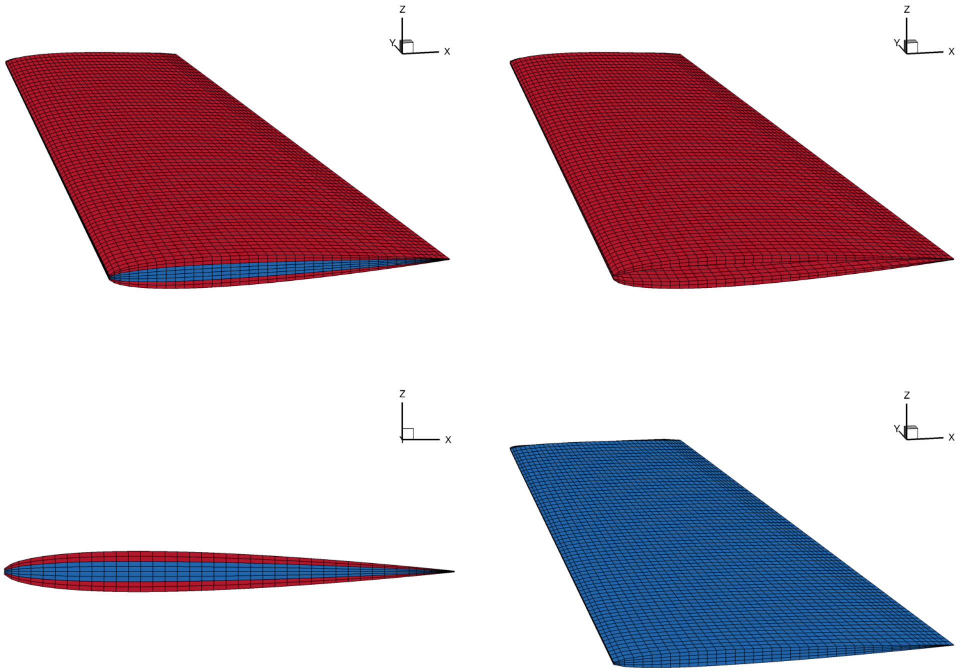

Figure 5.2: Structural model for the Multi-layer CFRP case. The outer layers are combined into one group (red). The inner layers are combined into one group (blue). Each group has an individual fiber orientation as a design variable.

two CFRP cases ($22°$ for the single-layer CFRP and $18°$ for the multi-layer CFRP). The difference in sweep angles might be a result of the cavitation, displacement, and material failure constraints. We will explain how these requirements influence the sweep angle in detail in Section 5.3.2. For the single-layer CFRP case, the fibers are placed with an $\theta_f = -23°$; for the multi-layer CFRP case, the fibers in the outer layers (top and bottom) are placed at $\theta_f = -23°$ while those in the inner layers are oriented forward with $\theta_f = 18°$ ($\theta_f = [-23°/18°]_s$). Table 5.2 summarizes the total weighted C_D, non-dimensional tip bending deflection δ_{tip}/b at $C_L = 0.6$ condition, maximum material failure indicator f_{max} at $C_L = 0.6$ condition, and active constraints for each case.

Table 5.2: Optimization results summary

Case	Weighted C_D	δ_{tip}/b at $C_L = 0.6$	KS_f at $C_L = 0.6$	Active constraints
Aluminum	0.0165	0.0362	1.0	Cavitation constraints ($C_L = 0.2$ and $C_L = 0.6$) Material failure constraint
Single-layer CFRP	0.0162	0.0486	0.86	Cavitation constraints ($C_L = 0.2$ and $C_L = 0.6$) Bending displacement constraint
Multi-layer CFRP	0.0161	0.0493	1.0	Cavitation constraints ($C_L = 0.2$ and $C_L = 0.6$) Material failure constraint Bending displacement constraint

5.3.1 Modal analysis comparison

We first examine the modes of the optimized hydrofoils to see how the structural characteristics differ between these optimized hydrofoils. Figure 5.3 compares the first three in-air modes between the three optimized hydrofoils. The first modes of the optimized hydrofoils are all bending-dominated. The second and third modes of the aluminum case significantly differ from the other two CFRP cases. While the second mode of the aluminum case is bending-dominated, the other two CFRP cases are twisting-dominated because the material anisotropy results in lower stiffness in the direction transverse to fibers. For the third mode, the dominant component of the aluminum case is twisting while those of the two CFRP cases are bending.

The in-air modes between the two CFRP cases are similar, in terms of both natural frequencies and mode shapes. Compared to the single-layer CFRP hydrofoil, the outer layer of the multi-layer

CFRP case has the fibers oriented further backward than the sweep angle, balancing the swept forward fibers in the inner layer. Although the forward angle of the fibers in the inner layer is significant (41° difference relative to those of the outer layer), the fibers in the outer layer play a more important in structural stiffness than the inner layer, especially for bending because of greater distance from the neutral axis. As a result, the first natural frequencies of these two CFRP cases are almost identical, and hence they have similar tip bending deflections, as shown in Table 5.2. The slightly higher tip bending deflection of the multi-layer CFRP indicates that the single-layer CFRP case has a slightly higher bending rigidity because all fibers are almost aligned with the sweep. On the other hand, there is a major difference in the natural frequencies of the second mode between these two CFRP hydrofoils. Rotating the fibers in the inner layer forward with an angle of 41° relative to the outer layers increases the twisting rigidity for the multi-layer CFRP hydrofoil. As a result of this higher twisting rigidity, the multi-layer CFRP hydrofoil has a higher second natural frequency than the single-layer CFRP hydrofoil. This difference in twisting rigidity leads to different tip twists, which will be discussed later.

5.3.2 Hydrodynamic performance comparison

To investigate the hydrodynamic performance, Figure 5.4 compares the C_p contours and streamlines on the suction of the optimized hydrofoils. Although the aluminum case has the highest drag at all three design conditions, the difference between the three optimization results is minor, with the largest difference of 2.6% between the aluminum case and the multi-layer CFRP cases at $C_L = 0.2$ condition. The maximum difference in the total weighted C_D is only 0.0003, as shown in Table 5.2. These optimized hydrofoils have similar C_p distributions on the suction side. The two CFRP cases are visually identical in terms of the C_p contours. The non-dimensional deformed sectional shapes (normalized by the local chord length) and C_p curves in Figure 5.5 provide a more direct comparison in terms of deformed cross-sectional shapes and the cavitation performance. The deformed optimized geometry (except for sweep) and performance of all three hydrofoils are

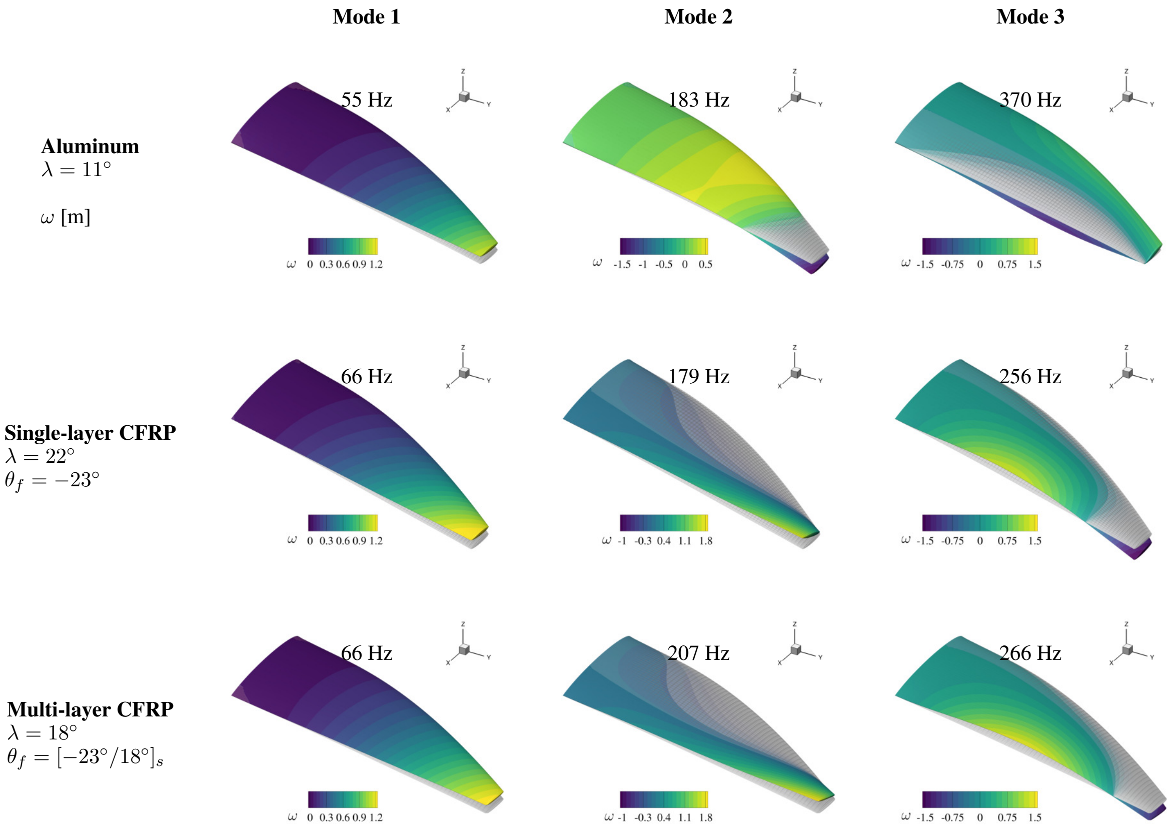

Figure 5.3: Comparison of mode shapes between different multipoint optimized hydrofoils. The multi-layer CFRP hydrofoil has a higher second mode natural frequency than the single-layer CFRP case because of the forward-oriented fibers in the inner layer.

similar, particularly at the highest loading condition. Although the sectional shapes at $y/b = 0.9$ are visually thicker than the inboard sections, they are actually thinner because of shorter chord lengths at the tip. In addition, this deformed sectional shapes in Figure 5.5a consider both the undeformed pre-twist and twist deformation, so there may be discrepancy between the θ_{tip} values listed in Figure 5.4 and the visualization in Figure 5.5a.

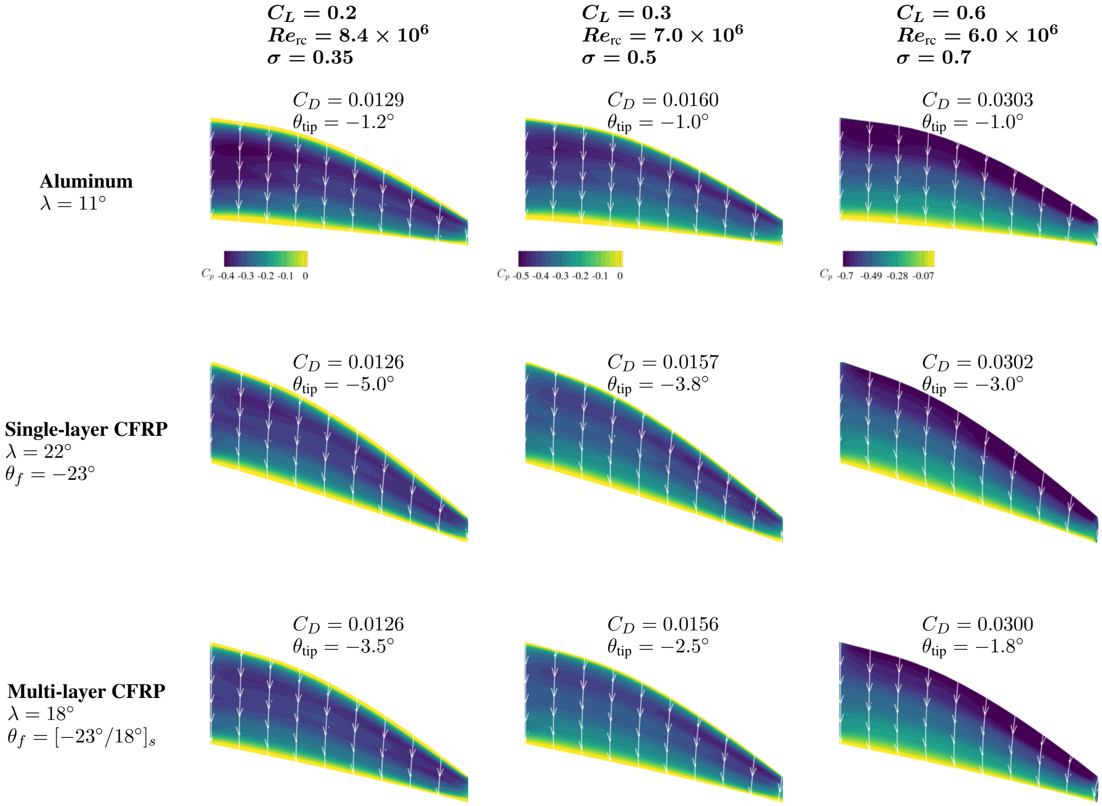

Figure 5.4: Comparison of surface pressure coefficient contours on the suction side and streamlines between different multipoint optimized hydrofoils. All optimization results have similar planform shapes and C_p contours. The aluminum case has the least sweep angle because of the higher stress induced by the sweep.

As shown by the listed θ_{tip} values in Figure 5.4 and the deformed sectional shapes in Figure 5.5a, the CFRP cases have higher tip twist deformation θ_{tip} than the aluminum hydrofoil at all three conditions due to a lower twisting rigidity, which is demonstrated earlier from the mode comparison.

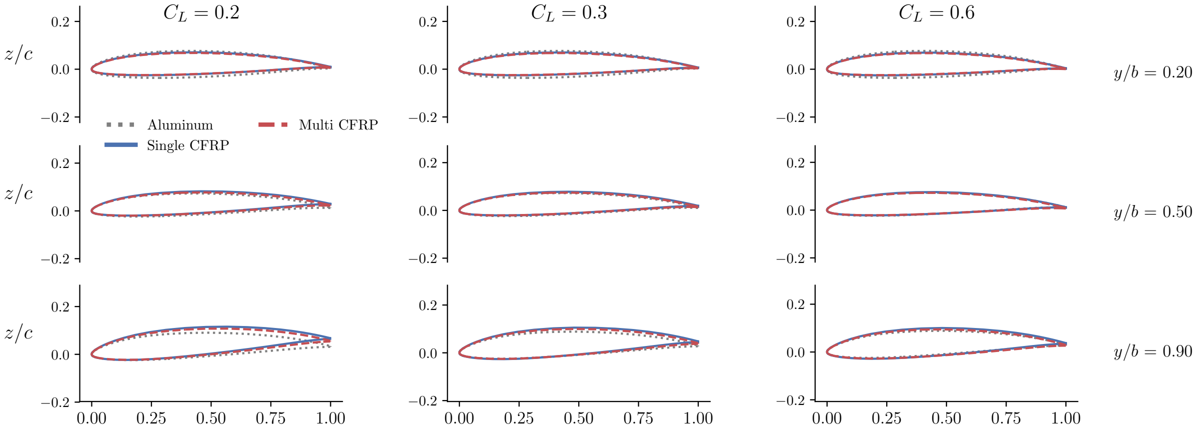

(a) Cross sectional shapes

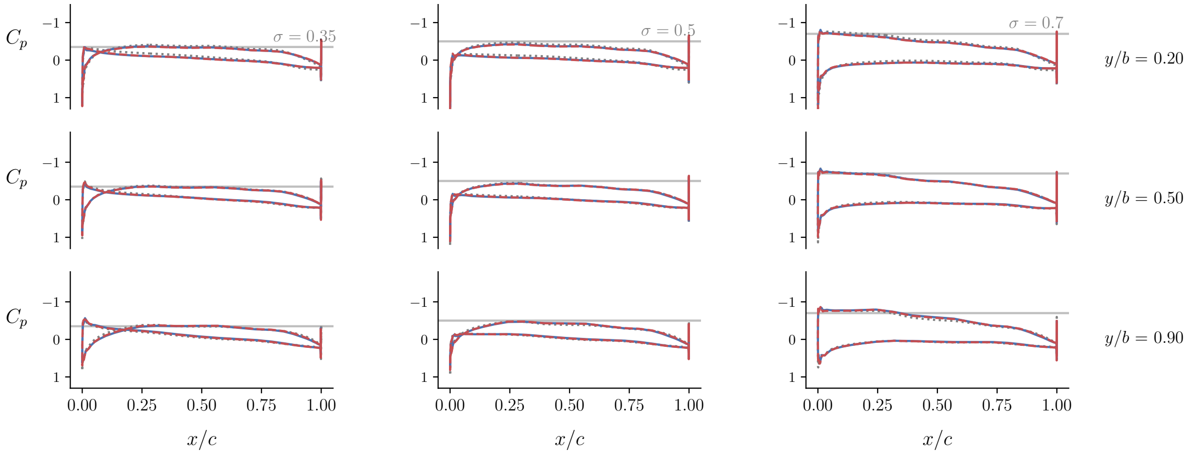

(b) Sectional C_p curves

Figure 5.5: Comparison of non-dimensional cross-sectional deformed shapes between different optimized hydrofoils. The deformed shapes and sectional C_p are similar between optimization results.

For all three optimized hydrofoils, the magnitude of the nose-down tip twist $|\theta_{\text{tip}}|$ decreases with higher C_L as the center of lift shifts towards the leading edge when C_L increases, as shown by the sectional C_p in Figure 5.5b. This behavior is also explained in Section 4.3.1. This effect is more prominent for CFRP cases because of their lower twisting rigidity.

In addition to the tip twist deformation, another difference in the cross-sectional shapes is the thickness near the root, as shown in Figure 5.5a. The aluminum case has slightly thicker cross-sections than the other two CFRP cases near the root because the aluminum case requires higher thickness to avoid material failure. On the other hand, the multi-layer CFRP case has the thinnest root. The difference in the root thickness between the two CFRP cases is caused by the bending displacement constraint. The maximum bending displacement ω_{max} can be reduced by decreasing the tip bending deflection δ_{tip} or the tip twist θ_{tip}, or both. Allowing the fiber orientation of the inner layer to vary from the outer layer enables optimization of the stiffness and strengths in different directions for a composite hydrofoil. Since the multi-layer CFRP case has a higher twisting rigidity, it has a smaller tip twist deformation than the single-layer CFRP case, enabling it to satisfy the bending displacement constraint even with a higher δ_{tip}. Adjusting twisting rigidity to satisfy the displacement constraint results in a less stringent requirement on the bending rigidity for the multi-layer CFRP hydrofoil compared to the single-layer CFRP. Contrarily, the single-layer has a higher tip twist deformation and thus requires a higher bending rigidity, resulting in a higher root thickness than the multi-layer CFRP case. These thickness differences can affect the hydrodynamic performance, especially drag distributions and the material failure initiation indicator.

Similarly, using multidirectional layup composites allows better tuning of the bending and twisting rigidity to delay cavitation. As discussed in Section 4, the sweep variable contributes to delaying cavitation by placing local sections at optimal effective angles of attack with both the geometric bend-twist coupling and the vorticity-induced downwash effects. However, the geometric bend-twist coupling and location of the center of pressure can counteract the vorticity effects.

For example, the nose-down geometric bend-twist coupling of a backward sweep angle can decrease the upwash effects at the outboard. Due to the isotropic properties and the higher twisting rigidity, the effects of the nose-down geometric bend-twist coupling and the nose-down pitching moment caused by the center of pressure are reduced for the aluminum hydrofoil compared to the other two CFRP cases. As a result of this reduced nose-down twist, the aluminum hydrofoil requires a smaller sweep angle to achieve the optimal local optimal effective angles of attack. On the other hand, since the single-layer CFRP has the lowest twisting rigidity, the geometric bend-twist coupling and the hydrodynamic pitching moment exhibit the most significant effects, leading to the largest nose-down twist deformation. This large nose-down twist counteracts more vorticity-induced downwash effects, and hence, the single-layer CFRP requires the largest sweep angle to achieve enough sweep-induced load-dependence. Although it is possible to tune the fiber orientation of the single-layer CFRP hydrofoil to reduce the nose-down twist, the bending displacement constraint limits the fiber orientation change. For the multi-layer CFRP hydrofoil, allowing two fiber orientation variables enables more fine tailoring the structural stiffness in different directions, achieving a twisting rigidity between the aluminum and the single-layer CFRP cases. Accordingly, the nose-down tip twist values of the multi-layer CFRP hydrofoil are between those of the aluminum and the single-layer CFRP cases. Hence, it can utilize a smaller sweep angle compared to the single-layer CFRP hydrofoil to achieve an optimal effective angle of attack distribution while being able to satisfy the bending displacement constraint. This combined effect of twist deformation and the vorticity-induced downwash can also be demonstrated by Figure 5.6.

Figure 5.6 compares the spanwise normalized lift, sectional drag coefficient C_d, sectional friction drag coefficient C_{dv}, and twist distributions of the optimized hydrofoils. From the spanwise normalized lift, all three optimization results have similar lift distribution except for the $C_L = 0.2$ condition. Although the aluminum case has a lift distribution closest to the elliptical at the $C_L = 0.2$ condition, it has the highest drag due to thicker sections at the inboard. This thicker section leads to higher friction drag and form drag. As shown by C_{dv} distributions at all design conditions, the aluminum case has higher C_{dv} near the root. Figure 5.6 also compares the spanwise twist distribution. Note that this twist distribution considers both the undeformed pre-twist and the twist deformation. At $C_L = 0.3$ condition, despite the difference in the twist distribution, the normalized lift distributions of the optimized results overlap. The discrepancy resulting from the twist distribution is compensated by the sweep. A higher backward sweep induces more upwash effects towards the tip, so even with higher nose-down tip twists, the CFRP cases have similar spanwise lifting distribution to the aluminum case. The observation, again, supports that the final sweep angle is determined based on the combined effects of the twist deformation and the vorticity-induced downwash.

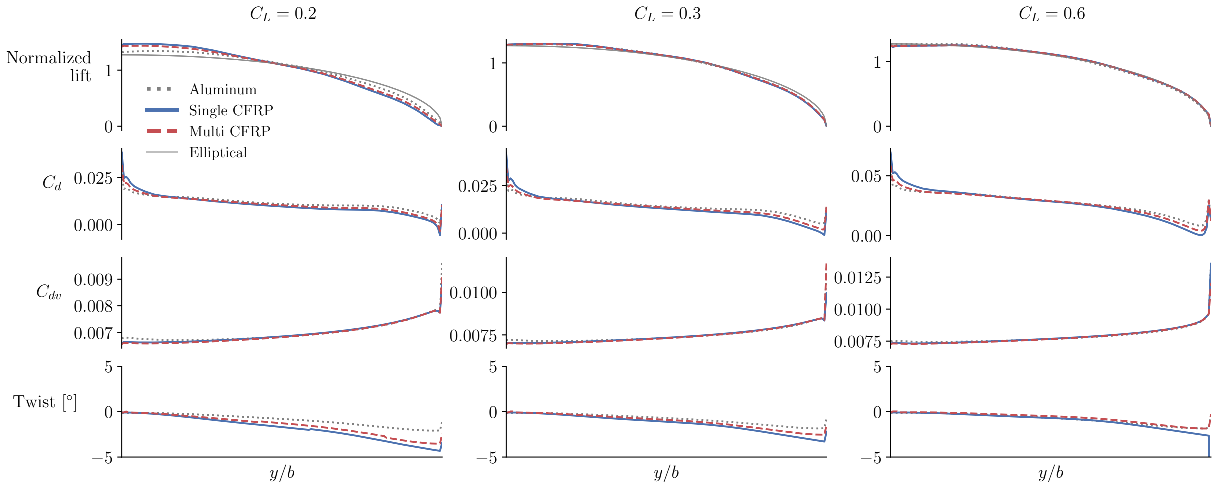

Figure 5.6: Comparison of spanwise normalized lift distribution, sectional drag coefficient C_d, sectional friction drag coefficient C_{dv}, and twist distributions between the optimized hydrofoils. The aluminum case has a higher friction drag near the root because of a thicker root. Three optimization results have similar normalized lift distributions at $C_L = 0.3$ and $C_L = 0.6$ conditions. The sweep-induced hydrodynamic effect counteract the difference in twist distributions, leading to similar normalized lift distributions for all three optimizations at $C_L = 0.3$ and $C_L = 0.6$.

5.3.3 Structural performance comparison

We have discussed the hydrodynamic performance of the optimized results in terms of drag and cavitation performance. Although all optimized hydrofoils are able to achieve similar hydrodynamic performance, they are different in terms of structural performance. First, they vary in terms of susceptibility to material failure. Table 5.2 summarizes the active constraints for each case. From the structural integrity perspective, the aluminum case is governed by material failure constraint, while the single-layer CFRP is governed by the bending displacement constraint. For the multi-layer CFRP case, both material failure constraint and bending displacement constraint are active. Note that we impose the material failure constraint over the entire structural domain instead of just the root part for the aluminum case. As shown in Figure 5.1, when the material failure constraint is only enforced at the root part, the optimized aluminum hydrofoil experiences material failure, and the failure onset occurs at around $y/b = 0.3$ spanwise position. Although material failure is avoided when we impose the material failure over the whole domain, the f_{max} still occurs slightly away from the root at around $y/b = 0.2$ position. Similarly, this is mainly attributed to the normal stress in the y direction and the shear stress in the xy plane, as shown by the stress contours shown in Figure A.2 in Appendix A. These observations from the aluminum case suggest that it is possible that the material failure onset does not occur at the root for cantilevered structures given chord and sweep distributions. In addition, the material failure constraint could pose a more demanding requirement than the bending displacement constraint for a metallic hydrofoil, which strengthens our previous conclusion that using composite allows the hydrofoil to have a large sweep angle and a large bending deflection without material failure.

On the other hand, the single-layer CFRP case is the least susceptible to material failure because it has CFRP mostly aligned with the bending axis and increases the root thickness to avoid violating the bending displacement constraint. This fiber alignment provides high enough strength to keep the hydrofoil away from the material failure margin. As a result, the material failure constraint was not active for the single-layer CFRP case.

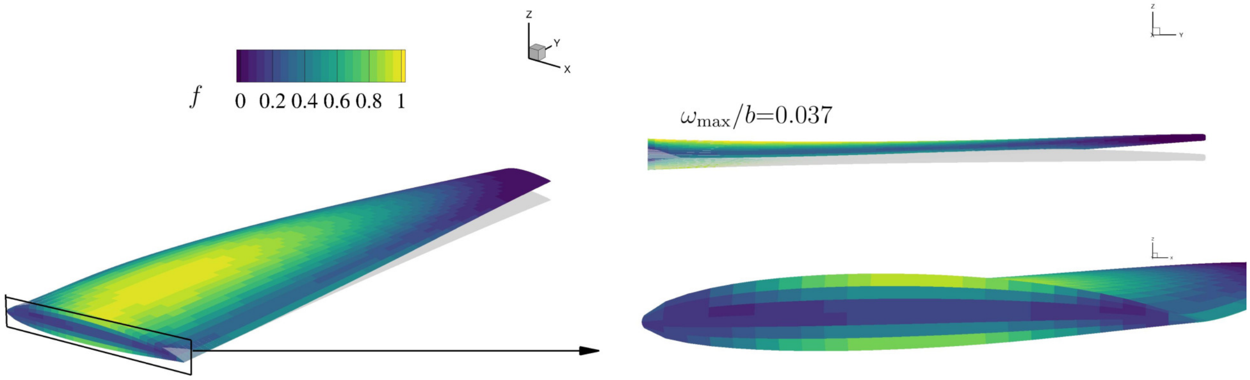

(a) Aluminum ($\mathrm{KS}_f = 1.0$)

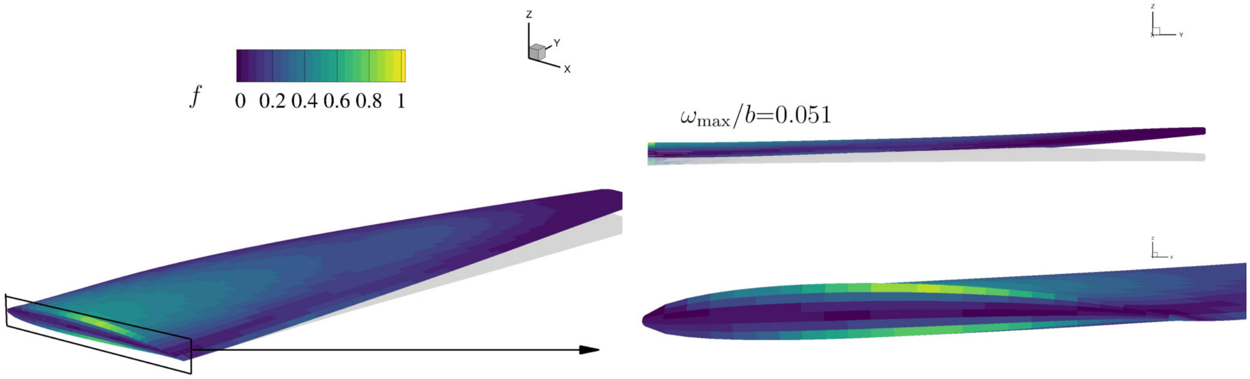

(b) Single-layer CFRP ($\mathrm{KS}_f = 0.86$)

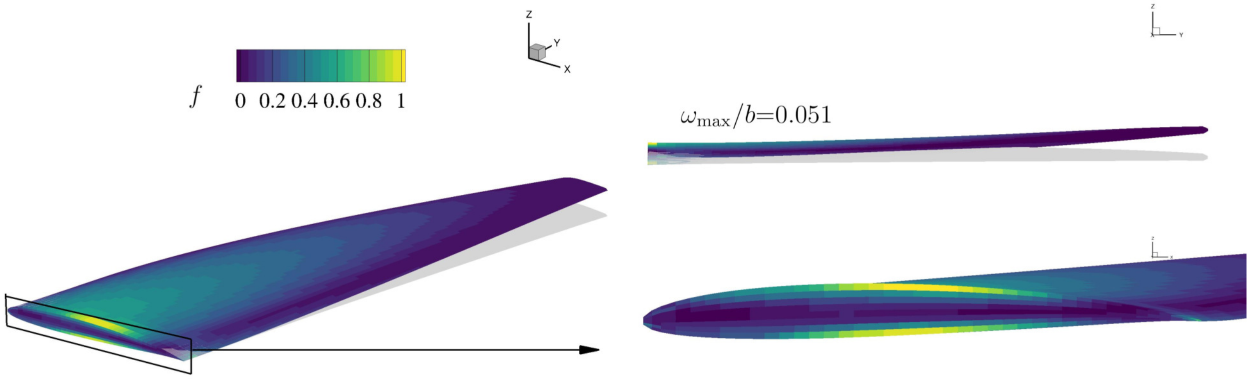

(c) Multi-layer CFRP ($\mathrm{KS}_f = 1.0$)

Figure 5.7: Material failure index contours and non-dimensional bending displacement for the optimized hydrofoils at the $C_L = 0.6$ condition. The aluminum case is the most susceptible to material failure. The trailing edge of the aluminum case experiences high stress concentration because of the curved deformation and thin thickness.

For the multi-layer CFRP case, both material failure constraint and bending displacement constraint were active. As explained earlier, varying the fiber orientations between layers allows the hydrofoil to better optimize both bending and twisting stiffness, so that the hydrofoil can still meet the displacement requirement without extra thickness increase. Additionally, detailed modeling of multi-layer configurations allows the determination of fiber orientation in each layer and hence provides more accurate material failure initiation prediction.

The stress contours of the single-layer CFRP and the multi-layer CFRP hydrofoils are shown as complements in Figures A.3 and A.4, respectively. As shown by the comparison of stress contours between these two cases, the multi-layer CFRP hydrofoil experiences significantly higher σ_{yy} because the fibers deviate from the bending axis.

5.4 Conclusions

In this chapter, we compared three different optimizations to demonstrate how using different material configurations would affect the hydrodynamic and structural performance of hydrofoil optimization. In addition to the single-layer CFRP optimization results shown in the previous chapter, the other two optimization cases were an aluminum hydrofoil and a hydrofoil with two equivalent layers CFRP. The multi-layer CFRP case effectively has two fiber orientations as design variables because we assume a symmetric layup.

The results show that all optimizations achieve similar hydrodynamic performance in terms of drag and cavitation inception. Despite the similarity in hydrodynamic performance shown in this chapter, using aluminum increases the likelihood of material failure. The difference in sweep angles between all three hydrofoils using different material configurations is caused by the combined effect of twist deformation and vorticity-induced downwash effects, and by the cavitation, displacement, and material failure constraints. Optimizing the fiber orientations of multiple layers of CFRP can achieve an optimal stiffness in different directions. The optimized multi-layer CFRP hydrofoil has forward-swept fibers in the inner layer, increasing the twisting rigidity compared to the single-layer CFRP hydrofoil. This twisting rigidity enhancement allows the multi-layer case to reduce the thickness without violating the bending displacement constraint, and thus this case provides a slightly lower drag compared to the single-layer CFRP hydrofoil. However, this drag reduction relative to the single-layer CFRP is not significant, suggesting that considering varying fiber orientation between layers during optimization might not offer much additional hydrodynamic benefit. Although optimizing one fiber orientation might be sufficient to achieve expected hydrodynamic performance, detailed modeling is needed to accurately predict the material failure to ensure safety.

In reality, composite laminates are often manufactured with multidirectional plies to sustain loading in different directions and to deter crack propagation. On the other hand, a single-layer structure easily suffers from crack growth once failure initiates. Hence, a structure designed with single-layer composite is less reliable than multi-layer configurations with varying fiber orientations. Despite the capability of deterring crack propagation, this advantage of multi-layer configurations is not captured in current optimizations because the hydrofoil is mainly subject to bending loads and the progressive damage is not modeled in this dissertation. Hence, although this dissertation shows that the single-layer CFRP optimized hydrofoils are less susceptible to material failure initiation, this result does not indicate that a laminate with a single fiber orientation is safer than a multi-layer configuration due to the limitations of the investigated loading conditions and the current material failure prediction model.

Additionally, the multi-layer CFRP result also shows that the inner layer does not contribute significantly to the structural strength, especially the bending stiffness, which suggests that the inner core can be replaced by other cheaper materials to reduce cost while still being able to optimize the twisting rigidity and achieve desirable performance.

CHAPTER 6

Influence of material failure model uncertainties on optimizations of composite hydrofoils

6.1 Introduction

In Chapter 5, we have compared optimizations of an aluminum hydrofoil, an equivalent unidirectional CFRP hydrofoil, and a multi-layer CFRP hydrofoil. It is well known that predicting the material failure for composites is challenging due to the complex and multi-scale failure mechanisms. In addition, the material failure initiation depends on the manufacturing quality, loading conditions, and material configurations. There are numerous failure models for composites, but there is no one model or theory that can be applied for all cases because each one has different simplifications and assumptions [7, 156–158]. Figure 6.1 compares the safe loading envelopes between two popular delamination initiation models, Hashin [5] and Ochoa-Engblom [6]. As shown by this figure, the safe loading envelopes of different failure initiation models can vary significantly from each other.

Hence, the objective of this chapter is to examine the influence of material failure model uncertainties on optimizations by comparing the optimized single-layer and multi-layer CFRP hydrofoils using two different material failure criteria.

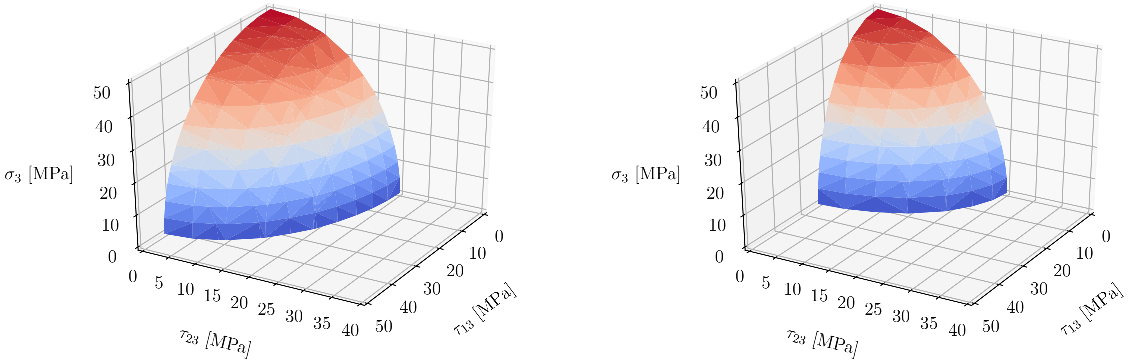

(a) Hashin delamination

(b) Ochoa-Engblom delamination

Figure 6.1: Safe loading envelopes of two different delamination failure initiation models, Hashin [5] and Ochoa-Engblom [6]. The color gradient is for ease of visualization. (Reproduced from Motley and Young [7])

6.2 Optimization problem setup

To make a fair comparison between all results in this chapter, we use the same fluid and structural mesh, which were used for the multi-layer CFRP case in Chapter 5. We re-evaluate the optimized single-layer CFRP hydrofoil that was shown in Chapters 4 and 5 with the same meshes. The CFD mesh corresponds to Figure 4.1a, and the structural mesh corresponds to Figure 5.2.

The first material failure criteria are MHY criteria described in Chapter 4. We implement another set of material failure criteria (MCO criteria), which consider maximum stress criterion for fiber breaking, Cuntze criterion [106] for matrix tensile cracking, and Ochoa-Engblom criterion [6] for delamination. Motley and Young [7] found that the Cuntze matrix tensile failure initiation criteria and the Ochoa-Engblom delamination failure initiation criteria provide the most conservative prediction. As shown by Figure 6.1, Ochoa-Engblom delamination model provides a smaller envelope than the Hashin delamination model, which is the same as the Ye-delamination model in the MHY criteria.

6.2.1 Material failure constraint

The fiber breaking indicator constraints are,

$$
\begin{aligned}
I_1 &= \frac{\sigma_{22}}{Y_T} \leq 1, \\
I_2 &= -\frac{\sigma_{22}}{Y_C} \leq 1.
\end{aligned}
\tag{6.1}
$$

The matrix tensile cracking indicator is [106],

$$
I_3 = \frac{\sigma_{11} + \sigma_{33} + \sqrt{(\sigma_{11} - \sigma_{33})^2 + 4\sigma_{13}^2}}{2X_T} \leq 1,
\tag{6.2}
$$

The delamination in tension indicator is [6],

$$
I_4 = \left(\frac{\sigma_{33}}{Z_T}\right)^2 + \frac{(\sigma_{23}^2 + \sigma_{13}^2)}{S_{13}^2} \leq 1,
\tag{6.3}
$$

where σ_{ij} are the element centroid stresses in different directions in the material coordinates. A safety factor of three is considered when evaluating the failure indicator values. Similar to the MHY criteria, the material failure index value of the element is conservatively evaluated by the maximum approximation using the KS function. Once the material failure value is computed for each element, we use the KS function again to aggregate values of all elements in the constrained region to yield the final material failure value for the constraint.

6.3 Results

The four optimized hydrofoils are summarized in Table 6.1. Note that the numeric results for the single-layer CFRP (MHY) hydrofoil in Table 6.1 are slightly different from Chapters 4 and 5 because we evaluated this optimized design with a new mesh, which is consistent with the single-layer CFRP (MCO) results and the multi-layer CFRP hydrofoils. From this summary, for both single-layer and multi-layer CFRP hydrofoils, the optimized geometries and results using two different sets of failure criteria are similar. A comparison of the planform shape is shown in Figure 6.2. The two single-layer optimized CFRP hydrofoils have almost identical sweep planform shape, and the same applies to the multi-layer optimized CFRP hydrofoils. There is a noticeable difference in the planform geometry between the single-layer and multi-layer CFRP hydrofoils, also being indicated by the sweep angles listed in Table 6.1. The reason for the difference in sweep angle between the single-layer CFRP hydrofoils and the multi-layer CFRP hydrofoils was explained in Chapter 5.

For the two single-layer optimized hydrofoils, because the bending displacement constraint dominates, using different material failure criteria does not make a difference in the optimized results except for a slight difference in the maximum material failure index value (equivalent to KS_f). The single-layer CFRP (MCO) has a slightly lower KS_f value because the matrix cracking criterion in the MHY criteria provides a more conservative estimation than the MCO criteria because of the used safety factor value and the quadratic form of the matrix cracking criterion in the MHY criteria.

Table 6.1: Optimization results summary

Case	Sweep	θ_f	Weighted C_D	δ_{tip}/b at $C_L = 0.6$	θ_{tip} at $C_L = 0.6$	KS_f at $C_L = 0.6$
Single-layer CFRP (MHY)	22°	$-23°$	0.0161	0.0478	$-3.3°$	0.88
Multi-layer CFRP (MHY)	18°	$[-23°/18°]_s$	0.0161	0.0493	$-1.8°$	1.0
Single-layer CFRP (MCO)	22°	$-23°$	0.0162	0.0483	$-3.1°$	0.80
Multi-layer CFRP (MCO)	17°	$[-21°/23°]_s$	0.0161	0.0492	$-2.0°$	1.0

6.3.1 Hydrodynamic performance comparison

In Chapter 5, we have shown that the pressure and lift distributions are similar between the single-layer and multi-layer CFRP optimized results using the MHY criteria.

We first show the pressure coefficient C_p contours for the two optimized hydrofoils using the MCO criteria in Figure 6.3. Similar to the comparison in Chapter 5, the surface pressure distri-

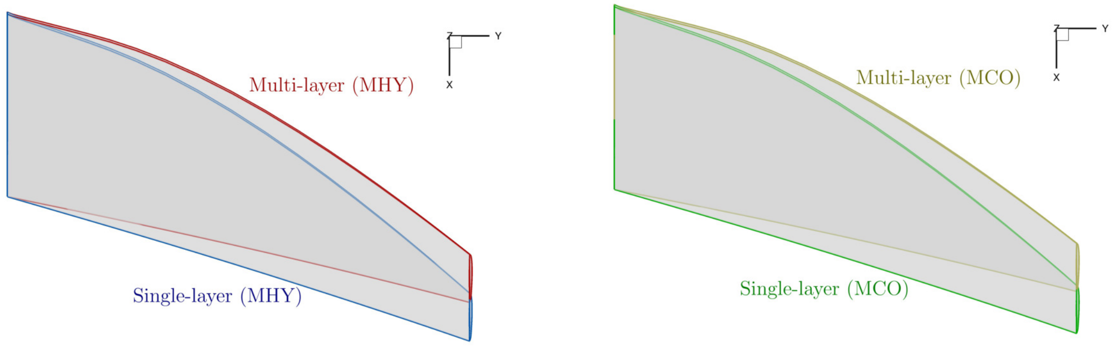

(a) Optimized single-layer and multi-layer hydrofoils using the MHY criteria.

(b) Optimized single-layer and multi-layer hydrofoils using the MCO criteria.

Figure 6.2: Planform shape comparison between optimized CFRP hydrofoils. With the same material configuration, the results using different failure criteria are almost identical. The significant differences in sweep between the single-layer and multi-layer CFRP hydrofoils are result of the combined effects of the sweep-induced geometric bend-twist coupling and vorticity-induced downwash effects, and the cavitation, displacement, and material failure constraints.

butions are similar between the single-layer CFRP (MCO) hydrofoil and the multi-layer CFRP (MCO) hydrofoil.

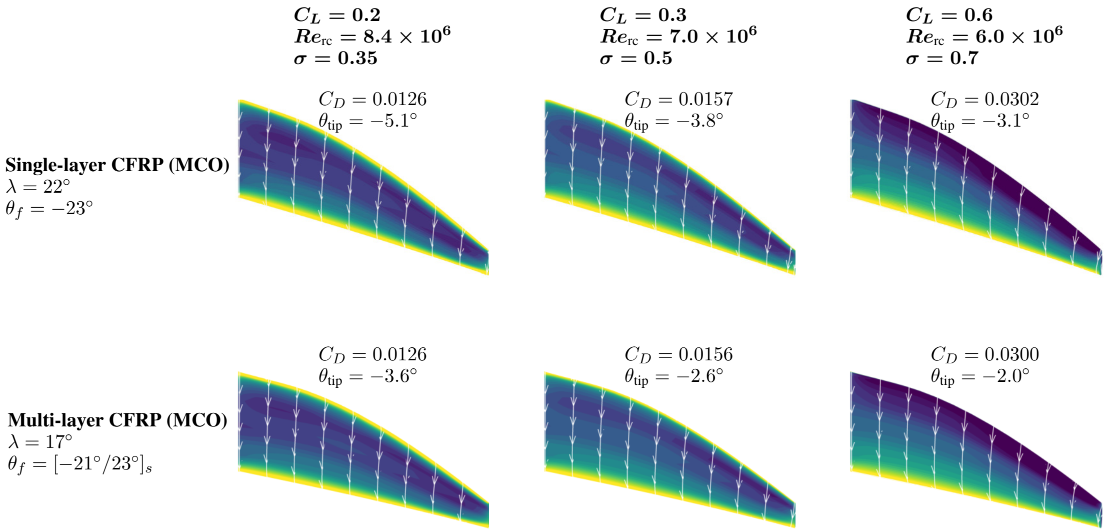

Figure 6.3: Comparison of surface pressure coefficient contours on the suction side and streamlines between the optimized single-layer and multi-layer CFRP hydrofoils using the MCO criteria.

To investigate the difference between the optimizations using different material failure criteria, we compare the four optimized CFRP hydrofoils in Figures 6.4 and 6.5. Figure 6.4 compares the non-dimensional deformed shapes and sectional C_p curves. Figure 6.5 compares the spanwise normalized lift distributions, sectional drag coefficient C_d, sectional friction drag coefficient C_{dv}, and twist distributions. From the comparisons shown in these two figures, we found that for the two failure criteria used in this dissertation, using the MCO criteria does not make a noticeable difference in terms of the deformed shape, pressure distribution, cavitation inception, and loading distributions.

6.3.2 Structural performance comparison

For the structural performance, we compare the material failure index contours on the suction side (Figure 6.6), the pressure side (Figure 6.7), and the root section (Figure 6.8) between the four optimized CFRP hydrofoils. The bending and shear stress contours of the single-layer and multi-layer optimized CFRP hydrofoils using the MCO criteria are shown in Figures A.5 and A.6.

As indicated by the KS_f values in Table 6.1, the material failure constraint is not active for both single-layer CFRP hydrofoils because the bending displacement poses a more stringent requirement on the structural stiffness than the two material failure initiation criteria. As shown by Figures 6.6, 6.7, and 6.8, for both the single-layer CFRP and the multi-layer CFRP, the MHY criteria tend to result in a higher failure index value at mid-chord of the root than the MCO criteria due to a more conservative estimation of the matrix cracking failure index value with a safety factor of three. Although the single-layer unidirectional CFRP designs can withstand the design loads, a multidirectional stacking sequence is typically preferred due to the capability to sustain various loadings and to stop crack growth once it initiates. The single-layer CFRP (MHY) hydrofoil shows a slightly high failure indicator value at approximately $y/b = 0.7$ due to the shear stress σ_{xz} (shown in Figure 6.9) and the stringent matrix cracking criteria. From the comparison at the root section in Figure 6.8, the multi-layer (MCO) hydrofoil has higher contour values in the inner

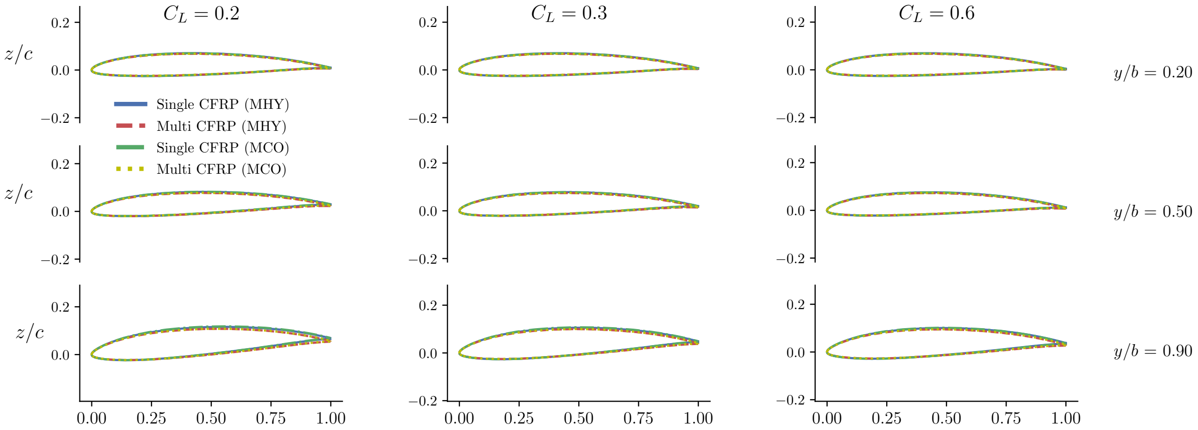

(a) Cross sectional shapes

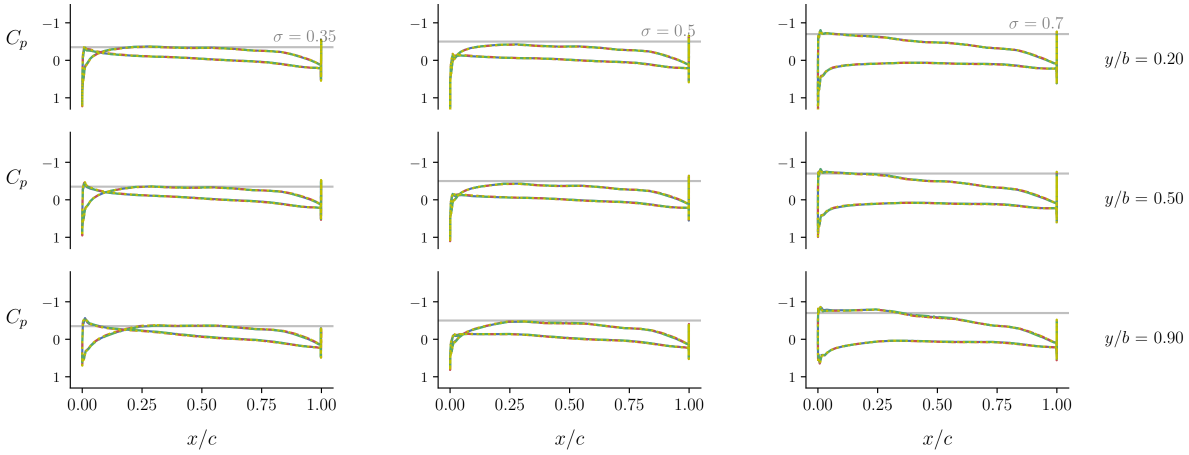

(b) Sectional C_p curves

Figure 6.4: Comparison of non-dimensional cross-sectional shapes between different optimized hydrofoils. The deformed shapes and sectional C_p are similar between optimization results.

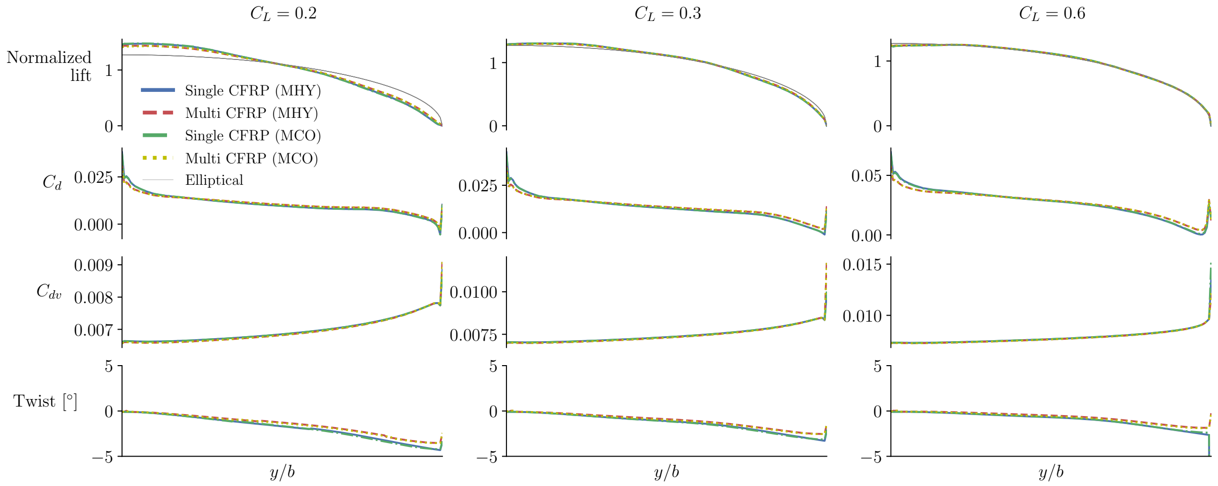

Figure 6.5: Comparison of spanwise normalized lift distribution, sectional drag coefficient C_d, sectional friction drag coefficient C_{dv}, and twist distributions between the optimized hydrofoils. The optimized hydrofoils results using different failure criteria show almost identical spanwise lift, drag, twist distributions.

layers because of the stringent Ochoa-Engblom delamination failure initiation model and the fiber orientation variation.

We identify the dominant mode for each optimized hydrofoil and list them in Table 6.2. Comparing the two single-layer CFRP hydrofoils, they are both dominated by matrix cracking. Although previous works show that the Cuntze matrix tensile cracking initiation model dominates more than the Hashin-type, its effects become less when a large safety factor is considered due to the linear form of the Cuntze criterion compared to the quadratic terms in the Hashin-type criteria. As a result, the KS_f value of the single-layer CFRP (MCO) hydrofoil is smaller than the single-layer CFRP (MHY) hydrofoil, as shown in Table 6.1. Due to the varying stiffness and strengths across thickness direction induced by the fiber orientation change, the multi-layer (MCO) hydrofoil is governed by delamination while the maximum failure index value of single-layer (MCO) hydrofoil is governed by matrix cracking.

The dominant mode comparison shown in Table 6.2 between the multi-layer CFRP hydro-

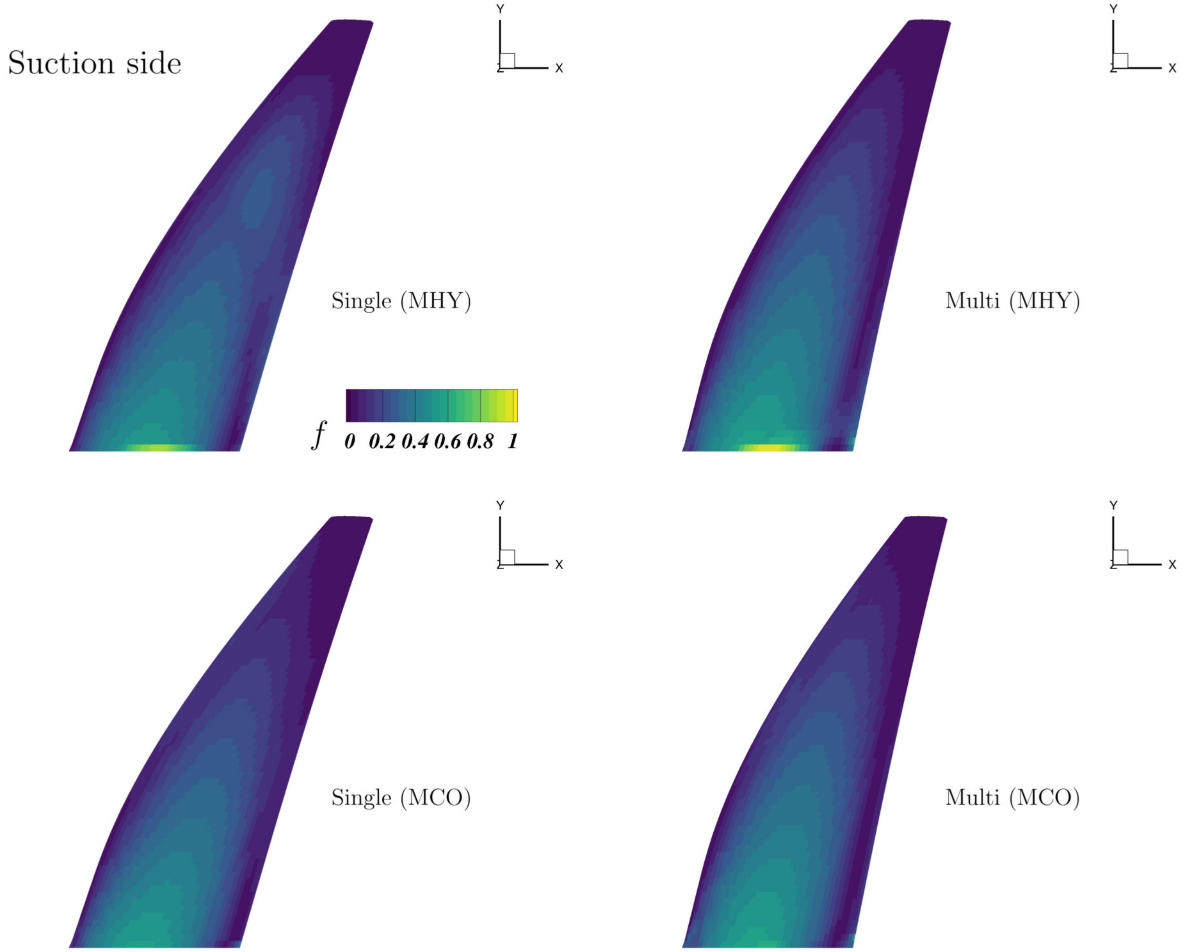

Figure 6.6: Material failure index contours on the suction side at $C_L = 0.6$ condition. The MHY criteria tends to result in a higher failure index value at mid-chord of the root than the MCO criteria.

Table 6.2: Dominant failure mode

Case	Dominant failure mode
Single-layer CFRP (MHY)	Matrix cracking
Multi-layer CFRP (MHY)	Matrix cracking
Single-layer CFRP (MCO)	Matrix cracking
Multi-layer CFRP (MCO)	Delamination

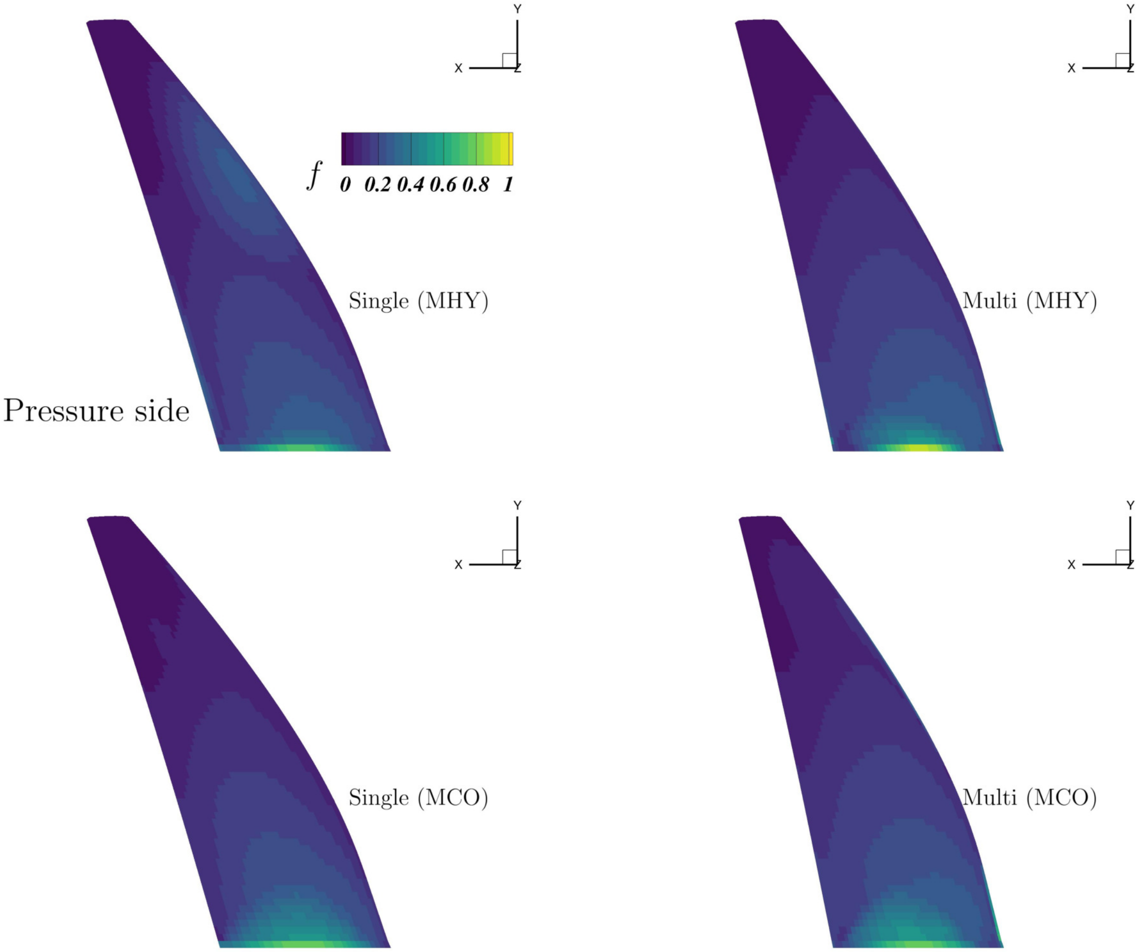

Figure 6.7: Material failure index contours on the pressure side at $C_L = 0.6$ condition. The MHY criteria tends to result in a higher failure index value at mid-chord of the root than the MCO criteria.

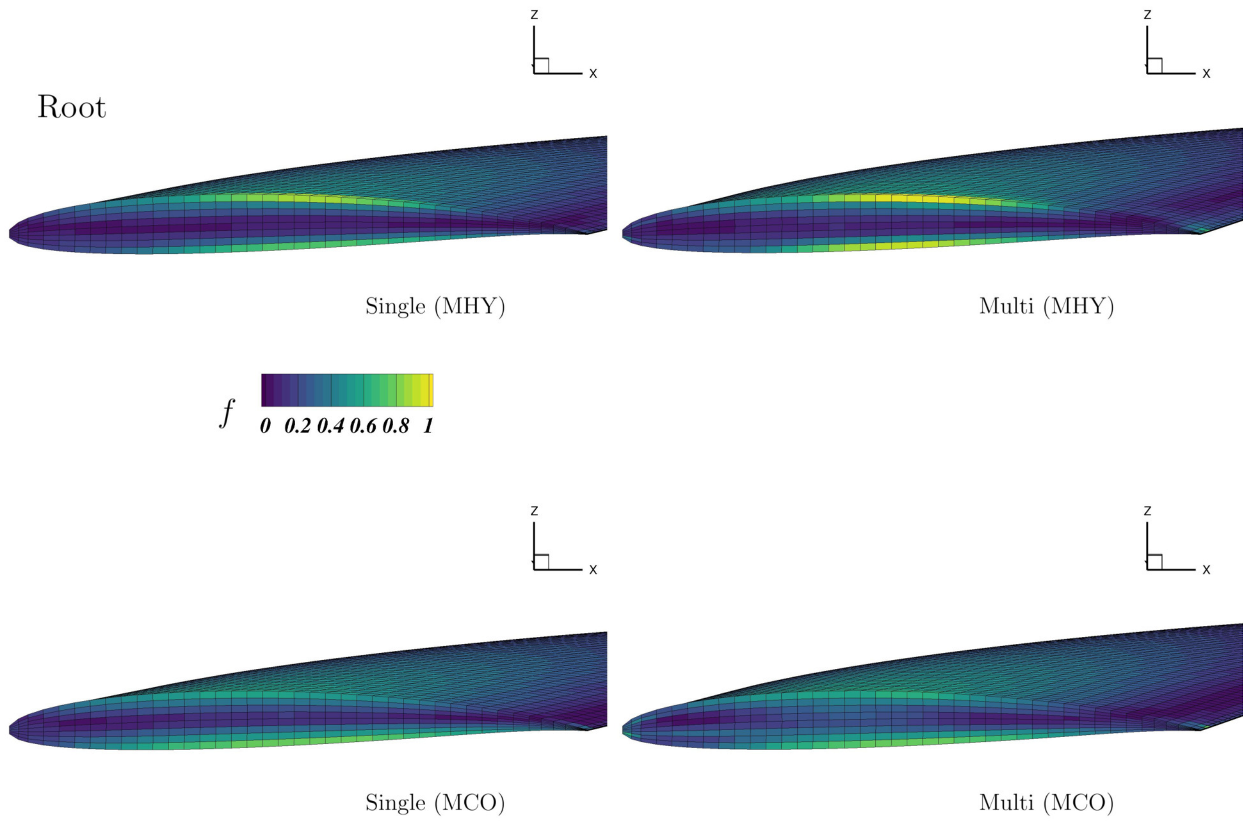

Figure 6.8: Material failure index contours at the root section at $C_L = 0.6$ condition. The multi-layer (MCO) optimized hydrofoil shows higher failure index value at the inner layers because of the more conservative delamination failure initiation model and fiber orientation variation across the thickness.

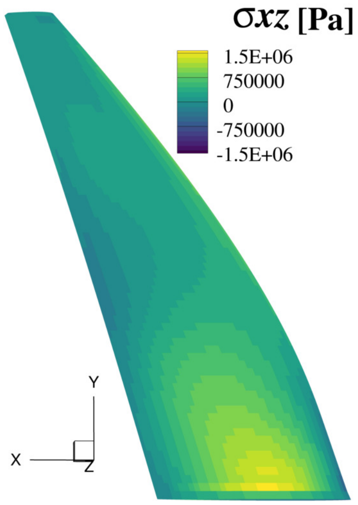

Figure 6.9: σ_{xz} contour of the single-layer CFRP (MHY) hydrofoil at $C_L = 0.6$ condition

foils shows that Ochoa-Engblom delamination initiation model is more stringent than the Ye-delamination initiation mode in the MHY criteria. To further demonstrate this, we evaluate the multi-layer (MHY) hydrofoil using the MCO criteria. As shown in Figure 6.10, the multi-layer (MHY) hydrofoil would violate the MCO material failure constraint with $f_{\mathrm{MCO}} \approx 1.6$. This violation is caused by the Ochoa-Engblom delamination failure mode mainly due to higher shear stress σ_{xz}. As a result, this active delamination failure constraint of the multi-layer (MCO) case drives the design to have a slightly less sweep angle than the multi-layer (MHY) result.

Maximum strain criterion and maximum stress criterion are two of the most popular failure criteria, but they ignore the interaction between different stress components and can overestimate the failure initiation loading. Additionally, maximum stress and maximum strain only consider simple linear terms, the influence of the safety factor is significantly reduced compared to the criteria that use quadratic terms. We evaluate the multi-layer (MCO) optimized hydrofoil with

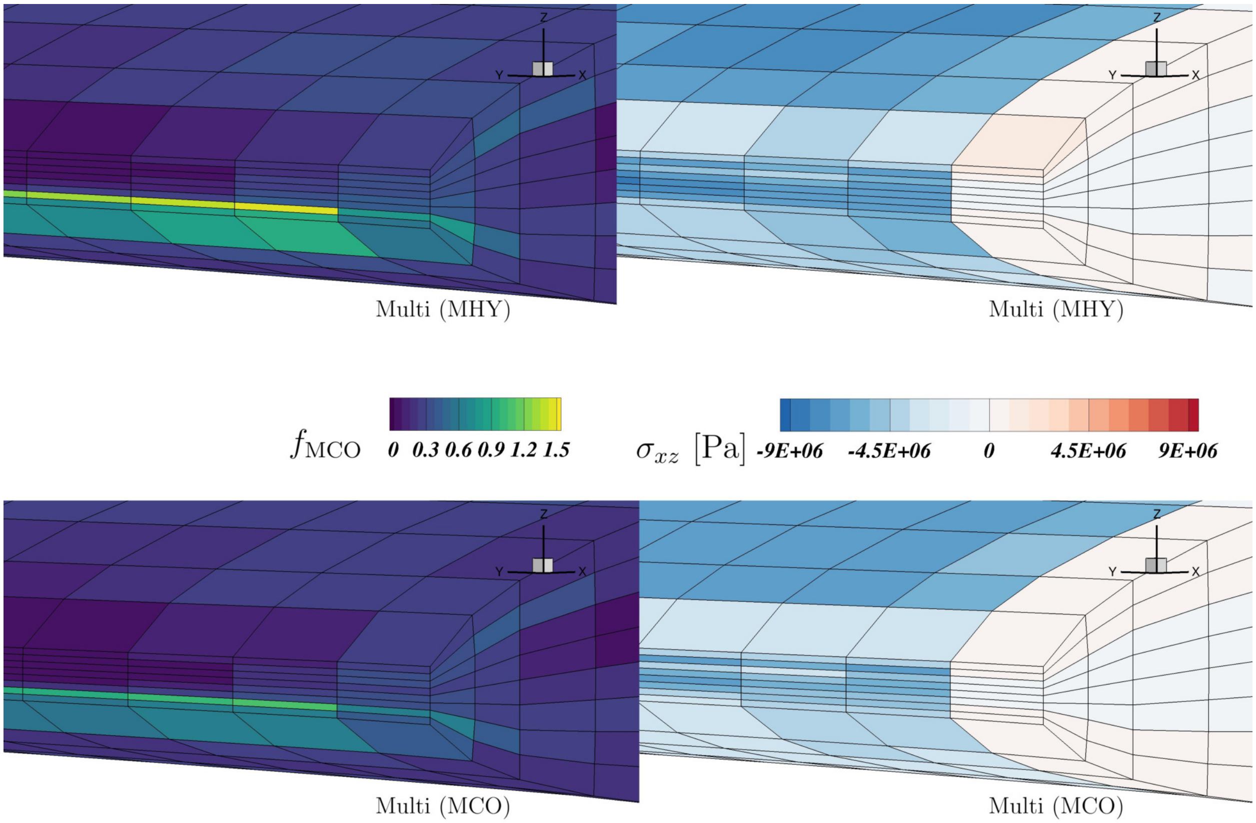

Figure 6.10: MCO failure criteria evaluation contour comparison between optimized multi-layer CFRP (MHY) and multi-layer CFRP (MCO) hydrofoils at the leading edge near the root. The top figures are the optimized multi-layer (MHY) result and the bottom two figures are the optimized multi-layer (MCO) result. The failure indicator contours using the MCO criteria are shown on the left and the σ_{xz} contours are shown on the right. The high σ_{xz} stress of the first row elements near the root is caused by the local stress concentration mainly due to the simplified fixed root boundary condition.

maximum stress criterion,

$$\max\left(\frac{\sigma_{11}}{X_T}, \frac{-\sigma_{11}}{X_C}, \frac{\sigma_{22}}{Y_T}, \frac{-\sigma_{22}}{Y_C}, \frac{\sigma_{33}}{Z_T}, \frac{-\sigma_{33}}{Z_C}, \frac{|\sigma_{12}|}{S_{12}}, \frac{|\sigma_{23}|}{S_{23}}, \frac{|\sigma_{13}|}{S_{13}}\right). \tag{6.4}$$

The failure criterion contour with maximum stress criterion is shown in Figure 6.11. The maximum value is 0.72, which is lower than the MCO criteria.

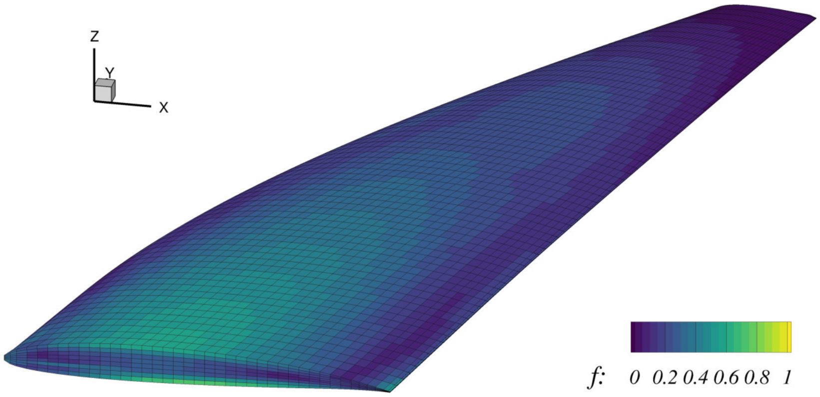

Figure 6.11: Failure index contour of multi-layer (MCO) optimized hydrofoil evaluated with the maximum stress criterion shown in Eqn (6.4). The maximum value is smaller than the one.

6.4 Conclusions

We compare four optimized CFRP hydrofoils to further investigate the difference between the single-layer CFRP hydrofoils and multi-layer CFRP hydrofoils, as well as the influence of failure initiation criteria on optimizations of composite lifting surfaces. Similar to the observation in Chapter 5, the bending displacement constraint places a more stringent requirement on the structural stiffness, so the material failure is not active for the single-layer CFRP hydrofoils, even with different failure criteria. By placing the fiber almost aligned with the bending axis, the hydrofoil is less susceptible to matrix cracking near the root. In addition, the similarity between single-layer

CFRP hydrofoils and multi-layer CFRP hydrofoils again suggests that an equivalent single-layer model can be used to achieve the same hydrodynamic performance. In the meantime, since the realistic structures are often constructed with multiple layers with different fiber orientations, detailed modeling of the actual composite material layup is needed to better predict the material failure initiation.

Predicting the failure initiation for composite structures remains challenging due to the failure model uncertainties. There exist numerous failure initiation models, but none of them can be applied for all scenarios because of the complex failure mechanisms of composites and different simplifications and assumptions in theories. The safe loading envelopes can vary significantly from one to another. In addition, material strength uncertainties make the prediction harder. As a consideration of the fatigue performance and variability in material strengths, a conservative safety factor of three is applied in the optimizations. We compare two sets of optimized results using two different material failure criteria. For both the single-layer and multi-layer configurations, using the two material failure criteria results in almost identical planform geometry and cross-sections. The similarity in the performance between these optimized hydrofoils using different failure criteria suggests that the difference between these two material failure criteria does not lead to significantly different designs. Hence, both designs can be considered safe, particularly with the safety factor of three. Nevertheless, the results suggest that a final analysis of the actual multi-layer design with a conservative material failure model along with progressive failure analysis is recommended to ensure structural integrity.

CHAPTER 7

Hydrodynamic optimization of a T-shaped hydrofoil-strut system

Now that we have demonstrated the usefulness of MDO in design composite lifting surfaces and how using composites can benefit the designs by using a canonical hydrofoil model, the next step is to advance the studies to more complex systems, which involve more components where the resultant interference effects cannot be neglected. Another reason that makes optimizing the shape of a more complex system and optimizing more detailed geometries (such as junction shapes) meaningful is the modern manufacturing technologies, such as 3-D printing and resin transfer molding, which enables generating of sophisticated geometry designs. We will focus on junction shape optimization here. The junction shape is critical because of interference drag, junction vortices, and stress concentration.

As the first step to such studies, we look at hydrodynamic optimization problems of a T-shaped hydrofoil-strut system, a critical component of hydrofoil-supported vessels. Later in this chapter, we refer to this system of hydrofoil-supported crafts as T-foil. We choose this system as an example because it is representative of more general problems and this system has emerged recently for fast and efficient sea and riverine transport. This system is representative for three main reasons. First, it involves a vertical strut and a horizontal foil, which have interference effects and the junction shape design becomes important. Second, this type of system typically operates at high speeds near the free surface, so their designs face the challenges of cavitation, ventilation, and separation. Third, it is also relatively simple to study, which suits our need of *investigating the problem* and *understanding the physics*.

In this chapter, we will first review some concepts about hydrofoil-supported vessels and T-foil designs, as well as some recent works designing intersection geometry. Later content is organized as follows: first, we describe the model used in the current study; next, we give the optimization problem formulation and introduce the cases; lastly, we show the optimization results, and discuss the insights and implications.

7.1 Introduction

Hydrofoil-supported crafts became popular in the mid-20th century as they can operate at high speeds and have good seakeeping characteristics [2, 159]. The supporting hydrofoils provide lift for vessels to operate with the hull bottom out of the water to reduce vessel wetted area and interaction with waves. Hence, these crafts experience less drag at foil-borne operation conditions and can achieve higher maximum speeds. However, their popularity dropped since the 1970s due to propulsion design difficulties, limited material choices, manufacturing techniques, and mechanical issues caused by the system's complexity. Today, due to advances in material science, manufacturing, analysis, and design techniques, as well as sensing and control strategies, hydrofoils are regaining interest. Hydrofoil designs have been increasingly adopted in competitive sailing communities[1] and recent novel water transport[2]. However, general hydrofoil applications still face challenges. Operating at high speeds near the free surface presents challenges for hydrofoil craft operation, as cavitation and ventilation can occur and lead to sudden and drastic lift loss, efficiency reduction, as well as hydrodynamic and hydroelastic instabilities [1, 26, 37, 44, 45, 160]. Hence, it is important to design hydrofoils with high efficiency while avoiding cavitation and ventilation

---

[1] International moth class and America's Cup

[2] Boundary Layer Technologies, Candela, FreightFish, and SeaBubbles

and simultaneously ensuring structural integrity.

Hydrofoils usually feature a complex 3-D geometry. The shape affects the pressure distribution and thus cavitation inception and separation. Three widely used types are L-foils, C-foils, and T-foils. With progress in control strategies, T-foils provide more stable performance and exhibit more controllable behaviors, as the foils are fully submerged in water. T-foils can also serve as a damper to mitigate or control wave-induced vessel heave motions [2, 161]. For a T-foil, the foil shape is important for providing the required lift while minimizing the drag, but the intersection or junction shape details are equally important, as they impact separation and vortex development, cavitation, and stress concentration. Recent advances in manufacturing robots and 3-D printing technology allow cost-effective manufacturing of highly optimized sections, including intersection details. In the past, the use of metallic materials limited the design freedom at the junction, as it depended on the welder's skills and materials used. For composite materials, conventional manufacturing technologies also made junction optimization challenging. Recently developed methods such as automated fiber placement and 3-D printing allow efficient and accurate manufacturing of optimized hydrofoils with higher performance, while avoiding cavitation and separation, as well as ensuring structural integrity.

Vortices and cavitation can cause pressure fluctuation, which can lead to noise, vibration, surface erosion, and accelerated fatigue issues [162]. Besides, it is important to avoid separation and cavitation, as both can cause ventilation. Ventilation can cause a rapid and sudden drop in the lift and moment, and in turn, affect the vessel performance and stability. Moreover, the junction details affect the structural response. Any drastic change in the junction shape can cause stress concentrations that can further develop into fatigue or other material failures. These failures can expose embedded sensing and hydraulic actuation units and eventually lead to hydrofoil system failure.

To better design T-foils, many experiments have been conducted to facilitate the understanding of the physics [163–168], but experiments are costly during the early design stage. We have discussed that numerical methods and design optimization have been developed to better design hydrodynamic lifting surfaces. To design a T-foil, we need not only a high-fidelity tool but also the capability to handle the geometric changes of each component and between components, with flexibility during optimization. CFD with the overset mesh approach provides the capability to handle relatively large geometry changes while preserving good mesh quality compared to multiblock meshes [99]. For a geometry with intersecting components, the surface mesh deformation near the intersection is challenging as the CFD solver requires the surface mesh nodes to conform with the changed design outer mold line and maintain the watertight property [96]. Secco et al. [95, 169] have developed a robust algorithm to handle this mesh deformation challenge with overset meshes and demonstrated the advantages with a wing-body configuration and a strut-braced wing.

The objectives of this chapter are to 1) optimize a T-foil considering a large number of design variables using a high-fidelity and adjoint-based optimization framework, and 2) investigate the tradeoffs between design considerations, and 3) investigate how detailed junction geometry design affects the design and performance.

7.2 Optimization problem setup

The design goals are to minimize drag, delay cavitation inception, and avoid separation. We will first introduce the model that is used in the optimization (Section 7.2.1). This will be followed by a validation study with experimental results (Section 7.2.2). Then we will describe how we define geometric variables (Section 7.2.3), cavitation constraint (Section 7.2.4), and separation constraint (Section 7.2.5). The design conditions are listed in Section 7.2.6. We conduct both single-point and multipoint optimizations. For single-point optimization problems, the objective is to minimize drag coefficient C_D, while for multipoint optimization we minimize the weighted drag to consider the contribution from different inflow velocities at each design condition. A summary of the optimization problem is given in Section 7.2.6. Lastly, Section 7.4 lists all the optimization cases that we will show in this chapter.

7.2.1 Model

We use a T-foil model from Ashworth Briggs [167] as our baseline hydrofoil. This model is a canonical representation of a rudder T-foil for the Moth Dinghy class. The T-foil has a semi-span of $b = 0.333$ m, a root chord c_{root} of 0.14 m, and a tip chord c_{tip} of 0.095 m. We immerse the foil at a water depth h of 0.4 m (h/c_{mean}=3.4) from the free surface. The dimensions of the T-foil are shown in Figure 7.1. Both the strut and foil geometries have a NACA 0012 cross section shape (the strut cross section might differ from the original work). The baseline cross section is not optimal for a lifting surface with respect to susceptibility to cavitation and ventilation. We choose this model because there are experimental results to compare with and it is relatively easy to model. Additionally, for a well-defined optimization problem, the choice of baseline shape should have a negligible impact on the optimized geometry in the absence of multimodal solutions. Previous works have shown that with proper constraints and problem formulation, optimizations starting from different initial designs converge to the same or similar results [149, 170].

For the mesh used in later optimization studies, the strut surface mesh has 1,944 cells; the collar, 3,888; the foil, 15,024. The triangulated meshes are much finer than the CFD meshes. The reason for using much finer triangulated surface meshes is explained in Section 2.2. The surface meshes are extruded to 0.2 m in the normal direction to generate volume meshes, as shown in Figure 7.2. For the foil and the strut, the volume meshes have 32 cells in the normal direction, while the collar has 40 layers to provide a smaller extrusion grid ratio (1.2951) compared to strut and foil (1.3916) so that collar cells are prioritized during implicit hole cutting process. The volume meshes of individual components and the final combined mesh are shown in Figure 7.2. This combined T-foil mesh is finally combined with a background mesh to form the final overset mesh. The background mesh is an O-grid that contains a cartesian grid bounding the T-foil volumes and the extrusion to the outer boundary. The final mesh has 991,712 cells. After the implicit hole cutting process,

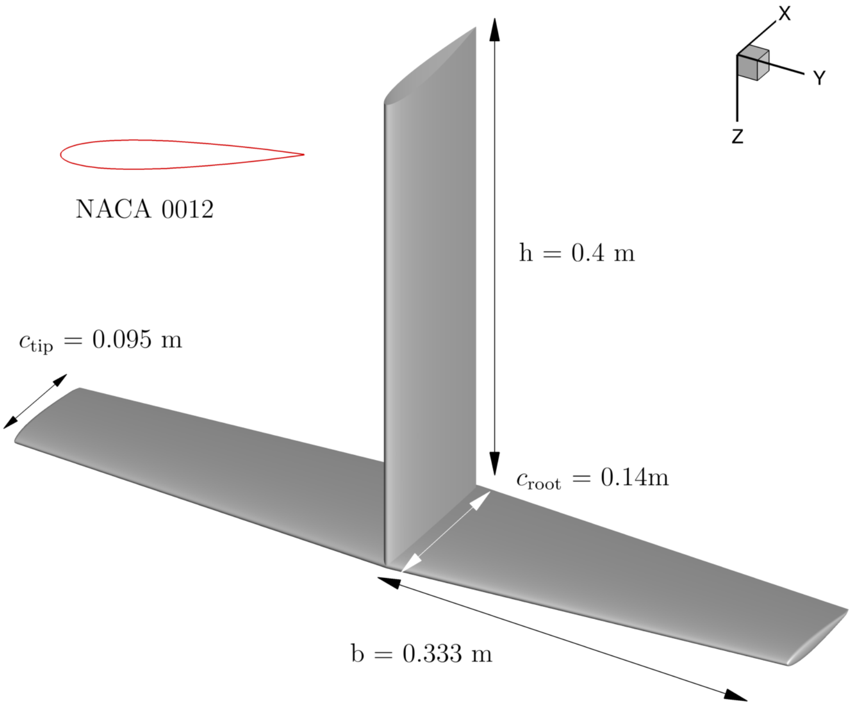

Figure 7.1: Geometric dimensions of the T-foil

there are 891,112 compute cells. The final mesh has a maximum y^+ of 2.7 at the nominal design condition. Design conditions will be introduced later in Section 7.2.

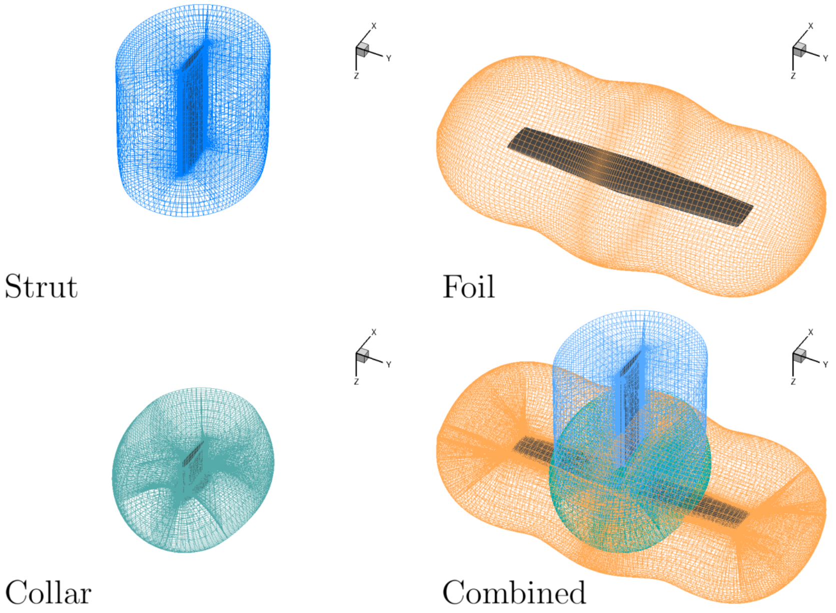

Strut

Foil

Collar

Combined

Figure 7.2: Individual volume mesh for each component and the final combined volume mesh (without the background mesh)

For this T-foil problem, the drag coefficient C_D and lift coefficient C_L are total drag and total lift non-dimensionalized by the dynamic pressure and the reference area of the horizontal foil, which is the product of the mean chord and span, 0.0783 m^2. Later in our results, we report the total drag and the drag for different components separately. Figure 7.3 shows how we group surfaces.

We apply the symmetry plane boundary condition at the top of the strut for the optimization results shown later in this chapter. This symmetry plane boundary condition is typically used to simulate the free surface at low speed (low submergence-based Froude numbers Fn_h) conditions. At high speed (high Fn_h) conditions, an antisymmetry boundary condition should be used to simulate the free surface. At low Fn_h limits, the lift increases when approaching the free surface; at high Fn_h conditions, the lift decreases when approaching the free surface. A comparison with the analytical prediction by Faltinsen is shown in Chapter 8. Ashworth Briggs [167] has observed that both lift and drag forces approach an asymptote at an h/c_{mean} of 1.7 at 2 m/s. Hence, the free

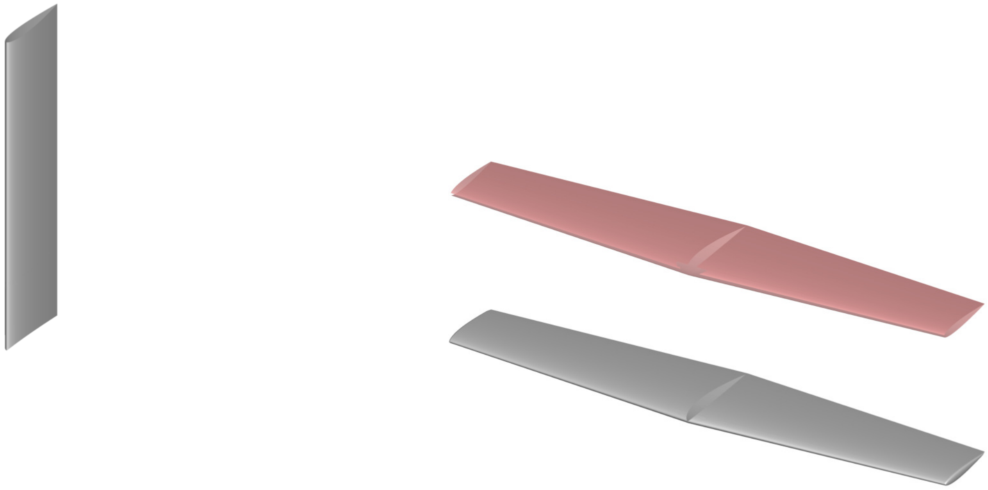

(a) Strut component surface

(b) Foil component surface

Figure 7.3: Surface groups for the T-foil. Only one surface is used for the foil. The red surface represent the region where the separation constraint is applied (excluding the leading edge).

surface effect on the steady force is minimal and can be neglected at an h/c_{mean} value of 3.4. To verify that the symmetry/antisymmetry plane boundary condition effect is small on the T-foil in our simulations with h/c_{mean}=3.4, we perform analyses at four different depth values by varying the distance between the foil and the symmetry/antisymmetry plane, each at an angle of attack of 4°. We describe details of the antisymmetry plane boundary condition in the next chapter. These analyses only include the foil and there is no strut. Figure 7.4 demonstrates the relative position between the symmetry/antisymmetry plane and the foil for each case. The C_L and C_D comparison is shown in Table 7.1.

Table 7.1: C_L and C_D comparison between four cases at different depth values

		$Re = 1.5 \times 10^6$	symmetry		antisymmetry	
h [m]	h/c_{mean}	Fn_h	C_L	C_D	C_L	C_D
0.2	1.7	10.0	0.311745	0.020016	0.277288	0.019904
0.3	2.6	8.1	0.301473	0.019865	0.284462	0.019867
0.4	3.4	7.1	0.298777	0.019821	0.288141	0.019877
0.5	4.3	6.3	0.297208	0.019862	0.290204	0.019918

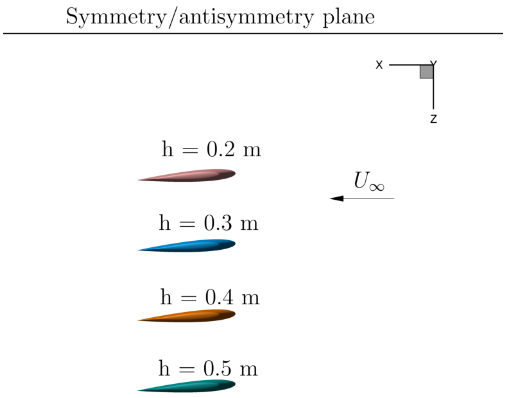

Figure 7.4: The foil position for each case at different distances from the symmetry/antisymmetry plane.

The results show that, at an h/c_{mean} of 3.4, the predicted lift and drag forces approach an asymptote, which means that the symmetry/antisymmetry plane effect is small on the foil. The difference between the case with $h/c_{\text{mean}} = 3.4$ ($h = 0.4$ m) and the case with $h/c_{\text{mean}} = 4.3$ ($h = 0.5$ m) is only 0.5% for C_L and 0.2% for C_D with the symmetry plane boundary condition. For the antisymmetry plane boundary condition, the differences are 0.7% and 0.2%, respectively. Hence, the symmetry/antisymmetry plane effect on the foil steady forces is small at the designed depth ($h = 0.4$ m). The difference between symmetry plane boundary condition and antisymmetry boundary condition at h/c_{mean} =3.4 ($h = 0.4$ m) is only 3.7%. Hence, using a symmetry plane boundary condition is an acceptable option for the designed inflow speeds given the designed depth here. We apply the far-field boundary condition at about 9 span lengths away from the bounding cartesian mesh.

7.2.2 Validation

We perform analyses at $U_\infty = 4$ m/s (mean-chord based Reynolds number $Re = 0.45 \times 10^6$) and compare the numerical results with the experimental data ($Re = 0.48 \times 10^6$) [167]. To make a better comparison, we generate a finer mesh for simulations. The finer mesh has 7,456,768 cells in total. After the implicit hole cutting process, the finer mesh has 6,910,434 compute cells. Figure 7.5 shows the surface compute cells with zipper meshes for both the coarse mesh and the finer mesh.

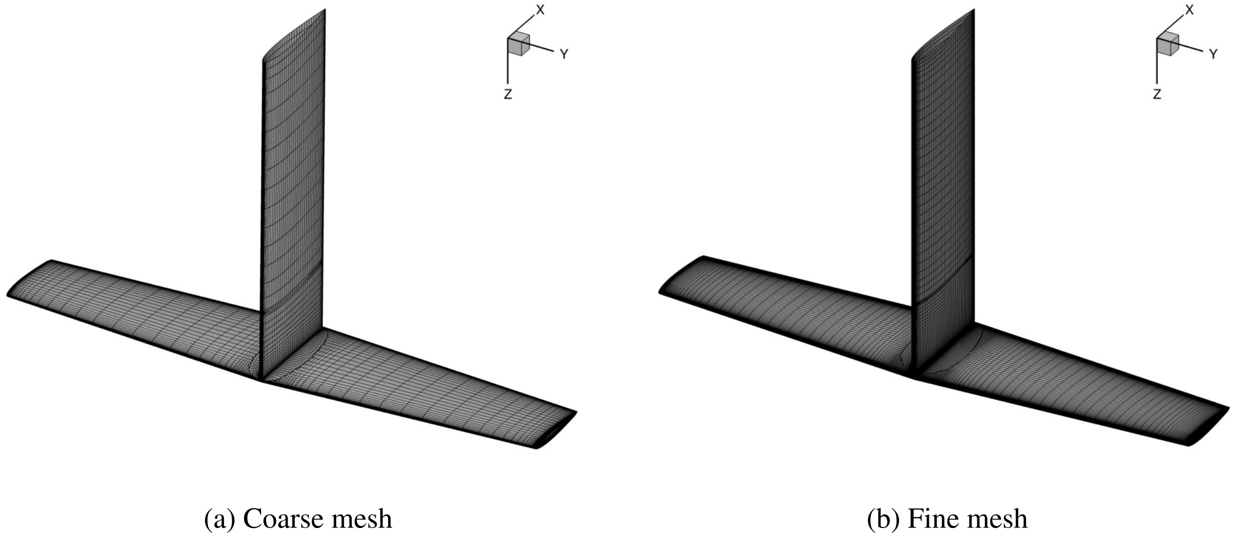

(a) Coarse mesh (b) Fine mesh

Figure 7.5: Surface compute cells with zipper meshes

The comparison of the numerical results and experimental data is shown in Figure 7.6. We show results using both the coarse mesh (with 991,712 cells and 891,112 compute cells) and the finer mesh in the comparison. As shown in Figure 7.6, the coarse mesh underestimates the lift and overestimates the drag. The finer mesh provides better prediction. The finer mesh overestimates the drag compared to experimental data because we assume fully turbulent flow in the simulations while laminar flow was observed in the experiment when the angle of attack is less than around 5° [164]. We perform a simulation with laminar Navier-Stokes equations at $\alpha = 0^\circ$ with the finer mesh. This laminar result is shown as a diamond symbol in Figure 7.6, which provides a closer approximation to the experimental data at this $\alpha = 0^\circ$ condition. Despite the more accurate predictions given by the finer mesh, we use the coarse mesh in later optimization for optimal computational efficiency. From our previous studies and experience, the trend and improvements resulting from the coarse mesh are still valid when evaluating with finer meshes.

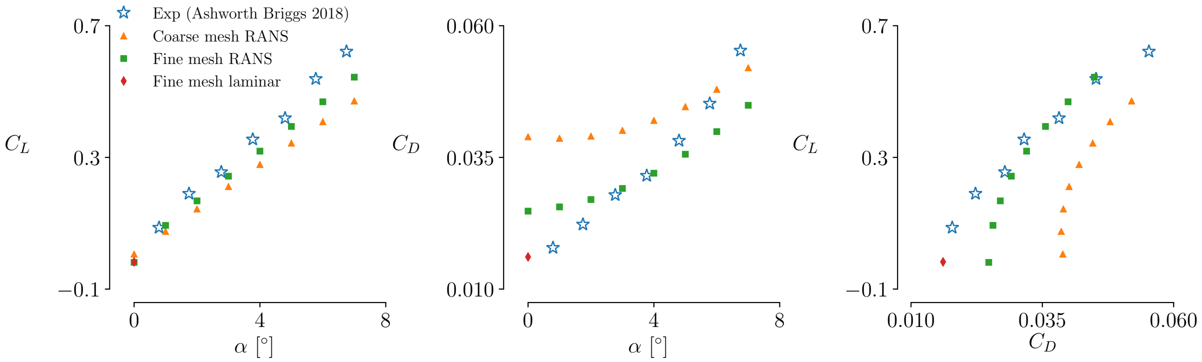

Figure 7.6: Comparison of numerical predictions and experimental data for the T-foil. The experimental data are shown in blue star symbols.

7.2.3 Geometric variables and constraints

The geometric design variables include twists, shape variables, and planform variables for the foil. The planform variables here refer to the chord and sweep variables. The design variable demonstration is shown in Figure 7.7. The red dots shown in Figure 7.7 are the FFD control points. We distribute the streamwise FFD points uniformly. In the spanwise direction, we define more control points near the intersection to have better control on the geometry manipulation. On the outboard portion, the control point distribution is uniform. The twist and chord variables are defined relative to the reference axis at 0.1% chordwise position from the leading edge. Using the FFD approach, we define twist variables to control the rotation of the FFD sections about the reference axis, as shown in Figure 7.7. While only three rotation arrows are shown in the Figure to demonstrate the twists, we have a total of eight twist variables for all the sections in the optimization. The sweep variable λ moves the FFD sections (except for the three sections at the intersection because shearing the adjacent two sections relative to the middle section can easily cause an invalid intersection and a failed mesh) along the streamwise direction. Similar to the twist variables, the chord variables are defined relative to the leading edge position, so the leading edge is kept straight during the optimization. The reason for defining chord variables with respect to the leading edge is to keep the intersection at the leading edge valid so that the mesh maintains watertightness during the optimization. Using a different reference axis for chord variables can shift the leading edge of the foil from the strut, which can lead to an invalid intersection line. There are three chord variables for the foil and one for the strut. A linear constraint is used to keep the strut chord consistent with the foil root chord. At the sections where the chord is not directly controlled by the chord variables, the chord values are linearly interpolated. These chord variables monotonically decrease from the middle of the foil to the tip. The span variable stretches the spanwise position of the control points, elongating or shortening the foil span accordingly. The rake variable is only defined for multipoint optimization problems because it is used to emulate the angle of attack of the T-foil. We use local shape variables to move FFD control points vertically to change the cross-sectional shapes. We separate the control points on the top and on the bottom of the three middle sections because in some optimization cases we want to limit the freedom of these control points to provide enough thickness at the intersection. We also conduct an optimization without this limitation on the intersection shape variables to investigate how designing the detailed geometry at the intersection could improve the performance. Thickness constraints, leading edge and trailing edge constraints, and a projected area constraint are also applied.

7.2.4 Cavitation constraint

For single-point optimization problems, we use the *original* cavitation constraint; for multipoint optimizations, we use the *improved* cavitation constraint as described in Section 4.2.3. Details about the cavitation constraint can be found in Chapter 4. Both cavitation constraints use a k of 10, which is lower than the value used in Chapter 4 due to the challenge of avoiding separation simultaneously. The offset γ used in the improved cavitation constraint here is 0.2. From Figure 4.3, we can observe that the original version can be conservative because it becomes significantly greater than zero even when the minimum pressure does not reach the critical onset point.

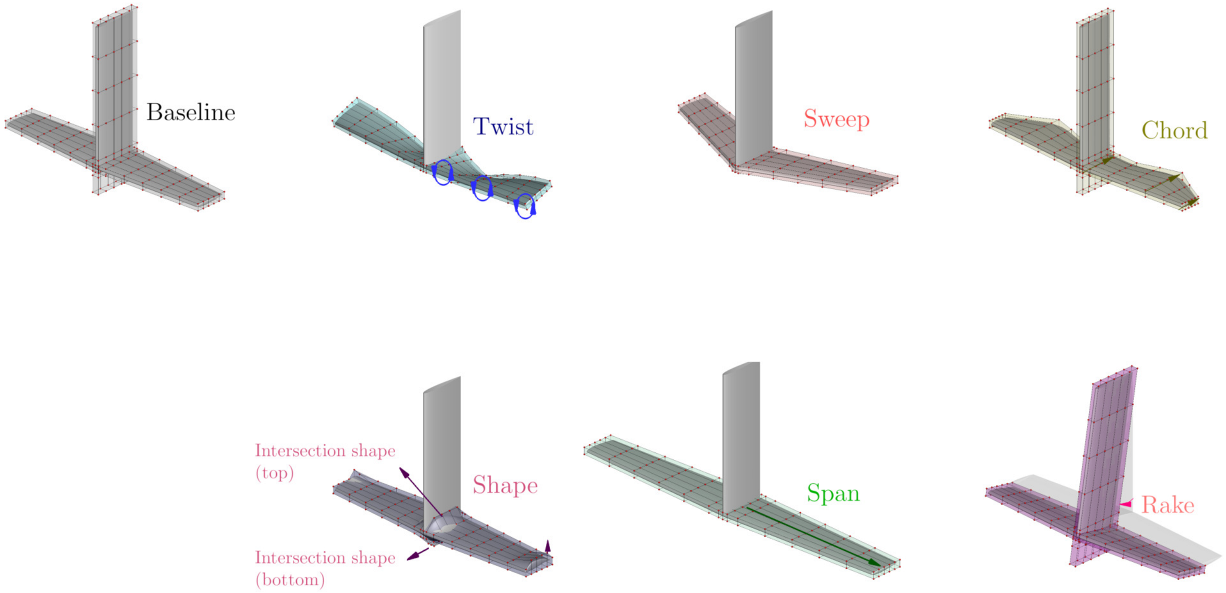

Figure 7.7: Geometric design variable demonstration

This conservativeness will be observed later in single-point optimization results. The cavitation constraints are only enforced on the foil surface because we only consider shape variables for the horizontal foil.

7.2.5 Separation constraint

We use the same separation constraint formulation as [150]. This constraint effectively considers the flow reversal as the flow separation indicator. We assume that if streamwise component of the flow velocity on the surface becomes negative, flow separation occurs,

$$\cos\theta = \frac{\vec{U}\dot{\vec{U}}_\infty}{|\vec{U}||\vec{U}_\infty|}, \tag{7.1}$$

where $\vec{U}$ is the local surface velocity and θ defines the angle between the local surface velocity and the inflow velocity $\vec{U}_\infty$. When $\cos\theta$ becomes negative, the separation sensor is active, which is defined as,

$$X = \begin{cases} 1 \quad \text{if} \quad \cos\theta \leq 0 \\ 0 \quad \text{if} \quad \cos\theta > 0 \end{cases} \tag{7.2}$$

Like the cavitation constraint, we use a smooth Heaviside function to blend the discontinuity of this original separation sensor to make it suitable for gradient-based optimization. The smooth Heaviside function is given as

$$\bar{X} = \frac{1}{1 + e^{2k(\cos\theta + \gamma)}}, \tag{7.3}$$

where k and γ are parameters that determine the sharpness of the transition and the shift of the function respectively. Next, the separation sensor is integrated over a defined region that we think the separation is likely to occur. We then normalize the integral by the reference area to yield the final separation constraint metric,

$$\bar{A}_{\text{sep}} = \frac{1}{2A_{\text{ref}}} \iint \bar{X} dA. \tag{7.4}$$

We exclude the leading edge part and the front portion of the intersection parts in the separation constraint integration because reverse flow can naturally occur at these regions and not necessarily indicate flow separation. The surface on which we apply the separation constraint is the light red surface shown above the foil surface in Figure 7.3b. Similar to the cavitation constraint, this separation metric is scaled by the target tolerance before providing it to the optimizer. For example, if we requires $\bar{A}_{\text{sep}} \leq 5 \times 10^{-4}$, then the constraint is,

$$\frac{\bar{A}_{\text{sep}}}{5 \times 10^{-4}} \leq 1. \tag{7.5}$$

7.2.6 Design conditions

We choose three flow conditions for optimizations, as shown in Table 7.2. For multipoint optimization problems, the operating probability weight of each condition is included in the last column in Table 7.2.

Table 7.2: Design conditions with a submergence depth of 0.4 m

Condition	U_∞	Re (10^6)	C_L	σ	Weight
1	18 m/s	2.0	0.2	0.6	15 %
2	14 m/s	1.6	0.3	1.0	60 %
3	11 m/s	1.3	0.5	1.5	25 %

The optimization problem is summarized in Table 7.3. For the baseline design, to match the target lift, we first solve an optimization problem with a C_L constraint with respect to a global twist variable (all sections follow the same change in twists). In subsequent studies, we initialize the optimization with all twists set to the corresponding angle, so the lift is matched at the initial point. Cavitation and separation constraints are enforced in each optimization case. For the multipoint optimization cases, separation constraint is only enforced at the highest C_L condition.

7.2.7 Optimization cases

We set up five different optimization cases to investigate the tradeoffs between delaying cavitation, reducing flow separation, and reducing drag, as well as how different shape variables interact to affect the flow and drag. The first two cases are single-point optimizations at $C_L = 0.2$ and $C_L = 0.3$ condition. We will refer to the single-point optimization at $C_L = 0.2$ as Single 1 and the one at $C_L = 0.3$ as Single 2. Afterward, we conduct three multipoint optimizations to investigate the importance of multipoint optimization, planform variables, and the detailed geometry design of the intersection shape. Table 7.4 summarizes all the optimization cases. Cases with "Multi" refer to multipoint optimizations. For all optimizations except for the Multi case, the shape variables at

Table 7.3: T-foil optimization problem description

		Description	Lower	Upper	Units	Quantity
Minimize	C_D	Drag coefficient (single-point)	-	-	-	
	$\sum \text{wt}_i \times \text{Drag}_i$	Weighted drag (multipoint)	-	-	-	
with respect to	s	Shape (FFD control points)	-0.05	0.05	m	180
		Twist	-10	10	[°]	8
	λ	Sweep	0	10	[°]	1
	c_{foil}	Foil chords	$0.5c_0$	$1.2c_0$	[m]	3
	c_{strut}	Strut chord	$0.5c_0$	$1.2c_0$	[m]	1
	r_{foil}	Foil rake (multipoint)	-5	5	[°]	2
	r_{strut}	Strut rake (multipoint)	-5	5	[°]	2
	$2b$	Span	$0.9b_0$	$2b_0$	[m]	1
		Total number of design variables (multipoint)				**198**
subject to	$C_L - C_L^*$	Lift coefficient (single-point)	0.0	0.0		1
		Lift coefficient (multipoint)	0.0	0.0		3
		Fixed leading edge and trailing edge				30
		Monotonic chord constraint				3
	$\bar{A}_{\text{cav}}$	Cavitation constraint (single-point)	-	1×10^{-3}		1
	$\bar{A}_{\text{cav}}$	Cavitation constraint (multipoint)	-	2×10^{-5}		3
	$\bar{A}_{\text{sep}}$	Separation constraint	-	5×10^{-4}		1
	t_{2D}	Thickness constraint	$0.6t_0$	-	m	42
	t_{1D}	Trailing edge thickness constraint	t_0	-	m	32
	S	Projected area constraint	$0.985S_0$	$1.015S_0$	m^2	1
		Chord consistency constraint				2
		Intersection twist difference constraint				3
		Symmetry shape constraint				84
		Total number of constraints (multipoint)				**204**

the intersection have restrictions that the top FFD control points only move up and the bottom FFD control points only move down to avoid colliding top and bottom surfaces. For the Multi NP case, no planform variable is considered.

Table 7.4: Optimization cases. Cases with *Single* refer to single-point optimizations. The inflow velocity and C_L used for each single-point optimization are listed in the Table. Cases with *Multi* refer to multipoint optimizations. For all optimizations except for the Multi case, the shape variables at the intersection have restrictions that the top FFD control points only move up and the bottom FFD control points only move down to avoid potential excessive thickness reduction at the intersection. For the Multi NP case, no planform variable is considered.

Cases	U_∞	C_L	σ	Note
Single 1	18 m/s	0.2	0.6	
Single 2	14 m/s	0.3	1.0	
Multi LS				Limited shape freedom at intersection
Multi NP				Limited shape freedom at intersection and no planform variables
Multi				With planform and more freedom on the intersection shape

7.3 Results

In this section, we first show the results of single-point optimization to demonstrate how operating conditions lead to different design considerations and affect the optimization. After showing the single-point optimization results, we show a multipoint optimization result to investigate how considering a range of operating conditions leads to a more reasonable design. We conduct two additional multipoint optimizations to further investigate how planform variables and the detailed geometry at the intersection influence the design.

For each result, we show the detailed geometry changes and the optimization results from different cases. We compare drag coefficient C_D, pressure coefficient (C_p) contours, separation regions, spanwise lift distributions, and structural performance between the baseline and the optimization results.

All optimizations converged to optimality of less than 7×10^{-4}. The optimized T-foils have lower drag, delay cavitation, and avoid separation compared to the NACA 0012 baseline T-foil.

7.3.1 Single-point optimizations

We first discuss two single optimization results at $C_L = 0.2$ and $C_L = 0.3$. Figure 7.8 shows the convergence histories of these two single-point optimizations. We show the planform shapes and the front views of the intersection region at selected iterations above the C_D histories to show how these shapes evolve during optimizations. As shown in Figures 7.8 and 7.9, these two optimized T-foil have different planforms, including sweep, chord, and span. The Single 1 case has a shortened span with a slightly backward sweep, while the Single 2 case has a longer span with no sweep (except for the initial leading edge sweep). Correspondingly, the Single 1 case has a wider chord distribution than the Single 2 case. Both optimizations increase the thickness near the intersection and introduce a fairing at the intersection to delay cavitation inception and avoid flow separation.

The span and chord are different mainly because the lift-induced drag occupies a larger proportion of the total drag at a higher C_L condition. A longer span and a shorter tip chord help to reduce the 3-D downwash effects and reduce the tip loading, which leads to lower lift-induced drag. On the other hand, as discussed by Bons et al. [149], a larger chord leads to a lower friction drag considering the same planform area and the same lift because of a higher local Re. Hence, the design can benefit more from a larger chord at a low C_L condition where the friction drag plays an important role.

The difference in sweep angles is mainly caused by the separation requirement. As discussed in the previous chapter, the backward sweep can help to improve cavitation and reduce the total drag. We observe the same total drag reduction in the Single 1 case, especially for iterations ranging from 40 to 60, as shown in the right enlarged optimization history in the middle of Figure 7.8. During this range, the sweep variable changes significantly; meanwhile, we observe a steady and slight decrease in C_D. When the sweep stops to vary, the slight decrease in C_D stalls. A backward

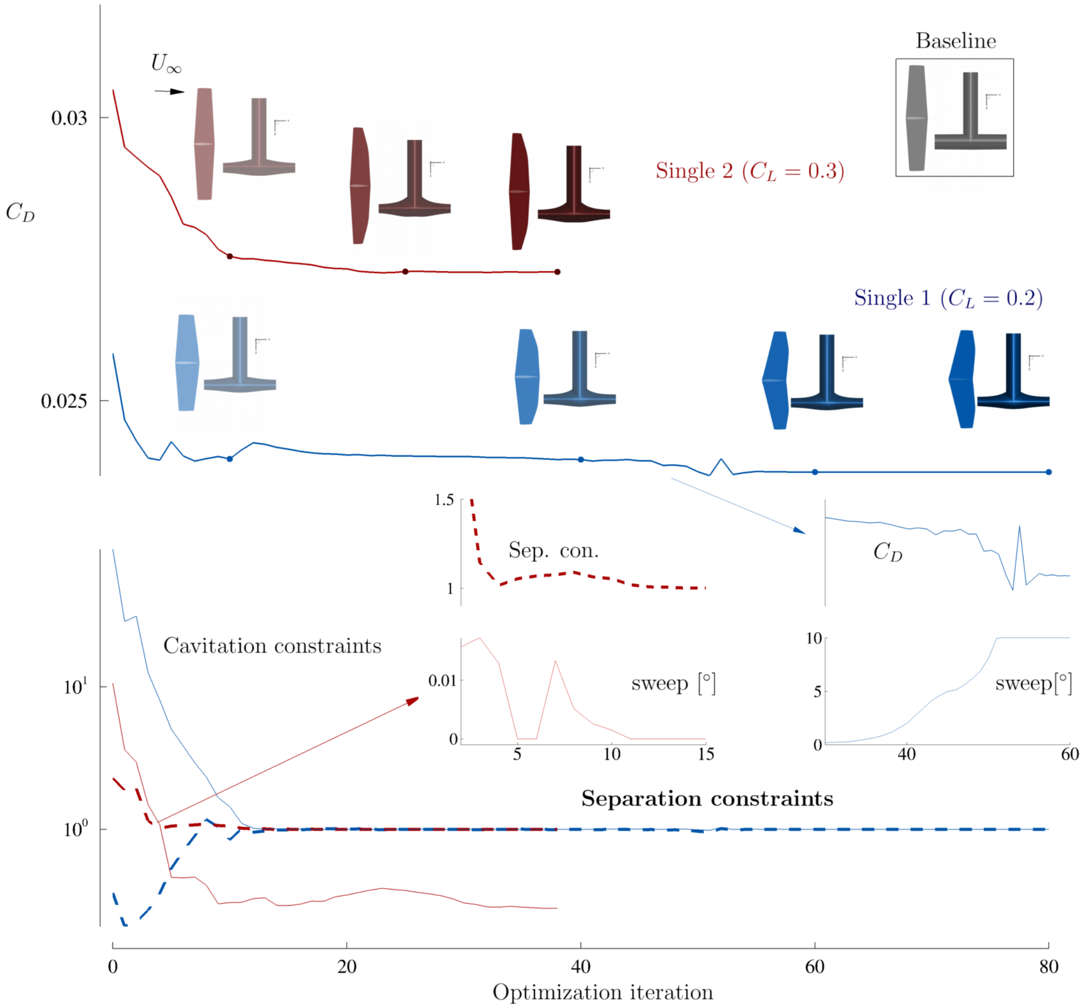

Figure 7.8: Optimization histories of single-point optimizations at $C_L = 0.2$ and $C_L = 0.3$. The planform shapes and the front view of the intersection region of the T-foil at selected iterations are shown above the iteration histories. At a lower C_L condition, the span tends to be shorter to reduce the friction drag. A longer span helps to reduce the lift-induced drag, which plays a more significant role at a higher C_L condition. The regions where the sweep changes significantly are enlarged and shown in the middle of this figure.

sweep also induces downwash on the inboard, which helps to reduce the loading at the intersection and hence delay cavitation and separation. The reason that the Single 2 case does not benefit from this backward sweep is that the separation constraint poses a limitation on the sweep variable and a longer span reduces the 3-D effects from the sweep. This separation constraint does not pose the same limitation to the Single 1 because at this low C_L condition the T-foil is not susceptible to separation, as shown by the low separation constraint value in the optimization history (Figure 7.8) and the rear view of the baseline T-foil (Figure 7.9). Looking at the convergence history of the case Single 2 in detail (left enlarged optimization history in the middle of Figure 7.8), during iterations ranging from 4 to 12 where the sweep moves backward, we observe an increase in the violation of the separation constraint. There are many ways that the sweep variable affects separation behavior, such as the sweep-induced upwash and downwash, and the spanwise flow modification. For our results, it is the backward sweep induced downwash at the root that makes the difference. As C_L increases, the lift-induced drag becomes more important, and having an elliptical lift distribution becomes more advantageous. Due to the presence of the strut, the middle of the T-foil hardly produces any lift. Sweeping the horizontal foil backward induces a downwash on the inboard, which further decreases the normalized lift at the middle, making the normalized lift distribution further away from the elliptical distribution at the intersection. Suppose we can compensate for the backward-sweep-induced lift loss at the intersection, maintain or achieve an optimal lift distribution with twist or camber, this requires a higher twist or camber at the intersection region, which increases the likelihood of separation because of the potential higher adverse pressure gradient. The spanwise flow modification might also play a role. A forward sweep can lead to a spanwise flow that moves from the tip to the root. This spanwise flow helps confine and rectify the flow at the intersection region, which helps to suppress separation.

We compare the two single-point optimization results in more detail in Figure 7.9. The yellow-brown shaded region indicates cavitation inception whereas the green-shaded region indicates flow separation. Similar to the message from the optimization histories, cavitation is a bigger issue at the $C_L = 0.2$ condition because of the lower σ at a higher speed. On the other hand, separation constraint is more important at the $C_L = 0.3$ condition with a higher σ, as shown in Figure 7.9. The cavitation inception is also evident from the sectional C_p curves at the bottom of Figure 7.9. If the C_p exceeds the gray dotted lines in the figures, cavitation occurs.

We observe different cross section shapes and sectional C_p distributions between these two single-point optimization results, as shown in Figure 7.9, As a result of the severe violation of cavitation constraint, the single-point optimization at $C_L = 0.2$ introduces a higher camber to the foil section to move the loading towards the trailing edge to remove the high suction peaks. On the other hand, the single-point optimization result at $C_L = 0.3$ has much less camber due to a milder violation of the cavitation constraint. The separation constraint also requires that the adverse pressure gradient cannot be too large near the trailing edge, preventing a high curvature near the trailing edge. The center of lift of the Single 1 case is more towards the trailing edge while that of the Single 2 case is more towards the leading edge.

Figure 7.10 compares the spanwise normalized lift, sectional drag coefficient C_d, sectional friction drag coefficient C_{dv}, twist, and chord distributions between the baseline and two single-point optimizations. The spanwise normalized lift distributions of the two single-point optimizations are similar, and both are closer to the elliptical distribution than the baseline. For both single-point optimization cases, the C_d near the intersection is lower than the baseline because of the reduced loading near the intersection. Comparing C_{dv} between the single-point optimization results, the C_{dv} increment from the baseline near the tip region is higher for the Single 2 case than the Single 1 case due to a shorter tip chord. Since the cavitation constraint drives the Single 1 case to increase camber, the twist is significantly reduced compared to the baseline. Near the intersection region, the twist is reduced to near zero. For the Single 2 case, because the cavitation constraint does not introduce camber as much as the Single 1 case, the twist decrease is less than the Single 1 case. The chord distribution is consistent with the observation from the planform shapes shown in the optimization convergence histories.

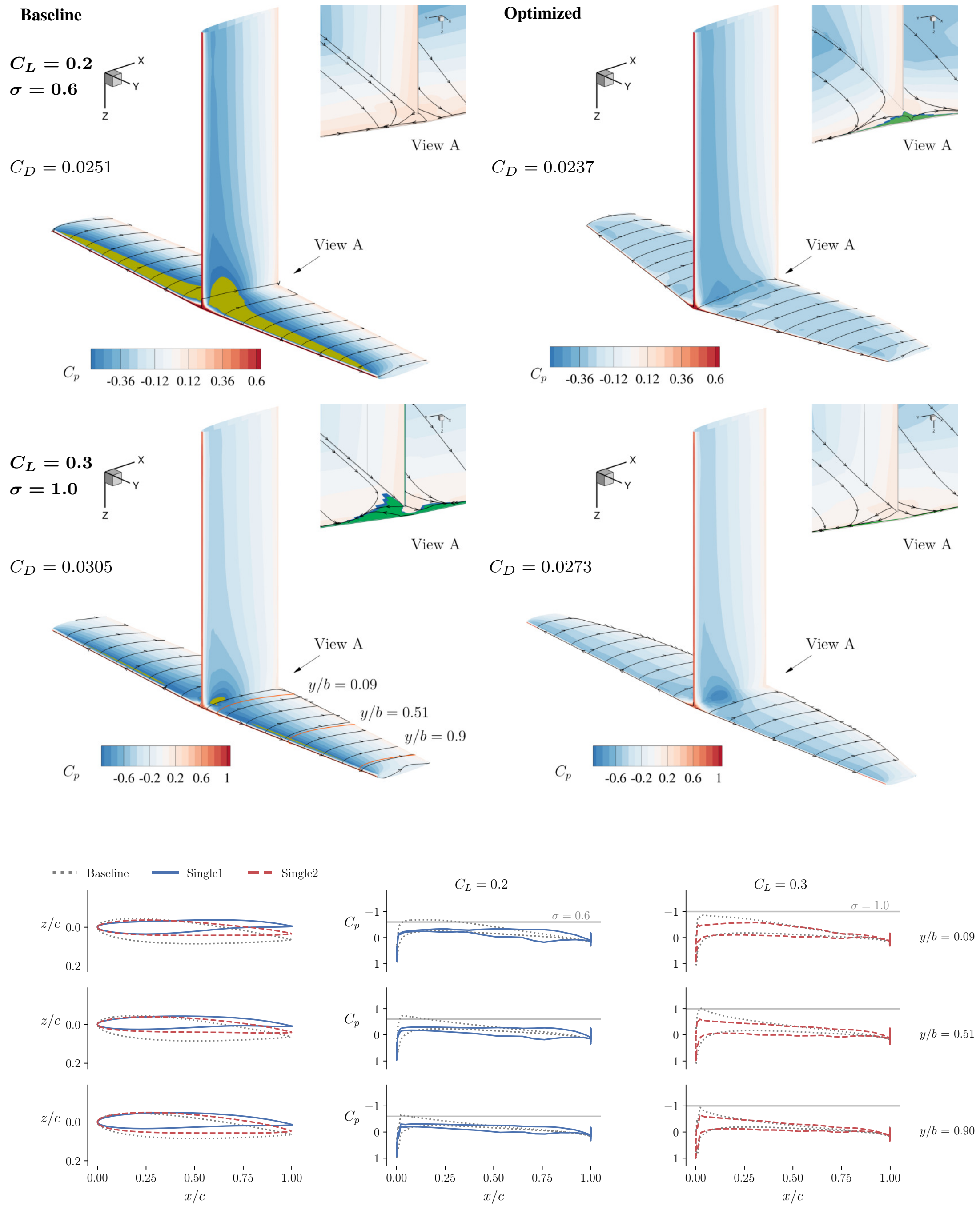

Figure 7.9: Comparison of surface pressure coefficient contours and cross-sectional shapes between the baseline and the single-point optimized T-foils. The yellow-brown region represents the area that is susceptible to cavitation. The green shade indicates separation occurrence. Single-point optimized T-foils are free of cavitation and separation at the corresponding design condition. The single-point optimizations reduce the drag by 5.6% ($C_L = 0.2$) and 10.5% ($C_L = 0.3$).

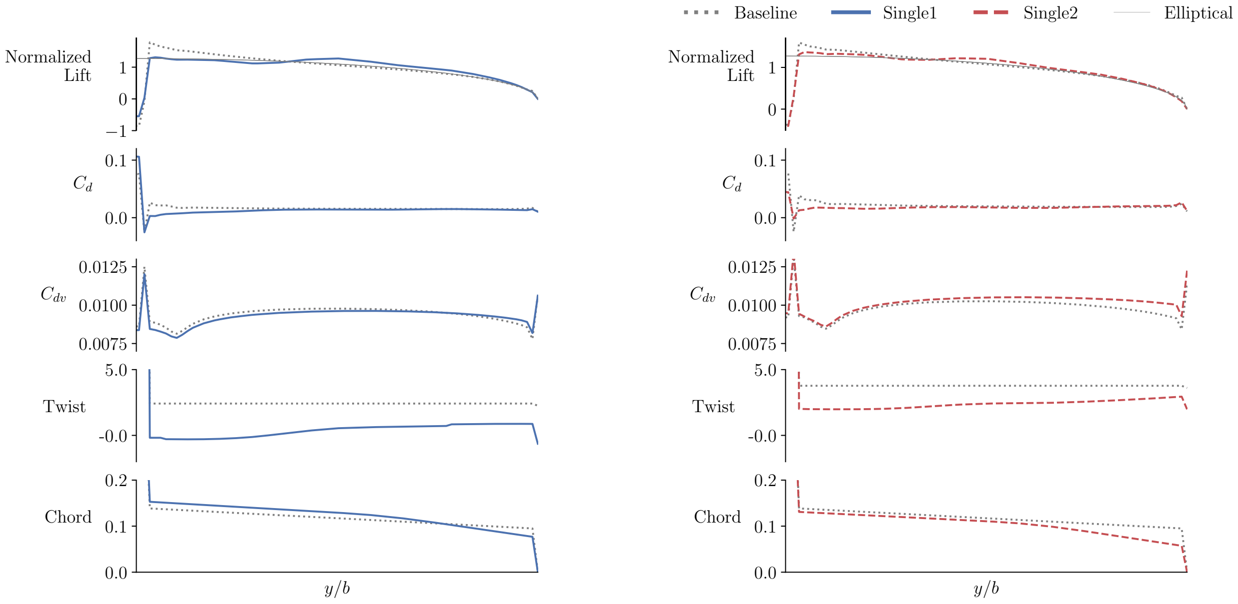

(a) $C_L = 0.2$

(b) $C_L = 0.3$

Figure 7.10: Spanwise normalized lift, sectional drag coefficient C_d, sectional friction drag coefficient C_{dv}, twist, and chord distributions of single-point T-foil optimizations.

7.3.2 Multipoint optimization

From the single-point optimization results, we have seen the different requirements at each condition lead to different and even opposite designs. To better resolve the design conflicts between conditions and balance the tradeoffs, it is necessary to conduct multipoint optimizations. In this section, we show a multipoint optimization result that has the same set of design variables as the previous single-point optimizations. We consider all three design conditions in this multipoint optimization. We only impose the separation constraint at the $C_L = 0.5$ condition because flow separation is most likely to occur at the highest C_L design condition. Although we have observed that the baseline also violates the separation constraint at $C_L = 0.3$ condition in the previous section, flow separation can be avoided at $C_L = 0.3$ if flow separation is avoided at a higher C_L condition.

We first show the optimization iterations in Figure 7.11. Similar to the single-point optimization results, the multipoint optimization creates fairing at the intersection to prevent the local low-pressure region. This multipoint optimization creates a planform that mixes the characteristics from each design condition. Compared to the single-point optimization at $C_L = 0.2$, this multipoint optimization has a longer span and a shorter tip chord due to the need to reduce the lift-induced drag at higher C_L conditions. Compared to $C_L = 0.3$ condition, the multipoint optimization has a slightly shorter span and a slightly large root chord as a compromise to the friction drag reduction at the $C_L = 0.2$ condition.

Figure 7.12 provides a more detailed comparison between the baseline and the multipoint optimized T-foil. Expectedly, the baseline experiences the most severe separation at the $C_L = 0.5$, as shown by the largest green-shaded region in Figure 7.12. We will also demonstrate the tradeoffs between design considerations at different design conditions and the optimization objectives by comparing the multipoint optimization to the single-point optimizations. As shown by the surface C_p contours and the streamlines, the multipoint optimized T-foil avoids separation and delays cavitation at all design conditions. The change of the sectional C_p follows a similar trend as the

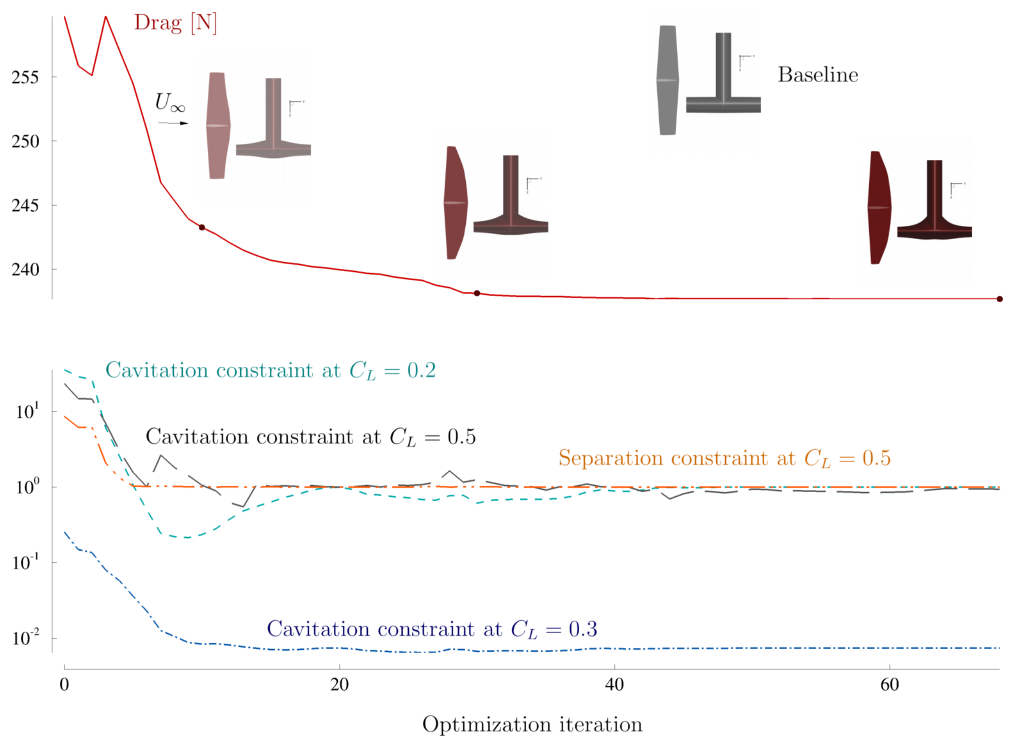

Figure 7.11: Optimization histories of the Multi LS optimization. The planform shapes and the front view of the intersection region of the T-foil at selected iterations are shown above the objective iteration history. The planform shape of the multipoint optimized T-foil is similar to the single-point optimization result at $C_L = 0.3$ condition because this condition has the highest operation probability. The total CPU time for the Multi LS optimization over the three C_L conditions is 4.7 days (108 cores, 3.0 GHz Intel Xeon Gold 6154).

single-point optimizations. The optimization moves the streamwise loading more towards the trailing edge to reduce the suction peaks. Although the multipoint optimized T-foil significantly delays cavitation compared to the baseline, there remains a cavitation-prone area near the intersection as shown by the yellow-brown shaded region in Figure 7.12. The multipoint optimization was not able to completely avoid cavitation because the separation constraint at $C_L = 0.5$ adds a restriction to the streamwise loading distribution. The separation constraint leads to a distinct characteristic of this multipoint optimized T-foil, a flat trailing edge curve near the intersection, as shown by the top-left plot among the sectional plots in Figure 7.12. This flat trailing edge decreases the adverse pressure gradient near the trailing edge to avoid separation. The sectional C_p curves near the intersection (first row of the sectional C_p plots) all exhibit an overlap between the suction-side C_p and pressure-side C_p at the trailing edge. Consequently, the multipoint optimization cannot move more loading towards the trailing edge as in the single-point optimizations.

The multipoint optimized T-foil achieves a weighted total drag reduction of 7.8% compared to the baseline over all three design conditions. Although the multipoint optimization result does not achieve the same cavitation performance at $C_L = 0.2$ as the single-point optimization, the drag of the multipoint optimized T-foil at $C_L = 0.2$ decreases by 1.7% compared to the corresponding single-point optimization. These opposite trends in the drag reduction and the cavitation performance at $C_L = 0.2$ between the multipoint optimization and the single-point optimization show the tradeoff between reducing drag and delaying cavitation. At nominal condition $C_L = 0.3$, the C_D increases by 3% compared to the single-point optimization result at $C_L = 0.3$ because of a higher lift-induced drag (the lower aspect ratio).

7.3.3 Comparison of different multipoint optimizations

To investigate how the planform variables and the detailed geometry design at the intersection benefit the design, we conduct two additional multipoint optimizations. The first has the same design variables as the previously shown multipoint optimization result but without planform vari-

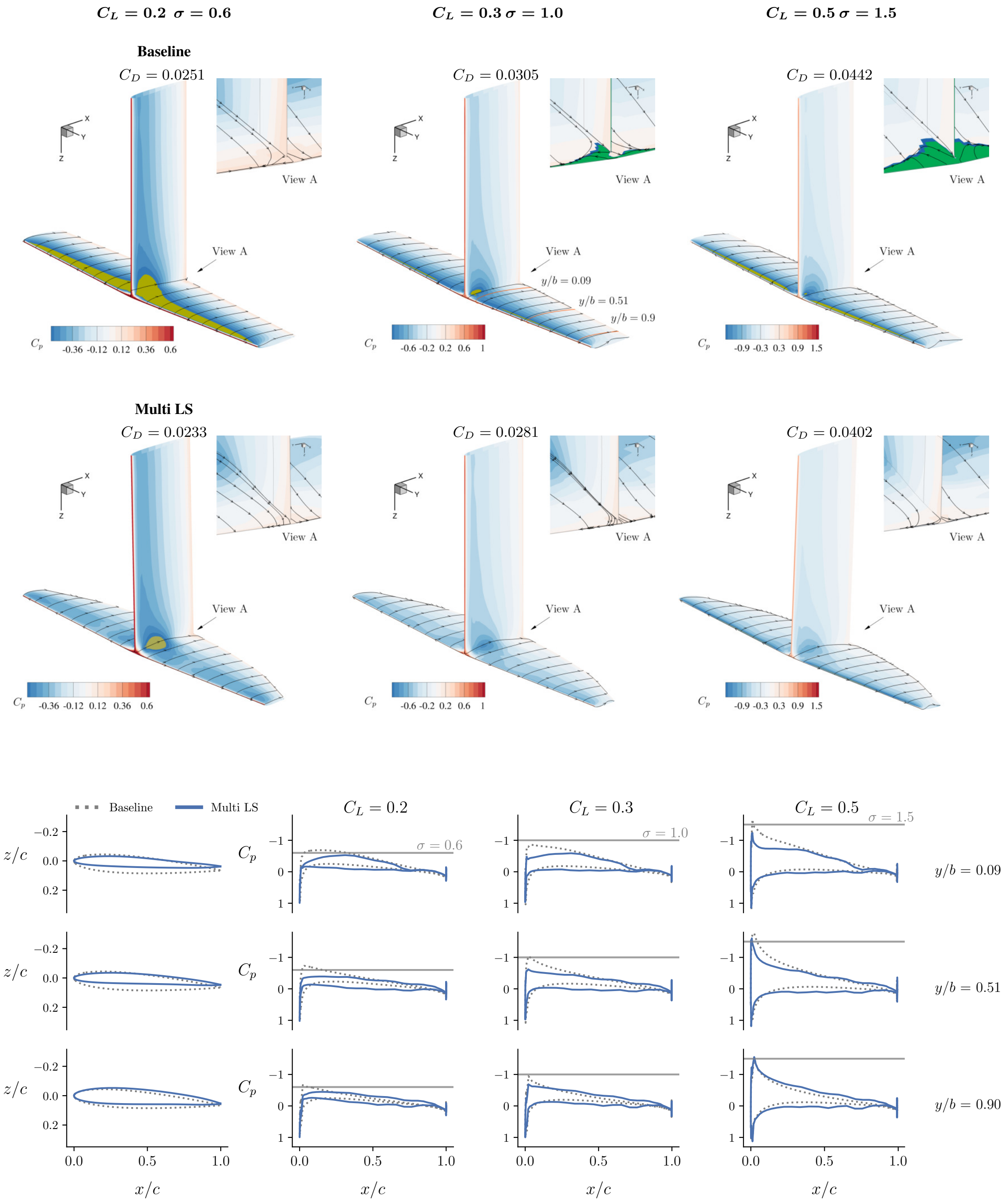

Figure 7.12: Comparison of surface pressure coefficient contours and cross-sectional shapes between the baseline and the multipoint optimized T-foils. The yellow-brown region represents the area that is susceptible to cavitation. The green shade indicates separation occurrence. Single-point optimized T-foils are free of cavitation and separation at the corresponding design condition. The multipoint optimization Multi LS reduces the drag by 7.2% ($C_L = 0.2$), 7.9% ($C_L = 0.3$) and 9% ($C_L = 0.5$). The Multi LS case flattens the trailing edge at the intersection to delay separation at the high C_L condition, as shown by the cross-sectional shape and pressure coefficient curves at $y/b = 0.09$.

ables. We will refer to this case as Multi NP (no planform). The second case has more freedom in changing the intersection shape compared to the multipoint optimization shown in the previous subsection. Specifically, the control points at the intersection are allowed to move both up and down, without the direction limitation based on their position on the FFD volume, and the foil planform is allowed to change. We will refer to this case as Multi. We first summarize all these multipoint optimization cases in Table 7.5 and compare the geometries of the baseline and multipoint optimization results in Figure 7.13. The surface C_p contours and streamlines comparisons are shown in Figure 7.14. Figure 7.15 compares the sectional shapes and C_p curves. Spanwise normalized lift distributions are shown in Figure 7.19.

Table 7.5: Summary of multipoint optimization cases. The planform variables are shown as the ratios relative to the baseline.

Cases	Total drag [N]	Δ total weighted drag	Foil drag [N]	Δ foil drag	Span	Root chord	Middle chord	Tip chord
Multi LS	238	7.8%	151	15.7%	1.03	1.06	0.98	0.5
Multi NP	253	1.6%	174	2.3%	-	-	-	-
Multi	243	6.1%	146	18.6%	1.05	1.08	0.92	0.65

The Multi NP and Multi cases have higher total weighted drag compared to the Multi LS case. Without planform variables and enough freedom on the intersection shape change, the Multi NP has the highest total drag. The Multi case has a similar planform shape as the Multi LS case. This Multi case has a slightly higher total drag compared to the Multi LS case as a result of a larger strut chord (foil root chord), as shown by Table 7.5 and Figure 7.13. As shown in Table 7.5, the Multi case achieves a higher foil drag reduction than the Multi LS case. One major contribution to this higher foil drag reduction is the reduced thickness near the intersection, as shown in Figure 7.13. In addition, with the greater ability to adjust the intersection shape, the Multi case is able to better leverage the camber effect to reduce drag at the outboard. This also suggests that if we allow changes of the strut planform and cross-section, we can achieve further improvements.

Figures 7.14 and 7.15 provide a more detailed comparison of how the cavitation and separation behaviors differ between cases. The Multi NP case avoids cavitation at the two higher C_L con-

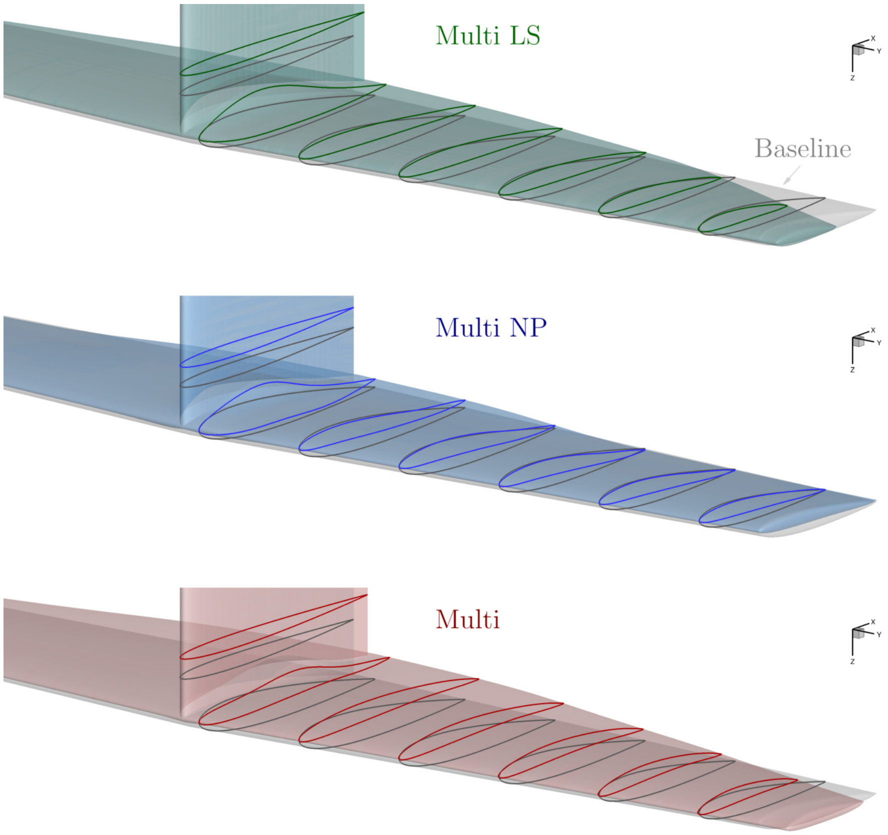

Figure 7.13: Detailed geometry comparison between multipoint optimization results. The light gray shape is the baseline geometry. Six slices are selected on the foil to show the cross-sectional shapes along the span. One slice is selected on the strut to show the strut chord change. To distinguish between the baseline and the optimized hydrofoil strut chord lengths, the selected slices on the strut are at different locations between the baseline and the optimized T-foils.

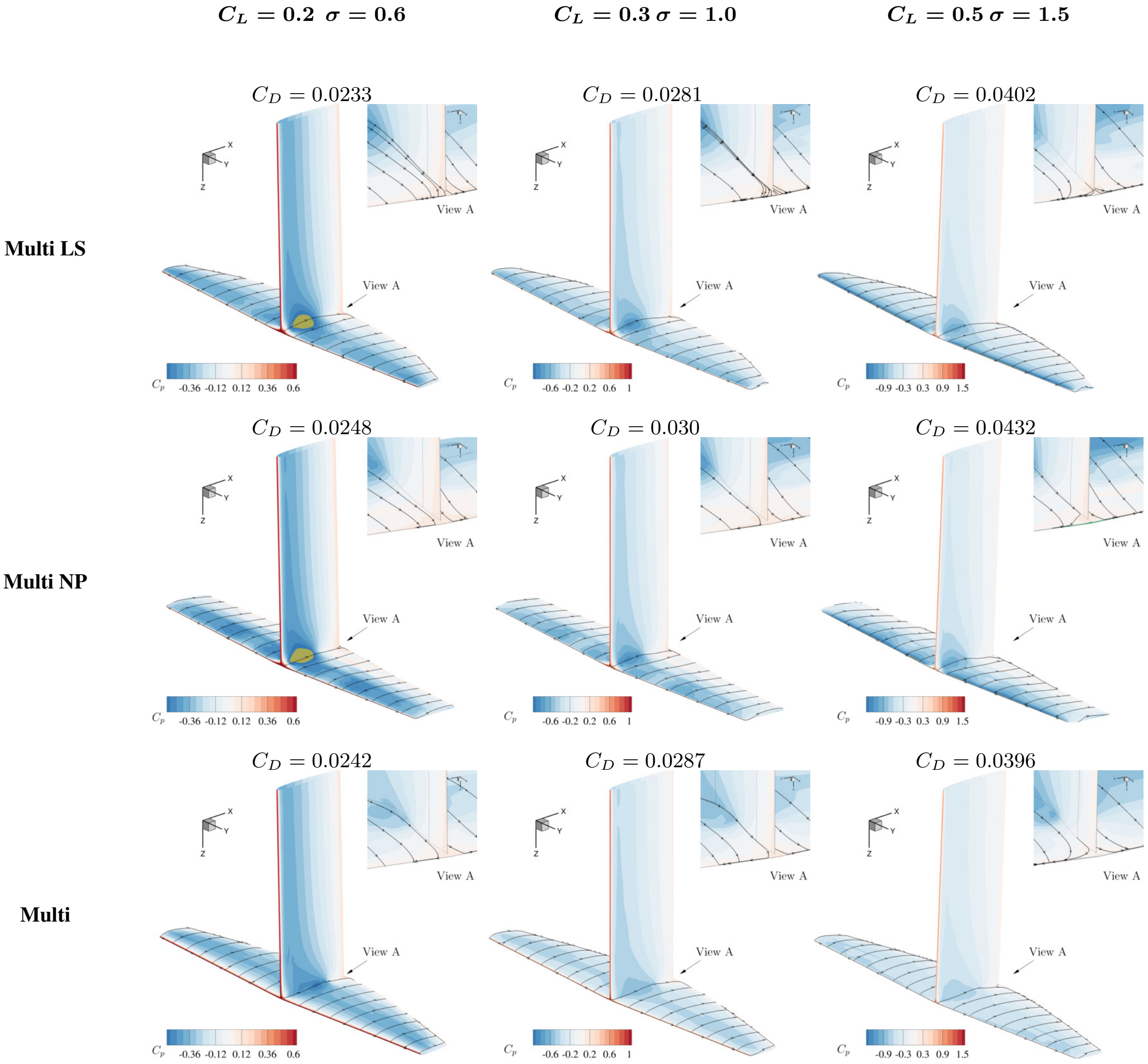

Figure 7.14: Comparison of surface pressure coefficient contours and streamlines between different multipoint optimized T-foils. The yellow-brown region represents the area that is susceptible to cavitation. The green shade indicates separation occurrence. The multipoint optimization Multi NP reduces the drag by 1.1% ($C_L = 0.2$), 1.4% ($C_L = 0.3$) and 2.3% ($C_L = 0.5$) compared to the baseline. With more freedom to design the intersection shape, the multipoint optimization *Multi* provides better cavitation performance. This case Multi reduces the drag by 3.8% ($C_L = 0.2$), 6% ($C_L = 0.3$) and 10.3% ($C_L = 0.5$) compared to the baseline.

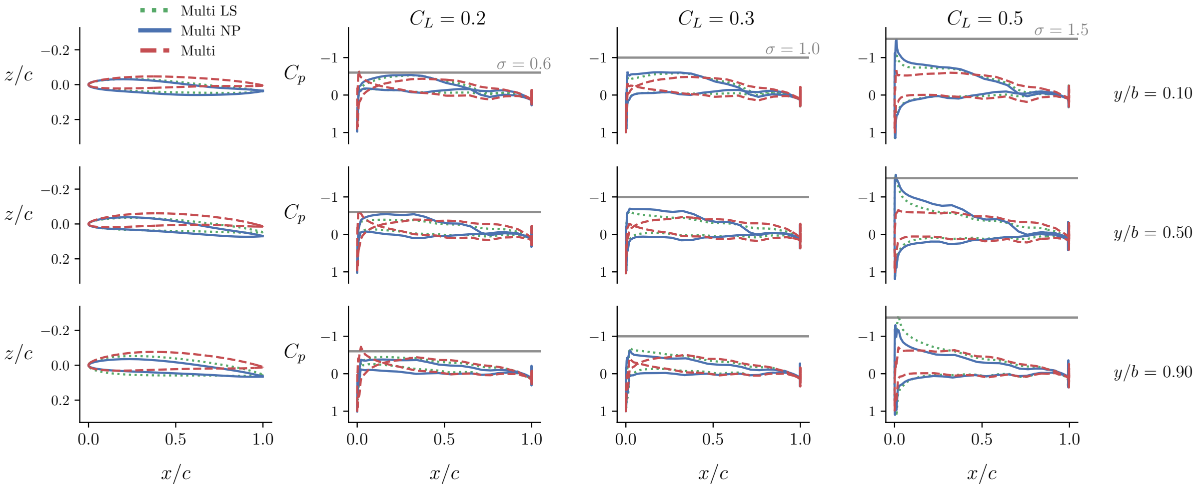

Figure 7.15: Comparison of cross-sectional shapes between different multipoint optimized T-foils. The Multi case has a higher camber across the span. With more freedom at the intersection shape, the Multi case can better utilize intersection shape change and camber to achieve optimal loading distribution to balance the cavitation requirements and the separation performance requirement at high C_L condition.

ditions while is still susceptible to cavitation at the intersection at C_L condition, the same as the Multi LS case. As shown in Figure 7.15, the cross section shapes and sectional C_p curves of the Multi NP case are similar to those of the Multi LS case. The C_p curves near the trailing edge at the inboard almost overlap as a result of avoiding separation. Despite this similar trend, we observe that for the Multi NP case, this C_p overlap near the trailing edge extends much further from the intersection compared to the Multi LS case, as shown by the discrepancy between the blue solid lines and the green dotted lines in the sectional C_p curves of the middle selected slices. The cross-sectional shapes in Figures 7.13 and 7.15 also show the Multi NP case has a flat trailing edge along almost the whole span. Without planform variables, satisfying separation constraint requires a near-zero loading near the trailing edge even at positions away from the intersection, suggesting that planform variables contribute to eliminating separation.

When allowing more freedom on the intersection shape change, the Multi case is able to avoid cavitation at the intersection although it has slight leading edge cavitation at outboard sections. The cavitation constraint tolerance that we chose allows the Multi case to have this minor leading edge cavitation at outboard when the intersection cavitation is completely removed. On the other hand, because the intersection cavitation is not avoided in the Multi LS and Multi NP cases, these two optimizations have to avoid any cavitation away from the intersection to satisfy the cavitation constraint tolerance. Allowing detailed geometry manipulation not only benefits cavitation performance, but also separation performance. Unlike the Multi LS and Multi NP cases, the Multi case does not exhibit zero loadings over a significant portion near the trailing edge but can still avoid separation. This behavior is attributed to the ability to achieve an optimal camber (shape) at the intersection and thus an optimal streamwise loading distribution. Not having to sustain zero loading near the trailing edge, the Multi case can move more loading aft and achieve a much higher cavitation inception speed. As shown in Figure 7.15, the Multi case has a much lower $-C_{p_{\min}}$ (suction peak) compared to the Multi LS and Multi NP cases. Again, allowing the strut planform and cross-sectional geometries to change might also help avoid the cavitation at the junction.

To evaluate the cavitation performance in a wider range, we plot cavitation inception speeds versus allowable loadings for all three multipoint optimization cases in Figure 7.16. We run analyses for the optimized hydrofoils with the nominal inflow velocity and then extract the $C_{p_{\min}}$ from the solution to inversely calculate the cavitation inception speed. With the cavitation inception speeds, we use the generated C_L to compute the loadings. The tips and the trailing edge were excluded when extracting the $C_{p_{\min}}$ to avoid the artificial extreme values caused by the grid. As shown in Figure 7.16, the Multi LS and Multi NP cases have similar dimensional cavitation buckets. The Multi case can carry higher loadings than the other two optimized T-foils at the same cavitation number. Note that we focus on the positive lift range, so the optimized T-foils exhibit better performance at positive loading range, while the cavitation performance substantially degrades when operating towards zero or negative lift range and even become worse than the baseline. Figure 7.17 shows the sectional C_p curves that correspond to the data points shown in Figure 7.16. At lower α, the three cases have similar C_p ranges, so the difference in cavitation inception speeds is mainly caused by the cavitation at the junction. At high α, the Multi case has higher cavitation inception speeds because of lower suction peaks.

Similarly, to compare the efficiency across a wider range, we plot the C_L versus C_D, as shown in Figure 7.18. Similar to the observation in Figure 7.14, the Multi NP has the highest drag over nearly the entire positive lift range. The Multi LS case has a lower total drag over the design range compared to the Multi case. This is mainly because the Multi LS case has a shorter root chord and strut chord. When the lift increases to sufficiently high that the lift-induced drag of the foil becomes dominant, the Multi case exhibits lower total drag compared to the Multi case.

Next, we compare the spanwise normalized lift, C_d, C_{dv}, twist, and chord distributions between multipoint optimizations in Figure 7.19. The Multi LS and Multi cases have similar normalized lift distributions and both are closer to the elliptical distribution than the Multi NP case. Hence, both optimization cases with planform variables achieve a lower lift-induced drag than the Multi NP case. The spanwise normalized lift distribution of the Multi NP case is wavy because the

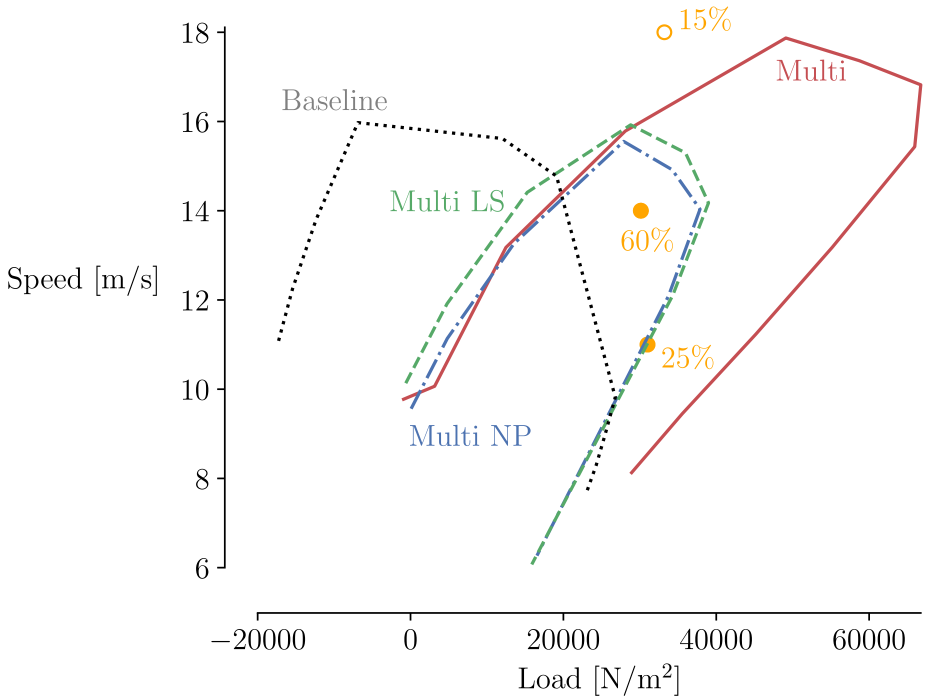

Figure 7.16: At a similar cavitation inception speed, the Multi case can carry higher loadings than the other multipoint optimized T-foils at the design condition range. The orange symbols represent the design conditions. The probability of operation of each design condition is listed next to the corresponding symbol.

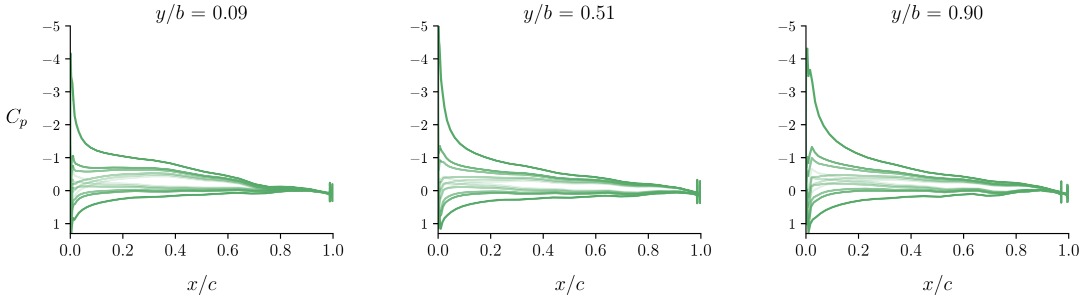

(a) Multi LS

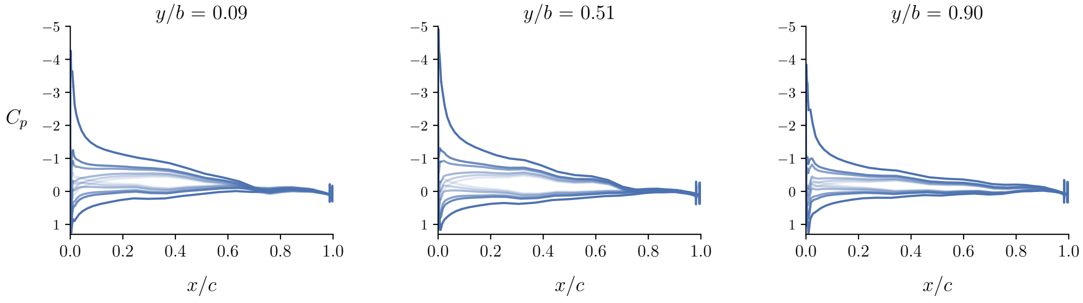

(b) Multi NP

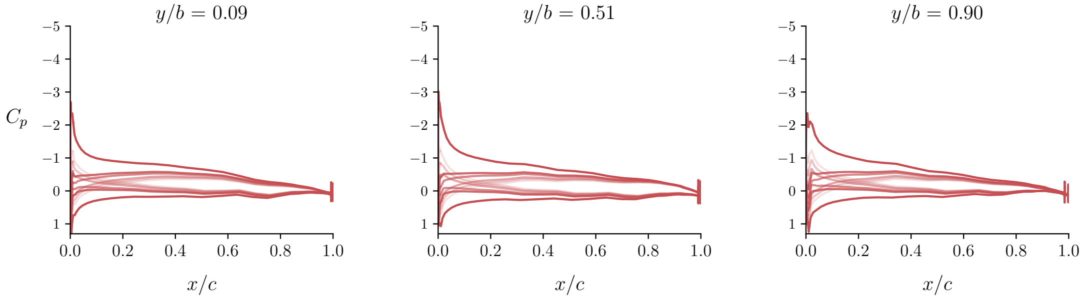

(c) Multi

Figure 7.17: Sectional C_p curves at with different α ranging from $-4°$ to $4°$. The line darkness increases with α. During the design condition range, the cavitation inception speeds of the Multi LS and Multi NP cases are mainly limited by the cavitation at the junction. At high α, the Multi case has lower suction peaks.

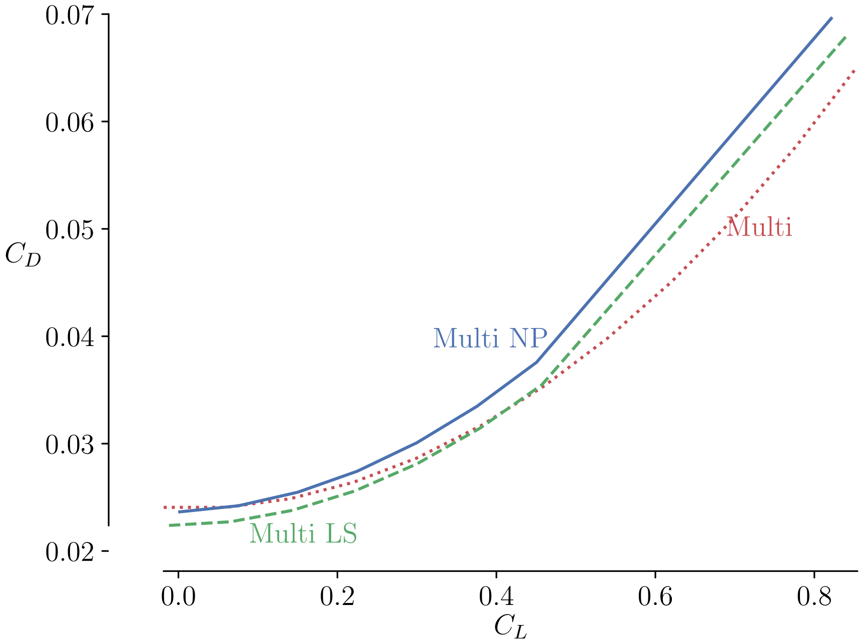

Figure 7.18: Lift-drag polars for multipoint optimized hydrofoils at the nominal inflow condition. The Multi LS has lower drag within the design range mainly because a shorter strut chord compared to the Multi case. When the C_L increases to sufficiently high, the Multi case outperforms the Multi LS case in terms of drag.

requirement of reducing loading near the intersection leads to a sudden variation in the loading distribution. Without planform variables and enough freedom to optimize the intersection shape, the optimization has to reduce the loading to delay cavitation and separation for the Multi NP case. From the C_d distribution, although the C_d of the Multi LS and Multi cases is higher than the Multi NP case on average, they still achieve a lower total drag because of reduced chord lengths. Similar to the spanwise C_{dv} distributions of single-point optimization results, the C_{dv} value is higher when the chord length is shorter.

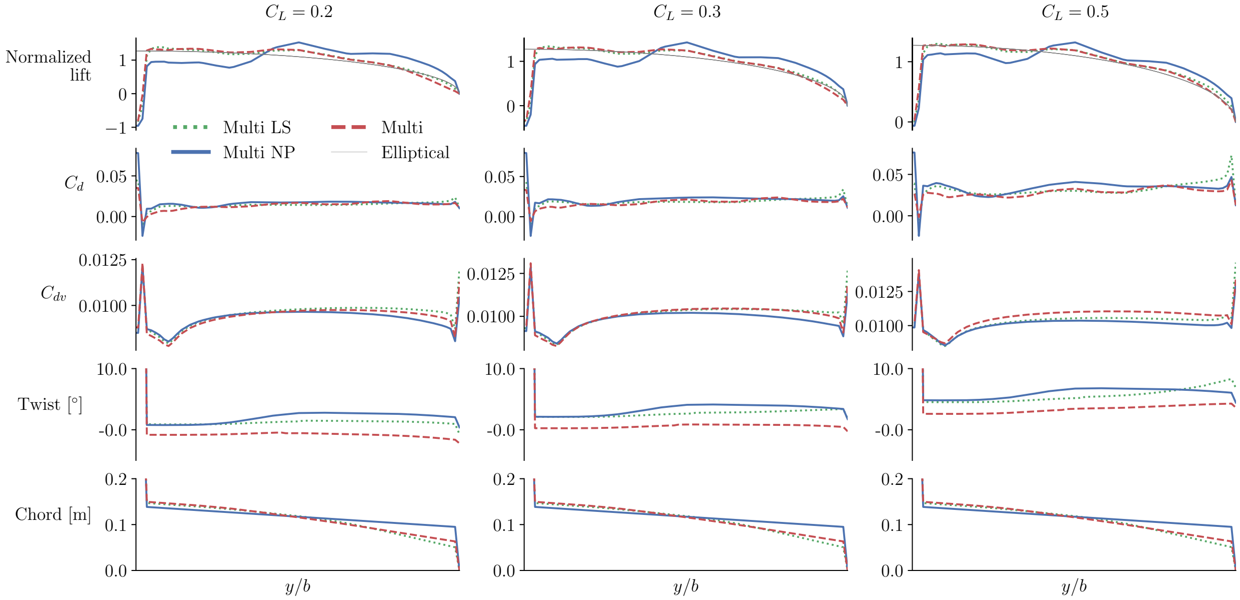

Figure 7.19: Spanwise normalized lift, C_d, C_{dv}, twist, and chord distributions of multipoint T-foil optimizations at design conditions.

Since the optimizations are conducted using the coarse mesh for efficiency, we evaluate the optimized designs and the baseline using the fine mesh. Figure 7.20 compares the cavitation loading buckets and Figure 7.21 compares the drag polars. As shown in Figure 7.20, when evaluating with the fine mesh, the cavitation performance is similar to the results with the coarse mesh. Although the optimized T-foils have higher cavitation inception speeds during the design condition range and higher lift range, the baseline T-foil has higher cavitation inception speeds around zero loading and negative lift ranges. As we discussed in Chapter 4, finding a design that can apply to all conditions is difficult due to various tradeoffs, so the optimal one should be selected based on the actual operating conditions. The comparison of the drag polar shown in Figure 7.21 shows the lift-drag relation follows the same trend as the results from the coarse mesh. The drag polar curves of the fine mesh are offset from the coarse mesh results. The optimized T-foils still have lower drag than the baseline during the design condition range when evaluating with the fine mesh. As shown by Figure 7.22, the optimized T-foils still show reduced separation compared to the baseline when being evaluated with the fine mesh. The relative performance in terms of drag is maintained between these T-foils compared to the coarse mesh results, demonstrating the validness of using the coarse mesh in the optimizations.

7.3.4 Structural performance of the optimized T-foils

Since we only consider hydrodynamic performance in the optimization, we perform hydrostructural analyses of the multipoint optimization results at the nominal condition $C_L = 0.3$ to see how the optimized T-foils will perform structurally and if they are practical in terms of structural behaviors. We extract the geometries from the hydrodynamic optimization results and create structural meshes using the geometries. The structural material is aluminum alloy 6061. The properties are listed in Table 5.1. Figure 7.23 shows the non-dimensional von Mises f contours of the baseline and the optimized T-foils, including both the undeformed and deformed shapes. The maximum failure indicator f_{max}, nondimensional tip deflection (by submergence depth h), and the tip twist θ_{tip} are listed in the figure captions. The x-sectional shape of the maximum stress position is extracted and shown behind the T-foil as a 2-D gray shape. All optimized T-foils have a higher f_{max} and higher deformations than the baseline because of the thickness reduction. The Multi case has a nose-down tip twist because its center of pressure is located more towards the trailing edge compared to the other cases, as shown in Figure 7.15. As shown in Figure 7.23, the f_{max} locations of the optimized T-foils correspond to the minimum thickness location in the x-sectional shape

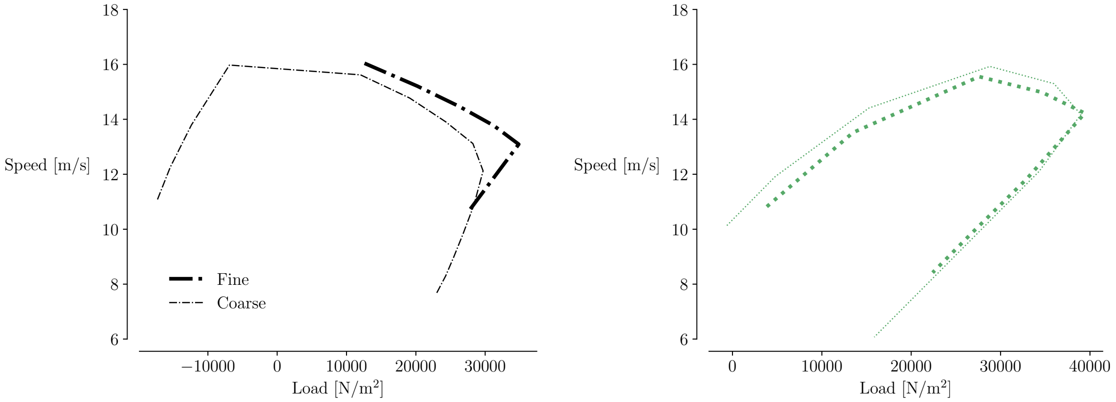

(a) Baseline

(b) Multi LS

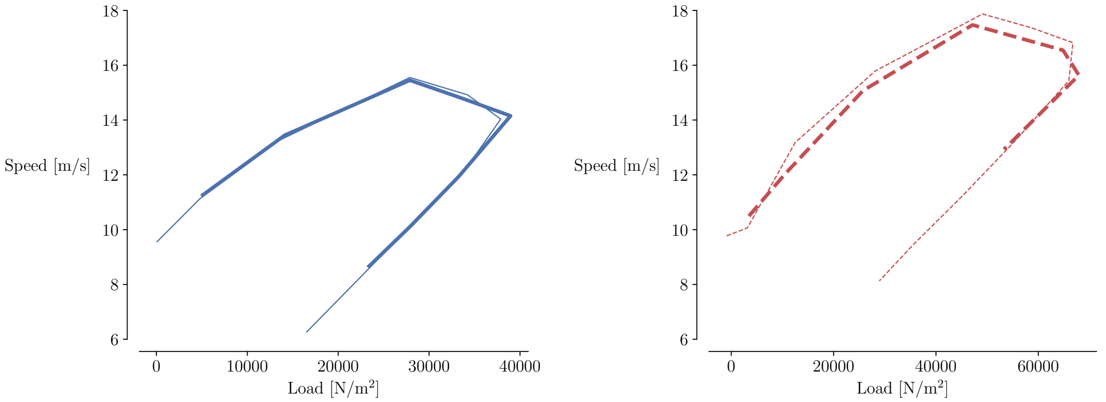

(c) Multi NP

(d) Multi

Figure 7.20: Cavitation bucket comparison between the coarse mesh and the fine mesh.

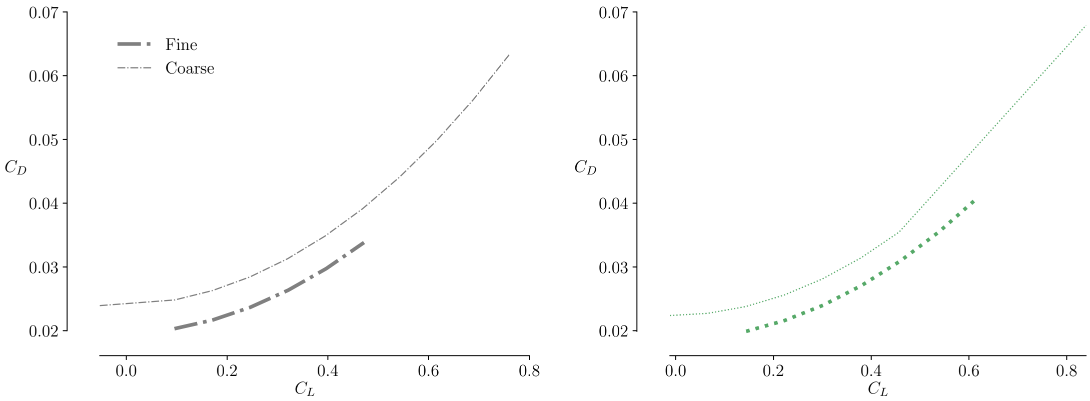

(a) Baseline (b) Multi LS

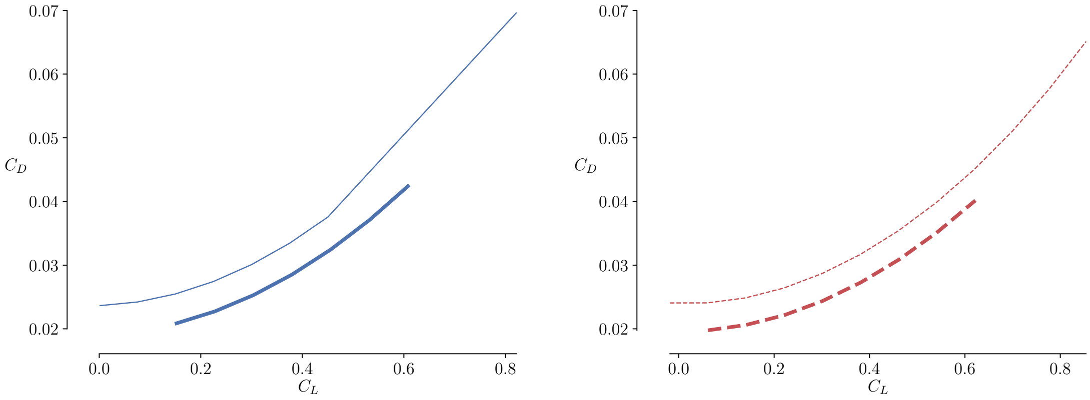

(c) Multi NP (d) Multi

Figure 7.21: Drag polar comparison between the coarse mesh and the fine mesh.

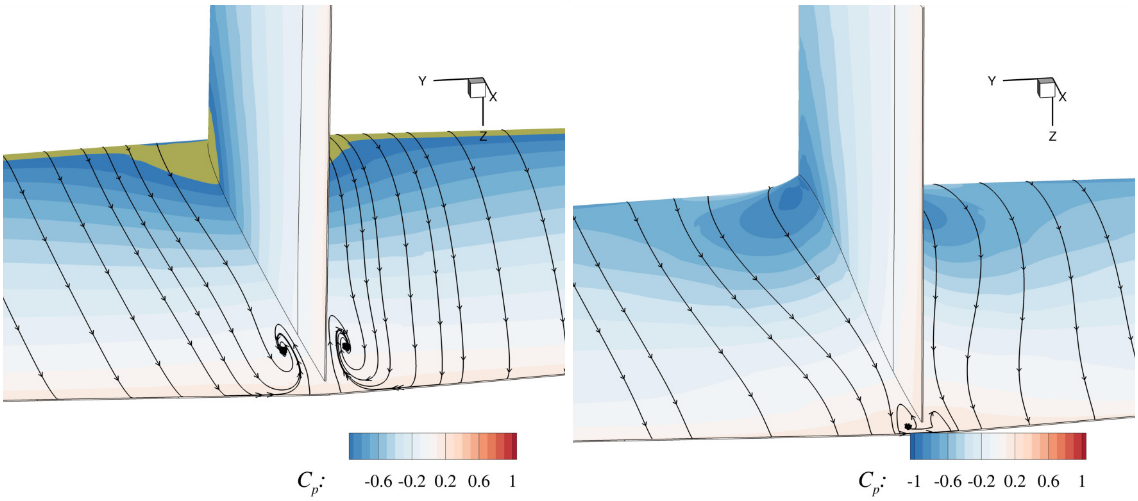

(a) Baseline

(b) Multi LS

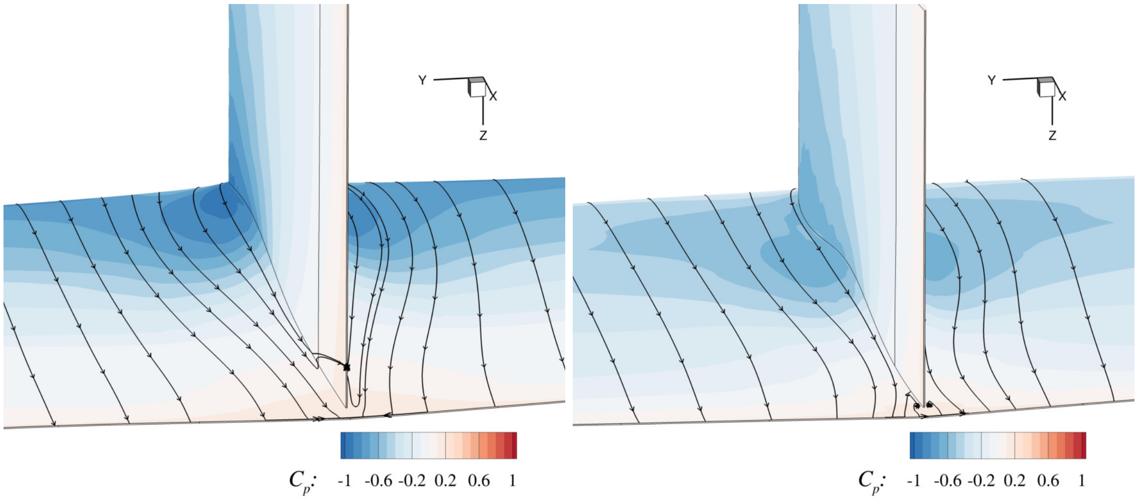

(c) Multi NP

(d) Multi

Figure 7.22: Flow streamlines at the intersection of the fine mesh analyses at $C_L \approx 0.38$ (rear view). The optimized T-foils still show reduced separation compared to the baseline when being evaluated with the fine mesh. The yellow-brown region represents the area that is susceptible to cavitation.

shown behind the T-foil. Although f_{max} increase for all optimized T-foils, the stress at the intersection is decreased compared to the baseline as a result of the thickness increase at the junction and the junction faring. The Multi NP case has a thicker fairing at the intersection but a higher f_{max} than the Multi case because the center of lift locates more towards the tip for the Multi NP case, as shown previously in Figure 7.19. As shown by Figure 7.23, the f_{max} does not exceed one, which means that the optimized T-foils do not experience structural failure if considering the yield strength and no safety factor. However, cyclic loadings and load fluctuations are common for marine structures. This highlights the need to consider fatigue performance during design. These hydrodynamic-optimized T-foils do not satisfy the fatigue strength requirement if they are constructed with aluminum alloy 6061. The higher δ_{tip} of the optimized T-foils suggest accelerated fatigue compared to the baseline because excessive tip deformation can indicate severe vibration issues. The Multi case experiences a negative tip twist because the center of pressure is more towards the trailing edge compared to the other two cases.

We also analyze the modes of the baseline and the multipoint optimized T-foils to access their dynamic performance. Figure 7.24 compares the first four modes of the baseline and the multipoint optimized T-foils. The mode shapes of the T-foils are governed by the basic configuration, so these four mode shapes are similar between the T-foils. The first three modes are governed by the strut, so the in-air natural frequencies of these three modes do not vary significantly between the baseline and the optimized T-foils. The first modes of the optimized T-foils have slightly higher natural frequencies than the baseline because of the increased strut bending stiffness due to a longer strut chord, decreased moment of inertia relative to the strut root due to a foil mass reduction, or both. Similarly, the second modes of the optimized T-foil have higher natural frequencies than the baseline. The third modes are a x-axis rotation mode about the intersection. The third mode in-air natural frequencies of the optimized T-foils remain approximately the same as the baseline because the relative change of the stiffness and moment of inertia is small. For higher modes where the horizontal foil governs, such as the fourth mode, the difference is more prominent. The

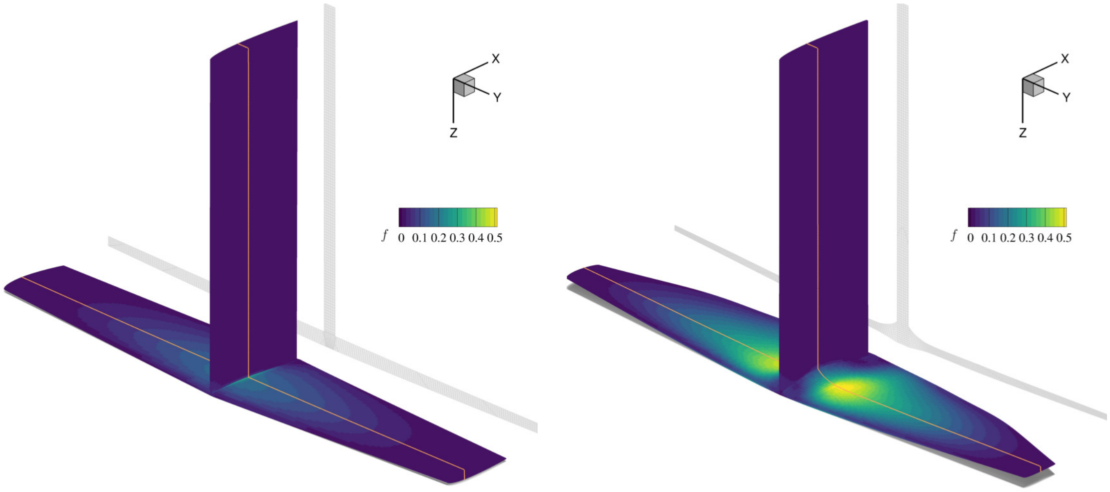

(a) Baseline
$f_{\text{max}} = 0.37$
$\delta_{\text{tip}}/h = 0.01$
$\theta_{\text{tip}} = 0.06^\circ$

(b) Multi LS
$f_{\text{max}} = 0.52$
$\delta_{\text{tip}}/h = 0.031$
$\theta_{\text{tip}} = 0.13^\circ$

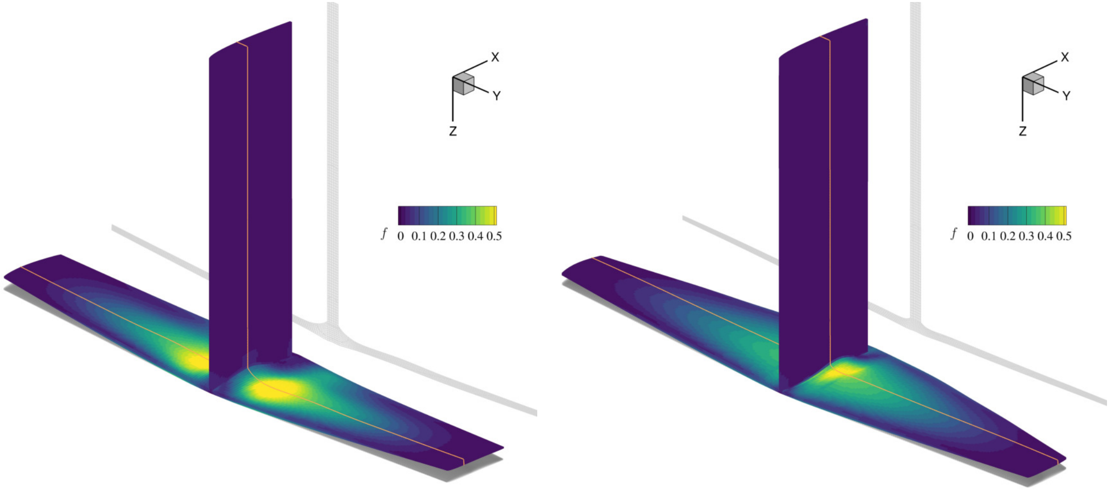

(c) Multi NP
$f_{\text{max}} = 0.62$
$\delta_{\text{tip}}/h = 0.0.035$
$\theta_{\text{tip}} = 0.15^\circ$

(d) Multi
$f_{\text{max}} = 0.54$
$\delta_{\text{tip}}/h = 0.030$
$\theta_{\text{tip}} = -0.16^\circ$

Figure 7.23: Nondimensional von Mises stress (by yield strength) comparison between the baseline and the multipoint optimized T-foils at nominal $C_L = 0.3$ condition. The undeformed shape is shown in gray. The optimized hydrofoils have higher stresses slightly away from the vertical mid-plane due to the reduced thickness. This thickness reduction can be observed in the chordwise slice projection shown behind the T-foil in the gray shape. Despite this higher maximum stress, the optimized hydrofoil has a less stress concentration at the intersection because of the increased thickness and smoother transition at the junction.

optimized T-foils have much lower natural frequencies than the baseline because of the reduced foil thickness. The smaller gaps between higher modes of the optimized T-foils might cause the optimized T-foils to be more susceptible to frequency coalescence in water. This in-water mode coalescence is more likely between the second and the third mode because the motion dependant added mass effect causes a more significant reduction for the third modal frequencies than the second modal frequencies, which further decreases the gap.

7.4 Conclusions

In this chapter, we develop methods to optimize hydrodynamic lifting surfaces with the ability to manipulate detailed geometry at the intersection. This is the first step towards designing more complex hydrodynamic configurations. We conduct hydrodynamic optimizations of a canonical T-shaped hydrofoil-strut system with high-fidelity RANS simulations and considering a large number of design variables (198). This T-shaped hydrofoil-strut system consists of a vertical strut and a horizontal foil, both contributing to the total drag of the system. We performed two single-point optimizations and three multipoint optimizations. The two single-point optimizations are at $C_L = 0.2$ and $C_L = 0.3$ conditions. The single-point optimization results show how each design condition and its design considerations affect the design. The single-point optimization result at $C_L = 0.2$ achieves a total drag reduction of 5.6% and the one at $C_L = 0.3$ achieves a total drag reduction of 10.5%. While the single-point optimization at $C_L = 0.2$ shows that a backward sweep can contribute to drag reduction, the optimization result at $C_L = 0.3$ shows that a backward sweep might not help avoid separation. Since the percentages of different drag components vary between design conditions, the objective of reducing drag can lead to different shapes for each design condition. These single-point optimization results highlight the need for multipoint optimizations.

Starting from the single-point optimizations, we performed multipoint optimizations. By conducting these different optimization studies, we investigated how planform shape and intersection

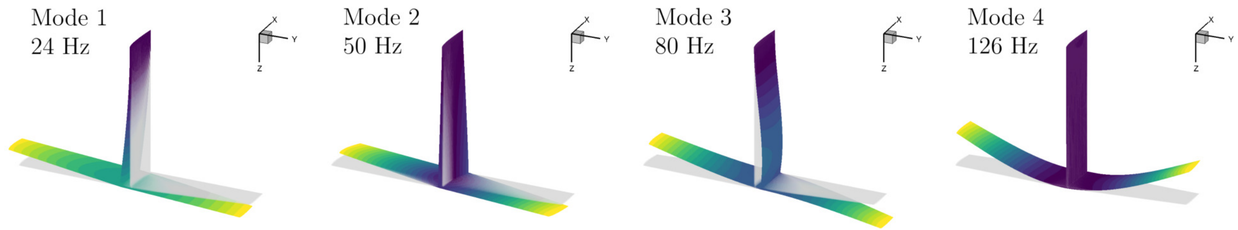

(a) Baseline

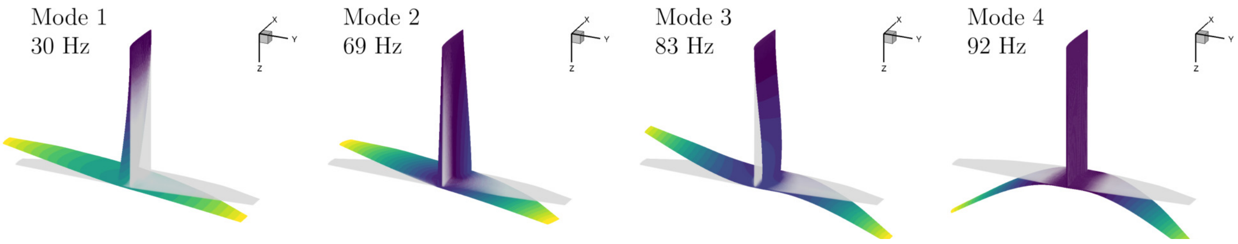

(b) Multi LS

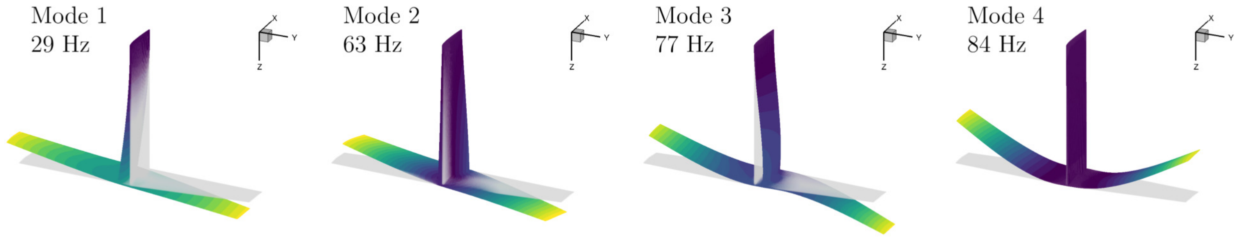

(c) Multi NP

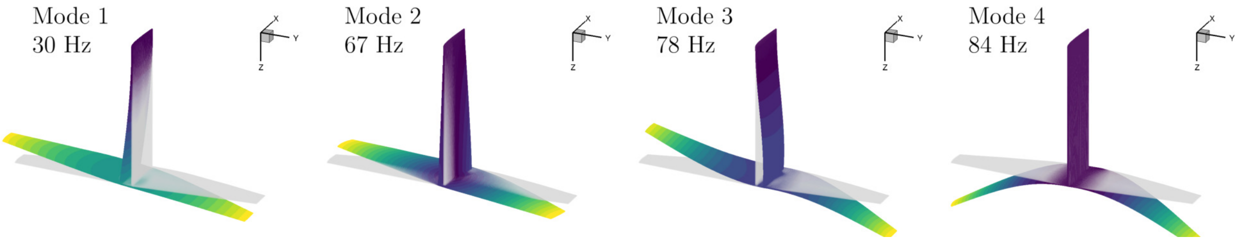

(d) Multi

Figure 7.24: First four mode shapes comparison between the baseline and the multipoint optimized T-foil at nominal $C_L = 0.3$ condition. These mode shapes of the T-foils are governed by the basic configuration, so the first four mode shapes of optimized T-foils are similar to the baseline T-foil. The first three modes are governed by the strut, so the in-air natural frequencies of these three modes do not vary significantly between the baseline and the optimized T-foils. For higher modes where the horizontal foil governs, such as the fourth mode, the difference is more prominent. Due to the reduced thickness, the fourth mode of the optimized T-foils have much lower in-air natural frequencies than the baseline. The smaller gap between higher modes of the optimized T-foils might cause the optimized T-foils to be more susceptible to frequency coalescence in water.

shape impact the performance and showed the importance of considering a large number of design variables (198) and intersection design when designing a complex system. We also investigated the tradeoffs between delaying cavitation and reducing drag at high lift conditions. In the first case, we consider planform variables but limit the freedom of the intersection shape. In the second case, there is no planform variable and the intersection shape change is also limited. In the third case, we consider planform variables and no limitation on the intersection geometry change. All multipoint optimizations created a fairing to delay cavitation at the intersection.

With planform variables and more freedom on the intersection shape design, the third multipoint optimization case achieves a total drag reduction of 6.1% and a foil drag reduction of 18.6%. Not only does not this case achieve the highest foil drag reduction among all the multipoint optimizations, but it also delays cavitation most effectively. This case completely removes intersection cavitation at $C_L = 0.2$ condition, and significantly increases the cavitation inception speed at the highest C_L condition (0.5). Since we mainly optimize the shape of the horizontal foil and the junction, the strut geometry is not optimal. Further drag reduction and cavitation delay can be achieved by allowing more strut geometric variables to change, such as the cross-sectional shape. The comparison between these three multipoint optimizations shows that the detailed geometry design of the intersection can significantly improve the performance. The methods used are useful for designing next-generation complex hydrodynamic lifting surface systems. The optimization studies and discussions can help to understand the physics of a T-shaped hydrofoil-strut system and provide valuable insights for designers.

The comparison between the optimized results with the coarsen mesh and the fine mesh shows that the cavitation performance is similar between using the coarse mesh and the fine mesh. Additionally, the drag polars of the coarse mesh follow similar trends with the finer mesh, demonstrating that the coarse mesh can be used in optimization even with complex geometry such as the T-foil with the complex junction.

However, we observe from the hydrostructural analyses that these hydrodynamic-optimized T-foils can experience higher deformation and structural failure, suggesting accelerated fatigue. This highlights the need to consider hydrostructural responses for T-foil and more complicated designs. Additionally, the modal analysis results suggest that the optimized T-foils might be susceptible to instabilities caused by frequency coalescence in water because the reduced foil thickness significantly decreases the frequency gaps between the second mode and third mode, as well as between third mode and fourth mode. This modal analysis comparison suggests that dynamic response prediction can be critical for designs of this type of system.

CHAPTER 8

High-speed free-surface boundary condition

We have used design optimization to delay cavitation and separation for hydrodynamic lifting surfaces. Another complex feature that is unique for marine structures is free surface wave effects. Free surface waves are not the only type of waves that exists in marine environments, but it is the one that concerns naval architects and offshore engineers the most [36]. Additional types of waves include inertial waves (tides) and internal waves. In this chapter, we focus on the linearized free surface conditions because we are interested in the wave loads and wave-induced motions on the structures. The linearized theory provides a good first-order approximation for those loads and motions and has been widely used.

We first review the concept and derivation of the linearized free surface boundary condition using potential flow theory. Next, we review two important simplified boundary conditions used for approximating the free surface effects at low Froude number conditions and high Froude number conditions, the image method for the former and the negative image method for the latter. In the context of CFD, symmetry plane boundary condition is often used as an equivalent to the image method, but not much work has been done to approximate the effects of the free surface at high Froude number conditions. Since this dissertation focuses on high-speed vessels and structures, we propose a strategy to implement the negative image method in the CFD solver to estimate the free surface effects on steady forces of structures. Hence, the main work and contribution of this chapter is the implementation of an equivalent negative image method boundary condition in the

CFD solver, which can be used to estimate the free surface effects on steady forces of the hydrofoil at high Froude number conditions.

8.1 Introduction

8.1.1 Linearized free surface boundary condition

In linearized theory, we assume the flow is ideal and the wave amplitudes are much smaller compared to the wavelength. By assuming ideal flow, the flow is inviscid, incompressible, and irrotational. Although this work focuses on RANS, we will derive the boundary condition with the help of potential flow theory. The derivation has been shown in previous works [2, 36]. We will briefly review this derivation here for completeness. Figure 8.1 depicts the free surface and coordinates definitions, which are used in later discussion. $z = 0$ describes the mean free surface.

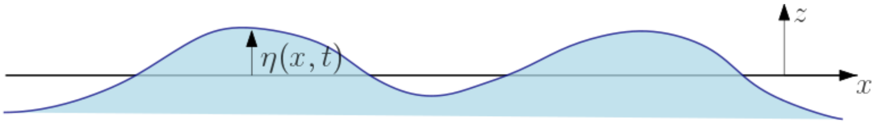

Figure 8.1: Free surface

The flow velocity potential Φ satisfies the Laplace equation,

$$\frac{\partial^2 \Phi}{\partial x^2} + \frac{\partial^2 \Phi}{\partial y^2} + \frac{\partial^2 \Phi}{\partial z^2} = 0 \tag{8.1}$$

The dynamic boundary condition describes the pressure on the free surface equals the atmospheric pressure. Using Bernoulli's equation, the dynamic boundary condition can be written as

$$-\frac{1}{\rho}(p - p_{\text{atm}}) = \frac{\partial \Phi}{\partial t} + \frac{1}{2}\nabla\Phi \cdot \nabla\Phi + gz \text{ on } z = \eta \tag{8.2}$$

where p is the local pressure, p_{atm} is the atmospheric pressure, g is the gravitational constant, and

η is the wave elevation.

For a body that moves with a forward speed U in the x direction, we can express the total velocity potential as

$$\Phi = \phi + \phi_0 = \phi + Ux \tag{8.3}$$

where ϕ is the velocity potential due to the body, and $\phi_0 = Ux$ is the velocity potential due to the forward speed.

Similarly, by neglecting the second and higher order terms, we yield the linearized dynamic boundary condition,

$$-\frac{1}{\rho}(p - p_{\text{atm}}) = \frac{\partial \phi}{\partial t} + U\frac{\partial \phi}{\partial x} + gz \text{ on } z = \eta \tag{8.4}$$

The kinematic boundary condition is the fluid particle on the free surface always stays on the free surface,

$$\frac{D(z-\eta)}{Dt} = 0 \tag{8.5}$$

Note that $\frac{D}{Dt}() \equiv \frac{\partial}{\partial t}() + \nabla\Phi \cdot \nabla()$. We can expand the kinematic boundary condition as,

$$\frac{D(z-\eta)}{Dt} = \frac{\partial z}{\partial t} + \left(U + \frac{\partial \phi}{\partial x}\right)\frac{\partial z}{\partial x} + \frac{\partial \phi}{\partial y}\frac{\partial z}{\partial y} + \frac{\partial \phi}{\partial z}\frac{\partial z}{\partial z} - \left(\frac{\partial \eta}{\partial t} + \left(U + \frac{\partial \phi}{\partial x}\right)\frac{\partial \eta}{\partial x} + \frac{\partial \phi}{\partial y}\frac{\partial \eta}{\partial y} + \frac{\partial \phi}{\partial z}\frac{\partial \eta}{\partial z}\right) \tag{8.6}$$

If we linearize the kinematic boundary condition by applying Taylor expansion about $z = 0$, assuming wave elevation is small and neglecting higher-order terms,

$$\frac{\partial \phi}{\partial z} - \frac{\partial \eta}{\partial t} - U\frac{\partial \eta}{\partial x} = 0 \quad \text{on} \quad z = 0, \tag{8.7}$$

Combining the linearized dynamic and kinematic boundary conditions, Eqn 8.4 and Eqn 8.7,

$$\frac{\partial^2 \phi}{\partial t^2} + 2U\frac{\partial^2 \phi}{\partial x \partial t} + U^2\frac{\partial^2 \phi}{\partial x^2} + g\frac{\partial \phi}{\partial z} = \frac{1}{\rho}\left(\frac{\partial (p - p_{\text{atm}})}{\partial t} + U\frac{\partial (p - p_{\text{atm}})}{\partial x}\right) \text{ on } z = 0, \tag{8.8}$$

Before dealing with the complexity of the wave motions, we focus on the steady free surface effects on hydrodynamic lifting surfaces. If only steady effects are of interests, we can neglect all the time derivative terms,

$$U^2\frac{\partial^2\phi}{\partial x^2}+g\frac{\partial\phi}{\partial z}=\frac{1}{\rho}\left(U\frac{\partial(p-p_{\text{atm}})}{\partial x}\right)\quad\text{on}\quad z=0, \tag{8.9}$$

Without externally applied pressure on the free surface, the pressure on the free surface equals atmospheric pressure,

$$U^2\frac{\partial^2\phi}{\partial x^2}+g\frac{\partial\phi}{\partial z}=0\quad\text{on}\quad z=0 \tag{8.10}$$

Conventionally, there are two conditions that we can apply further simplification to approximate the steady free surface effects. One is low Froude number limits and the other is at the high end.

8.1.2 Low Froude number conditions - the image method

The submergence-based Froude number Fn_h indicates the relative significance of the inertial forces and gravitational force. At low Fn_h conditions, the inertial effect is much smaller than the gravitational effects. Hence, we can neglect the first term in Eqn (8.10), which gives,

$$\frac{\partial\phi}{\partial z}=0\quad\text{on}\quad z=0 \tag{8.11}$$

This no-penetration boundary condition indicates that at low Fn_h conditions, the free surface acts as a rigid wall. Suppose a foil at submergence of h induces a circulation Γ, the boundary condition can be satisfied by adding an opposite circulation with the same strength at the mirror position above the free surface, as shown in Figure 8.2. This treatment ensures no penetration on the mean free surface. While this derivation is based on potential flow, it is useful for simulations with higher fidelities, such as RANS. In RANS CFD, the commonly used symmetry plane boundary

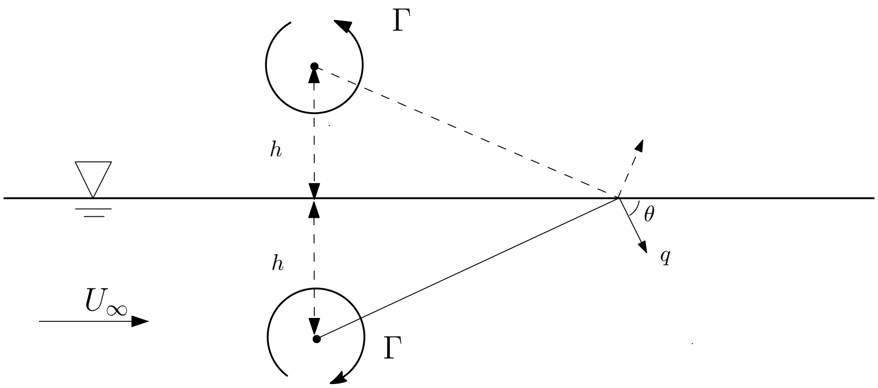

Figure 8.2: The image method for approximating flow around foil at low Froude number conditions.

condition is analogous to the image method. The symmetry plane boundary condition requires zero flux across the symmetry plane. Because the CFD cells adjacent to the symmetry plane have the same tangential velocities, there is no shear stress across the symmetry plane. Several works have used the symmetry plane boundary condition to consider the steady free surface effects at low Fn_h conditions [171].

8.1.3 Infinite Froude number conditions - the negative image method

When the Froude number is high enough, the flow inertia effect is much larger than the gravity effect. When $Fn_h > 10/\sqrt{h/c}$, the gravity term in dynamic boundary condition can be neglected [2]. Hence, the free-surface boundary condition can be simplified as $\phi = 0$ on the free surface. This is equivalent to saying that the horizontal velocity induced by the foil is zero on the mean free surface $z = 0$.

$$\frac{\partial \phi}{\partial x} = \frac{\partial \phi}{\partial y} = 0 \quad \text{on} \quad z = 0 \tag{8.12}$$

This requirement leads to a negative image method that can be used for approximating the flow around foil at high Froude number conditions.

Again, suppose the foil at submergence of h induces a circulation Γ, the boundary condition can be imposed by another circulation with the same strength and the same distance from free surface on the opposite side of the free surface, as shown in Figure 8.3. This negative image method has been used in previous works to provide a good approximation of the steady free surface effects at high Fn_h conditions [172–176].

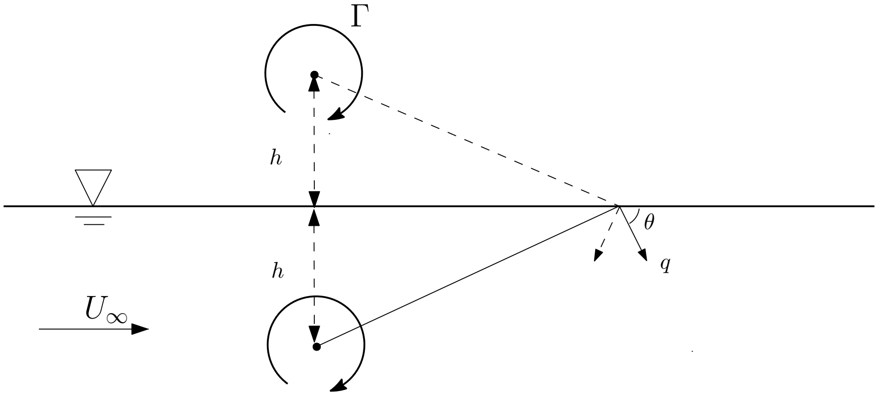

Figure 8.3: The negative image method for approximating flow around foil at high Froude number conditions.

8.2 Antisymmetric boundary condition in CFD

Compared to the image method, only limited work has been done to investigate the feasibility of using the concept of the negative image method to estimate the free surface effects on steady forces of surface vessels with RANS. This is because the translation of the negative image method from potential flow to CFD is less straightforward. First, in the negative image method, the tangential velocities caused by the foil perturbation are zero on the mean free surface. In CFD, it is difficult to separate the perturbation caused by foil from the total states. Second, we have demonstrated that for a lift problem, the negative image method results in another circulation with the same strength on the image position above the mean free surface. For a non-zero thickness problem, it would require a source with negative strength above the mean free surface to result in zero tangential velocities, but this negative source equivalently translates into a negative thickness problem, which is not feasible to directly model in CFD. To simplify the problem, we come up with an indirect way to consider the effect of the negative image method. There are two main effects on the states at the mean free surface boundary:

1. Vertical velocity is allowed at the mean free surface.
2. The pressure at the mean free surface is constant and equals the reference pressure at the far-field.

From the discussion and derivation in Section 8.1.3, the perturbation caused by the foil induces a vertical velocity component at the mean free surface. For the second one, constant pressure on the mean free surface, we can derive from the negative image method using further linearization.

8.2.1 Constant pressure boundary condition

According to Figure 8.3, we can show how the negative image method can be approximated as a constant pressure boundary condition. The horizontal velocity induced by the vortices system according to the negative method is zero on the mean free surface. According to Bernoulli's equations on the mean free surface

$$p_\infty + \frac{\rho U_0^2}{2} = p + \frac{\rho}{2}[(U_0 + u_x)^2 + u_y^2 + u_z^2] \tag{8.13}$$

Since the linearized free surface boundary condition requires that $\nabla\phi \ll U_0$, $u_z \ll U_0$. As a result,

$$p_\infty + \frac{\rho U_0^2}{2} \approx p + \frac{\rho}{2}(U_0^2 + 2U_0 u_x) \tag{8.14}$$

The tangential velocities induced by the perturbation should be zero on the free surface, so $u_x = 0$ and thus

$$p_\infty + \frac{\rho U_0^2}{2} \approx p + \frac{\rho U_0^2}{2} \tag{8.15}$$

which implies that, by using the negative image method, the pressure on the mean free surface p equals the atmospheric pressure p_∞ by dropping the higher order terms.

This constant pressure boundary condition can also be derived from RANS directly, as shown in Appendix B.

8.2.2 Implementation and validation

We have discussed and derived a boundary condition that can be used as an equivalent to the negative image method. Now we will discuss in more detail how we model it in the CFD solver. Halo cells are used to impose this constant boundary condition to be consistent with other types of boundary conditions in the framework. By using halo cells, we can set the constant pressure boundary condition as

$$p_{\text{asym}} = 2p_\infty - p_i \tag{8.16}$$

Now we need to determine the velocities on the mean free surface. We assume the velocities in the halo cells equal those of the internal cells with a conditional normal component. The same tangential velocities ensure zero velocity gradient across the free surface and thus shear stress. Since the linearized free surface boundary condition requires that $\nabla\phi \ll U_0$, the normal velocity on the mean free surface needs to be limited within a reasonable range. The normal velocity is determined by,

$$\begin{aligned} &(u_{z_i} + u_{z_{\text{asym}}})/2 < \text{factor} \times U_0 \\ &u_{z_{\text{asym}}} = u_{z_i},\ \text{if } |u_{z_i}| < \text{factor} \times U_0 \\ &u_{z_{\text{asym}}} = \text{sign}(u_{z_i})(2 \times \text{factor} \times U_0) - u_{z_i},\ \text{if } |u_{z_i}| \geq \text{factor} \times U_0 \end{aligned} \tag{8.17}$$

where the factor is the ratio of the allowed normal velocity to the inflow speed. A factor of 0.2 is considered in this work.

We use this boundary condition implementation to run analyses for foil-only cases at different chord-to-depth ratios, similar to the Figure 7.4. An angle of attack α of 4° and is used in the comparison. We perform simulations in ADflow with $U_\infty = 14$ m/s (mean-chord based $Re_{\text{mc}} = 1.6 \times 10^6$). The submergence-based Froude number Fn_h varies from 6 to 10. We compare the analysis results with analytical predictions from previous literature [2, 160, 177]. We first compare the C_L trend with predictions from Faltinsen [2] and Damley-Strnad et al. [160]. For a 2-D foil, the analysis from Faltinsen [2] gives,

$$C_L(h/c) = C_L(h/c = \infty) \cdot \left[\frac{1 + 16(h/c)^2}{2 + 16(h/c)^2}\right], \text{ when } Fn_h > 10/\sqrt{h/c}. \tag{8.18}$$

The empirical predictions for a 3-D foil given by Damley-Strnad et al. [160] are

$$C_L = \frac{a_0 \sin\alpha}{\frac{E}{F} + \frac{a_0}{AR}} + \frac{4}{3}\left[-\frac{AR}{10}\right] \sin^2\alpha \cos\alpha \text{ for } 0 \le AR \le 10, \tag{8.19}$$

where a_0 is 2-D lift slope; α is the effective angle of attack (geometric angle of attack subtracts the zero lift angle of attack); AR is the aspect ratio; E is the edge correction factor for 3-D flows, given by

$$E = \sqrt{1 + \left(\frac{a_0}{\pi AR}\right)^2}, \tag{8.20}$$

and F is the free surface correction factor, given by

$$F = 1 - 0.422 e^{-1.454 \; h/c} \tag{8.21}$$

For the C_L comparison, we use the case at depth h of 0.5 m as the reference ($h/c = 4.3$), and we normalized the C_L from cases with other submergence depths. The analytical predictions from Faltinsen [2] and Damley-Strnad et al. [160] are also normalized by the value with $h/c = 4.3$ for a fair comparison. We also compare our C_D/C_L^2 with predictions from Breslin [177]. In the

C_D/C_L^2 comparison, we use the difference between the C_D at $\alpha = 4°$ and C_D at $\alpha = 0°$ as the final C_D for comparison to exclude the zero-lift drag component, so our predicted values are more consistent with the analytical values with minimal viscous and thickness effects. The comparisons in Figure 8.4 show that our predictions follow the same trends as previous literature [2, 160, 177].

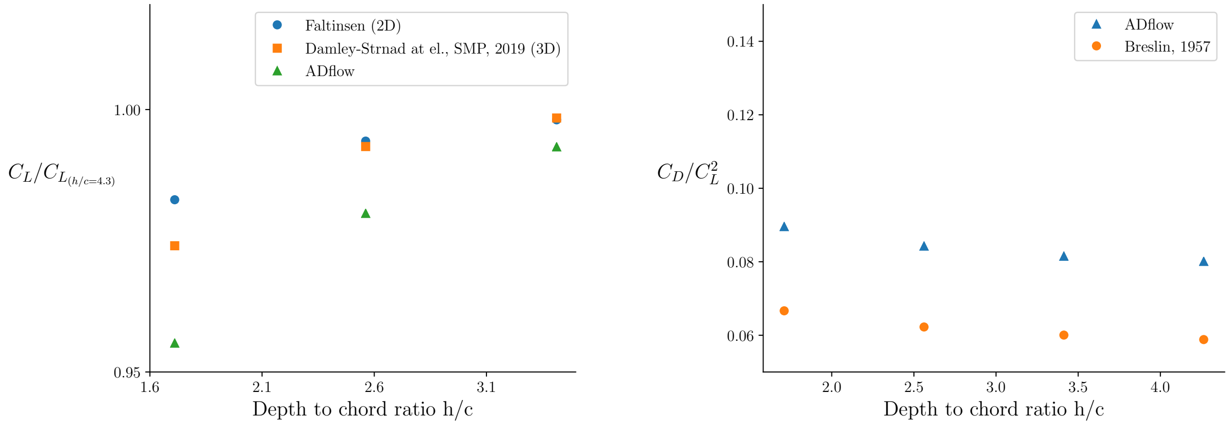

(a) C_L validation (b) C_D/C_L^2 validation

Figure 8.4: Validation of the antisymmetry plane boundary conditions with analytical predictions. The normalized lift coefficient (by lift coefficient at infinite depth) $C_L/C_{L\infty}$ is shown on the left, and drag coefficient C_D over C_L^2 is shown on the right. The submergence-based Froude number Fn_h varies from 6 to 10.

However, this constant pressure boundary condition is not applicable to problems that involve components intersected with the mean free surface plane. Physically, when a surface-piercing hydrofoil operates at high speeds, the gravity effect is significant and the surface perturbation is not small at the region very close to the foil surface on the free surface. Hence, the assumptions used for the negative image method are no longer valid. When we use this boundary condition for a foil that intersects with the mean free surface, it leads to extreme pressure values for interior cells adjacent to the mean free surface. An example of the leading edge for a strut is shown in Figure 8.5. Due to the cross-section shape of the strut, a high-pressure region that has a positive gauge pressure naturally develops around the leading edge area even without or near the constant pressure boundary in reality, this stagnation point will lead to the formation of jet spray, which locally violates the flat free surface assumption. In numerical simulations, with the pressure constant at p_∞, the corresponding halo cells in the mirror domain have a negative gauge pressure. As a result, this pressure difference leads to the positive normal flux to the halo cells in the mirror domain. This positive normal flux can in turn further increase the pressure difference until the normal velocities hit the limits, which can eventually lead to extremely high or low pressure in the interior cells adjacent to the constant pressure boundary. Hence, additional treatment might be needed when using the constant pressure boundary condition to properly balance or attenuate the pressure difference. This observation shows that the gravity effect and actual surface elevation might be necessary for cases that involve components intersected with the mean free surface plane.

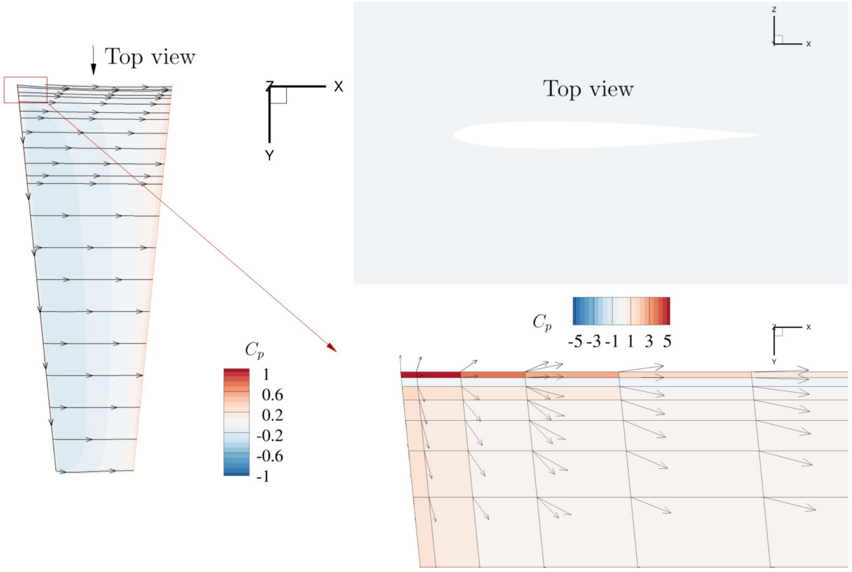

Figure 8.5: High pressure at the leading edge when using a constant pressure boundary condition. Arrows represent velocity vectors.

8.3 Conclusion

In this chapter, we review the linearized free surface boundary conditions, and two commonly used simplified ones for low Froude number conditions (the image method) and high Froude number conditions (the negative image method) respectively. We implemented an equivalent negative image method (for high Froude number conditions) in the CFD solver, but current applications are limited to bodies near but not pierce the free surface. We conducted preliminary analyses to discuss the feasibility and limitations of this implementation. For the problem when the foil operates underneath the free surface, our implementation provides a reasonable approximation and the prediction follows similar trends with previous analytical approximation and experimental observations. However, we found that the current implementation is not suitable for structures that intersect with the free surface. To address these issues, improvements are needed in the future, such as a linearized free surface boundary condition considering the gravitational forces and wave elevations, or the volume of fluid method, especially within the region near the body.

CHAPTER 9

Final Remarks

The increasingly stringent regulations and the goals towards decarbonization and a sustainable future have driven the marine sector to improve the design of hydrodynamic lifting surfaces because of their wide use in marine structures. With recent progress in material science and manufacturing techniques, efforts towards this improvement increasingly focus on composite materials and unconventional geometries. Additionally, multidisciplinary design optimization has been proven to be a powerful tool to explore the optimal material and geometry configurations. Despite the improvements of composite hydrodynamic lifting surfaces by using design optimization in the past decades, several key challenges still remain unsolved due to the harsh sea environments (including effects such as free surface effects, cavitation, ventilation, and separation), high computational cost, and geometry parametrization complexity. This dissertation addresses these challenges by developing a framework for efficient high-fidelity design optimization of hydrodynamic lifting surfaces. In addition to demonstrating that the framework produces superior designs, I also investigate several key questions that have long concerned designers and researchers. I summarize the results and findings in Section 9.1. My contributions are detailed in Section 9.2.

9.1 Conclusions

Material anisotropy complicates the hydroelastic responses of composite hydrodynamic lifting surfaces. Before conducting design optimization, it is important to understand how material anisotropy interacts with geometric variables to change the hydroelastic response. In Chapter 3, I investigated the interplay effects of sweep and material anisotropy with a series of parametric studies using coupled RANS and FEM structural solvers. Different combinations of sweep angle and material anisotropy effects result in diverse structural behaviors, including both static deformation and dynamic characteristics. This change in structural response also impacts the hydroelastic response, as the deformed shape changes the hydrodynamic loads, which highlights the need to consider FSI for composite hydrodynamic lifting surface design. In addition to the structural response, sweep affects the spanwise lift distribution due to vorticity-induced upwash and downwash, which can increase or decrease the lift-induced drag based on the actual profile. Moreover, the sweep can reduce the form drag compared to the unswept hydrofoils due to the spanwise flow that acts to reduce the strength and coherent structure of the vortices shed from the suction and pressure sides of the thick foil trailing edge. This sweep-induced reduction in trailing edge vortex strength also suggests that we can purposely design sweep angle to mitigate separation, flow-induced vibration, and noise. By tailoring hydrodynamic effects caused by the induced downwash and upwash of a swept hydrofoil, the geometric bend-twist coupling, and material bend-twist coupling, improved performance can be achieved. Both sweep and fiber orientation also change the material failure inception and location. Strategic material design is required to not only consider the optimal hydroelastic response, but also based on adequate structural safety to avoid material failure.

Working from this understanding of the interplay effect between material anisotropy and sweep, I presented multipoint hydrostructural optimizations of a full-scale canonical composite hydrofoil made with an equivalent single-layer CFRP in Chapter 4. I improved the cavitation constraint to provide better convergence behaviors for multipoint optimization problems. To ensure the structural safety of the optimized hydrofoil, I implemented failure criteria that consider various failure modes in the framework to predict the material failure onset. Since vibration analyses were not considered in the optimization and due to their high computational cost, I used a displacement constraint to limit the maximum deformation as a surrogate for such dynamic analyses. A conservative safety factor of three is used in optimizations as considerations of material strength variability, uncertainties in manufacturing, loading condition variability, and fatigue strengths. I solved two optimization problems for composite hydrofoils. The second does not include sweep and chord variables compared to the first one. In the first optimization study, the cavitation inception speed increased by 82% at the nominal operating condition of $C_L = 0.3$ compared to the baseline. The optimized result showed a 1.2% decrease in the weighted drag compared to the baseline. We also learned that there are tradeoffs between design considerations, such as drag reduction and cavitation inception. By comparing the optimized hydrofoil to the baseline hydrofoil and the E1127 hydrofoil (E1127 section is known as a gold standard hydrofoil section that delays cavitation), I showed that 3-D effects, such as downwash and tip vortex, significantly altered the cavitation performance. The 2-D cavitation performance of the optimized hydrofoil sections and the E1127 section was comparable, while the 3-D cavitation performance of the E1127 hydrofoil was significantly degraded due to tip vortex cavitation. The second optimization aimed to investigate how sweep and chord variables affect the design. The comparison between the two optimized hydrofoils demonstrates that sweep contributes to drag reduction and delaying cavitation by optimizing the local effective angle of attack, while optimizing chord distribution helps to improve loading distribution to reduce drag and adjust bending moments. Chapter 4 shows that multipoint optimization is necessary to balance the tradeoffs between the design considerations and 3-D effects are important to consider.

In practical applications, composites are typically constructed with multiple layers with varying fiber orientations to sustain loading in various directions and to prevent crack growth once local failure initiates. Additionally, we can vary the fiber orientation across layers to further improve the performance. Hence, in Chapter 5, I presented a comparison between three optimized hydrofoils to investigate the influence of material configurations on the optimized hydrofoil and answer the question of how varying fiber orientation across layers changes the performance. The three optimization cases were an aluminum hydrofoil, a single-layer CFRP hydrofoil, and a multi-layer CFRP hydrofoil. The three optimized hydrofoils feature different sweep angles. The difference in sweep angles is caused by the combined effect of twist deformation and vorticity-induced downwash effects, and by the cavitation, displacement, and material failure constraints. Varying fiber orientations across layers can optimize the structural stiffness in different directions. The multi-layer CFRP hydrofoil has forward-swept fibers in the inner layer and backward ones in the outer layers, increasing its twist rigidity and reducing the tip twist compared to the single-layer CFRP hydrofoil. It is worthy to note that except for the sweep angle, the deformed geometries of all three hydrofoils are very similar. Hence, all three optimized hydrofoils achieved similar hydrodynamic performance in terms of drag and cavitation inception speed. Despite the similarity in hydrodynamic performance shown in this chapter, both CFRP hydrofoils showed slight performance improvement compared to the aluminum hydrofoil and it was observed that using aluminum increased the likelihood of structural failure. Comparison between the two CFRP cases shows that using one unidirectional layer for an effective single-layer composite might be sufficient to achieve the desirable deformed geometry, expected load-dependent deformation, and hydrodynamic performance, but detailed modeling of the stacking sequence is needed to precisely tailor the structural stiffness and strengths in different directions and accurately predict the material failure initiation to ensure safety.

It has been widely known that predicting the material failure initiation for composite structures is a challenging job due to the complex and multi-scale failure mechanisms. Although previous works developed numerous failure models to predict material failure initiation, there is no universal material failure model for different configurations and loading conditions. To investigate the influence of failure model uncertainties on the optimizations of composite hydrodynamic lifting surfaces, I compared optimized hydrofoils with two different failure criteria, for both single-layer CFRP and multi-layer CFRP cases. The comparison shows that using the two investigated failure criteria leads to similar designs. The pressure and loading distributions are almost identical while the structural performance varies slightly for the multi-layer CFRP case because one set of criteria provides a more conservative prediction for delamination initiation than the other. Since a conservative safety factor of three was applied, both optimized hydrofoils are safe. Nevertheless, the results point to the importance of considering uncertainties in material failure models, and thus a safety factor may need to be applied in the optimization process given the difficulties to quantify the various uncertainties.

In Chapter 7, I advanced the optimization studies to more complex systems, which involve more components where interference effects at junctions cannot be neglected. As the first step to such studies, I investigated hydrodynamic optimization problems of a T-shaped hydrofoil-strut system. Two single-point optimizations and three multipoint optimizations were performed. The significantly different single-point optimizations highlight the need for conducting multipoint optimizations to balance the performance across the range of expected operating conditions. All multipoint optimizations effectively created a fairing to delay cavitation at the intersection. These optimized hydrofoils also have delayed leading edge cavitation inception and avoid separation. The case with planform variables and more freedom on the intersection shape design achieved the highest foil drag reduction of 18.6% and delays cavitation most effectively. The comparison between these three multipoint optimizations shows that the detailed geometry design of the intersection can significantly improve the performance. I also performed hydrostructural analysis and modal analysis for the baseline and all multipoint optimization results. The foil thickness reduction increases the deformation and structural stresses, suggesting accelerated fatigue. Therefore, hydrostructural response needs to be considered for ensuring structural integrity.

In Chapter 8, I reviewed two methods that are used to approximate the free surface effects at low Froude number and high Froude number conditions. I implemented an equivalent negative image method in the CFD solver and studied the effect of free surface on the steady mean forces on a hydrofoil. The comparison with previous analytical values shows the implementation provides a reasonable prediction for bodies operating near but beneath the free surface at high Froude number conditions. However, this implementation has difficulties when the structure is intersected with the free surface. I discussed the potential causes and proposed future improvements.

9.2 Contributions

The research in this dissertation builds on a previously developed framework, MACH. The specific contributions of my research are:

1. I presented parametric studies to investigate the interplay between sweep and material anisotropy.

   The interplay of these two factors is important for composite lifting surfaces because they both affect the bend-twist coupling behavior. These parametric studies show how the sweep and material anisotropy change the hydrodynamic forces, separation, static divergence, and material failure.

2. I added the prediction of the material failure initiation for composite solid elements and implemented the corresponding sensitivities for composite hydrodynamic lifting surface.

   There are two reasons that this contribution is critical for composite hydrodynamic lifting surface designs. First, due to high loadings in water, hydrodynamic lifting surfaces typically have a solid interior rather than the hollow foam type structures used for aircraft wings or wind turbine blades. This property necessitates composite solid elements to model and design hydrodynamic lifting surfaces. Secondly, composite structures feature complex failure mechanisms because of their anisotropic characteristics. This second property raises the need of implementing failure criteria that consider the major failure modes so that the design is safe and reliable.

3. I developed an improved cavitation constraint in the CFD solver to better design cavitation-free hydrodynamic lifting surfaces.

   Designing composite hydrodynamic lifting surfaces faces a variety of unique challenges because of the exposure to marine environments. Cavitation is one of the challenges that significantly impacts performance. It does not only cause detrimental erosion on the surfaces, but also impacts the stability of the structure. As stated in Chapter 4, earlier works have developed cavitation constraints and demonstrated the practical usefulness in design optimization. The unique contribution was improving the constraint to allow the framework to consider different cavitation numbers across design conditions and more effectively delay cavitation in a multipoint optimization.

4. I performed the multipoint hydrostructural optimizations with varying cavitation requirements at different design conditions with constraints on structural failures and bending deformation.

   Most of the previous works on composite hydrodynamic lifting surface optimization are restricted to a small number of design variables, 2-D designs, or using low-fidelity tools. Several recent developments have advanced the state-of-art into using high-fidelity tools and 3-D designs, the problem of a cavitation-free composite hydrodynamic lifting surface across a range of operating conditions remains unresolved. Therefore, working from my improvements done to the framework, I addressed this design problem using a canonical NACA 0009 hydrofoil made of a single-layer CFRP for optimization. Because dynamic responses are crucial for hydrodynamic lifting surfaces, I also pioneered a bending deformation constraint as a surrogate for dynamic performance consideration in the current static hydroelastic optimization to improve the fatigue performance in practice. In addition to the optimization results, I presented a thorough study to discuss how 3-D effects impact cavitation performance.

5. I investigated how the sweep and chord variables contribute to the cavitation performance of

hydrodynamic lifting surfaces.

Sweep and chord are two geometric variables of interest for both academia and industry. I used two optimization studies to investigate their contribution to designing cavitation-free hydrodynamic lifting surfaces. The comparison showed that sweep has a higher impact on multipoint condition design because of its load-dependent effects.

6. I developed methods to model multi-layer composite hydrodynamic lifting surfaces and investigated the influence of material configurations on the optimization of hydrodynamic lifting surfaces.

   In reality, composite structures are constructed with multiple layers with varying fiber orientations to prevent crack propagation and to improve reliability. Using an equivalent single-layer CFRP can achieve similar load-dependent deformation and hydrodynamic performance, but detailed multi-layer modeling is needed to more accurately capture the failure initiation.

7. I examined the influence of material failure model uncertainties on optimizations of composite hydrodynamic lifting surfaces.

   Complex failure mechanisms of composites challenge the failure initiation prediction and the reliability of the designs. I presented a study comparing optimized composite hydrofoils with different material failure initiation criteria to investigate how using different material failure criteria might affect the design.

8. I extended the framework to design a hydrofoil-strut system with the capability to optimize the junction shape.

   Previous work on hydrodynamic lifting surface shape design optimization only focused on one single part, but the interference effects between components can be critical. I improved the framework to optimize more complex hydrodynamic lifting surface systems with the capability to design more detailed geometry, such as the junction shape.

9. I presented the first series of high-fidelity hydrodynamic optimization studies of a T-foil considering the junction geometry and showed how the planform shape and detailed junction geometry significantly affect the design.

   I presented a series of optimization studies of a T-shaped hydrofoil-strut system to simultaneously reduce drag, delay cavitation and avoid separation across a range of operating conditions. The optimized hydrofoils significantly delay cavitation and separation. For a hydrodynamic lifting surface operating near the free surface, these delays imply a lower susceptibility to ventilation. I also demonstrated that including planform variables, such as chord and span, and adjusting the detailed junction geometry benefit the design.

10. I experimented with an equivalent negative image method in the CFD solver to account for the free surface effects on steady forces of hydrofoils at high Froude number conditions.

9.3 Recommendations for future work

High-fidelity design optimization becomes increasingly viable for engineering designs because of advances in other scientific areas, such as material science, manufacturing techniques, computing science, and numerical methods. Composite materials do not only provide long-known benefits in terms of weight reduction, resistance to corrosion, and operating life extension, but also open the door to better sensing, control, and heath-monitoring, which are important for the next-generation intelligent marine platforms. We have identified several future research directions that promote the use of composites and design optimization to create more efficient and reliable marine structures.

1. More realistic configurations and physical constraints

   Interference effects between each sub-component are critical to the performance of marine structures. Considering more complete configurations in design optimization allows for further performance improvements that can be substantial. Examples of more realistic configurations with multiple components include vehicles with control surfaces, hulls with rudders and propellers, and hulls with hydrofoils. On the other hand, when complete modeling of the whole vehicle is not available, surrogate constraints based on physical design considerations can be developed and enforced. An example is a side-force constraint for the T-shaped hydrofoil-strut system problem.

2. Other hydrodynamic lifting surface applications

   This dissertation mainly focuses on non-symmetrical lifting surfaces that operate at positive lift conditions, while symmetrical hydrodynamic lifting surfaces that mostly operate near zero loadings are preferred for rudder and other control surface applications. The optimal design is highly dependent on the operational requirement. The optimized results in this dissertation might not be suitable for those applications. A symmetric design that is intended for rudder or control surfaces can be investigated in the future using the methodology in this dissertation.

3. Improve geometric parametrization and mesh deformation capabilities

   In this dissertation, only constant chord scaling and rake variables are considered for the T-shaped hydrofoil-strut system problem. However, the chord can vary along the span for the vertical strut. This chord variation together with the cross-sectional shape optimization can further improve the performance. In addition, topology changes are not allowed due to mesh deformation ability and the need for continuity for gradient-based optimization. This limits more complex designs. For example, the relative position between the strut and the foil is fixed in this work because of the water-tightness requirement on the geometry of the components, while the relative position is usually adjustable during manual designs. This relative position plays an important role in reducing the interference effects between the strut and the foil. We can observe foils with different configurations in terms of this relative position between teams competing for the 36th America's Cup.

4. Hydrostructural optimization of the hydrofoil-strut system

   This dissertation only investigates the hydrodynamic optimization problem for the hydrofoil-strut system. From our hydrostructural analysis and modal analysis results, these hydrodynamic optimized T-foils could be susceptible to accelerated fatigue and instabilities. Hence, it is important to include the hydrostructural responses and structural failure inception during optimization to ensure a structurally sound design.

5. Uncertainty quantification and optimization under uncertainties

   Uncertainty quantification is important to achieve more robust and reliable designs. Uncertainty exists in every stage of the engineering design process, such as manufacturing precision, material property variation, and operating condition change. Typically complete information is not available during the design stage. Additionally, there is a large variability in material strengths for composites. Different material failure initiation prediction models can provide different safe loading envelopes and impact the design [7]. Designers need to take the potential variabilities into consideration [148]. Otherwise, optimized results might not perform well as expected in real-life operations.

6. Importance of dynamic load amplification and accelerated fatigue

   In this dissertation, only steady responses are considered. However, marine structures are subject to spatially and temporally varying loads caused by waves, current, unsteady vessel motions, and interactions with adjacent bodies or boundaries. These varying loadings can cause load fluctuations, dynamic load amplification, and accelerated fatigue. Hence, considering dynamic responses and fatigue performance in design optimization is important to yield realistic and reliable designs. The dynamic response can be predicted with time-domain or frequency-domain approaches. Since time-accurate solutions are expensive, frequency-domain or time-spectral methods are more feasible in the early design optimization stage. This dynamic response prediction results can be used for fatigue analysis. There are three commonly used models: fatigue life model, residual strength and stiffness model, and progressive damage model. Although a lot of work has been done on the fatigue damage modeling of composites, most of them are extremely case-sensitive. Additionally, the validity of the model depends on the actual laminate stacking sequences, manufacturing qualities, and boundary conditions, which introduce uncertainties. A previous work by Philippidis et al. [178] showed that no model was able to consistently predict the residual strength of different laminates subject to general loading conditions. Using complicated phenomenological models require massive experiment data for implementation, so it may not payback in terms of accuracy. Hence, simple models might be more promising. Nevertheless, experiments will be needed to validate these models.

7. Incorporate sensing and control in the optimization

   Composite materials and modern manufacturing techniques enable easier sensor placements in the structures. By incorporating sensing techniques in design optimization, we can use sensing and control techniques to dynamically change the structure performance in real-time, which facilitates multifunctional and intelligent marine structures. Example studies are optimizing the sensor locations to maximize the ratio of measurement quality to cost and using smart materials or control techniques to morph structures in real-time.

8. Curved fiber paths

   Manufacturing technologies such as automatic fiber placement enable curved fiber paths that can provide superior performance to traditional composite layups [22, 88, 179]. With the potential to use more complex and novel geometries in the future, the advantages of using curved fiber path composite have become increasingly pronounced. Hence, using high-fidelity hydrostructural design optimization to investigate and quantify the benefits of using curved fiber paths for marine structures will provide valuable insights for future applications.

9. Transition prediction

In this work, fully turbulent flow is used throughout the optimization, while laminar flow can be utilized to reduce drag significantly as long as laminar flow separation does not occur [180, 181].

10. Free surface modeling

    In this work, a simplified approximation was used for accounting for the free surface effects. In reality, free surface effects are much more complex and a more accurate prediction is critical to the design of marine structures. A linearized free surface boundary condition with considerations of the gravitational force and wave elevations or the volume of fluid method can be used in the future.

Bibliography

[1] C. M. Harwood, Y. L. Young, S. L. Ceccio, Ventilated cavities on a surface-piercing hydrofoil at moderate froude numbers: cavity formation, elimination and stability, Journal of Fluid Mechanics 800 (2016) 5–56. `doi:10.1017/jfm.2016.373`.

[2] O. M. Faltinsen, Hydrodynamics of high-speed marine vehicles, Cambridge University Press, 2006. `doi:10.1017/CBO9780511546068`.

[3] H. J. Lugt, Numerical modelling of vortex flows in ship hydrodynamics. a review, in: Proc. Third Int. Conf. on Numerical Ship Hydrodynamics, 1981, pp. 297–316.

[4] A. B. Lambe, J. R. R. A. Martins, Extensions to the design structure matrix for the description of multidisciplinary design, analysis, and optimization processes, Structural and Multidisciplinary Optimization 46 (2012) 273–284. `doi:10.1007/s00158-012-0763-y`.

[5] Z. Hashin, Failure criteria for unidirectional fiber composites, Journal of Applied Mechanics 47 (2) (1980) 329–334. `doi:10.1115/1.3153664`.

[6] O. Ochoa, J. Engblom, Analysis of progressive failure in composites, Composites Science and Technology 28 (2) (1987) 87–102. `doi:10.1016/0266-3538(87)90092-3`.
URL `https://doi.org/10.1016/0266-3538(87)90092-3`

[7] M. R. Motley, Y. L. Young, Influence of uncertainties on the response and reliability of self-adaptive composite rotors, Composite Structures 94 (1) (2011) 114–120. `doi:10.1016/j.compstruct.2011.07.011`.
URL `https://doi.org/10.1016/j.compstruct.2011.07.011`

[8] Y. L. Young, M. R. Motley, R. Barber, E. J. Chae, N. Garg, Adaptive composite marine propulsors and turbines: Progress and challenges, Applied Mechanics Reviews 68 (6) (2016) 060803. `doi:10.1115/1.4034659`.

[9] A. Mouritz, E. Gellert, P. Burchill, K. Challis, Review of advanced composite structures for naval ships and submarines, Composite structures 53 (1) (2001) 21–42. `doi:10.1016/s0263-8223(00)00175-6`.

[10] Y. L. Young, N. Garg, P. A. Brandner, B. W. Pearce, D. Butler, D. Clarke, A. W. Phillips, Load-dependent bend-twist coupling effects on the steady-state hydroelastic response of

composite hydrofoils, Composite Structures 189 (1) (2018) 398–418. doi:10.1016/j.compstruct.2017.09.112.

[11] D. Gay, Composite Materials: Design and Applications, 3rd Edition, CRC Press, 2015.

[12] J.-M. Berthelot, M. Assarar, Y. Sefrani, A. E. Mahi, Damping analysis of composite materials and structures, Composite Structures 85 (3) (2008) 189–204. doi:https://doi.org/10.1016/j.compstruct.2007.10.024.

[13] H. Lee, M.-C. Song, S. Han, B.-J. Chang, J.-C. Suh, Hydro-elastic aspects of a composite marine propeller in accordance with ply lamination methods, Journal of Marine Science and Technology 22 (3) (2017) 479–493. doi:10.1007/s00773-016-0428-4.

[14] P. Davies, Y. D. S. Rajapakse (Eds.), Durability of Composites in a Marine Environment, Solid Mechanics and Its Applications, Springer, 2014.

[15] A. D. Kersey, M. A. Davis, T. A. Berkoff, A. D. Dandridge, R. T. Jones, T.-E. Tsai, G. B. Cogdell, G. Wang, G. B. Havsgaard, K. Pran, S. Knudsen, Transient load monitoring on a composite hull ship using distributed fiber optic Bragg grating sensors, in: R. O. Claus (Ed.), Smart Structures and Materials 1997: Smart Sensing, Processing, and Instrumentation, Vol. 3042, International Society for Optics and Photonics, SPIE, 1997, pp. 421 – 430. doi:10.1117/12.275763.

[16] G. A. Johnson, Vibration monitoring of a ship waterjet with fiber Bragg gratings, in: B. Y. Kim, K. Hotate (Eds.), 13th International Conference on Optical Fiber Sensors, Vol. 3746, International Society for Optics and Photonics, SPIE, 1999, pp. 68 – 71. doi:10.1117/12.2302002.

[17] D. Guillaume, D. Samuel, B. Franck, M. Pol, L. L. Frédérique, Composite propeller in marine industry: first steps toward a technological breakthrough, in: OCEANS 2019 - Marseille, 2019, pp. 1–6. doi:10.1109/OCEANSE.2019.8867439.

[18] Benefits of Carbon Composite Marine Propeller.
URL https://www.classnk.or.jp/classnk-rd/assets/pdf/katsudou201511_D.pdf

[19] P. Mallick, Fiber-Reinforced Composites: Materials, Manufacturing, and Desgin, 3rd Edition, CRC Press, 2007.

[20] C. Soutis, Fiber reinfroced composites in aircraft construction, Progress in Aerospace Sciences 41 (2005) 143–151.

[21] S. Guo, W. Cheng, D. Cui, Aeroelastic tailoring of composite wing structures by laminate layup optimization, AIAA Journal (2006) 3146–3150doi:10.2514/1.20166.

[22] T. R. Brooks, J. R. R. A. Martins, G. J. Kennedy, High-fidelity aerostructural optimization of tow-steered composite wings, Journal of Fluids and Structures 88 (2019) 122–147. `doi:10.1016/j.jfluidstructs.2019.04.005`.

[23] K. Hayat, S. K. Ha, Load mitigation of wind turbine blade by aeroelastic tailoring via unbalanced laminates composites, Composite Structures 128 (2015) 122–133.

[24] Y. L. Young, Fluid–structure interaction analysis of flexible composite marine propellers, Journal of Fluids and Structures 24 (6) (2008) 799–818. `doi:10.1016/j.jfluidstructs.2007.12.010`.

[25] X. Guo, J. Yang, Z. Gao, T. Moan, H. Lu, The surface wave effects on the performance and the loading of a tidal turbine, Ocean Engineering 156 (2018) 120–134. `doi:10.1016/j.oceaneng.2018.02.033`.

[26] Y. L. Young, Hydroelastic response of lifting bodies in separated flows, in: NATO-AVT-307: Symposium on Separated Flow: Prediction, Measurement and Assessment for Air and Sea, Trondheim, Norway, 2019.

[27] J. Bosschers, A semi-empirical prediction method for broadband hull-pressure fluctuations and underwater radiated noise by propeller tip vortex cavitation †, Journal of Marine Science and Engineering 6 (2). `doi:10.3390/jmse6020049`.

[28] R. Arndt, P. Pennings, J. Bosschers, T. van Terwisga, The singing vortex, Interface Focus 5 (5) (2015) 20150025. `doi:10.1098/rsfs.2015.0025`.

[29] C. E. Brennen (Ed.), Cavitation and bubble dynamics, Cambridge University Press, 2014.

[30] J.-P. Franc, Physics and control of cavitation, in: Design and Analysis of High Speed Pumps, no. 2, 2006, pp. 1–36.

[31] P. C. Pennings, J. Westerweel, T. J. C. van Terwisga, Flow field measurement around vortex cavitation, Experiments in Fluids 56 (11) (2015) 206. `doi:10.1007/s00348-015-2073-9`.

[32] S. Jahangir, E. Ghahramani, M. Neuhauser, S. Bourgeois, R. E. Bensow, C. Poelma, Experimental investigation of cavitation-induced erosion around a surface-mounted bluff body, Wear (2021) 203917`doi:https://doi.org/10.1016/j.wear.2021.203917`.

[33] T. Yamatogi, H. Murayama, K. Uzawa, K. Kageyama, N. Watanabe, Study on cavitation erosion of composite materials for marine propeller, in: The 17th International Conference on Composites (ICCM-17), Edinburgh, UK, 2009.

[34] J. P. Breslin, R. Skalak, NASA Technical Reports Server (NTRS), Tech. Rep. C-476 NASA-MEMO-2-23-59W (Apr. 1959).
URL `https://ntrs.nasa.gov/citations/19980228299`

[35] R. Hecker, Flow separation, reattachment, and ventilation of foils with sharp leading edge at low Reynolds number, Naval Ship Research and Development Center, Ship Performance Department, Research and Development Report No. 4390, Bethesda, Md 20034, USA. URL `https://repository.tudelft.nl/islandora/object/uuid%3A731f5618-d83e-4a4a-b37a-09d97f364572`

[36] J. N. Newman, Marine Hydrodynamics, The MIT Press, 2018.

[37] Y. L. Young, C. M. Harwood, M. F. Montero, J. C. Ward, S. L. Ceccio, Ventilation of lifting bodies: Review of the physics and discussion of scaling effects, Applied Mechanics Reviews 69 (1) (2017) 010801.

[38] M. Motley, Z. Liu, Y. Young, Utilizing fluid–structure interactions to improve energy efficiency of composite marine propellers in spatially varying wake, Composite Structures 90 (3) (2009) 304–313. `doi:10.1016/j.compstruct.2009.03.011`.

[39] D. T. Akcabay, E. J. Chae, Y. L. Young, A. Ducoin, J. A. Astolfi, Cavity induced vibration of flexible hydrofoils, Journal of Fluids and Structures 49 (2014) 463–484. `doi:10.1016/j.jfluidstructs.2014.05.007`.

[40] E. J. Chae, D. T. Akcabay, Y. L. Young, Influence of flow-induced bend–twist coupling on the natural vibration responses of flexible hydrofoils, Journal of Fluids and Structures 69 (2017) 323–340. `doi:10.1016/j.jfluidstructs.2016.12.008`.

[41] D. T. Akcabay, Y. L. Young, Steady and dynamic hydroelastic behavior of composite lifting surfaces, Composite Structures 227 (2019) 111240. `doi:10.1016/j.compstruct.2019.111240`.

[42] D. T. Akcabay, Y. L. Young, Material anisotropy and sweep effects on the hydroelastic response of lifting surfaces, Composite Structures 242 (2020) 112140. `doi:https://doi.org/10.1016/j.compstruct.2020.112140`.

[43] M. R. Motley, Y. L. Young, Performance-based design and analysis of flexible composite propulsors, Journal of Fluids and Structures 27 (8) (2011) 1310–1325. `doi:10.1016/j.jfluidstructs.2011.08.004`.

[44] C. M. Harwood, M. Felli, M. Falchi, S. L. Ceccio, Y. L. Young, The hydroelastic response of a surface-piercing hydrofoil in multi-phase flows. part 1. passive hydroelasticity, Journal of Fluid Mechanics 881 (2019) 313–364. `doi:10.1017/jfm.2019.691`.

[45] C. M. Harwood, M. Felli, M. Falchi, N. Garg, S. L. Ceccio, Y. L. Young, The hydroelastic response of a surface-piercing hydrofoil in multiphase flows. part 2. modal parameters and generalized fluid forces, Journal of Fluid Mechanics 884. `doi:10.1017/jfm.2019.871`.

[46] Y. Young, T. Wright, H. Yoon, C. Harwood, Dynamic hydroelastic response of a surface-piercing strut in waves and ventilated flows, Journal of Fluids and Structures 94 (2020) 102899. doi:https://doi.org/10.1016/j.jfluidstructs.2020.102899.

[47] D. T. Akcabay, Y. L. Young, Parametric excitations and lock-in of flexible hydrofoils in two-phase flows, Journal of Fluids and Structures 57 (2015) 344–356.

[48] M. R. Kramer, Z. Liu, Y. L. Young, Free vibration of cantilevered composite plates in air and in water, Composite Structures 95 (2013) 254–263. doi:10.1016/j.compstruct.2012.07.017.

[49] Y. L. Young, H. Yoon, T. Wright, C. Harwood, The effect of waves and ventilation on the dynamic response of a surface-piercing hydrofoil, in: 32nd Symposium on Naval Hydrodynamics, Hamburg, Germany, 2018.

[50] N. Garg, High-fidelity hydrostructural design optimization of lifting surfaces, Ph.D. thesis, University of Michigan (2017).

[51] Added Resistance and Added Power of the KCS in Head Seas, Vol. Day 2 Wed, September 30, 2020 of SNAME Maritime Convention, d023S007R005. arXiv:https://onepetro.org/SNAMESMC/proceedings-pdf/SMC20/2-SMC20/D023S007R005/2256559/sname-smc-2020-089.pdf.

[52] J. DUGUNDJI, J. M. CALLIGEROS, Similarity laws for aerothermoelastic testing, Journal of the Aerospace Sciences 29 (8) (1962) 935–950. arXiv:https://doi.org/10.2514/8.9663, doi:10.2514/8.9663.

[53] J. R. R. A. Martins, A. B. Lambe, Multidisciplinary design optimization: A survey of architectures, AIAA Journal 51 (9) (2013) 2049–2075. doi:10.2514/1.J051895.

[54] L. A. Schmit, W. A. Thornton, Synthesis of an airfoil at supersonic Mach number, Tech. Rep. CR 144, NASA (January 1965).

[55] R. T. Haftka, Optimization of flexible wing structures subject to strength and induced drag constraints, AIAA Journal 15 (8) (1977) 1101–1106. doi:10.2514/3.7400.

[56] I. M. Kroo, MDO for large-scale design, in: N. Alexandrov, M. Y. Hussaini (Eds.), Multidisciplinary Design Optimization: State-of-the-Art, SIAM, 1997, pp. 22–44.

[57] A. Papanikolaou, Holistic ship design optimization, Computer-Aided Design 42 (11) (2010) 1028–1044. doi:10.1016/j.cad.2009.07.002.

[58] D. Peri, E. F. Campana, Multidisciplinary Design Optimization of a Naval Surface Combatant, Journal of Ship Research 47 (01) (2003) 1–12. doi:10.5957/jsr.2003.47.1.1.

[59] N. Kolekar, A. Banerjee, A coupled hydro-structural design optimization for hydrokinetic turbines, Journal of Renewable and Sustainable Energy 5 (5) (2013) 053146. `doi:10.1063/1.4826882`.

[60] C. Lin, Y. Lee, Stacking sequence optimization of laminated composite structures using genetic algorithm with local improvement, Composite structures 63 (3) (2004) 339–345.

[61] M. M. Pluciński, Y. L. Young, Z. Liu, Optimization of a self-twisting composite marine propeller using genetic algorithms, 16th International conference on composite materials, Kyoto, Japan (2007).

[62] Z. Liu, Y. L. Young, Utilization of bend–twist coupling for performance enhancement of composite marine propellers, Journal of Fluids and Structures 25 (6) (2009) 1102–1116. `doi:10.1016/j.jfluidstructs.2009.04.005`.

[63] P. Ploe, Surrogate-based optimization of hydrofoil shapes using RANS simulations, Theses, École centrale de Nantes (June 2018).
URL `https://tel.archives-ouvertes.fr/tel-02050026`

[64] B. Yang, X. Shu, Hydrofoil optimization and experimental validation in helical vertical axis turbine for power generation from marine current, Ocean Engineering 42 (2012) 35 – 46. `doi:https://doi.org/10.1016/j.oceaneng.2012.01.004`.

[65] N. Garg, G. K. W. Kenway, J. R. R. A. Martins, Y. L. Young, High-fidelity multipoint hydrostructural optimization of a 3-D hydrofoil, Journal of Fluids and Structures 71 (2017) 15–39. `doi:10.1016/j.jfluidstructs.2017.02.001`.

[66] S. Volpi, M. Diez, F. Stern, Multidisciplinary Design Optimization of a 3D Composite Hydrofoil via Variable Accuracy Architecture, American Institute of Aeronautics and Astronautics, 2018. `doi:doi:10.2514/6.2018-4173`.

[67] A. Kaddour, M. Hinton, Maturity of 3d failure criteria for fibre-reinforced composites: Comparison between theories and experiments: Part b of WWFE-II, Journal of Composite Materials 47 (6-7) (2013) 925–966. `doi:10.1177/0021998313478710`.
URL `https://doi.org/10.1177/0021998313478710`

[68] M. Hinton, A. Kaddour, The background to the second world-wide failure exercise, Journal of Composite Materials 46 (19-20) (2012) 2283–2294. `doi:10.1177/0021998312449885`.
URL `https://doi.org/10.1177/0021998312449885`

[69] A. Kaddour, M. Hinton, P. Smith, S. Li, A comparison between the predictive capability of matrix cracking, damage and failure criteria for fibre reinforced composite laminates: Part a of the third world-wide failure exercise, Journal of Composite Materials 47 (20-21) (2013) 2749–2779. `doi:10.1177/0021998313499476`.
URL `https://doi.org/10.1177/0021998313499476`

[70] Y. T. Shen, R. Eppler, Wing sections for hydrofoils - part 2: Nonsymmetrical profiles, Journal of Ship Research 25 (3) (1981) 191–200.

[71] R. Eppler, Y. T. Shen, Wing sections for hydrofoils–part 1: Symmetrical profiles, Journal of Ship Research 23 (3) (1979) 209–217.

[72] O. Scherer, R. Stairs, Propeller blade section with improved cavitation performance, in: Propellers/Shafting '94 Symposium, The Society of Naval Architects and Marine Engineers, Virginia Beach, Virginia, 1994.

[73] N. Garg, G. K. W. Kenway, Z. Lyu, J. R. R. A. Martins, Y. L. Young, High-fidelity hydrodynamic shape optimization of a 3-D hydrofoil, Journal of Ship Research 59 (4) (2015) 209–226. `doi:10.5957/JOSR.59.4.150046`.

[74] F. Vesting, R. Bensow, Propeller Optimisation Considering Sheet Cavitation and Hull Interaction, Second International Symposium on Marine Propulsors (2011) 79–88.
URL `https://research.chalmers.se/en/publication/148233`

[75] F. Vesting, R. E. Bensow, R. Johansson, R. Gustafsson, N. Costa, Procedure for application-oriented optimisation of marine propellers, Journal of Marine Science and Engineering 4 (4). `doi:10.3390/jmse4040083`.

[76] F. Gand, S. Deck, V. Brunet, P. Sagaut, Flow dynamics past a simplified wing body junction, Physics of Fluids 22 (11) (2010) 115111. `arXiv:https://doi.org/10.1063/1.3500697`, `doi:10.1063/1.3500697`.

[77] Z. Lyu, Z. Xu, J. R. R. A. Martins, Benchmarking optimization algorithms for wing aerodynamic design optimization, in: Proceedings of the 8th International Conference on Computational Fluid Dynamics, Chengdu, Sichuan, China, 2014, iCCFD8-2014-0203.

[78] Y. Yu, Z. Lyu, Z. Xu, J. R. R. A. Martins, On the influence of optimization algorithm and starting design on wing aerodynamic shape optimization, Aerospace Science and Technology 75 (2018) 183–199. `doi:10.1016/j.ast.2018.01.016`.

[79] J. R. R. A. Martins, J. J. Alonso, J. J. Reuther, Aero-structural wing design optimization using high-fidelity sensitivity analysis, in: H. Hölinger (Ed.), Proceedings of the CEAS Conference on Multidisciplinary Aircraft Design and Optimization, Köln, Germany, 2001, pp. 211–226.

[80] J. R. R. A. Martins, A coupled-adjoint method for high-fidelity aero-structural optimization, Ph.D. thesis, Stanford University (2002).

[81] J. R. R. A. Martins, J. J. Alonso, J. J. Reuther, Complete configuration aero-structural optimization using a coupled sensitivity analysis method, in: Proceedings of the 9th AIAA/ISSMO Symposium on Multidisciplinary Analysis and Optimization, Atlanta, GA, 2002, aIAA 2002-5402.

[82] Z. Lyu, G. K. Kenway, C. Paige, J. R. R. A. Martins, Automatic differentiation adjoint of the Reynolds-averaged Navier–Stokes equations with a turbulence model, in: 21st AIAA Computational Fluid Dynamics Conference, San Diego, CA, 2013. doi:10.2514/6.2013-2581.

[83] Z. Lyu, G. K. W. Kenway, J. R. R. A. Martins, RANS-based aerodynamic shape optimization investigations of the Common Research Model wing, in: Proceedings of the AIAA Science and Technology Forum and Exposition (SciTech), National Harbor, MD, 2014, aIAA 2014-0567. doi:10.2514/6.2014-0567.

[84] Z. Lyu, High-fidelity aerodynamic design optimization of aircraft configurations, Ph.D. thesis, University of Michigan (2014).

[85] G. K. W. Kenway, J. R. R. A. Martins, Multipoint high-fidelity aerostructural optimization of a transport aircraft configuration, Journal of Aircraft 51 (1) (2014) 144–160. doi:10.2514/1.C032150.

[86] D. Burdette, G. K. W. Kenway, Z. Lyu, J. R. R. A. Martins, Aerostructural design optimization of an adaptive morphing trailing edge wing, in: Proceedings of the AIAA Science and Technology Forum and Exposition (SciTech), Kissimmee, FL, 2015. doi:10.2514/6.2016-1294.

[87] D. A. Burdette, G. K. Kenway, J. R. R. A. Martins, Performance evaluation of a morphing trailing edge using multipoint aerostructural design optimization, in: 57th AIAA Structures, Structural Dynamics, and Materials Conference, AIAA, 2016. doi:10.2514/6.2016-0159.

[88] T. R. Brooks, J. R. R. A. Martins, G. J. Kennedy, Aerostructural trade-offs for tow-steered composite wings, Journal of Aircraft 57 (5) (2020) 787–799. doi:10.2514/1.C035699.

[89] N. P. Bons, J. R. R. A. Martins, Aerostructural design exploration of a wing in transonic flow, Aerospace 7 (8) (2020) 118. doi:10.3390/aerospace7080118.

[90] N. P. Bons, J. R. R. A. Martins, C. A. Mader, M. McMullen, M. Suen, High-fidelity aerostructural optimization studies of the Aerion AS2 supersonic business jet, in: Proceedings of the AIAA Aviation Forum, 2020. doi:10.2514/6.2020-3182.

[91] N. Garg, B. W. Pearce, P. A. Brandner, A. W. Phillips, J. R. R. A. Martins, Y. L. Young, Experimental investigation of a hydrofoil designed via hydrostructural optimization, Journal of Fluids and Structures 84 (2019) 243–262. doi:10.1016/j.jfluidstructs.2018.10.010.

[92] G. K. W. Kenway, G. J. Kennedy, J. R. R. A. Martins, Scalable parallel approach for high-fidelity steady-state aeroelastic analysis and adjoint derivative computations, AIAA Journal 52 (5) (2014) 935–951. doi:10.2514/1.J052255.

[93] N. Secco, G. K. W. Kenway, P. He, C. A. Mader, J. R. R. A. Martins, Efficient mesh generation and deformation for aerodynamic shape optimization, AIAA Journal 59 (4) (2021) 1151–1168. doi:10.2514/1.J059491.

[94] G. K. Kenway, G. J. Kennedy, J. R. R. A. Martins, A CAD-free approach to high-fidelity aerostructural optimization, in: Proceedings of the 13th AIAA/ISSMO Multidisciplinary Analysis Optimization Conference, no. AIAA 2010-9231, Fort Worth, TX, 2010. doi:10.2514/6.2010-9231.

[95] N. R. Secco, J. P. Jasa, G. K. W. Kenway, J. R. R. A. Martins, Component-based geometry manipulation for aerodynamic shape optimization with overset meshes, AIAA Journal 56 (9) (2018) 3667–3679. doi:10.2514/1.J056550.

[96] A. Yildirim, C. A. Mader, J. R. R. A. Martins, A surface mesh warping method near component intersections for high-fidelity design optimization, Engineering with Computersdoi:10.1007/s00366-020-01247-w.

[97] E. Luke, E. Collins, E. Blades, A fast mesh deformation method using explicit interpolation, Journal of Computational Physics 231 (2) (2012) 586–601. doi:10.1016/j.jcp.2011.09.021.

[98] C. A. Mader, G. K. W. Kenway, A. Yildirim, J. R. R. A. Martins, ADflow: An open-source computational fluid dynamics solver for aerodynamic and multidisciplinary optimization, Journal of Aerospace Information Systems 17 (9) (2020) 508–527. doi:10.2514/1.I010796.

[99] G. K. W. Kenway, N. Secco, J. R. R. A. Martins, A. Mishra, K. Duraisamy, An efficient parallel overset method for aerodynamic shape optimization, in: Proceedings of the 58th AIAA/ASCE/AHS/ASC Structures, Structural Dynamics, and Materials Conference, AIAA SciTech Forum, Grapevine, TX, 2017. doi:10.2514/6.2017-0357.

[100] Y. Lee, J. Baeder, Implicit hole cutting—a new approach to overset grid connectivity, in: 16th AIAA Computational Fluid Dynamics Conference, 2003. doi:10.2514/6.2003-4128.

[101] A. Yildirim, G. K. W. Kenway, C. A. Mader, J. R. R. A. Martins, A Jacobian-free approximate Newton–Krylov startup strategy for RANS simulations, Journal of Computational Physics 397 (2019) 108741. doi:10.1016/j.jcp.2019.06.018.

[102] G. K. W. Kenway, C. A. Mader, P. He, J. R. R. A. Martins, Effective adjoint approaches for computational fluid dynamics, Progress in Aerospace Sciences 110 (2019) 100542. doi:10.1016/j.paerosci.2019.05.002.

[103] G. J. Kennedy, J. R. R. A. Martins, A parallel finite-element framework for large-scale gradient-based design optimization of high-performance structures, Finite Elements in Analysis and Design 87 (2014) 56–73. doi:10.1016/j.finel.2014.04.011.

[104] Y. Liao, N. Garg, J. R. R. A. Martins, Y. L. Young, Viscous fluid structure interaction response of composite hydrofoils, Composite Structures 212 (2019) 571–585. `doi:10.1016/j.compstruct.2019.01.043`.

[105] L. Ye, Role of matrix resin in delamination onset and growth in composite laminates, Composites Science and Technology 33 (4) (1988) 257 – 277.

[106] R. Cuntze, A. Freund, The predictive capability of failure mode concept-based strength criteria for multidirectional laminates, Composites Science and Technology 64 (3-4) (2004) 343–377. `doi:10.1016/s0266-3538(03)00218-5`.
URL `https://doi.org/10.1016/s0266-3538(03)00218-5`

[107] N. M. K. Poon, J. R. R. A. Martins, An adaptive approach to constraint aggregation using adjoint sensitivity analysis, Structural and Multidisciplinary Optimization 34 (1) (2007) 61–73. `doi:10.1007/s00158-006-0061-7`.

[108] G. J. Kennedy, J. E. Hicken, Improved constraint-aggregation methods, Computer Methods in Applied Mechanics and Engineering 289 (2015) 332–354. `doi:10.1016/j.cma.2015.02.017`.

[109] S. A. Brown, Displacement extrapolation for CFD+CSM aeroelastic analysis, in: Proceedings of the 35th AIAA Aerospace Sciences Meeting, Reno, NV, 1997, aIAA 1997-1090.

[110] J. R. R. A. Martins, J. J. Alonso, J. J. Reuther, A coupled-adjoint sensitivity analysis method for high-fidelity aero-structural design, Optimization and Engineering 6 (1) (2005) 33–62. `doi:10.1023/B:OPTE.0000048536.47956.62`.

[111] P. E. Gill, W. Murray, M. A. Saunders, SNOPT: An SQP algorithm for large-scale constrained optimization, SIAM Journal of Optimization 12 (4) (2002) 979–1006. `doi:10.1137/S1052623499350013`.

[112] P. E. Gill, W. Murray, M. A. Saunders, User's Guide for SNOPT Version 7: Software for Large-Scale Nonlinear Programming, Systems Optimization Laboratory, Stanford University, California, 94305-4023, technical Report (2007).

[113] N. Wu, G. Kenway, C. A. Mader, J. Jasa, J. R. R. A. Martins, pyOptSparse: a Python framework for large-scale constrained nonlinear optimization of sparse systems, Journal of Open Source Software 5 (54) (2020) 2564. `doi:10.21105/joss.02564`.

[114] D. McLean, Understanding Aerodynamics: arguing from the real physics, Wiley, West Sussex, UK, 2013.

[115] D. H. Hodges, G. A. Pierce, Introduction to Structural Dynamics and Aeroelasticity, 2nd Edition, Cambridge Aerospace Series, Cambridge University Press, 2011.

[116] A. Ihara, H. Watanabe, S. Shizukuishi, Experimental research of the effects of sweep on unsteady hydrofoil loadings in cavitation, Journal of Fluids Engineering 111 (3) (1989) 263. doi:10.1115/1.3243640.

[117] R. A. Cumming, W. B. Morgan, R. J. Boswell, Highly skewed propellers, in: Annual Meeting of SNAME, 1972.

[118] K. R. Laberteaux, S. L. Ceccio, Partial cavity flows. part 2. cavities forming on test objects with spanwise variation 431 (2001) 43–63. doi:10.1017/S0022112000002937.

[119] M. H. Shirk, T. J. Hertz, T. A. Weisshaar, Aeroelastic tailoring — theory, practice, and promise, Journal of Aircraft 23 (1) (1986) 6–18. doi:10.2514/3.45260.

[120] M. Blair, T. A. Weisshaar, Swept composite wing aeroelastic divergence experiments, Journal of Aircraft 19 (11) (1982) 1019–1024. doi:10.2514/3.44806.

[121] I. Lottati, Flutter and divergence aeroelastic characteristics for composite forward swept cantilevered wing, Journal of Aircraft 22 (11) (1985) 1001–1007. doi:10.2514/3.45238.

[122] T. A. Weisshaar, Aeroelastic stability and performance characteristics of aircraft with advanced composite sweptforward wing structures, Tech. rep., AFFDL (1978).

[123] T. A. Weisshaar, Aeroelastic tailoring of forward swept composite wings, Journal of Aircraft 18 (8) (1981) 669–676. doi:10.2514/3.57542.

[124] G. Zarruk, P. Brandner, B. Pearce, A. W. Phillips, Experimental study of the steady fluid-structure interaction of flexible hydrofoils, Journal of Fluids and Structure 51 (2014) 326–343. doi:10.1016/j.jfluidstructs.2014.09.009.

[125] M. T. Herath, B. G. Prusty, A. W. Phillips, N. St. John, Structural strength and laminate optimization of self-twisting composite hydrofoils using a genetic algorithm, Composite Structures 176 (2017) 359 – 378. doi:https://doi.org/10.1016/j.compstruct.2017.05.012.

[126] J. Jeong, F. Hussain, On the identification of a vortex, Journal of Fluid Mechanics 285 (1995) 69–94. doi:10.1017/S0022112095000462.

[127] D. T. Akcabay, Y. L. Young, Parametric analysis of the dynamic elastic response of composite hydrofoils and airfoils, in: Sixth International Symposium on Marine Propulsors, SMP'19, Rome, Italy, 2019.

[128] E. J. Chae, D. T. Akcabay, A. Lelong, J. A. Astolfi, Y. L. Young, Numerical and experimental investigation of natural flow-induced vibrations of flexible hydrofoils, Physics of Fluids 28 (7) (2016) 075102. doi:10.1063/1.4954785.

[129] E. J. Chae, D. T. Akcabay, Y. L. Young, Dynamic response and stability of a flapping foil in a dense and viscous fluid, Physics of Fluids 25 (10) (2013) 104106. doi:10.1063/1.4825136.

[130] A. Phillips, R. Cairns, C. Davis, P. Norman, P. Brandner, B. Pearce, Y. L. Young, Effect of material design parameters on the forced vibration response of composite hydrofoils in air and in water, in: Fifth International Symposium on Marine Propulsors, Espoo, Finland, 2017.

[131] D. Howe, Aircraft Loading and Structural Layout, AIAA, 2004.

[132] M. Felli, M. Falchi, G. Dubbioso, Hydrodynamic and hydroacoustic analysis of a marine propeller wake by TOMO-PIV, in: Fourth International Symposium on Marine Propulsors, Austin, Texas, 2015.

[133] J. Carlton, Marine Propellers and Propulsion, Butterworth-Heinemann, 2018.

[134] S. M. Smith, J. A. Venning, B. W. Pearce, Y. L. Young, P. A. Brandner, The influence of fluid–structure interaction on cloud cavitation about a stiff hydrofoil. part 1., Journal of Fluid Mechanics 896 (2020) A1. doi:10.1017/jfm.2020.321.

[135] S. M. Smith, J. A. Venning, B. W. Pearce, Y. L. Young, P. A. Brandner, The influence of fluid–structure interaction on cloud cavitation about a flexible hydrofoil. part 2., Journal of Fluid Mechanics 897 (2020) A28. doi:10.1017/jfm.2020.323.

[136] Y. Young, N. Garg, P. Brandner, B. Pearce, D. Butler, D. Clarke, A. Phillips, Material bend-twist coupling effects on cavitating response of composite hydrofoils, in: 10th International Cavitation Symposium (CAV2018), Baltimore, MD, 2018.

[137] S. Mishima, Design of cavitating propeller blades in non-uniform flow by numerical optimization, Ph.D. thesis, Massachusetts Institute of Technology. Dept. of Ocean Engineering (1996).

[138] S. Mishima, S. A. Kinnas, Application of a numerical optimization technique to the design of cavitating propellers in nonuniform flow, Journal of Ship Research 41 (02) (1997) 93–107.

[139] P. E. Griffin, S. A. Kinnas, A Design Method for High-Speed Propulsor Blades, Journal of Fluids Engineering 120 (3) (1998) 556–562. doi:10.1115/1.2820698.

[140] Z. Liu, Y. L. Young, Static divergence of self-twisting composite rotors, Journal of Fluids and Structures 26 (5) (2010) 841–847. doi:10.1016/j.jfluidstructs.2010.05.002.

[141] B. H. Maines, R. E. A. Arndt, Tip Vortex Formation and Cavitation, Journal of Fluids Engineering 119 (2) (1997) 413–419. doi:10.1115/1.2819149.

[142] V. H. Arakeri, Cavitation inception, Proceedings of the Indian Academy of Sciences Section C: Engineering Sciences 2 (2) (1979) 149–177. doi:10.1007/BF02845030.

[143] O. Ram, K. Agarwal, J. Katz, On the mechanisms that sustain the inception of attached cavitation, Journal of Fluid Mechanics 901 (2020) R4. doi:10.1017/jfm.2020.646.

[144] Z. ru Li, T. van Terwisga, On the capability of multiphase rans codes to predict cavitation erosion, in: Second International Symposium on Marine Propulsors, Hamburg, Germany, 2011.

[145] D.-Q. Li, M. Grekula, P. Lindell, A modified sst k-ω turbulence model to predict the steady and unsteady sheet cavitation on 2d and 3d hydrofoils, in: Proceedings of the 7th International Symposium on Cavitation, Ann Arbor, Michigan, USA, 2009.

[146] B. Ji, X. Luo, R. E. Arndt, X. Peng, Y. Wu, Large eddy simulation and theoretical investigations of the transient cavitating vortical flow structure around a naca66 hydrofoil, International Journal of Multiphase Flow 68 (2015) 121 – 134. doi:https://doi.org/10.1016/j.ijmultiphaseflow.2014.10.008.

[147] Y. Young, Time-dependent hydroelastic analysis of cavitating propulsors, Journal of Fluids and Structures 23 (2) (2007) 269–295. doi:https://doi.org/10.1016/j.jfluidstructs.2006.09.003.

[148] Y. Young, J. Baker, M. Motley, Reliability-based design and optimization of adaptive marine structures, Composite Structures 92 (2010) 244–253. doi:10.1016/j.compstruct.2009.07.024.

[149] N. P. Bons, X. He, C. A. Mader, J. R. R. A. Martins, Multimodality in aerodynamic wing design optimization, AIAA Journal 57 (3) (2019) 1004–1018. doi:10.2514/1.J057294.

[150] G. K. W. Kenway, J. R. R. A. Martins, Buffet-onset constraint formulation for aerodynamic shape optimization, AIAA Journal 55 (6) (2017) 1930–1947. doi:10.2514/1.J055172.

[151] Y. Liao, S. He, J. R. R. A. Martins, Y. L. Young, Hydrostructural optimization of generic composite hydrofoils, in: AIAA SciTech Forum, AIAA, Orlando, FL, 2020. doi:10.2514/6.2020-0164.

[152] P. Papanikos, K. I. Tserpes, S. Pantelakis, Modelling of fatigue damage progression and life of cfrp laminates, Fatigue & Fracture of Engineering Materials & Structures 26 (1) (2003) 37–47.

[153] P. Soden, A. Kaddour, M. Hinton, Recommendations for designers and researchers resulting from the world-wide failure exercise, Composites Science and Technology 64 (3-4) (2004) 589–604. doi:10.1016/s0266-3538(03)00228-8.
URL https://doi.org/10.1016/s0266-3538(03)00228-8

[154] J. R. R. A. Martins, N. M. K. Poon, On structural optimization using constraint aggregation, in: Proceedings of the 6th World Congress on Structural and Multidisciplinary Optimization, Rio de Janeiro, Brazil, 2005.

[155] M. Drela, XFOIL — An analysis and design system for low Reynolds number airfoils, in: Low Reynolds number aerodynamics, Notre Dame,Germany, Federal Republic of, 1989.

[156] U. Icardi, S. Locatto, A. Longo, Assessment of recent theories for predicting failure of composite laminates, Applied Mechanics Reviews 60 (2) (2007) 76. `doi:10.1115/1.2515639`.
URL `https://doi.org/10.1115/1.2515639`

[157] A. Orifici, I. Herszberg, R. Thomson, Review of methodologies for composite material modelling incorporating failure, Composite Structures 86 (1-3) (2008) 194–210. `doi:10.1016/j.compstruct.2008.03.007`.
URL `https://doi.org/10.1016/j.compstruct.2008.03.007`

[158] A. Kaddour, M. Hinton, P. Soden, A comparative study of failure theories and predictions for fibre polymer composite laminates, in: Failure Criteria in Fibre-Reinforced-Polymer Composites, Elsevier, 2004, pp. 644–701. `doi:10.1016/b978-008044475-8/50022-6`.
URL `https://doi.org/10.1016/b978-008044475-8/50022-6`

[159] A. J. Acosta, Hydrofoils and Hydrofoil Craft, Annual Review of Fluid Mechanics`doi:10.1146/annurev.fl.05.010173.001113`.

[160] A. Damley-Strnad, C. M. Harwood, Y. L. Young, Hydrodynamic Performance and Hysteresis Response of Hydrofoils in Ventilated Flows, in: Sixth International Symposium on Marine Propulsors, Rome, Italy, 2019.

[161] J. Giron-Sierra, S. Esteban, B. De Andres, J. Diaz, J. Riola, Experimental Study of Controlled Flaps and T-Foil for Comfort Improvement of a Fast Ferry, IFAC Proceedings Volumes 34 (7) (2001) 261–266. `doi:10.1016/s1474-6670(17)35093-0`.

[162] T. Simpson, J. R. R. A. Martins, The future of multidisciplinary design optimization: Advancing the design of complex engineered systems., NSF workshop report, NSF (September 2010).

[163] J. O. Scheeer, J. Auslaender, Experimental and theoretical performance of a supercavitating hydrofoil operating near a free surface, Journal of Aircraft 2 (2) (1965) 144–152. `doi:10.2514/3.43631`.

[164] J. R. Binns, P. A. Brandner, J. Plouhinec, The effect of heel angle and free-surface proximity on the performance and strut wake of a moth sailing dinghy rudder t-foil, in: 3rd High Performance Yacht Design Conference, Auckland,, 2008.

[165] B. Beaver, J. Zseleczky, Full scale measurements on a hydrofoil International Moth, in: 19th Chesapeake Sailing Yacht Symposium, CSYS, 2009.

[166] J. Mehr, M. R. Davis, J. Lavroff, Low Reynolds number performance of a model scale T-foil, Transactions of the Royal Institution of Naval Architects Part A: International Journal of Maritime Engineering 157 (Part A3) (2015) 175–188. doi:10.3940/rina.ijme.2015.a3.336.

[167] A. J. E. Ashworth Briggs, Free surface interaction of a ‘ T-foil ’ hydrofoil, Ph.D. thesis, University of Tasmania (2018).

[168] S. Day, M. Cocard, M. Troll, Experimental measurement and simplified prediction of T-foil performance for monohull dinghies, in: THE 23RD CHESAPEAKE SAILING YACHT SYMPOSIUM, ANNAPOLIS, MARYLAND, 2019.

[169] N. R. Secco, J. R. R. A. Martins, RANS-based aerodynamic shape optimization of a strut-braced wing with overset meshes, Journal of Aircraft 56 (1) (2019) 217–227. doi:10.2514/1.C034934.

[170] Z. Lyu, G. K. W. Kenway, J. R. R. A. Martins, Aerodynamic shape optimization investigations of the Common Research Model wing benchmark, AIAA Journal 53 (4) (2015) 968–985. doi:10.2514/1.J053318.

[171] P. F. White, R. Beck, K. J. Maki, D. J. Piro, A Combined CFD / Potential Flow Simulation Method for Prediction of Hydrodynamic Maneuvering Forces, in: 33rd International Workshop on Water Waves and Floating Bodies, Guidel-Plages, FRANCE, 2018.

[172] K. L. Wadlin, C. L. Shuford, J. R. McGehee, A Theoretical and Experimental Investigation of the Lift and Drag Characteristics of Hydrofoils at Subcritical and Supercritical Speeds, Report NACA-TR-1232, Langley Aeronautical Laboratory National Advisory Committee for Aeronautics. Langley Aeronautical Lab (1955).
URL https://digital.library.unt.edu/ark:/67531/metadc60622/

[173] A. N. Vladimirov, Approximate hydrodynamic design of a finite span hydrofoil, Tech. Rep. NACA TECHNICAL MEMORANDUM 1341 (Jun. 1955).

[174] T. Kaiho, A new method for solving surface-piercing-strut problems, Michigan Univ. Final Report.

[175] M. Daskovsky, The hydrofoil in surface proximity, theory and experiment, Ocean Engineering 27 (10) (2000) 1129–1159. doi:https://doi.org/10.1016/S0029-8018(99)00032-3.

[176] Y. L. Young, S. A. Kinnas, Analysis of supercavitating and surface-piercing propeller flows via BEM, Computational Mechanics 32 (4-6) (2003) 269–280. doi:10.1007/s00466-003-0484-6.

[177] J. P. Breslin, Application of Ship-Wave Theory to the Hydrofoil of Finite Span, Journal of Ship Research 1 (02) (1957) 27–55. doi:10.5957/jsr.1957.1.2.27.

[178] T. P. Philippidis, V. A. Passipoularidis, Residual strength after fatigue in composites: Theory vs. experiment, International Journal of Fatigue 29 (12) (2007) 2104–2116. doi:https://doi.org/10.1016/j.ijfatigue.2007.01.019.
URL http://www.sciencedirect.com/science/article/pii/S0142112307000369

[179] P. T. Maung, B. G. Prusty, A. W. Phillips, N. A. St John, Curved fibre path optimisation for improved shape adaptive composite propeller blade design, Composite Structures 255 (2021) 112961. doi:https://doi.org/10.1016/j.compstruct.2020.112961.

[180] Y. Shi, T. Yang, J. Bai, L. Lu, H. Wang, Research of transition criterion for semi-empirical prediction method at specified transonic regime, Aerospace Science and Technologydoi:10.1016/J.AST.2019.03.012.

[181] Y. Shi, C. A. Mader, S. He, G. L. O. Halila, J. R. R. A. Martins, Natural laminar-flow airfoil optimization design using a discrete adjoint approach, AIAA Journal 58 (11) (2020) 4702–4722. doi:10.2514/1.J058944.

[182] M. O. Woolliscroft, A linearized free-surface method for prediction of unsteady ship maneuvering, Ph.D. thesis, Naval Architecture and Marine Engineering in The University of Michigan (2015).

APPENDIX A

Stress distributions for optimized hydrofoil with different material configurations

A.1 Optimized aluminum hydrofoil with material failure

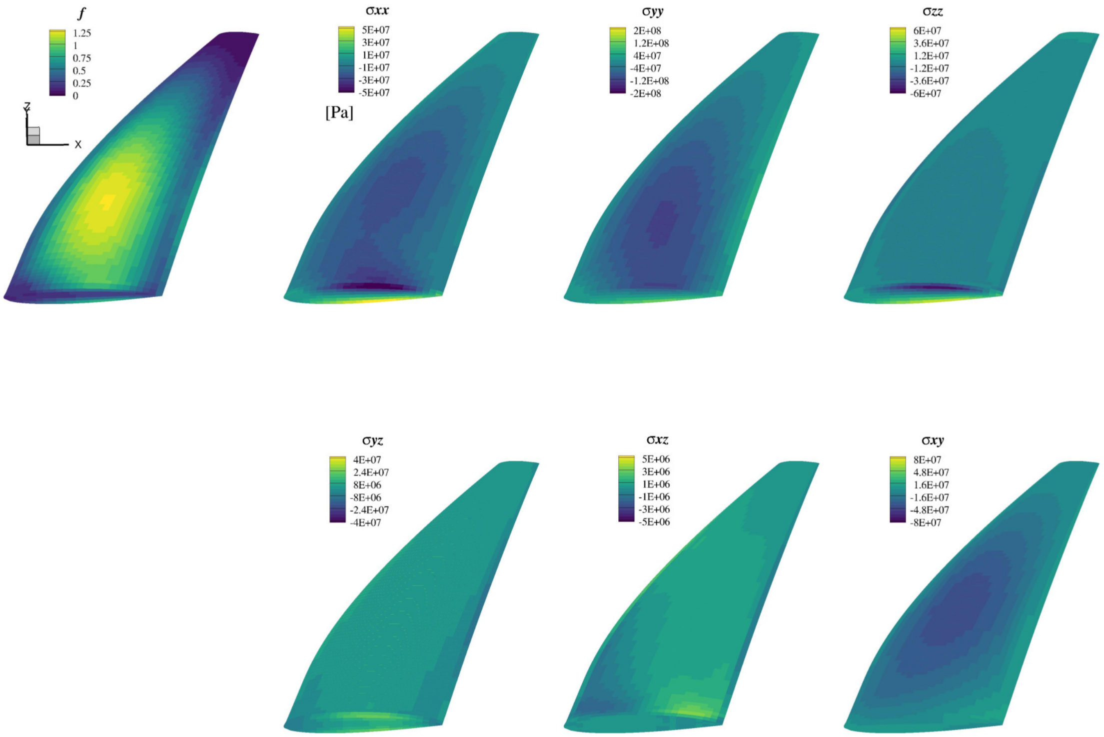

Figure A.1: Material failure indicator and stress contours for the optimized aluminum hydrofoil with the material failure constraint only imposed near the root region. The material failure occurs around $y/b = 0.3$ and is mainly caused by σ_{yy} and σ_{xy}.

A.2 Optimized aluminum hydrofoil without material failure

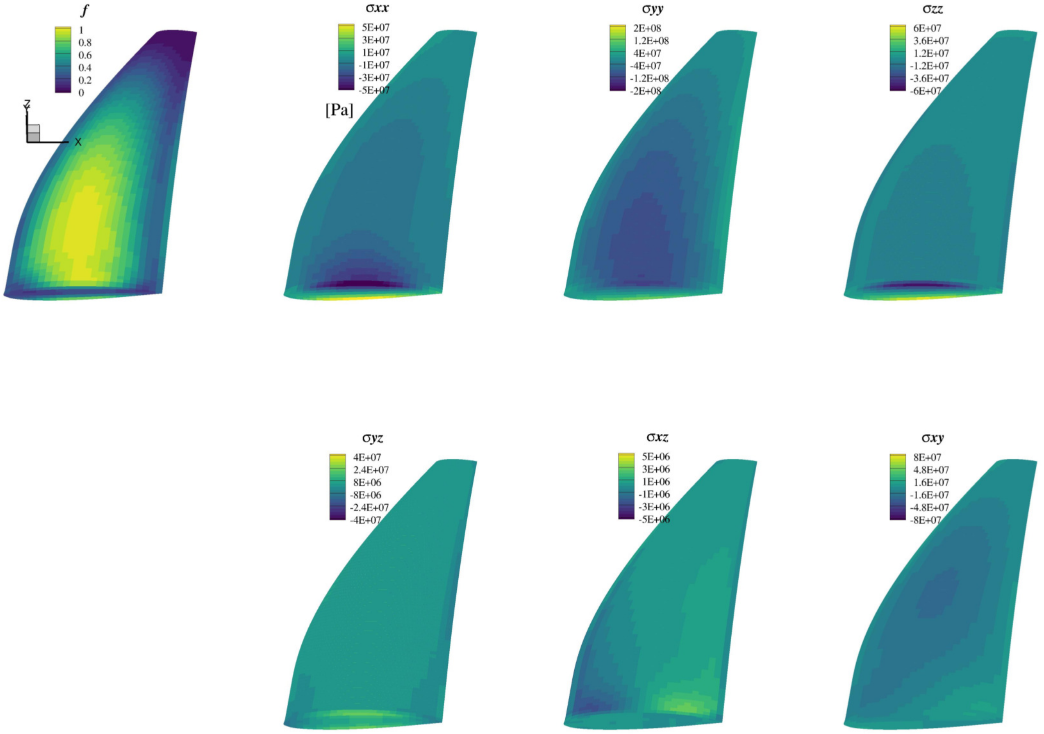

Figure A.2: Material failure indicator and stress contours for the optimized aluminum hydrofoil with the material failure constraint imposed over the whole structural domain. The maximum material failure index f_{max} occurs around $y/b = 0.2$ and is mainly caused by σ_{yy} and σ_{xy}.

A.3 Optimized single-layer CFRP (MHY) hydrofoil

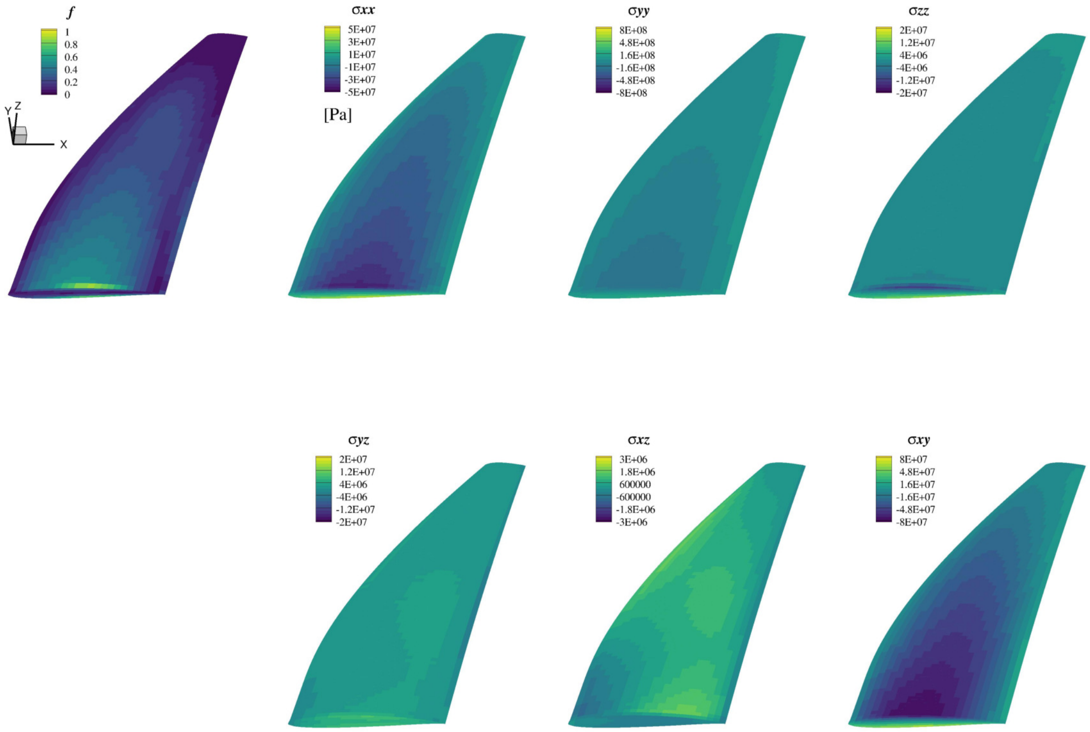

Figure A.3: Material failure indicator and stress contours for the optimized single-layer CFRP hydrofoil.

A.4 Optimized multi-layer CFRP (MHY) hydrofoil

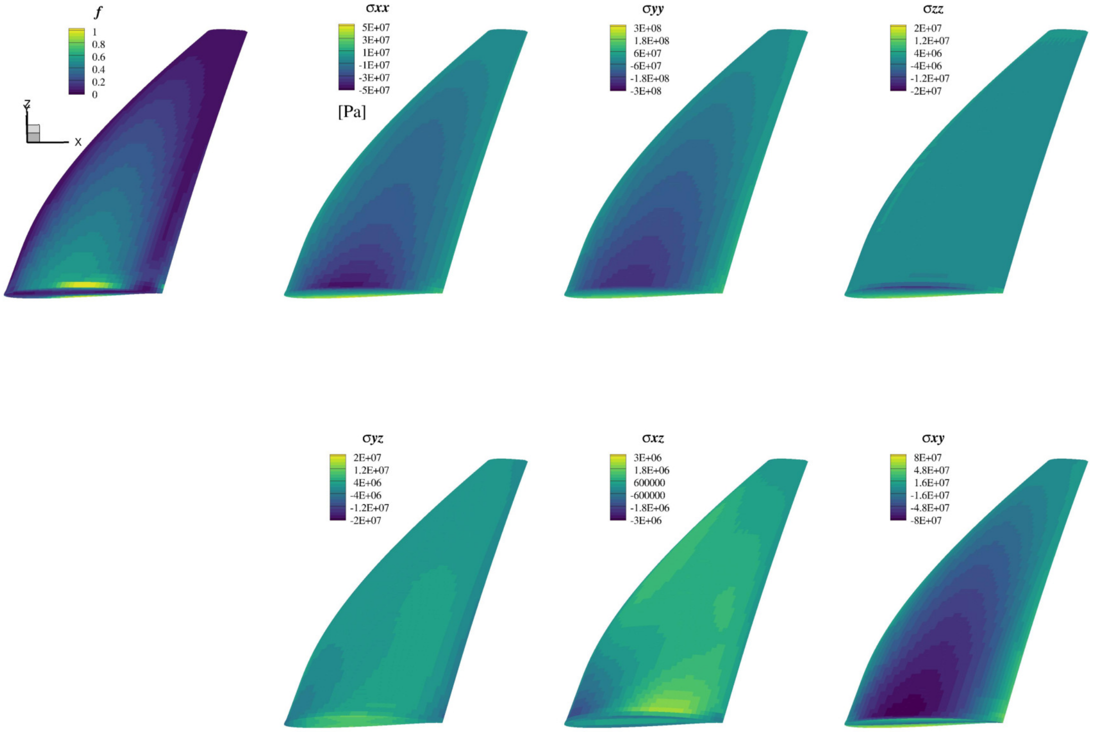

Figure A.4: Material failure indicator and stress contours for the optimized multi-layer CFRP hydrofoil.

A.5 Optimized single-layer CFRP (MCO) hydrofoil

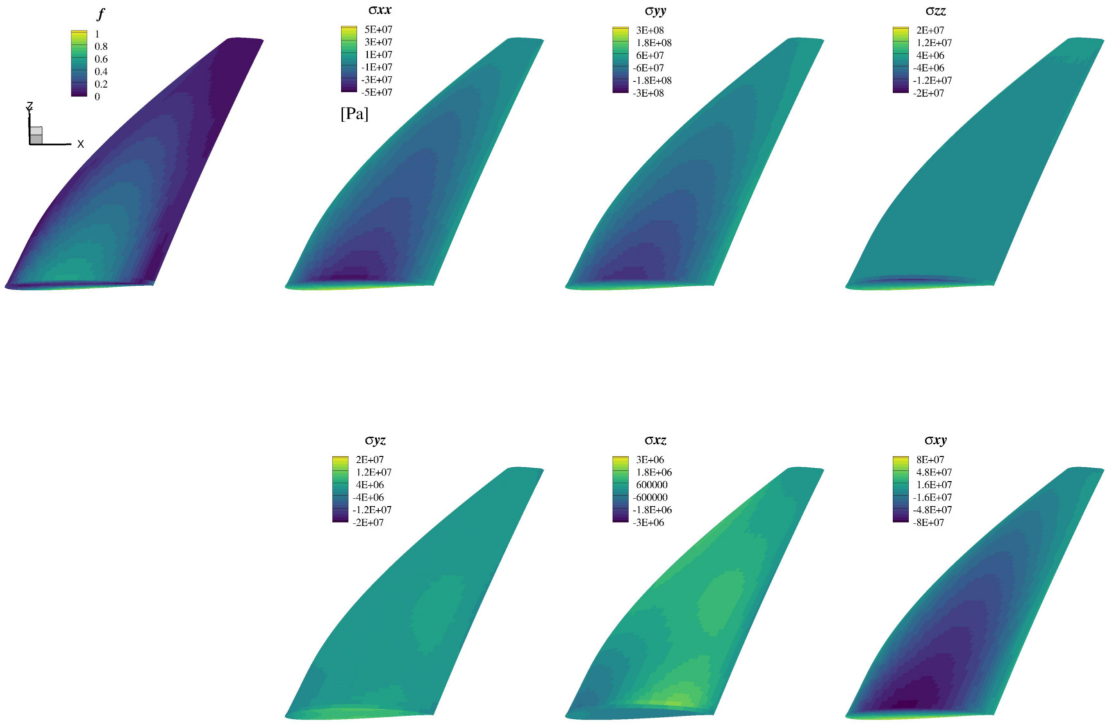

Figure A.5: Material failure indicator and stress contours for the optimized single-layer CFRP (MCO) hydrofoil.

A.6 Optimized multi-layer CFRP (MCO) hydrofoil

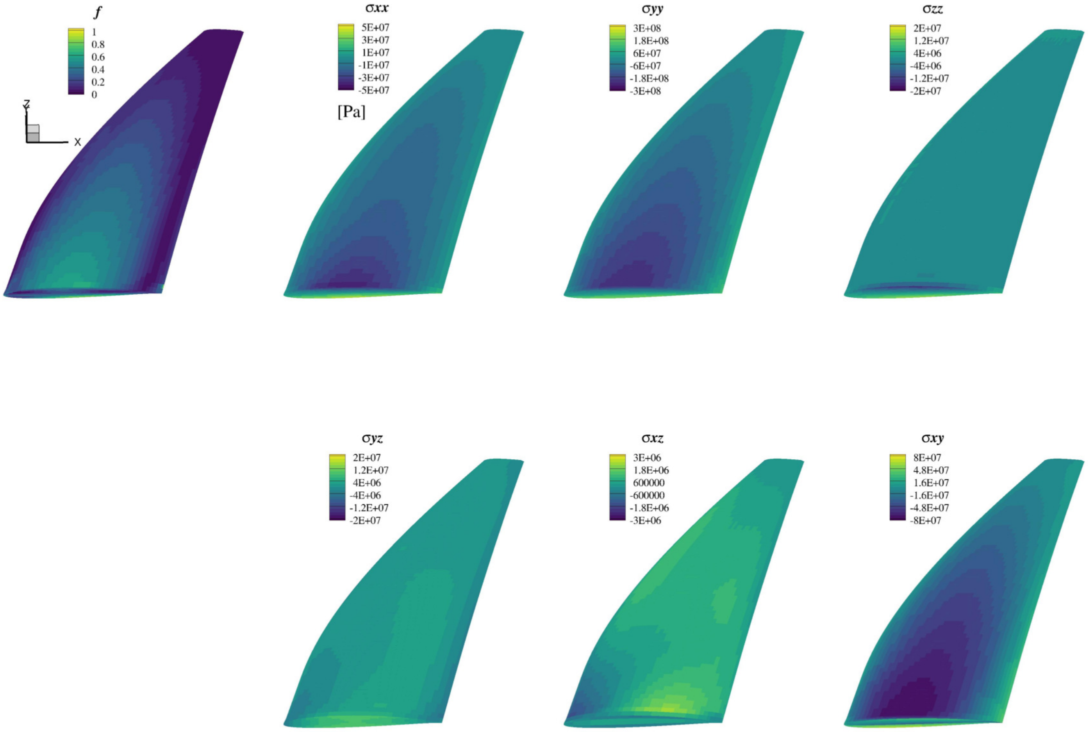

Figure A.6: Material failure indicator and stress contours for the optimized multi-layer CFRP (MCO) hydrofoil.

APPENDIX B

A derivation of the constant pressure boundary condition from RANS

The constant pressure boundary condition can also be derived from RANS directly A derivation of the linearized free surface boundary condition in RANS has been shown by [182]. We will briefly review the procedure here. If we start from the RANS equations, the total zero stress on the free surface gives

$$\begin{aligned}
&(p-\rho g\eta)\,\eta_x - 2\mu\left(\frac{\partial u_x}{\partial x} - \frac{1}{3}\left(\frac{\partial u_y}{\partial y} + \frac{\partial u_z}{\partial z}\right)\right)\eta_x - \mu\left(\frac{\partial u_x}{\partial y} + \frac{\partial u_y}{\partial x}\right)\eta_y + \mu\left(\frac{\partial u_x}{\partial z} + \frac{\partial u_z}{\partial x}\right)\eta_z = p_{\text{atm}}\eta_x \\
&(p-\rho g\eta)\,\eta_y - \mu\left(\frac{\partial u_y}{\partial x} + \frac{\partial u_x}{\partial y}\right)\eta_x - 2\mu\left(\frac{\partial u_y}{\partial y} - \frac{1}{3}\left(\frac{\partial u_x}{\partial x} + \frac{\partial u_z}{\partial z}\right)\right)\eta_y + \mu\left(\frac{\partial u_y}{\partial z} + \frac{\partial u_z}{\partial y}\right)\eta_z = p_{\text{atm}}\eta_y \qquad \text{(B.1)} \\
&(p-\rho g\eta)\,\eta_z - \mu\left(\frac{\partial u_z}{\partial x} + \frac{\partial u_x}{\partial z}\right)\eta_x + \mu\left(\frac{\partial u_z}{\partial y} + \frac{\partial u_y}{\partial z}\right)\eta_y - 2\mu\left(\frac{\partial u_z}{\partial z} - \frac{1}{3}\left(\frac{\partial u_y}{\partial y} + \frac{\partial u_x}{\partial x}\right)\right)\eta_z = p_{\text{atm}}\eta_z
\end{aligned}$$

where η_x, η_y, and η_z are x, y, z components of the normal vector of free surface $\vec{n}$.

If assuming small wave height, wave slopes, and small velocity gradients, we can simplify the boundary condition by neglecting higher-order terms,

$$\begin{aligned}
(p)\,\eta_x + \mu\left(\frac{\partial u_x}{\partial z} + \frac{\partial u_z}{\partial x}\right)\eta_z &= p_{\text{atm}}\eta_x \\
(p)\,\eta_y + \mu\left(\frac{\partial u_y}{\partial z} + \frac{\partial u_z}{\partial y}\right)\eta_z &= p_{\text{atm}}\eta_y \qquad \text{(B.2)} \\
(p-\rho g\eta) - 2\mu\left(\frac{\partial u_z}{\partial z} - \frac{1}{3}\left(\frac{\partial u_y}{\partial y} + \frac{\partial u_x}{\partial x}\right)\right) &= p_{\text{atm}}
\end{aligned}$$

Again, assuming small wave height ($\eta_x, \eta_y \ll \eta_z \approx 1$)

$$\begin{aligned} \mu\left(\frac{\partial u_x}{\partial z}+\frac{\partial u_z}{\partial x}\right) &= 0 \\ \mu\left(\frac{\partial u_y}{\partial z}+\frac{\partial u_z}{\partial y}\right) &= 0 \\ (p-\rho g\eta)-2\mu\left(\frac{\partial u_z}{\partial z}-\frac{1}{3}\left(\frac{\partial u_y}{\partial y}+\frac{\partial u_x}{\partial x}\right)\right) &= p_{\text{atm}} \end{aligned} \tag{B.3}$$

If we consider a high Froude number condition (inertia >> gravity effect),

$$p-2\mu\left(\frac{\partial u_z}{\partial z}-\frac{1}{3}\left(\frac{\partial u_y}{\partial y}+\frac{\partial u_x}{\partial x}\right)\right) = p_{\text{atm}} \tag{B.4}$$

There are two ways to treat the boundary conditions:

1. We can assume high Reynolds number conditions and thus neglect the small viscous terms

$$p = p_{\text{atm}} \tag{B.5}$$

2. We can separate the pressure and viscous terms, and enforce

$$\begin{aligned} &p = p_{\text{atm}} \\ &\frac{\partial u_z}{\partial z}-\frac{1}{3}\left(\frac{\partial u_y}{\partial y}+\frac{\partial u_x}{\partial x}\right) = 0 \end{aligned} \tag{B.6}$$

Both of these two ways lead to a constant pressure boundary condition, which is also derived from the negative image method.